Identifying and Distinguishing Quenching Galaxies with Spatially Resolved Star Formation

by

Cameron Lawlor-Forsyth

A thesis
presented to the University of Waterloo
in fulfillment of the
thesis requirement for the degree of
Doctor of Philosophy
in
Physics

Waterloo, Ontario, Canada, 2026

© Cameron Lawlor-Forsyth 2026

Examining Committee Membership

The following served on the Examining Committee for this thesis. The decision of the Examining Committee is by majority vote.

External Examiner:	Rachel Bezanson Associate Professor, Dept. of Physics and Astronomy, University of Pittsburgh
Supervisor:	Michael Balogh Professor, Dept. of Physics and Astronomy, University of Waterloo
Internal Member:	Will Percival Professor, Dept. of Physics and Astronomy, University of Waterloo
Internal-External Member:	Andrea Brookfield Associate Professor, Dept. of Earth and Environmental Sciences, University of Waterloo
Other Members:	James Taylor Associate Professor, Dept. of Physics and Astronomy, University of Waterloo
	Dustin Lang Adjunct Faculty, Dept. of Physics and Astronomy, University of Waterloo

Author's Declaration

This thesis consists of material all of which I authored or co-authored: see Statement of Contributions included in the thesis. This is a true copy of the thesis, including any required final revisions, as accepted by my examiners.

I understand that my thesis may be made electronically available to the public.

Statement of Contributions

I am the sole author of Chapter 1 and Chapter 5, which were written under the supervision of Michael Balogh. The remaining chapters in this thesis are based on the following articles:

Chapter 2: **Cameron Lawlor-Forsyth**, Michael L. Balogh, Elizaveta Sazonova, Cameron R. Morgan, Sean L. McGee, and Gregory H. Rudnick, 2026, *Identifying and Distinguishing Quenching Galaxies with Spatially Resolved Star Formation in TNG50*, The Astrophysical Journal, 1000, 61 (26pp). doi:10.3847/1538-4357/ae4502

Chapter 3: **Cameron Lawlor-Forsyth**, Michael L. Balogh, Sean L. McGee, and Gregory H. Rudnick, 2026, *Identifying and Distinguishing Quenching Galaxies with Spatially Resolved Star Formation in Mock CASTOR and NGRST Observations*, The Open Journal of Astrophysics, submitted (23pp). doi:10.48550/arXiv.2607.15638

Chapter 4: **Cameron Lawlor-Forsyth**, Michael L. Balogh, Sean L. McGee, and Gregory H. Rudnick, 2026, *Identifying and Distinguishing Quenching Galaxies with Spatially Resolved Star Formation in the Hubble Frontier Fields*, The Open Journal of Astrophysics, submitted (25pp). doi:10.48550/arXiv.2607.21560

Appendix C.2: **Cameron Lawlor-Forsyth**, 2026, *Estimating Galaxy Cluster Infall Time from Phase Space in TNG*, The Open Journal of Astrophysics, submitted (5pp). doi:10.48550/arXiv.2607.20406

In each of the above listed articles, I am the first author, where I prepared the data, performed the analysis, and wrote the initial draft of the manuscript. The second author, Michael Balogh, is my supervisor, and provided supervision, consultation, and feedback for each project, as well as comments for the manuscript draft. The remaining coauthors are collaborators that provided comments on how to improve the manuscript before submission for publication. Figures adapted from the literature in Chapter 1 are labeled as such. All other work in this thesis is my own. The use of "we" in Chapters 1 and 5 was chosen to be consistent with Chapters 2, 3, and 4.

Abstract

This thesis is concerned with understanding galaxy evolution, in particular how galaxies have their star formation shut down, or "quenched." The process of quenching transforms actively star forming galaxies into passive, quiescent, or otherwise dormant galaxies with very low levels of star formation. Many physical mechanisms have been proposed to describe quenching, and can be divided into internal processes or external processes due to environment. These quenching mechanisms should result in different spatial signatures when viewing the distribution of star formation in a galaxy, but the spatial and temporal evolution of these different processes remains unclear. Therefore, spatially resolved observations of star formation are necessary to investigate quenching mechanisms, and will prove critical for understanding galaxy evolution in the next decade.

The first section of this thesis is concerned with understanding galaxy quenching in simulations. Using the high-resolution IllustrisTNG simulation, quenching signatures for 361 galaxies with $M_* \geqslant 10^{9.5}\ M_\odot$ by $z = 0$ are investigated, and four morphological metrics that collectively describe the spatial distribution of star formation within these galaxies are developed. The evolution of the metrics is studied through the galaxy quenching episodes, relative to a control sample of normal star forming galaxies which show no evolution. Two prominent modes are found which describe the evolution of quenching, where the first is consistent with inside-out quenching, and numbers 78 galaxies, while the second is consistent with outside-in quenching, numbering 185 galaxies. Inside-out quenched galaxies are generally centrals in the field, and are more massive than outside-in quenched galaxies, which tend to be satellites in denser environments like groups and clusters. Inside-out quenched galaxies take $\sim$2.5 Gyr to quench, while outside-in quenched galaxies take $\sim$1.5 Gyr to quench, and begin quenching $\sim$1 Gyr after being accreted onto a more massive structure.

The second section of this thesis concentrates on adapting the morphological metrics from the simulation for use with mock observations. Using the sample of simulated galaxies, high-resolution mock observations consistent with Cosmological Advanced Survey Telescope for Optical and UV Research (CASTOR) and Nancy Grace Roman Space Telescope (NGRST) imaging are produced for nearly 70,000 galaxies at $z = 0.5$, covering the ultraviolet to the near-infrared. These mock observations are additionally consistent with Hubble Space Telescope imaging. A flexible hybrid star formation history is used to fit the resulting spectral energy distributions from the mock photometry. Spatially resolved star formation rate and stellar mass are accurately recovered when compared with the simulation, and with observational adaptations to the morphological metrics, these parameters are likewise recovered to high fidelity.

The third section of this thesis investigates galaxy quenching for observed galaxies in the Hubble Frontier Fields at $z \approx 0.4$, and builds on the previous sections. The spatially resolved spectral energy distributions are fit for a sample of 1437 galaxies with $M_* \geqslant 10^8\ M_\odot$ and SFR $\geqslant 10^{-3}\ M_\odot\ \mathrm{yr}^{-1}$, to determine star formation rate and stellar mass radial profiles. The observational morphological metrics are then calculated using these profiles, and are compared with the simulated galaxies from IllustrisTNG. A population consistent with an inside-out quenching mechanism is found, and numbers 129 galaxies, as well as a population consistent with an outside-in quenching mechanism, numbering 70 galaxies. Inside-out quenching galaxies are more massive than outside-in quenching galaxies, and are more often found in clusters, while the outside-in population often reside in the field. The inside-out population makes up $\sim$30% of the sample in clusters at high stellar mass ($M_* \gtrsim 10^{10.5}\ M_\odot$). Both populations show little dependence on cluster infall time, except the high mass inside-out population, which commonly has older inferred infall times. These results also suggest that the quenching prescription within simulations is incomplete, as it does not predict inside-out quenching for high-mass satellites.

Collectively, this thesis highlights the need for spatially resolved observations to investigate different quenching mechanisms, in both simulations and observations, where simulations can help form a framework which can be adapted to observations. Fortunately, upcoming large-scale galaxy surveys will provide millions of galaxies suitable for spatially resolved analyses, in order to better understand galaxy quenching and evolution.

Acknowledgements

I would like to thank my supervisor, Michael Balogh, for his guidance, patience, and encouragement throughout the course of my PhD. Your insight and expertise in the field has been invaluable during my studies. Thank you for sticking with me, and for being a sounding board for different ideas and approaches through the years. Truly, the deepest thanks.

I would also like to thank the members of my committee, Will Percival, James Taylor, Dustin Lang, and Andrea Brookfield for their helpful comments and suggestions throughout the years.

I would next like to thank my collaborators, including Sean McGee, Greg Rudnick, Liza Sazonova, and Cam Morgan for conversations, comments, suggestions, and encouragement on my various projects. Without your contributions, the papers would not be in their present state, so thanks very much.

Next, I would like to thank my fellow grad students and members of the Waterloo Centre for Astrophysics for providing levity and distractions through my time at the university. I could always count on good times on Friday afternoons at the Grad House.

I would like to thank my friends and family for supporting and encouraging me throughout my PhD. Living in Ontario and flying back and forth to Winnipeg multiple times a year was busy, but I always enjoyed being able to see the people that I care about the most in this world. Without their help, this degree would have gone from challenging to completely unbearable.

Finally, and most importantly, I want to thank my best friend, my constant champion, and the most beautiful and intelligent person that I have ever had the good fortune to meet, my wife Anissa. Honestly, I do not know if I could have gotten through this without you. Both of us working on a PhD at the same time was not the easiest, but you have always had my back and I know that you will always be there for me, no matter what happens. Thanks for being by my side every step of the way on this long journey. I cannot put into words how much you mean to me. Lots of love Niss!

Dedication

This thesis is dedicated to the memory of my dad, Craig Forsyth. I wish you were here.

Table of Contents

Examining Committee Membership ii

Author's Declaration iii

Statement of Contributions iv

Abstract v

Acknowledgements vii

Dedication viii

List of Figures xiv

List of Tables xvii

List of Abbreviations xviii

Quote xxi

1 Introduction 1

1.1 A Brief Historical Perspective 1

1.2 Galaxy Evolution 2

1.2.1 Structure and Galaxy Formation 2

1.2.2 Secular Evolution and Gas Cooling . . . 5
1.2.3 Star Formation, Stellar Evolution, and Stellar Properties . . . 7
1.2.4 Star Formation Rate Indicators . . . 11
1.2.5 Galaxy Classification and the Star Forming Main Sequence . . . 13
1.2.6 The Role of Environment and Mergers . . . 18
1.3 Galaxy Quenching . . . 19
1.3.1 Internal Mechanisms . . . 20
1.3.2 External Mechanisms . . . 21
1.3.3 The Inside-out and Outside-in Framework . . . 23
1.4 Spectral Energy Distribution Fitting . . . 25
1.4.1 Stellar Population Synthesis . . . 25
1.4.2 Model Parameter Choices . . . 28
1.5 Spatially Resolved Observations . . . 31
1.6 Cosmological Simulations . . . 33
1.7 This Thesis . . . 34

2 Identifying and Distinguishing Quenching Galaxies with Spatially Resolved Star Formation in TNG50 36
2.1 Introduction . . . 36
2.2 Methodology . . . 40
2.2.1 IllustrisTNG . . . 40
2.2.2 Distinguishing star forming galaxies from quenched galaxies using star formation histories . . . 41
2.2.3 Morphological metrics . . . 49
2.2.4 Classifying galaxies according to morphological evolution during quenching . . . 52
2.3 Results . . . 54
2.3.1 Differences between populations . . . 54
2.3.2 Metric evolution per population . . . 60

2.3.3 Recovering quenched populations and progress . . . 63
2.4 Discussion . . . 69
2.4.1 Comparison with literature results . . . 70
2.4.2 Feasibility with galaxy surveys . . . 73
2.4.3 Limitations and future directions . . . 76
2.5 Summary and Conclusion . . . 77

3 Identifying and Distinguishing Quenching Galaxies with Spatially Resolved Star Formation in Mock CASTOR and NGRST Observations 80
3.1 Introduction . . . 80
3.2 Methodology . . . 84
3.2.1 IllustrisTNG and Galaxy Sample . . . 84
3.2.2 CASTOR Surveys . . . 85
3.2.3 NGRST Surveys . . . 89
3.2.4 Creating Mock Observations . . . 90
3.2.5 Spectral Energy Distribution Fitting . . . 98
3.2.6 Morphological Metrics . . . 104
3.3 Results . . . 105
3.4 Discussion . . . 111
3.4.1 Comparison with Literature Results . . . 112
3.4.2 Surface Brightness Effects . . . 113
3.4.3 Application to Future CASTOR and NGRST Surveys . . . 115
3.4.4 Limitations and Future Directions . . . 118
3.5 Summary and Conclusion . . . 122

4 Identifying and Distinguishing Quenching Galaxies with Spatially Resolved Star Formation in the Hubble Frontier Fields 124
4.1 Introduction . . . 124
4.2 Data . . . 128

4.2.1 Hubble Frontier Fields . . . 128
4.2.2 Data Preparation . . . 134
4.2.3 Sample Selection . . . 135
4.3 Methodology . . . 137
4.3.1 Annular Photometry and Visual Inspection . . . 137
4.3.2 Spectral Energy Distribution Fitting . . . 138
4.3.3 Star Forming Main Sequence Determination . . . 141
4.3.4 Quenching Process Classification . . . 143
4.4 Results . . . 145
4.5 Discussion . . . 156
4.5.1 Comparison with Literature Results . . . 157
4.5.2 Feasibility with Galaxy Surveys . . . 162
4.5.3 Limitations and Future Directions . . . 163
4.6 Summary and Conclusion . . . 166

5 Conclusion and Future **168**
5.1 Summary . . . 168
5.2 Synthesis of Results . . . 171
5.3 Future Directions . . . 173
5.3.1 Future Surveys . . . 174

References **176**

APPENDICES **208**

A Appendices from Chapter 2 **209**
A.1 Example diagnostic figures for an inside-out quenched galaxy . . . 209
A.2 Morphological metrics using 3D positional information . . . 212
A.3 Morphological metric evolution plots for the ambiguously quenched class . . . 214
A.4 Relative importance of the morphological metrics . . . 216

B Appendices from Chapter 3 **218**

B.1 Alternative Morphological Metric Adaptations 218

C Appendices from Chapter 4 **221**

C.1 Filters per Cluster/Field 221

C.2 IllustrisTNG and Phase Space Diagrams 221

C.3 SED Fitting Procedure for COSMOS-Web 226

C.4 Morphological Metric Distributions for Star Forming Galaxies 227

C.5 Overlap with CANUCS and UNCOVER 229

D Technical Acknowledgments **231**

List of Figures

1.1 Hierarchical growth of structure in the Universe 4
1.2 Schematic showing components of secular galaxy evolution 6
1.3 Example stellar spectra, evolutionary tracks, and isochrones 9
1.4 Star formation rate as a function of stellar mass for SDSS galaxies 15
1.5 Hubble sequence of morphological classification for galaxies 17
1.6 Schematic illustrating inside-out and outside-in quenching 24
1.7 Spectral energy distributions for stellar populations of different ages 27
1.8 Star formation histories and resulting spectral energy distributions 30

2.1 Star formation histories for different galaxy types 44
2.2 Star formation rate as a function of stellar mass at $z = 0$ 45
2.3 Galaxy stellar mass functions 48
2.4 Postage stamps and sSFR radial profiles for an outside-in quenched galaxy 50
2.5 Morphological metric evolution for an outside-in quenched galaxy 53
2.6 Quenching onset time as a function of satellite time 57
2.7 Quenching timescale as a function of stellar mass 59
2.8 Morphological metric evolution for all galaxies, binned by progress epoch . 61
2.9 $R_{\rm SF}$ as a function of $C_{\rm SF}$, binned by progress epoch 64
2.10 Nearest neighbor classification accuracy as a function of quenching progress 66
2.11 Recovery of quenching episode progress, binned by quenched population . . 68

3.1 CASTOR and NGRST filter curves 87
3.2 Dust extinction profiles 93
3.3 Mock observation image creation process 94
3.4 Star formation histories and resulting spectral energy distributions 100
3.5 Fitted physical parameters compared with intrinsic values 101
3.6 Example radial profiles for different recovery cases 103
3.7 Morphological metric observational proxies compared with simulation values 106
3.8 Nearest neighbor classification accuracy as a function of quenching progress 108
3.9 Recovery of quenching episode progress, binned by quenched population . . 110
3.10 Expected number of galaxies as a function of mass, binned by redshift . . . 117
3.11 Color–color diagrams of median quenching progress, binned by population 119

4.1 HST filter curves for the Frontier Fields 131
4.2 Example postage stamp cutouts for a Frontier Fields galaxy 133
4.3 Star formation histories and resulting spectral energy distributions 140
4.4 Example radial profiles for different quenching populations 142
4.5 Morphological metric distributions for different quenching populations . . . 146
4.6 Phase space locations for galaxies in the sample 148
4.7 Star formation rate as a function of stellar mass for the sample 150
4.8 Fraction of different quenching modes, binned by environment 153
4.9 Fraction of different quenching modes, binned by cluster infall time 155
4.10 Fraction of quenching modes in the green valley, binned by environment . . 161

A.1 Postage stamps and sSFR profiles for an inside-out quenched galaxy 210
A.2 Morphological metric evolution for an inside-out quenched galaxy 211
A.3 3D morphological metrics compared with 2D morphological metrics 213
A.4 Morphological metric evolution for the ambiguous quenched population . . 215
A.5 Morphological metric importance, binned by progress epoch 217

B.1 Morphological metric proxies compared with photometric alternatives . . . 220

C.1 Phase space diagrams for snapshots 64–79 in TNG 225

C.2 Morphological metric distributions for star forming galaxies 228

List of Tables

2.1 Environment statistics for each quenched population at $z = 0$ 55

3.1 Design parameters for CASTOR and NGRST surveys 88
3.2 Noise parameters for CASTOR and NGRST filters 96
3.3 Spectral energy distribution fitting model parameters 99

4.1 Clusters and properties for the Hubble Frontier Fields 129
4.2 Spectral energy distribution fitting model parameters 139

C.1 Available HST filters per cluster and parallel field 221

List of Abbreviations

ΛCDM Λ cold dark matter

Abell Abell galaxy cluster catalog

ACS Advanced Camera for Surveys

AGN active galactic nuclei

A_V V-band dust extinction

bCG bright cluster galaxy

BCG brightest cluster galaxy

CALIFA Calar Alto Legacy Integral Field Area survey

CANDELS Cosmic Assembly Near-infrared Deep Extragalactic Legacy Survey

CASTOR Cosmological Advanced Survey Telescope for Optical and UV Research

CLASH Cluster Lensing And Supernova Survey with Hubble

COSMOS Cosmic Evolution Survey

C_{SF} concentration of star formation, $C_{\rm SF} = {\rm SFR}_{<1\ {\rm kpc}}/{\rm SFR}_{\rm total}$

CSP composite stellar population

Euclid Euclid space telescope

FAST Fitting and Assessment of Synthetic Templates

FWHM full width half maximum

GALAXEV models of Bruzual & Charlot (2003)

GAMA Galaxy And Mass Assembly survey

HFF Hubble Frontier Fields

HLWAS High-Latitude Wide-Area Survey

HST Hubble Space Telescope

ICM intracluster medium

IMF initial mass function

IR infrared

ISM interstellar medium

JWST James Webb Space Telescope

kNN k-nearest neighbors

KS Kolmogorov-Smirnov test

LoS line of sight

LSST Legacy Survey of Space and Time

MACS Massive Cluster Survey

MaNGA Mapping Nearby Galaxies at Apache Point Observatory survey

NGRST Nancy Grace Roman Space Telescope

PSF point spread function

$\mathbf{R_e}$ effective radius, or half mass radius

RELICS Reionization Lensing Cluster Survey

$\mathbf{R_{inner}}$ inner truncation radius, $R_{\rm inner} = \log\left[{\rm sSFR}(r)\right] \leqslant -10.5 \cap {\rm d}({\rm sSFR})/{\rm d}r \geqslant 1$

RMS root mean square

$\mathbf{R_{outer}}$ outer truncation radius, $R_{\rm outer} = \log\left[{\rm sSFR}(r)\right] \leqslant -10.5 \cap {\rm d}({\rm sSFR})/{\rm d}r \leqslant -1$

$\mathbf{R_{SF}}$ disk size ratio, $R_{\rm SF} = \log\left(R_{\rm e,\ SF}/R_{\rm e}\right)$

SAMI Sydney-AAO Multi-object Integral field spectrograph galaxy survey

SDSS Sloan Digital Sky Survey

SED spectral energy distribution

SFH star formation history, ${\rm SFH} = {\rm SFR}(t)$

SFMS star forming main sequence, or (galaxy) main sequence

SFR star formation rate

SMBH supermassive black hole

SMF stellar mass function

SNR signal-to-noise ratio

SPS stellar population synthesis

sSFR specific star formation rate, ${\rm sSFR} = {\rm SFR}/M_*$

SSP simple/single stellar population

TNG IllustrisTNG galaxy simulation

UV ultraviolet

WFC3 Wide Field Camera 3

z redshift

Z stellar metallicity

Quote

All we have to decide is what to
do with the time that is given us

J. R. R. Tolkien,
The Lord of the Rings

Chapter 1

Introduction

1.1 A Brief Historical Perspective

The field of modern extragalactic astrophysics is a young one. A century ago, a picture was beginning to emerge that the galaxy that we reside in, the Milky Way, was not the only galaxy in the Universe. Starting with early spectroscopic observations by Fath (1909) and Slipher (1913, 1915), astronomical sources with origins outside our own galaxy were being discovered. This suggested that instead of being "spiral nebulae" (as they had previously been known; e.g., Shields 1999) within the confines of the Milky Way, these sources were in fact distinct galaxies like the Milky Way, with their own formation scenarios and histories. Such observations of spiral nebulae continued to be found (e.g., Curtis 1918; Hubble 1926), and Hubble (1929) ultimately determined the distances to these objects using Cepheid variable stars (e.g., Leavitt 1907; Leavitt & Pickering 1912). The distances established that the nebulae were in fact extragalactic in origin, consistent with the finding of Lemaître (1927, 1931). Further, Hubble (1929) determined that the more distant objects were receding at a faster rate, suggesting an expanding Universe. The time of an isolated Milky Way embedded in a static Universe was over, and the time of billions of galaxies embedded in a dynamic, evolving Universe was being born (e.g., Lemaître 1933; Lemaître & MacCallum 1997).

In the decades following the start of the 20^{th} century, progress was made regarding theories of galaxy formation (e.g., Press & Schechter 1974; Blumenthal et al. 1984) and evolution (e.g., Gunn & Gott 1972; Dressler 1980). In particular, with improved detectors, radio observations were providing increasing numbers of observations of a new type of galaxy, those with strong radio features (e.g., Baade & Minkowski 1954; Bennett 1962;

Matthews & Sandage 1963; Schmidt 1963), which would come to be associated with activity from active galactic nuclei (AGN; e.g., Fabian 2012).

More recently, in the past two decades, the field of galaxy evolution (Section 1.2) has greatly accelerated our understanding of how galaxies are born, live, and notably, die (Section 1.3). In particular, continued advancements in our understanding of stellar evolution has enabled determinations of the physical properties of large numbers of galaxies (Section 1.4). As well, new observatories and technologies have enabled deeper investigations into galaxy evolution, by resolving distinct parts of galaxies through spatially resolved observations (Section 1.5). In addition, in recent years, the use of large cosmological galaxy simulations (Section 1.6) has become increasingly common, enabling a direct testbed for formation and evolution theories, as well as a comparison point for observations. These aspects will be covered in the following sections, providing the necessary background for the investigations that will be presented in this thesis, as described below (Section 1.7).

1.2 Galaxy Evolution

1.2.1 Structure and Galaxy Formation

Before discussing how galaxies evolve, the current understanding of galaxy formation will be briefly reviewed, in order to provide better context for subsequent discussions of evolution.

The current leading theory to describe the Universe as a whole is the ΛCDM model, which includes the contribution of dark energy, denoted by Λ, as well as cold dark matter (e.g., Peebles & Ratra 2003; Planck Collaboration et al. 2020). The dark matter component is described as cold as it has negligible velocities in the early Universe (e.g., Mo et al. 2010; Bovy 2026). ΛCDM additionally includes ordinary, or baryonic, matter which make up the stars and gas that form the visible part of a galaxy, and relies on general relativity (Einstein 1916) to describe gravity on large, cosmological scales. As the current standard cosmological model, ΛCDM agrees reasonably well with a number of key observations, including the large-scale structure of the Universe and the distribution of galaxies (e.g., Alam et al. 2021; Adame et al. 2025), as well as the accelerating expansion (e.g., Riess et al. 1998; Perlmutter et al. 1999) of the Universe (e.g., Planck Collaboration et al. 2020). When considering the entire mass–energy budget of the Universe, the ΛCDM model posits that dark energy accounts for ∼68%, dark matter contributes ∼27%, and the remaining ∼5% is comprised of ordinary baryonic matter (Planck Collaboration et al. 2020). While not visible, dark energy is detectable through its effect on the accelerating expansion of the

Universe (e.g., Frieman et al. 2008). Dark matter is similarly not visible and thus does not emit or absorb electromagnetic radiation, but interacts gravitationally like regular matter (e.g., Bertone et al. 2005; Bertone & Hooper 2018). Under the ΛCDM model, the Universe is currently 13.8 Gyr old (Planck Collaboration et al. 2020).

In the modern view of galaxy formation, the early Universe is described with a nearly-uniform density field with scale-small perturbations (e.g., Press & Schechter 1974; Bond et al. 1991), where some regions are overdense compared to other regions (e.g., Blumenthal et al. 1984). The fingerprints of these small-scale perturbations are readily observed through observations of the cosmic microwave background (Planck Collaboration et al. 2020), radiation which originated from a few hundred thousand years after the Big Bang (∼0.38 Myr; e.g., Mo et al. 2010). With increasing time, overdense regions grow until they gravitationally collapse into small dark matter halos, which begin to merge and cluster hierarchically, or "bottom up," where smaller structures are formed first, before larger structures (e.g., White & Rees 1978). Disk (i.e. spiral) galaxies begin forming in the dark matter halos as gas falls into the halo, subsequently cools, and settles at the center of the halo to form stars (e.g., Fall & Efstathiou 1980; Binney & Tremaine 2008; Mo et al. 2010). Small galaxies form in small dark matter halos, before large galaxies form in large dark matter halos (e.g., Bovy 2026). When small halos are nearby large halos, this simultaneously prompts the merging of small galaxies into large galaxies, as well as the creation of satellite galaxies, which are less massive, around central galaxies, which are more massive. This process ultimately leads to the formation of galaxy clusters (e.g., Blumenthal et al. 1984), the largest gravitationally bound objects in the Universe, with masses on the order of 10^{14}–10^{15} $M_{\odot}$, that can contain hundreds or even thousands of galaxies (e.g., Kravtsov & Borgani 2012).

Figure 1.1 shows slices through a cosmological simulation (described below) at various redshifts, or times in the history of the Universe, highlighting the hierarchical growth of structure. Moving from the top panels to the bottom, it is evident that both dark matter (left column) and baryons (galaxies; right column) cluster together more strongly with increasing time. This growth of structure has been likened to the adage "the rich get richer and the poor get poorer" (e.g., Ryden 2016). In the bottom panels of Figure 1.1, the large-scale structure of the Universe, the cosmic web (e.g., Bond et al. 1996; Libeskind et al. 2018), is most apparent, and shows filamentary structures (bright regions), as well as cosmic voids (dark regions). Galaxy clusters (brightest regions) form at the nodes of cosmic filaments (e.g., Geller & Huchra 1989; Gott et al. 2005; Tully et al. 2014).

This standard hierarchical growth is in contrast to a "top down" or anti-hierarchical formation scenario, where structure forms via fragmentation (e.g., Dayal & Ferrara 2018). In a top down scenario, the largest structures in the Universe form first, before segmenting

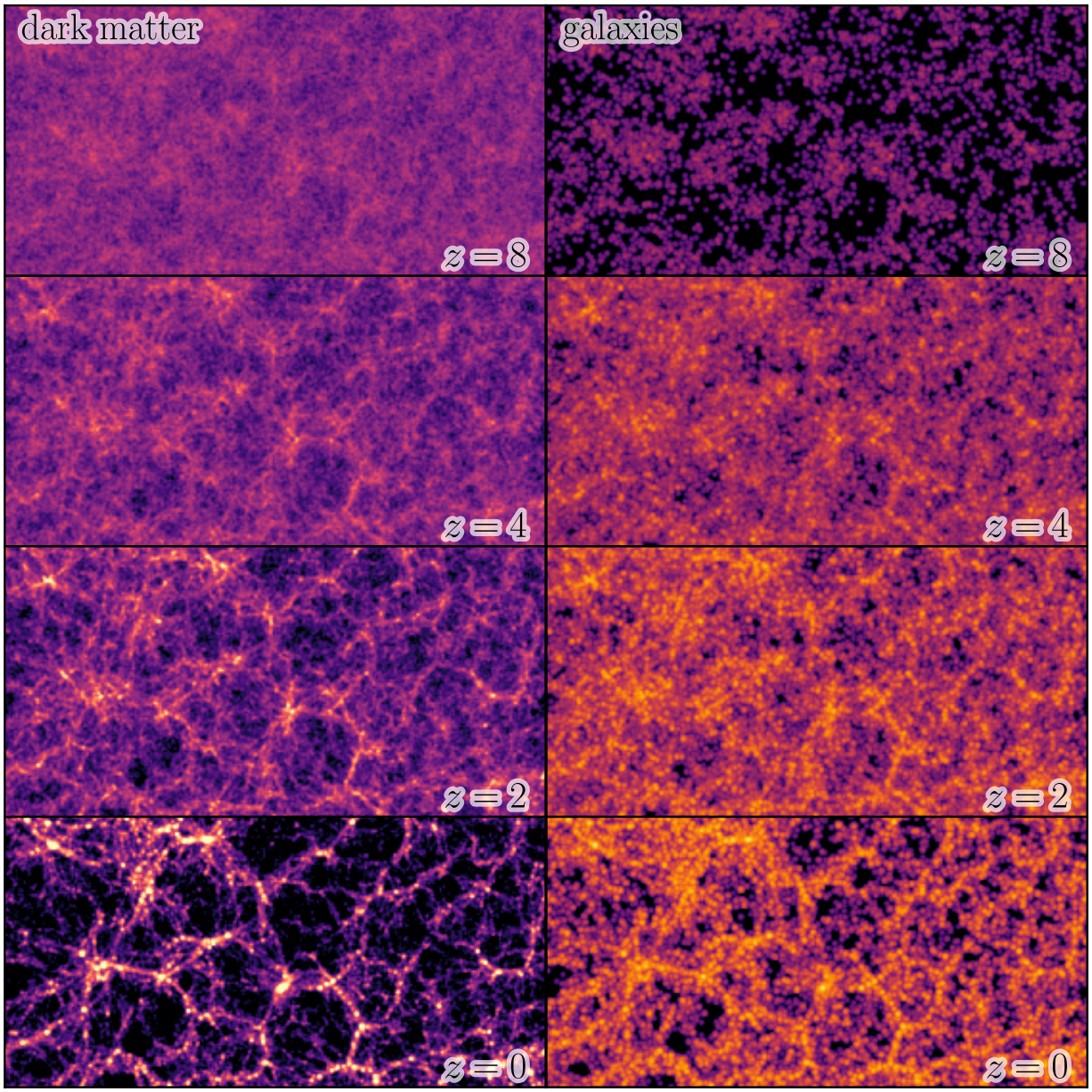


Figure 1.1: The hierarchical growth of structure, shown as slices through the IllustrisTNG simulation (e.g., Nelson et al. 2018). The density of dark matter is shown on the left, while the density of stellar mass (in galaxies) is shown on the right. Time increases from the top to the bottom, highlighting how small structures at early times (top panels) cluster and merge to form large structures (filaments and galaxy clusters; bottom panels). Based on a similar figure in Springel et al. (2006).

into smaller structures like galaxies. Such a top down scenario is not consistent with ΛCDM (e.g., Mo et al. 2010).

It has also been suggested, on the basis of observations, that massive galaxies form their stars earlier and faster than small ones (e.g., Silk & Mamon 2012), a phenomenon known as galaxy downsizing (e.g., Neistein et al. 2006; Fontanot et al. 2009). This piece of observational evidence appears inconsistent with the bottom up scenario of hierarchical structure formation from ΛCDM, and indeed has been difficult for simulations to reproduce (e.g., Neistein et al. 2006). However, the physics governing galaxy assembly are complex. For instance, the physical mechanisms controlling heating and cooling, as well as feedback processes, are inherently more complicated than the gravitational physics required to explain the formation of dark matter halos (e.g., Naab & Ostriker 2017). Therefore, while baryonic feedback mechanisms seemingly break the direct link between the growth of dark matter halos and stellar assembly (e.g., Neistein et al. 2006; Fontanot et al. 2009), galaxy formation remains hierarchical (Cole et al. 2000).

With our understanding of galaxy formation established, especially in the early Universe, we are now in a position to explore how galaxies evolve. Given the subject matter of this thesis, we leave a more detailed description of galaxy "death" to a later section.

1.2.2 Secular Evolution and Gas Cooling

As established above, all galaxies in the Universe are embedded within dark matter halos, where the baryonic matter that comprises a galaxy constitutes only a small fraction of the overall mass within a dark matter halo (e.g., Shull et al. 2012). Indeed, as stated, the baryonic content of the Universe as a whole is only about $\lesssim$5% (Planck Collaboration et al. 2020). Thus, when we discuss galaxy evolution, we are discussing the evolution of only a small part of the visible part of the Universe.

To best understand galaxy evolution, we must understand the typical composition of a galaxy. Beyond the surrounding dark matter halo, galaxies are made up of gas, dust, and stars, along with stellar remnants, all bound together through gravity (e.g., Binney & Tremaine 1987, 2008; Binney & Merrifield 1998). It has also been well established that the center of nearly every galaxy hosts a supermassive black hole (SMBH; e.g., Ferrarese & Merritt 2000; Kauffmann et al. 2003a; Padovani et al. 2017). Galaxy evolution is thus governed by the interaction and evolution of these components, where the primary concern, as regards this thesis, is the conversion of available gas into stars. In Figure 1.2, we show a schematic diagram illustrating the components and their interactions, which collectively describe the evolution of an individual galaxy.

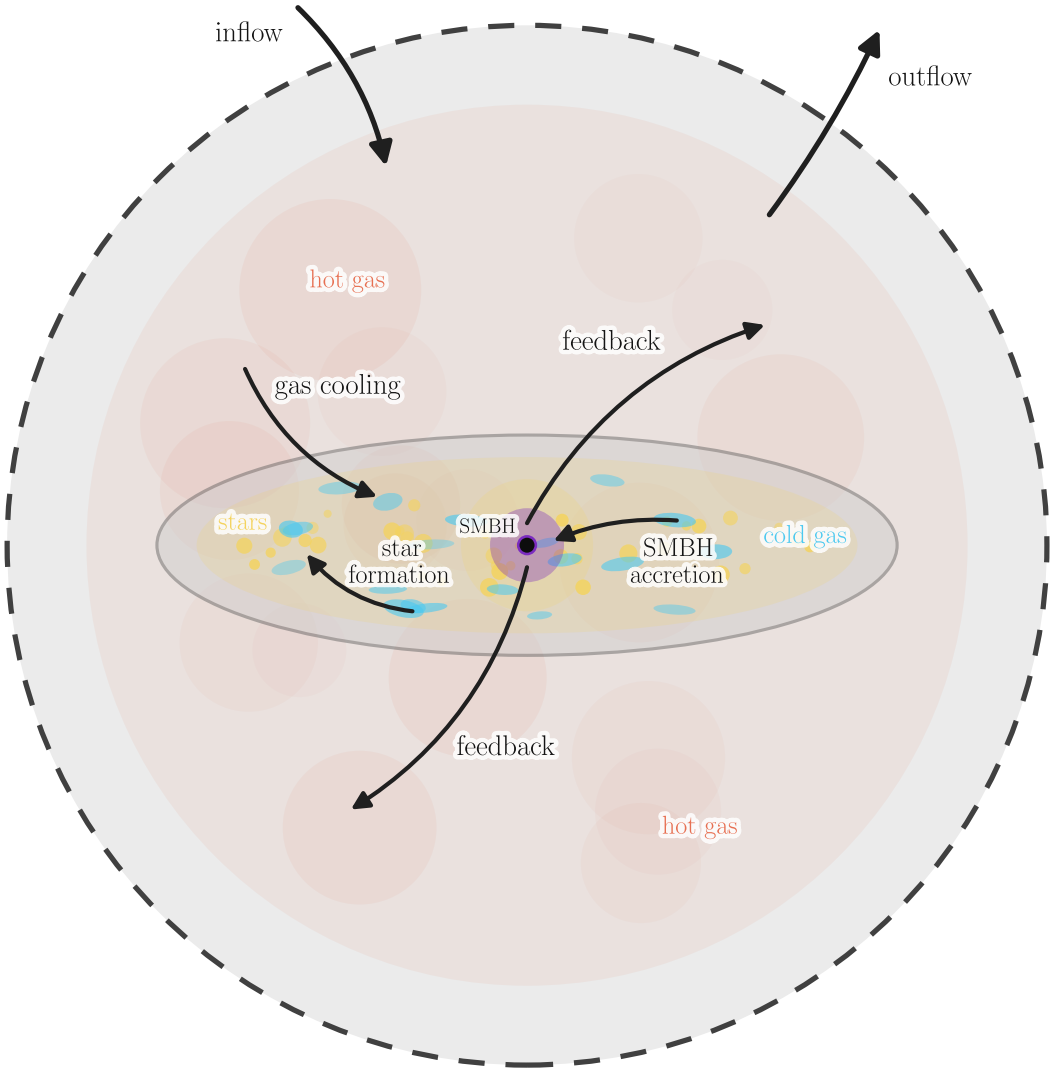


Figure 1.2: A schematic showing the evolution of an individual galaxy, represented by the outer dashed line. The hot gas, cold gas, stars, and a supermassive black hole are highlighted, as well as the interplay between them, respectively. Hot gas cools to form cold gas, which in turn can fuel star formation. Stellar feedback output energy, mass, and metals into the interstellar medium, enriching the gas for subsequent generations of star formation. AGN can additionally power feedback (see Section 1.3), likewise injecting energy into the gas components. The system is not closed, and can additionally experience gas inflows and outflows, from/to the intergalactic medium. Mergers and interactions will additionally disrupt this system. Based on a similar figure in Mo et al. (2010).

Galaxies contain hot gas which must cool in order to become fuel available for star formation. The primary gas cooling processes are two-body radiative processes, where the temperature of the gas describes the process that is most efficient. At high temperatures, $>10^6$ K, primordial gas composed of hydrogen and helium is nearly fully ionized, and enriched gas containing heavier elements is fully ionized at $\gtrsim 10^7$ K (e.g., Mo et al. 2010). Such hot gas radiates energy primarily through X-rays via free–free, or bremsstrahlung, emission, where free electrons are accelerated as they encounter atomic nuclei, thereby emitting an X-ray photon (e.g., Benson 2010). At lower temperatures, $10^4 < T/\mathrm{K} < 10^6$, collisional ionization, recombination, and collisional excitation are important (e.g., Benson 2010). In collisional ionization, atoms colliding with electrons are ionized and remove kinetic energy from the gas, where the amount of kinetic energy removed is set by the ionization threshold (e.g., Mo et al. 2010). In recombination, electrons and ions recombine, producing photons, while in collisional excitation, atoms collide with electrons and become excited, before experiencing radiative decay back to the ground state. Below 10^4 K, electrons have mostly recombined and collisional excitation becomes uncommon. If significant amounts of molecular hydrogen, H_2, can form in the gas, then further cooling is possible for a primordial gas (e.g., Mo et al. 2010).

We will shortly consider the process of star formation in galaxies, as well as stellar evolution. In addition, a discussion of active galactic nuclei feedback remains for a subsequent section. However, beyond these components, galaxies additionally experience gas inflows and outflows. Outflows will similarly be covered below, but inflows are important for rejuvenating the gas supply within galaxies (e.g., Ceverino et al. 2016). As we will see, if this gas supply is shut off or becomes less efficient, a galaxy can evolve in dramatic ways.

1.2.3 Star Formation, Stellar Evolution, and Stellar Properties

Star formation requires cold gas, on the order of $\sim$10 K (e.g., Binney & Merrifield 1998; Mo et al. 2010). For gas to reach these temperatures, it must cool beyond the levels discussed above. Critically, gas can lose energy and collapse into cold molecular hydrogen clouds through molecular gas cooling (e.g., Yoshida et al. 2006; Maio et al. 2007; Benson 2010). This process is driven by metallic line emission (e.g., carbon monoxide and oxygen) and dust interactions. Unsurprisingly, it has also been established empirically that star formation rate correlates strongly with the density of cold gas, when viewed on galaxy scales (e.g., Schmidt 1959; Kennicutt 1989, 1998a; Kennicutt & Evans 2012).

Cold molecular clouds, formed in the interstellar medium of galaxies through shocks, turbulence, and disturbances, are the stellar nurseries that stars form in, with stellar masses

in the range 10^3–10^6 $M_\odot$ (e.g., Larson 1981; Shu et al. 1987). Stellar evolution formally begins when such giant molecular clouds are no longer in hydrostatic equilibrium with their surroundings (e.g., Binney & Merrifield 1998). They will then experience gravitational collapse and fragment in a hierarchical manner during the collapse, into increasingly smaller clumps (e.g., Lada & Lada 2003). These fragments will condense, and accrete additional interstellar material, thereby increasing in density, forming hot stellar embryos (e.g., Larson 1969). These objects continue to increase in temperature, until their gas is hot enough to support against gravity, reestablishing hydrostatic equilibrium, forming a protostar (e.g., Binney & Merrifield 1998). The continued accretion of material supports the formation of jets, which expel surrounding gas and dust, and the protostar becomes a pre-main sequence star. Continued contraction leads the pre-main sequence star onto the stellar main sequence, at which point hydrogen fusion begins (e.g., Mo et al. 2010). Through burning hydrogen, hydrostatic equilibrium can again be maintained against the inward pull of gravity. In the gravitational collapse of a giant molecular cloud as described above, tens to thousands of stars are formed almost simultaneously (e.g., Lada & Lada 2003).

At this point, stars burning hydrogen into helium will remain on the main sequence for millions to billions of years, depending on their stellar mass (e.g., Binney & Merrifield 1998). The main sequence describes where stars reside for the majority of their lives on color–magnitude diagrams, such as the Hertzsprung-Russel diagram (e.g., Sandage 1953; de Jager et al. 1988). In Figure 1.3, we show the main sequence as a gray band in the lower plots. We will shortly describe these figures more fully.

Regarding stellar evolution, stars on the stellar main sequence have hydrogen burning into helium in their cores, via the proton–proton chain or the carbon-nitrogen-oxygen cycle (e.g., Binney & Merrifield 1998; Mo et al. 2010). Through hydrogen fusion, the core of a star increases in mass, making it denser. With this increase in density, to continue to support against gravitational collapse, the core will have to then burn hotter, meaning brighter (e.g., Binney & Merrifield 1998). However, this hotter stage of fusion also uses fuel more quickly. Low-mass stars with $0.8 \lesssim M_*/M_\odot \lesssim 2$ will continue burning until they exhaust hydrogen in their cores, at which point they contract and become denser, while puffing out their outer layers (e.g., Mo et al. 2010). These outer layers become cool, and these stars then become subgiants, moving off the main sequence. Once the temperature just outside the core becomes hot enough to support fusion, the star then becomes a red giant (e.g., Mo et al. 2010). Continued evolution enables a red giant to burn helium as fuel, and later a stellar wind will blow away weakly bound gas, exposing a dense carbon/oxygen core. This dense core has ultraviolet radiation that can ionize the ejected gas, but the star is not hot enough to burn carbon into heavier metals (e.g., Binney & Merrifield 1998). The core then cools as a white dwarf. Intermediate mass stars with $2 \lesssim M_*/M_\odot \lesssim 8$ have

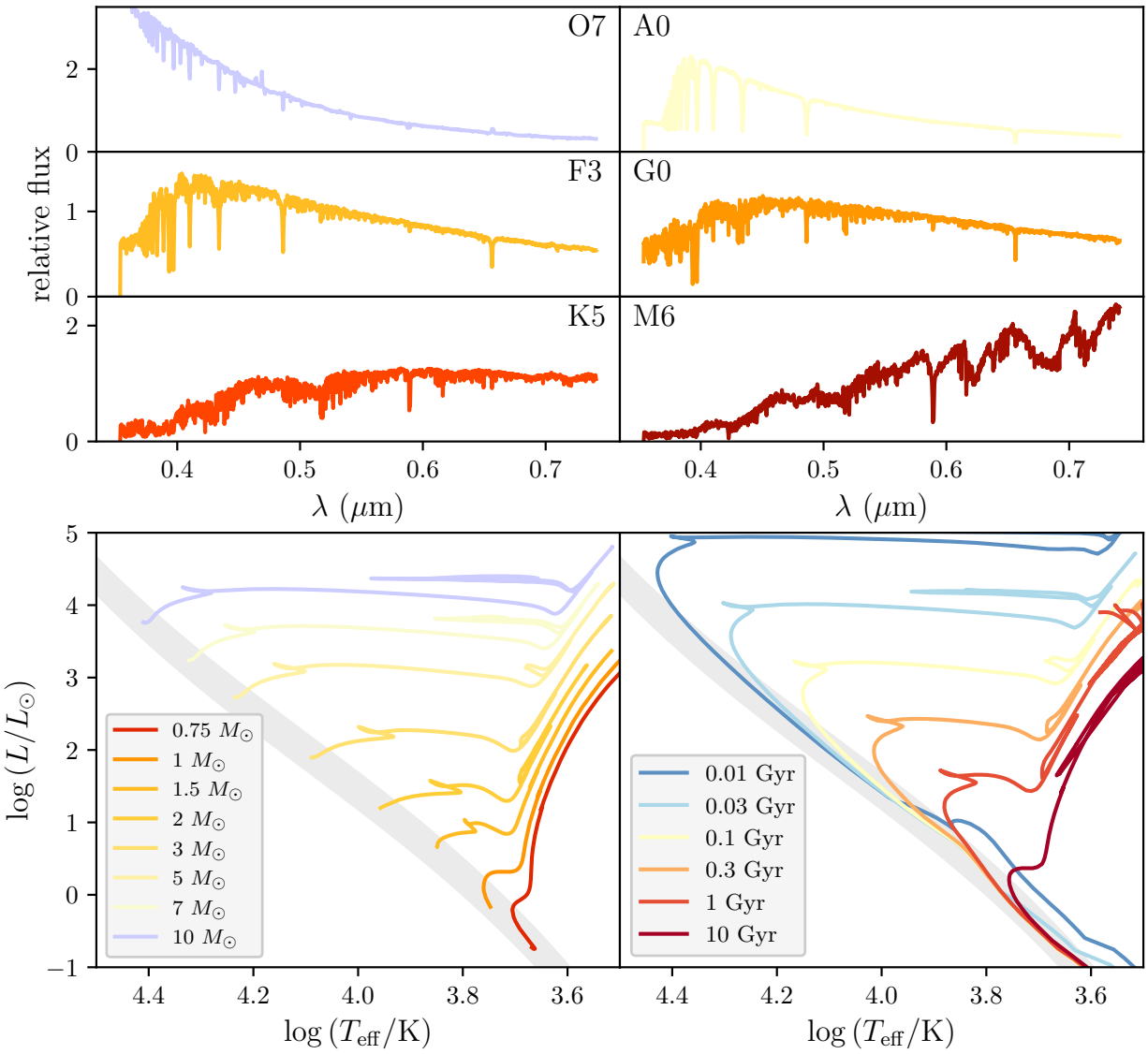


Figure 1.3: Examples of stellar spectra (top) from the Medium-resolution Isaac Newton Telescope library of empirical spectra (MILES; Sánchez-Blázquez et al. 2006), and tracks of stellar evolution for solar-metallicity stars of different stellar masses (bottom left) and solar-metallicity stellar isochrones at different characteristic ages (bottom right) from the Padova Trieste Stellar Evolution Code (PARSEC; Bressan et al. 2012), respectively. Spectra are color-coded roughly according to their temperature, as are the evolutionary tracks. Stellar isochrones are color-coded by age. For clarity, evolutionary tracks for stars with $M_* < 2\ M_\odot$ terminate at the helium flash.

evolution that is quite similar, except once they are capable of fusing helium in their cores they become red, and continued helium burning forces them to become bluer, until helium is depleted in the core (e.g., Mo et al. 2010). They eventually become white dwarfs as well.

High mass stars with $8 \lesssim M_*/M_\odot \lesssim 40$ similarly evolve as their lower-mass counterparts, but can continue burning progressively heavier and heavier elements given their high temperatures (see below; e.g., Binney & Merrifield 1998). However, burning iron requires energy, as iron is the most tightly bound nucleus. Stars with $M_* \gtrsim 10\ M_\odot$ can burn their cores until reaching iron. Once this point is reached, fusion in the core stops, and the core will contract until it is supported by electron degeneracy pressure (e.g., Mo et al. 2010). Continued burning of lighter metals outside the core will deposit material onto the core, causing it to increase in mass, until electron degeneracy pressure is insufficient to prevent collapse. The dense iron core will become hotter and eventually experiences catastrophic collapse, where the outer layers of the star collapse inward at $\sim 0.1c$, before bouncing off the dense core (e.g., Woosley & Weaver 1986). This produces a Type II supernova (e.g., Bethe 1990). These core-collapse supernovae output large amounts of energy into the interstellar medium, on the order of $\sim 10^{51}$ erg (e.g., Bovy 2026). The stellar remnant is then a neutron star for stars with $M_* \lesssim 3\ M_\odot$, and a black hole for higher masses (e.g., Mo et al. 2010). Stellar evolutionary tracks for stars of different birth masses are shown in the bottom left panel of Figure 1.3, color-coded by birth mass.

With our understanding of the broad aspects of stellar evolution established, we must also consider typical properties of stars as well, in order to better understand observations of galaxies. As we have seen, the evolution of a star is dictated by its initial mass. Further, the luminosity, temperature (therefore color), and lifetime for a star are all dictated by birth mass. It has been found that for characteristic stellar mass ranges, these properties scale with mass through simple power-law scaling relations (e.g., Bressan et al. 1993). For instance, for stars with $0.5 \lesssim M_*/M_\odot \lesssim 50$, their main sequence luminosity, $L_{\rm MS}$, scales with mass as $L_{\rm MS}/L_\odot \propto (M_*/M_\odot)^{3.5}$ (e.g., Popper 1980; Torres et al. 2010). Thus, it is clear that while on the main sequence, low-mass stars are much less luminous than their more massive siblings. This can be seen in the bottom left panel of Figure 1.3.

In addition, the time that a star spends on the main sequence also scales with stellar mass (e.g., Bressan et al. 1993). These main sequence lifetimes, $t_{\rm MS}$, scale with mass as $t_{\rm MS}/10\ {\rm Gyr} \simeq (M_*/M_\odot)^{-2.5}$ (e.g., Binney & Merrifield 1998). From these simple scaling relations, it is clear that, while the Sun will have a main sequence lifetime of $\sim$10 Gyr (Sackmann et al. 1993), high-mass stars of 10 $M_\odot$ will have main sequence lifetimes of only $\sim$30 Myr. In particular, for masses above $\sim$15 $M_\odot$, stellar lifetimes are less than 10 Myr, while for stars less massive than $\sim$0.88 $M_\odot$, their main sequence lifetimes are >13.8 Gyr. This means that these low mass stars have not yet moved off the main sequence in the

history of the Universe.

As mentioned above, in the collapse of a giant molecular cloud, tens to thousands of stars will be born nearly simultaneously (e.g., Lada & Lada 2003). These stars will form according to an initial mass function (IMF; e.g., Salpeter 1955; Miller & Scalo 1979; Scalo 1986; Kroupa 2001; Chabrier 2003), which describes the initial distribution of masses for a population of stars during formation. We will revisit initial mass functions below, but in general, they take power-law forms, where many more low-mass stars are formed relative to the number of high-mass stars. For example, for every 1000 stars with $\sim$1 $M_\odot$ that are formed, $\sim$5 stars are formed with $\sim$10 $M_\odot$, while only $\sim$1 star is formed with $\sim$30 $M_\odot$ (Chabrier 2003). Such a population of stars with the same age trace out isochrones on color–magnitude diagrams, and given their differing time evolution off the main sequence for stars of different ages, plots of color–magnitude diagrams can serve as diagnostic tools to estimate the age of a coeval stellar population (e.g., Friel 1995; Jørgensen & Lindegren 2005). Isochrones at solar-metallicity for different ages are shown in the bottom right panel of Figure 1.3, and are color-coded by age.

Further, stars can be approximated as emitting black-body radiation, and through the Stefan-Boltzmann law, their luminosity, L, is related to their effective temperature, $T_{\rm eff}$, as $L \propto R^2 T_{\rm eff}^4$, where R is the radius of the star (e.g., Mo et al. 2010). Thus, at a fixed radius, more luminous stars will also be hotter. Though Wien's law, the peak of the black-body radiation curve provides the peak wavelength of light, which is directly measurable as the color of the star. Therefore, more massive stars will be more luminous on the main sequence, have hotter temperatures, and their radiation will additionally be shifted toward the ultraviolet, making them appear blue. Conversely, for lower mass stars, which are less luminous on the main sequence and are cooler, their radiation will correspondingly peak at longer wavelengths, making them appear redder. These properties, in combination with others, have enabled observers to classify a large number of stars into stellar sequences based on their spectral characteristics. One such system typically used employs the letters O, B, A, F, G, K, M to describe stars from hottest (O-type) to coolest (M-type; e.g., Cannon & Pickering 1918). Example empirical spectra for stars of different spectral types are shown in the top panels of Figure 1.3, and are color-coded roughly according to their temperature.

1.2.4 Star Formation Rate Indicators

With the features we have identified above for stars of different stellar masses, there are naturally several possible routes to determine the star formation rate (SFR) of a galaxy,

which rely on different SFR indicators. Here we will briefly describe a few of the main indicators that are relevant to this work, though we will provide a more thorough review of the exact methods below (Section 1.4).

As noted above, massive stars will reside on the main sequence for relatively short times. In particular, massive O and B stars with $M_* > 5\ M_\odot$ have main sequence lifetimes of $\leqslant$100 Myr (e.g., Binney & Merrifield 1998). The number of massive stars is then directly proportional to the current SFR (e.g., Mo et al. 2010), as these massive stars emit most of their energy as UV continuum radiation, and should dominate at UV wavelengths (e.g., Calzetti 2013). The optimal wavelength range is 1250–2500 Å to simultaneously minimize contamination from old stars, and avoid the Lyα forest (e.g., Kennicutt 1998b). For galaxies at $z \lesssim 0.5$, they must be observed from space due to the opacity of the atmosphere for UV radiation, but higher redshift galaxies ($1 \lesssim z \lesssim 2$) can be observed without issue from the ground (e.g., Kennicutt 1998b). These types of observations are sensitive to the assumed initial mass function, and are further best suited to galaxies with star forming timescales $\gtrsim$100 Myr (e.g., Kennicutt 1998b). The primary concern with UV observations is the sensitivity to dust extinction, as star formation may be preferential in highly obscured regions (e.g., Kennicutt 1998b; Kennicutt & Evans 2012).

Optical emission and recombination lines are additionally robust SFR indicators. The ISM around young massive stars, ionized by Lyman continuum photons, produce H II regions (e.g., Mo et al. 2010). The recombination of this ionized gas produces hydrogen emission lines which can be used as a SFR diagnostic, as their flux is proportional to the Lyman continuum flux produced by the young massive stars (e.g., Kennicutt 1998b; Mo et al. 2010). Here, Hα at 6562.8 Å is the most commonly used line, but others are also possible, including Hβ, Pα, and Pβ, for instance (e.g., Kennicutt 1998b). Only stars with $M_* \gtrsim 10\ M_\odot$, and lifetimes $\lesssim$20 Myr contribute significantly to the Lyman continuum luminosity (e.g., Calzetti 2013), where the largest contribution of ionizing UV radiation comes from massive stars with $30 \lesssim M_*/M_\odot \lesssim 40$ (Kennicutt & Evans 2012). Therefore, nebular emission line strength is almost an instantaneous ($\sim$10 Myr) measure of SFR (e.g., Kennicutt & Evans 2012). As with UV observations, nebular emission lines are also sensitive to the assumed initial mass function, as are concerns with dust extinction (e.g., Kennicutt 1998b; Kennicutt & Evans 2012). However, using an additional emission line, like Hβ alongside Hα, allows for a dust correction (e.g., Baldwin et al. 1981; Kewley et al. 2001; Kauffmann et al. 2003a; Kennicutt & Evans 2012; Calzetti 2013). For galaxies with $z \gtrsim 0.5$, Hα is redshifted outside the optical window, and thus other empirical calibrations have been used, such as the [O II] forbidden line at 3727 Å (e.g., Mo et al. 2010). However, the luminosity of forbidden lines is not directly related to the UV luminosity produced by young massive stars (e.g., Kennicutt 1998b), but such methods can still serve as useful

SFR diagnostics.

The ISM around young massive stars in star forming regions is dusty, where a significant fraction of the UV luminosity from the young massive stars can be absorbed by the dust (e.g., Mo et al. 2010). This heats the dust and is re-radiated in the far-infrared (e.g., Kennicutt 1998b; Kennicutt & Evans 2012). As the absorption efficiency of dust peaks in the UV (e.g., Calzetti 2013), the far-infrared luminosity is likewise used as a SFR indicator, where the far-infrared has wavelengths of ∼10–300 μm (e.g., Kennicutt 1998b). Critically, this diagnostic depends on the opacity of the dust, so the fraction of UV photons that can escape un-extincted must be specified (e.g., Kennicutt 1998b). However, combining the far-infrared luminosity with the UV luminosity avoids this issue (e.g., Kennicutt & Evans 2012; Calzetti 2013). Galaxies have emission around ∼60 μm due to dust around star forming regions, and around ∼100 μm from dust heated by the visible light from weakly UV radiating, old, low-mass stars (e.g., Kennicutt 1998b; Mo et al. 2010; Calzetti 2013). Thus, this second longer wavelength component can serve as contamination for the SFR signal, and must be accounted for. Infrared SFR indicators are also well matched to observations of starbursts, as the star formation occurs over short timescales, and starbursts are very dusty (e.g., Mo et al. 2010). As above, this method is once again sensitive to assumed IMF (e.g., Kennicutt 1998b).

Beyond these direct tracers of star formation within galaxies, spectral energy distribution fitting can also be completed to determine estimates for physical properties of galaxies, including star formation rate. This method will be detailed below (Section 1.4). Next, we look to leverage our understanding of star formation, as detailed above, as well as galaxy morphology, in order to understand galaxy classification schemes.

1.2.5 Galaxy Classification and the Star Forming Main Sequence

Galaxies can be classified in a multitude of ways, including on the basis of color, morphology, star formation rate, environment, local dominance, and activity from a supermassive black hole. Here we will discuss the relevant classification schemes that will appear throughout this thesis.

Over the past two decades, a picture has emerged where galaxies display a bimodality in terms of color (e.g., Strateva et al. 2001; Blanton et al. 2003; Baldry et al. 2004; Bell et al. 2004; Driver et al. 2006; Wyder et al. 2007; Brammer et al. 2009; Gavazzi et al. 2010; Peng et al. 2010; Taylor et al. 2015). This has been facilitated through large galaxy surveys such as the Sloan Digital Sky Survey (SDSS; York et al. 2000), which has collected observations for millions of galaxies with $z \lesssim 0.5$ (e.g., Abazajian et al. 2009). In this bimodal color

distribution, there exists a blue cloud alongside a prominent red sequence, when viewed on a color–magnitude diagram or similar. Galaxies that reside in the blue cloud appear as spiral disk galaxies, where the blue color is a consequence of their young stellar populations (see above; e.g., Binney & Merrifield 1998). Conversely, the galaxies that populate the red sequence appear as smooth and featureless elliptical galaxies, where the red color for these galaxies is due to their older stellar populations (e.g., Mo et al. 2010). These red sequence galaxies therefore lack the young blue stellar populations emblematic of the spiral galaxies, and have been described as "red and dead" (e.g., Brammer et al. 2009; Schawinski et al. 2014).

Further, through careful modeling (see below), star formation rates and stellar masses can be estimated for these galaxies. It has been determined that blue spiral galaxies host active levels of star formation (e.g., Strateva et al. 2001; Bell et al. 2004; Bluck et al. 2020a,b), while the red ellipticals have low rates of star formation (e.g., Blanton & Moustakas 2009; Bluck et al. 2020a,b). Given this, ellipticals have been additionally described as passive, retired, quiescent, or quenched, while star forming galaxies have been described as normal (e.g., Mo et al. 2010). If an actively star forming galaxy has its star formation interrupted, and is no longer able to form new stars, the young stellar populations it hosts will age and die, leaving only the longer lived stars which are more red in color. This suppression of star formation will therefore move the galaxy from the blue cloud onto the red sequence, among its new peers (e.g., Bell et al. 2004; Faber et al. 2007; Martin et al. 2007). We will reserve further comment on this suppression of star formation for a subsequent section, given the importance it has in this thesis.

When plotting the star formation rate for galaxies as a function of stellar mass, a linear sequence becomes apparent, where there is a clear correlation between a galaxy's stellar mass and its star formation rate. This observation has been described as the star forming main sequence (SFMS; e.g., Brinchmann et al. 2004; Peng et al. 2010; Speagle et al. 2014; Popesso et al. 2023), and is analogous to the blue cloud described above. In Figure 1.4, we show a plot of star formation rate as a function of stellar mass for galaxies with $0.02 < z < 0.2$ present in SDSS (York et al. 2000) with measurable levels of star formation (Kauffmann et al. 2003b). From the bottom left ($M_* \approx 10^{8.5}\ M_\odot$, SFR $\approx 0.1\ M_\odot\ \mathrm{yr}^{-1}$) to the upper right ($M_* \approx 10^{11}\ M_\odot$, SFR $\approx 10\ M_\odot\ \mathrm{yr}^{-1}$), the star forming main sequence appears as the locus of the visible density contours, and thus defines a ridge line in this plane (Renzini & Peng 2015). Galaxies can be classified based on their distance from the SFMS, where galaxies below the main sequence with non-negligible levels of star formation can be described as residing in the green valley (e.g., Schawinski et al. 2014; Belfiore et al. 2018). For galaxies far from the main sequence, they have negligible levels of star formation, and form a passive or quiescent population. This is analogous to

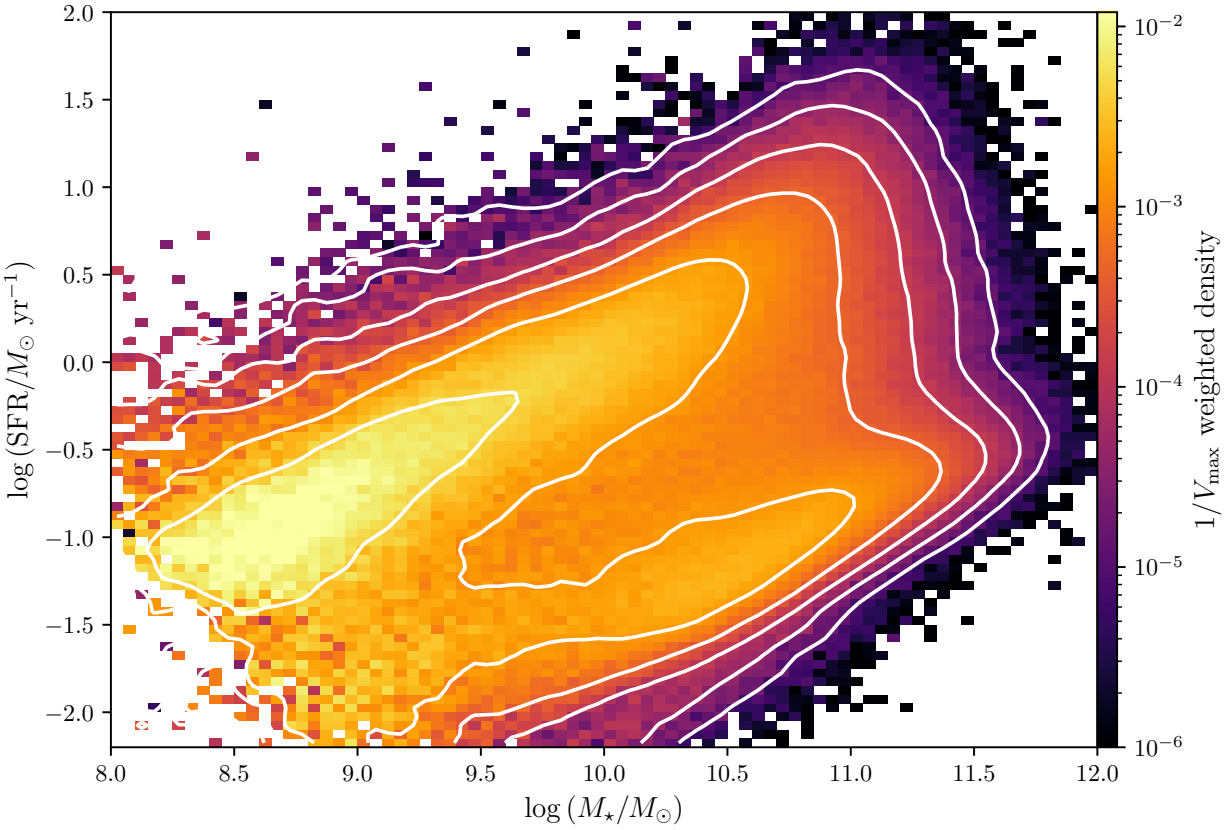


Figure 1.4: 2D histogram showing star formation rate as a function of stellar mass for 627,983 galaxies with $0.02 < z < 0.2$ in SDSS (York et al. 2000) Data Release 7 (Abazajian et al. 2009), using stellar masses and star formation rates from Kauffmann et al. (2003b) and Brinchmann et al. (2004), respectively. Bins are color-coded by the number of galaxies, where brighter colors correspond to a higher number of galaxies. Contours describing the density are shown in white. The star forming main sequence is the linear relation between stellar mass and star formation rate, visible from the lower left to the upper right. A $V/V_{\rm max}$ correction has been applied.

the red sequence mentioned above.

Thus, we have described how levels of star formation can be used, somewhat interchangeably, with morphological descriptions to identify different populations of galaxies. As well, on the basis of morphology, spiral galaxies additionally have prominent disks and bulges, along with ordered rotation for their stellar populations. Given their active levels of star formation, they host large quantities of gas (e.g., Binney & Merrifield 1998). On the other hand, elliptical galaxies contain stars with random motions, and unsurprisingly have little cool gas, but host an abundance of hot gas (e.g., Mo et al. 2010).

An additional morphological classification scheme introduced by Hubble (1926) described galaxies based on their location in the Hubble sequence. Here, Hubble separated galaxies into three classes, including elliptical galaxies, spiral galaxies, and lenticular galaxies, which have an appearance intermediate between the prior classes. He further classified the ellipticals and spirals based on how smooth they were (for the former), and how tightly wound the spiral arms appeared (for the latter). Spirals were additionally separated based on the existence of a prominent bar feature. Hubble (1926) then arranged galaxies into a sequence, starting with the smoothest ellipticals, and ending with the least ordered spirals. Given their location in the Hubble sequence, Hubble (1926) described ellipticals as "early," and spiral galaxies as "late." However, these descriptors are based purely on a galaxy's location in the sequence, and do not encode any evolutionary information. In Figure 1.5, we show an example of the Hubble sequence using galaxies as observed by Euclid (Euclid Collaboration et al. 2025). Galaxies are labeled by morphological type in the top left corner of each image.

Beyond features intrinsic to these different types of galaxies, we can also consider their typical environments. Spiral galaxies are more often found in the field, or less dense regions of space, while elliptical galaxies are found more frequently in dense environments such as galaxy clusters (e.g., Oemler 1974; Postman & Geller 1984). This result has become known as the morphology–density relation (Dressler 1980). Indeed, the most massive galaxies, living at the center of large galaxy clusters, are massive elliptical galaxies known as brightest cluster galaxies (e.g., De Lucia & Blaizot 2007), as their light profile is dominant compared with other cluster members. We will return to consider the role of environment in galaxy evolution below.

In addition to the large-scale environment in which a galaxy resides, we can also consider the small-scale environment. In this scope, we can describe galaxies as centrals and satellites, if they are the dominant galaxy within their dark matter halo or not, respectively (van den Bosch et al. 2008; Peng et al. 2012). When comparing this description with the large-scale environment, it is clear that a brightest cluster galaxy will naturally

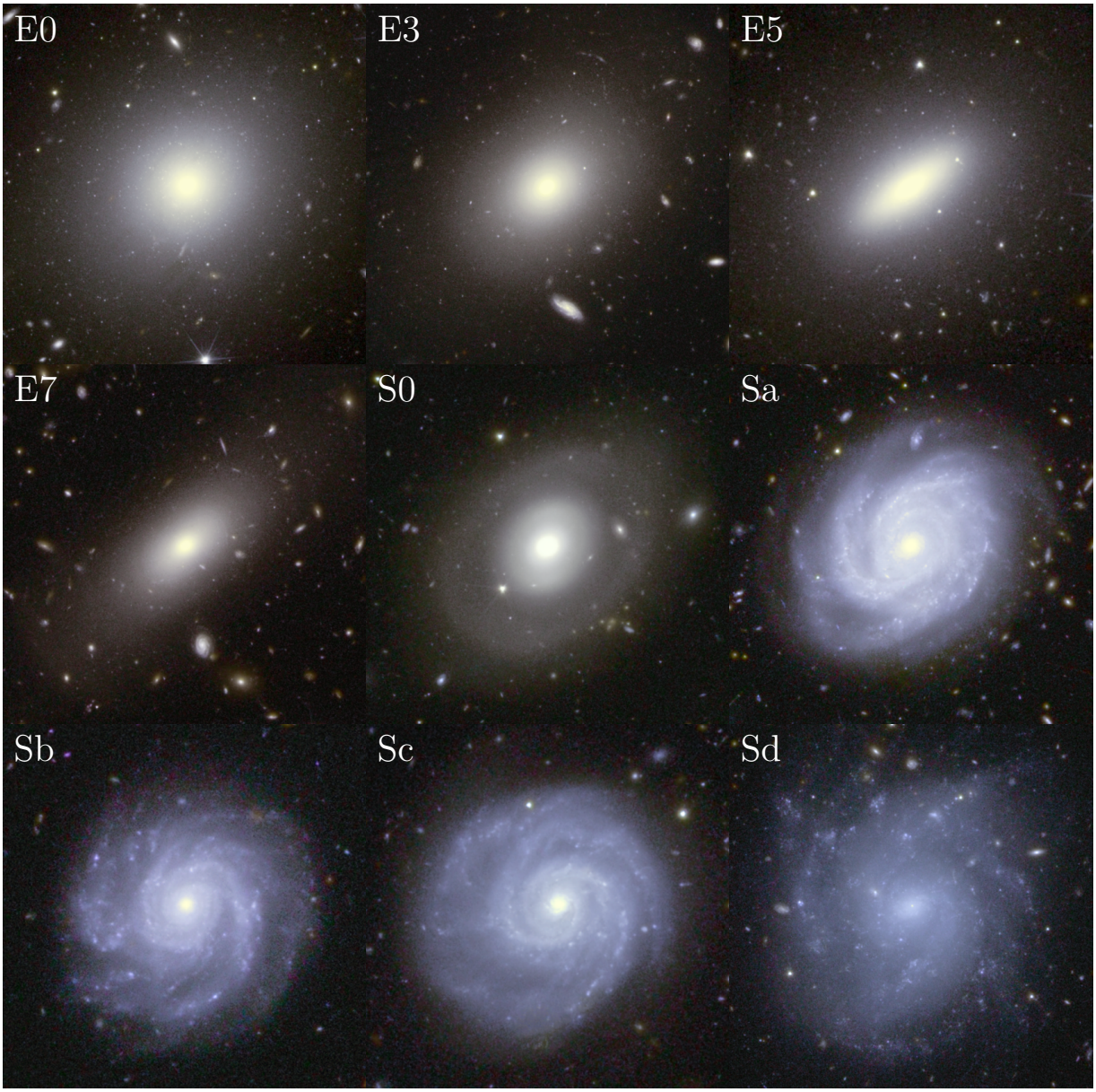


Figure 1.5: The Hubble sequence, showing the morphological classification of galaxies of Hubble (1926). Galaxies are labeled according to their morphological type. Moving from left to right and top to bottom, elliptical galaxies (denoted with "E"), are arranged before spiral galaxies (denoted with "S"). Image credits: ESA/Euclid/Euclid Consortium/NASA, image processing by J.-C. Cuillandre, E. Bertin, G. Anselmi.

be the central galaxy within a cluster, with the other cluster galaxies acting as members, or satellites, of the cluster. Besides dense environments like clusters, central galaxies can additionally exist in the field, where they may have companion satellite galaxies as well. The Milky Way galaxy itself has several satellite galaxies, including the Large and Small Magellanic Clouds (Binney & Merrifield 1998; Binney & Tremaine 2008).

Finally, galaxies can additionally be classified based on the presence of an active galactic nucleus (AGN). We will detail this process below with regards to feedback mechanisms (e.g., Fabian 2012). However, at present, this remains a supplementary classification scheme to divide galaxies into (AGN) active or (AGN) passive (e.g., Kauffmann et al. 2003a; Padovani et al. 2017; Sánchez et al. 2018). While descriptive, these terms could cause confusion given the similar terms used above to describe galaxies based on the level of star formation activity. For the remainder of this thesis, we will use active and passive or quiescent to refer to the level of star formation within galaxies.

1.2.6 The Role of Environment and Mergers

Apart from the influence of environment on disrupting star formation (see below), the environment a galaxy resides in can also have a dramatic impact on its evolution. In particular, galaxy mergers and interactions can disturb the ordered rotation of stars within disk galaxies, generating random motions for the stellar populations (e.g., Mo et al. 2010). Such interacting and merging galaxies are often visually striking, showing tidal features such as bridges and tails (e.g., Toomre & Toomre 1972), like seen in the Antennae Galaxies (e.g., Schweizer et al. 2008) and the Mice Galaxies (e.g., Cortijo-Ferrero et al. 2017).

Mergers and interactions ultimately lead to the formation of elliptical galaxies (e.g., Toomre 1977; Kauffmann et al. 1993), where these galaxies were built up through consecutive generations of mergers (Barnes & Hernquist 1992; Springel et al. 2005a; Mo et al. 2010). Specifically, for mergers between galaxies of similar masses, the resulting galaxy will not appear similar to either of its progenitors (e.g., Barnes 1989). This is known as a major merger. For two galaxies of significantly different masses, a minor merger takes place, which can induce structural changes (e.g., Toomre & Toomre 1972; Naab & Burkert 2003). Through mergers, galaxies in dense environments are observed to be more massive than their field counterparts (e.g., Oemler 1974; Dressler 1980; Butcher & Oemler 1984; Bell et al. 2003; Kauffmann et al. 2003b, 2004).

Mergers can additionally trigger starbursts (e.g., Sanders et al. 1988; Springel et al. 2005a,b; Hopkins et al. 2006), as the gravitational interaction between such systems can drive shocks which compress gas residing in the galaxies. These starbursts can produce star

formation rates of several thousand solar masses per year (e.g., Tacconi et al. 2008), though values of ∼100–300 $M_\odot$ yr^{-1} are more typical (e.g., Sanders & Mirabel 1996; Kennicutt 1998a; da Cunha et al. 2010). Beyond triggering star formation activity, we will see below how mergers can also disrupt star formation, given the chaotic and violent process that mergers enact on their constituent galaxies.

We are now in a position where we have described galaxy formation, radiative cooling processes to support the formation of stars, their evolution, and the role of galaxy mergers on galaxy evolution. This covers nearly all of the components of galaxy evolution as identified in Figure 1.2 above. We have additionally touched on galaxy classification schemes, in order to provide a framework for understanding galaxy evolution. The last topic related to galaxy evolution is how galaxies "die," which we are now in a position to address. This topic will play a central role in the remainder of this thesis.

1.3 Galaxy Quenching

As stated above when discussing the location of galaxies in color–magnitude diagrams, there exists much observational evidence for two distinct populations of galaxies. One forms a blue cloud, while the other populates a red sequence, thus creating the bimodal color distribution for galaxies (e.g., Strateva et al. 2001; Blanton et al. 2003; Baldry et al. 2004; Bell et al. 2004; Peng et al. 2010). Further, we saw above that these two populations have differing characteristic star formation rates, relative to their stellar mass (e.g., Brinchmann et al. 2004; Peng et al. 2010). This is evidence for the last piece of galaxy evolution that we have alluded to above, how galaxies "die," or have their star formation suppressed or quenched. This action will move actively star forming galaxies from the blue cloud, or equivalently the star forming main sequence (see Figure 1.4), onto the red sequence (e.g., Bell et al. 2004; Faber et al. 2007; Martin et al. 2007).

We can additionally consider stellar mass functions (SMFs; e.g., Baldry et al. 2012; Ilbert et al. 2013; Muzzin et al. 2013; Weaver et al. 2023), which describe the number density of galaxies as a function of stellar mass. It has been observed that there is a lack of evolution of the massive end of the star forming SMF with redshift, which is considered strong supporting evidence for quenching (e.g., Faber et al. 2007; Ilbert et al. 2010, 2013; Pozzetti et al. 2010; Muzzin et al. 2013; Weaver et al. 2023). This results in a corresponding build-up of quiescent galaxies with time (Drory et al. 2009; Tomczak et al. 2014; Davidzon et al. 2017).

Clearly, understanding how galaxies have their star formation suppressed or quenched is an integral component of galaxy evolution, and any successful theory of evolution must

also incorporate and explain quenching. As described in previous sections, the availability of cold gas governs the level of star formation. Therefore, if this reservoir of cold gas can be disturbed, then star formation will decline and possibly shut off completely (e.g., Man & Belli 2018). This results in a continually aging stellar population, and ultimately in a quenched galaxy with no active star formation. The process of disturbing the cold gas, or interrupting any of the necessary conditions for star formation, is then paramount in our understanding of galaxy evolution.

There are several broad classes of quenching mechanisms, each capable of interrupting star formation (e.g., Man & Belli 2018). It has been found that these quenching mechanisms can largely be separated into two regimes (e.g., Peng et al. 2010, 2012). The first concerns internal mechanisms, while the second considers external mechanisms, which are largely associated with environment.

1.3.1 Internal Mechanisms

Internal mechanisms are governed by material available within galaxies. Here, this refers to the interactions with the available cold gas supply that is fuel for star formation. Broadly, if this cold gas is prevented from initially forming, or is heated, or removed from the system, a galaxy will be unable to form stars and will quench.

As previously mentioned, the hot gas present in a dark matter halo must cool before it can become fuel for star formation. However, in massive dark matter halos, this gas can heat up (e.g., Birnboim & Dekel 2003) due to virial shocks (e.g., Rees & Ostriker 1977). If this gas is prevented from cooling, then star formation will quench temporarily (e.g., Man & Belli 2018). Further, energy injected into the cold gas supply will cause it to heat, removing it as a fuel source. Energy injection mechanisms include stellar feedback (e.g., Su et al. 2019), where supernovae, radiation pressure, jets, and radiative heating from massive stars output energy into the interstellar medium (e.g., Mo et al. 2010), causing nearby gas reservoirs to heat up, leading to quenching (e.g., Bovy 2026). Supernovae feedback, in particular, produce large amounts of energy which gets deposited into the interstellar medium ($\sim 10^{51}$ erg; e.g., Bovy 2026).

Regarding the effects of active galactic nuclei (AGN), Lynden-Bell (1969) suggested that accretion onto a supermassive black hole at the center of galaxies can power AGN activity. This activity is seen in the radiative and kinetic modes (e.g., Fabian 2012), which can power outflows and jets, respectively, that inject energy and momentum into the interstellar medium (e.g., Di Matteo et al. 2005; Bower et al. 2006; Croton et al. 2006; McNamara & Nulsen 2012). In particular, the radiative mode occurs when large amounts

of gas flow inward and fall onto the supermassive black hole, which produces powerful energy-driven outflows capable of clearing gas from the galaxy (e.g., Fabian 2012; Zubovas & King 2012; King & Pounds 2015). In the kinetic mode, lower accretion rates produce jets which inject energy into the surrounding medium. The added energy will likewise heat the cold gas, preventing star formation from taking place (e.g., Fabian 2012). Thus, for both AGN modes, feedback from AGN will lead to star formation suppression (e.g., Schawinski et al. 2007).

In addition to these feedback mechanisms which promote quenching, other internal mechanisms include disk and bar instabilities (Cole et al. 2000; Martig et al. 2009; Gensior et al. 2020). These mechanisms rearrange the gas content in galaxies, increasing turbulence (e.g. Spinoso et al. 2017), resulting in a suppression of star formation (e.g., Fraser-McKelvie et al. 2020), especially within the inner regions where bars form (Zhang et al. 2021).

1.3.2 External Mechanisms

Beyond the internal mechanisms described above, external mechanisms may interrupt the conditions necessary for star formation (e.g., Peng et al. 2010, 2012). These external mechanisms are due to the environment that a galaxy resides in, and primarily consider the effects of limited gas accretion, as well as gas removal.

First, if a galaxy experiences reduced gas accretion onto its dark matter halo, then with enough time, the cold gas which acts as fuel for star formation can be exhausted. This leads the galaxy to quench, and is described as cosmological starvation (Feldmann & Mayer 2015). In this mode, gas production through stellar evolution can support continued star formation, and so an additional quenching mechanism is needed to fully quench the galaxy (Feldmann & Mayer 2015; Man & Belli 2018). In a related manner, if the inflow of gas is simply cutoff, then a galaxy cannot replenish its cold gas supply, and it will quench. This is known as strangulation (Larson et al. 1980; Kawata & Mulchaey 2008; Peng et al. 2015). As well, the process of simply interrupting the fresh gas supply into a galaxy can cause quenching, as the remaining gas will be eventually exhausted, through overconsumption (e.g. McGee et al. 2014). Related to these processes is the concept of pre-processing, where galaxies in groups and along filaments begin to quench before they are accreted onto more massive structures like galaxy clusters (Fujita 2004; McGee et al. 2009; Wetzel et al. 2013). Here, the primary mechanisms include strangulation/starvation, but gas removal processes can also be important (e.g., Oxland et al. 2024).

Gravitational effects such as dynamical friction, tidal stripping, and gravitational harassment are also capable of quenching galaxies (e.g., Farouki & Shapiro 1981; Moore et al.

1996, 1998, 1999). In these mechanisms, gas is stripped through gravitational interactions, and is therefore common in dense environments like galaxy clusters (e.g., Park & Hwang 2009). Aside from these types of gravitational interactions, galaxy mergers appear as a feasible pathway for quenching, given that they can disrupt the cold gas reservoirs required for star formation. However, the role of mergers in galaxy quenching is currently poorly constrained (e.g., Birnboim et al. 2007; Quai et al. 2021; Ellison et al. 2022). While several authors have found evidence for merger-induced quenching (e.g., Ellison et al. 2022, 2024), others have concluded that mergers are not a significant pathway for galaxy quenching (e.g., Birnboim et al. 2007; Moustakas et al. 2013; Weigel et al. 2017).

Gas removal is the other main environmental mechanism that can promote quenching. Clearly, if a galaxy lacks the cold gas from which it would typically form stars, its star formation rate will drop precipitously. Of course, this clearly depends on the timescales associated with the gas removal. Ram pressure stripping has long been proposed as a viable mechanism capable of removing the cold gas reservoirs from galaxies (Gunn & Gott 1972; Abadi et al. 1999; McCarthy et al. 2008; Boselli et al. 2022). Here, fast moving galaxies in dense environments like galaxy clusters will experience ram pressure, exerted on them by the hot intracluster medium. This ram pressure, $P_{\rm ram}$, scales with the the velocity of the galaxy, v, as $P_{\rm ram} \approx \rho v^2$, where ρ is the density of the medium (Gunn & Gott 1972). It is clear that, when comparing two galaxies in a similar region of a galaxy cluster (i.e. where the intracluster medium density is the same), the faster moving object will experience more ram pressure. Further, as a galaxy travels closer to the cluster center, where the intracluster medium density rises (e.g., Cavaliere & Fusco-Femiano 1976; Jones & Forman 1984; Peterson & Fabian 2006), it will also experience additional ram pressure. This ram pressure will then strip away the interstellar medium from galaxies in such dense environments, and therefore the cold gas as well. This results in quenching. Ram pressure stripping has been proposed as an efficient method to quench galaxies in clusters, with short inferred timescales (e.g., Balogh et al. 2000; Quilis et al. 2000). Notable observational examples of ram pressure stripping include "jellyfish" galaxies, which have distinctive trailing trails along their direction of motion, offset from their optical disks (Ebeling et al. 2014; Poggianti et al. 2016, 2017).

As described above, there are a variety of different mechanisms that have been proposed to explain galaxy quenching. While detailed observations are required to better understand the different mechanisms and associated timescales (see below), a practical framework for investigating different quenching mechanisms is also required.

1.3.3 The Inside-out and Outside-in Framework

We expect that these different quenching modes will present different spatial signatures morphologically (e.g., Zhang et al. 2019), and so studying the spatial distribution of star formation in galaxies that are experiencing quenching will provide insights into the spatial and temporal evolution of these systems. Further, such observations can additionally place constraints on the timescales associated with different quenching mechanisms, and highlight cases for future follow-up.

Regarding internal mechanisms, stellar feedback can in principle take place throughout the disk of a galaxy, whereas evolution driven by bar instabilities will promote quenching in the inner regions of galaxies (Zhang et al. 2021). Notably, active galactic nuclei feedback will lead to suppressed star formation in the central regions of galaxies (Dubois et al. 2013). Concerning external mechanisms, these will largely act to suppress star formation in the outer regions of a galaxy first, prior to the inner regions. Here, strangulation or starvation is thought to result in centrally concentrated star formation (e.g., Finn et al. 2018). As well, ram pressure stripping will remove gas at larger radii first (e.g., Gunn & Gott 1972; Abadi et al. 1999; Quilis et al. 2000; Vollmer et al. 2001; Boselli et al. 2008; Poggianti et al. 2016), similarly resulting in suppressed outer regions. Gravitational harassment can additionally promote nuclear starbursts (e.g., Moore et al. 1996).

Given these expected spatial signatures, a framework that considers 'inside-out' and 'outside-in' quenching is logical (e.g., Lin et al. 2019; Jian et al. 2025; Ho et al. 2026). In this framework, quenching mechanisms that proceed from the inside out will produce suppressed levels of star formation in the inner regions of a galaxy before the outer regions (e.g., Li et al. 2015; Tacchella et al. 2015; Belfiore et al. 2017a; Guo et al. 2019; Bluck et al. 2020a,b; Papaderos et al. 2022). Outside-in quenching proceeds in the opposite direction, where the outer regions of a galaxy are quenched before the inner regions (e.g., Koopmann & Kenney 2004a,b; Schaefer et al. 2017). In Figure 1.6, we show a schematic of these evolutionary signatures, highlighting how quenching proceeds for both cases. Galaxies are assumed to begin as actively star forming (blue regions) across their entirety, before quenching begins. With increasing time (by moving to the right, across the panels), we see the effect of continued quenching on the mock galaxies. In the top row, inside-out quenching produces low levels of star formation (red regions) in the center, before the galaxy is fully quenched (far right). In the bottom row, outside-in quenching acts first on the outskirts of the galaxy, and continues to move inward, until the galaxy is similarly fully quenched. We can therefore use this framework as a shorthand to describe the different quenching mechanisms that may be acting on galaxies.

With our understanding of galaxy evolution now fully established, we next describe

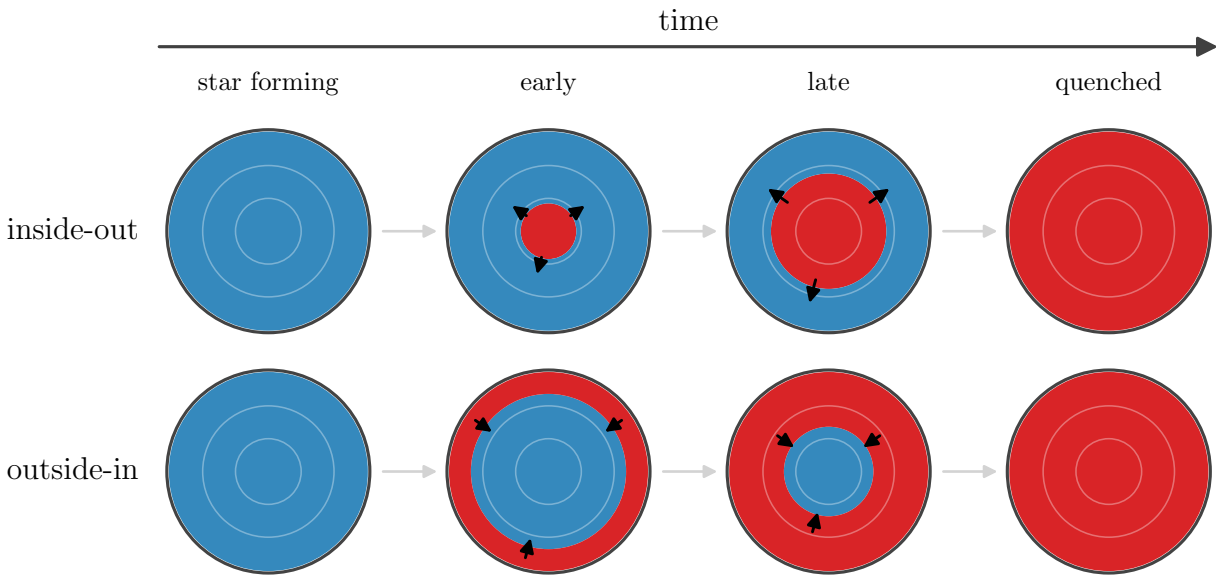


Figure 1.6: Schematic showing the progression of inside-out quenching (top), compared with outside-in quenching (bottom). Time increases from left to right, showing galaxies moving from star forming (left most column), to quenched (rightmost column). Star forming regions are colored blue, while quenched regions are colored red. Based on similar figures in Tacchella et al. (2015) and Lin et al. (2019).

practical considerations related to the methodology presented in the body of this thesis. We begin with a discussion on how to infer physical properties of galaxies, such as stellar mass and star formation rate, from observations.

1.4 Spectral Energy Distribution Fitting

When we observe galaxies in the Universe, we are not directly measuring their physical properties like star formation rate or stellar mass, but instead the imprint of those physical properties on their luminosity output, or spectral energy distribution, as produced by their respective stellar populations. We thus require a procedure for turning observations of galaxies into estimates of their physical properties. This procedure is known as stellar population synthesis, and can be applied to entire galaxies, or parts of a galaxy, if performing a spatially resolved analysis (see below).

1.4.1 Stellar Population Synthesis

Observations of galaxies can largely be separated into spectroscopic and photometric observations. With spectroscopy, an instrument collects the spectrum of a galaxy using a prism or grating. With photometric observations, the spectrum is integrated over a smaller wavelength range through the use of a filter (e.g., Bovy 2026). These filters can be narrow or broad, depending on the analysis. For photometric observations, we generally discuss the resulting spectrum of a galaxy as a spectral energy distribution (SED), as will be used throughout this thesis. Spectroscopic observations of galaxies contain more information than photometric observations, especially photometry obtained with broad bands. However, photometry is less resource intensive, and therefore exists as an attractive option for large galaxy surveys and for faint sources (e.g., Bovy 2026).

To turn observations of galaxy SEDs into physical quantities, like present and historical star formation rate (SFR), stellar mass, metallicity, and dust attenuation, we must essentially consider the contribution of all stars over the lifetime of a galaxy (e.g., Tinsley 1980; Mo et al. 2010). While this sounds daunting, theoretical models governing the number of stars formed as a function of stellar mass, in combination with predictions for the lifetimes of those stars, enables us to determine the corresponding star formation history, SFH = SFR(t), of a galaxy (e.g., Walcher et al. 2011; Conroy 2013). With the star formation history, and again with appropriate models which describe the evolution of stellar populations, we can determine the resulting SED of a galaxy, and therefore fit these models

to observations. These fits then provide the physical information of interest. Specifically, for our purposes here, this includes the stellar mass and star formation rate. Additionally considering the evolution of the recent SFH provides estimates for time-averaged SFRs over characteristic timescales associated with star formation (e.g., Carnall et al. 2019; Leja et al. 2019a), like 10 Myr for Hα observations, and 100 Myr for ultraviolet observations (e.g., Kennicutt 1998b; Calzetti 2013; Madau & Dickinson 2014).

To begin, as detailed above, stars of different initial masses will have different stellar lifetimes, and will produce different SEDs. Massive, hot young stars are short-lived, and emit radiation largely at shorter wavelengths, especially in the ultraviolet. Conversely, less massive, cooler stars that are long-lived emit at longer wavelengths due to Wien's law. This was seen above in Figure 1.3. As well, we know that stars have ages ranging from $\sim$5 Myr to hundreds of Gyr, and even Tyr, which is considerably longer than the current age of the Universe. The star formation history of a galaxy is thus determined from the contributions of the high- and low-mass stars.

The initial mass function (IMF) of the stellar populations must also be considered, where the IMF controls the relative numbers of stars with every stellar mass (e.g., Salpeter 1955; Kroupa 2001; Chabrier 2003). With a fixed number of high-mass stars, the IMF then provides the total number of stars formed in the time equal to their lifetime. This process is then extended to lower-mass stars, and thus to earlier epochs, from which the entire star formation history is then established (e.g., Bovy 2026). For galaxies, the modeling of the composite spectrum from many stars is the procedure of stellar population synthesis (SPS; e.g., Walcher et al. 2011; Conroy 2013). As well, stars born within a giant molecular cloud are born simultaneously as detailed above, and therefore form a coeval population. We show representative SEDs for such coeval stellar populations with different ages in Figure 1.7. It is clear that measuring the SED of a galaxy then provides information on the constituent stellar populations, particularly regarding the level of star formation, as is apparent from the strong evolution of the ultraviolet region in Figure 1.7. The contribution to the red-optical and near-infrared regions of a galaxy SED are then the product of the older, longer-lived stars, and thus trace the stellar mass of a galaxy (e.g., Conroy 2013).

The coeval stellar populations from Figure 1.7 form one of the basic ingredients of stellar population synthesis modeling, the simple stellar population (SSP), which describes the evolution in time of a single coeval population for a single metallicity, Z, and age, t (e.g., Conroy 2013; Bovy 2026). SSPs require three basic ingredients, including an IMF, stellar spectral libraries, and isochrones, which encapsulate stellar evolution theory (e.g., Conroy 2013). An SSP is then constructed by, at a given age t and metallicity Z, drawing a sample of stars from the IMF, using the stellar isochrones to obtain stellar properties for those stars, and using the spectral libraries to get the resulting spectra, given those

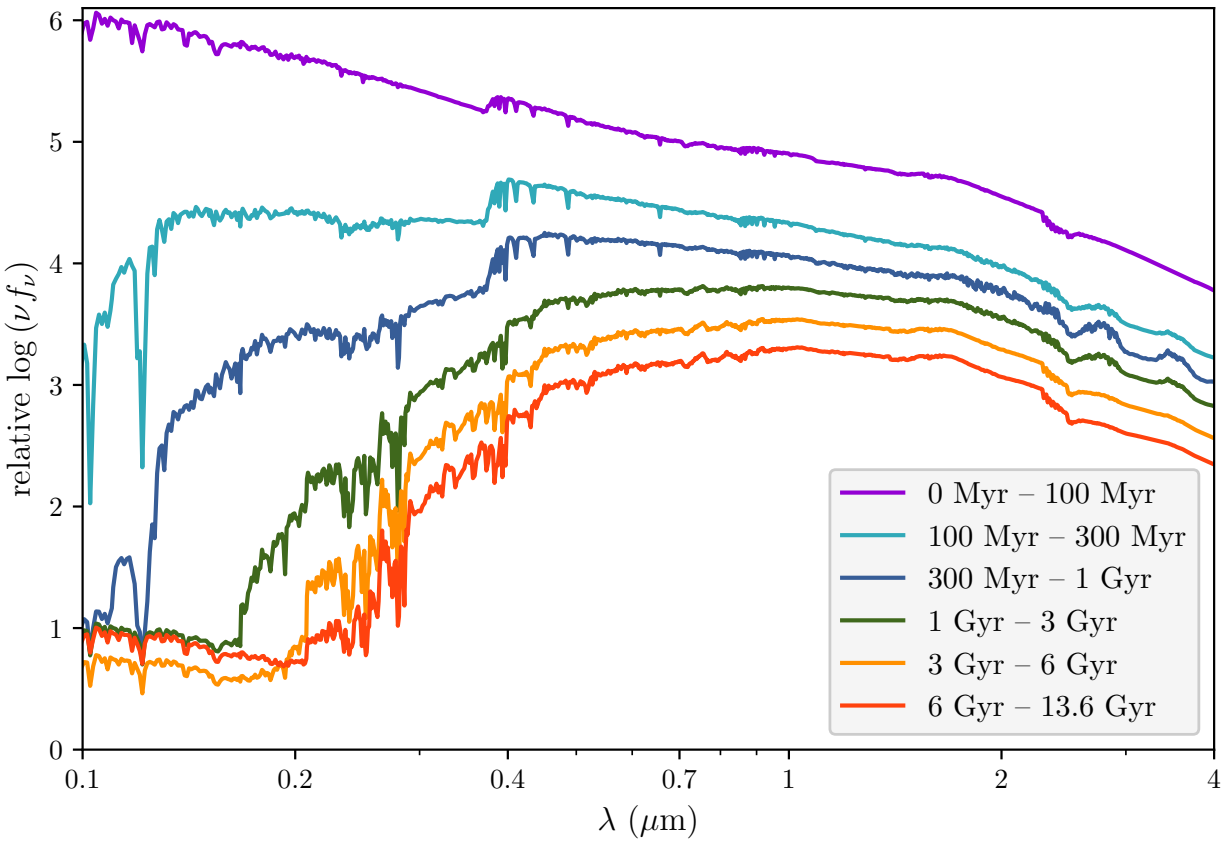


Figure 1.7: Spectral energy distributions for coeval stellar populations with different ages from Bruzual & Charlot (2003). Populations are color-coded by age, and by moving from top to bottom, the stellar populations become older. This results in less ultraviolet flux at short wavelengths, due to a lack of short-lived massive stars. For ancient populations ($t \sim$ 3–5 Gyr, i.e. green, orange, red lines), less evolution is seen from one epoch to the next, given the lack of short-lived stars and dominant presence of long-lived stars. Each spectrum is normalized such that 1 $M_\odot$ formed at $t = 0$. Based on a similar figure in Leja et al. (2017).

properties (e.g., Bovy 2026). The spectrum across all stars is then determined by summing the spectra for the individual sample stars, thereby forming the spectrum for the simple stellar population.

Next, by assuming some shape for the star formation history (SFH; see below), as well as the chemical evolution of Z with time, this collectively describes the distribution of (t, Z) in the galaxy (e.g., Bovy 2026). Further, by accounting for the impact of dust attenuation and emission (e.g., Walcher et al. 2011), simple stellar populations can be combined to form composite stellar populations (CSPs; e.g., Conroy 2013). These composite stellar populations can then be used to model a full galaxy (e.g., Conroy 2013), and the modeled spectrum can be likewise integrated over small wavelength ranges, like broadband filters, to predict observed photometry (e.g., Bovy 2026).

It is therefore clear that SED fitting is a powerful tool to infer the properties of galaxies such as SFR and stellar mass, built on the framework of stellar population synthesis modeling. However, this procedure presents many opportunities for different models and libraries, which we will briefly review below.

1.4.2 Model Parameter Choices

As stellar population synthesis itself builds on simple stellar populations, and simple stellar populations are formed by considering the initial mass function, stellar spectral libraries, and isochrones, the choice of which library or package to use can seem daunting.

Indeed, there are a few viable options for the choice of the initial mass function (e.g., Kroupa 2001), but in this thesis we rely on the lognormal initial mass function, $\xi(M_*)$, of Chabrier (2003), described as

$$\xi(M_*) \propto \begin{cases} e^{-\log(M_*/M_\odot)}, & M_* \leqslant 1\ M_\odot, \\ (M_*/M_\odot)^{-2.3}, & M_* > 1\ M_\odot, \end{cases}$$

where M_* is the stellar mass. We see that while the expression is lognormal for low stellar masses, above 1 $M_\odot$ it takes the form of a power law, consistent with earlier work by Salpeter (1955) and Kroupa (2001).

There additionally exist many options for stellar isochrones (e.g., Schaller et al. 1992; Girardi et al. 2000; Pietrinferni et al. 2004; Bressan et al. 2012; Choi et al. 2016; Eldridge et al. 2017; Marigo et al. 2017), as well as stellar spectral libraries (e.g., Lejeune et al. 1997; Pickles 1998; Prugniel & Soubiran 2001; Le Borgne et al. 2003; Sánchez-Blázquez et al. 2006; Husser et al. 2013; Abdurro'uf et al. 2022b). Taken together, these ingredients

have also been incorporated into simple stellar population packages (e.g., Fioc & Rocca-Volmerange 1997; Leitherer et al. 1999; Maraston 2005; Conroy et al. 2009; Conroy & Gunn 2010; Vazdekis et al. 2010) that can provide spectra and integrated fluxes for every SSP in their library, before being combined into composite stellar populations (e.g., Bovy 2026). In this work we rely on the GALAXEV package of Bruzual & Charlot (2003), updated in 2016 to include improved metallicity and wavelength coverage. Moving from simple stellar populations to composite stellar populations additionally requires an appropriate treatment of dust attenuation and emission (e.g., Conroy 2013). As above, many choices are available for attenuation curves (e.g., Cardelli et al. 1989; Charlot & Fall 2000; Witt & Gordon 2000; Gordon et al. 2003; Kriek & Conroy 2013), but here we employ the simple foreground dust screen described by Calzetti et al. (2000), but with a spatially varying component as described in the body of the thesis. Though not required here, given their emission at long wavelengths ($\lambda \gtrsim 3$ μm; e.g., Bovy 2026), there exist several dust emission treatments (e.g., Draine & Li 2007; Dale et al. 2014; Jones et al. 2017) that can additionally be incorporated when forming CSPs (e.g., Conroy 2013). As well, intergalactic medium absorption can also be accounted for (e.g., Inoue et al. 2014), and here we use the parameterization of Madau (1995).

Finally, the last component that must be specified in order to generate composite stellar populations from simple stellar populations is the shape of the star formation history. Star formation histories can generically be divided into parametric models (e.g., Carnall et al. 2019), as well as nonparametric models (e.g., Leja et al. 2019a). Here, parametric models take functional forms that are analytic expressions. These include simple exponentially declining SFHs (or "tau" models), where SFR(t) $\propto \exp(-t/\tau)$, as well as delayed exponentially declining SFHs, with SFR(t) $\propto t\exp(-t/\tau)$, which are also known as delayed-tau models (e.g., Carnall et al. 2019). Other parametric models include Gaussian SFHs with SFR(t) $\propto \exp[-(t/\tau)^2]$, lognormal SFHs with SFR(t) $\propto \exp[-(\ln t/\tau)^2]/t$, and double power law SFHs with SFR(t) $\propto [(t/\tau)^\alpha + (t/\tau)^\beta]^{-1}$ (e.g., Carnall et al. 2019).

Nonparametric forms are not constrained by any analytic expression, but common choices include a superposition of Gaussians (Iyer et al. 2019), or binned SFHs that divide the SFH into discrete time ranges that can be modeled with a piecewise constant SFH (Leja et al. 2019a; Johnson et al. 2021). For detailed studies of star formation, the choice of star formation history can be important (e.g., Carnall et al. 2019; Leja et al. 2019a). However, more complicated SFHs, such as those in the nonparametric class, are often faced with a computational penalty, where they are slower than parametric models. To mitigate this, and for other physical reasons, some authors have proposed a class of models described as "hybrid" SFHs, which act as an extension to the parametric forms above. These hybrid models often have a parametric form for the majority of the SFH, with

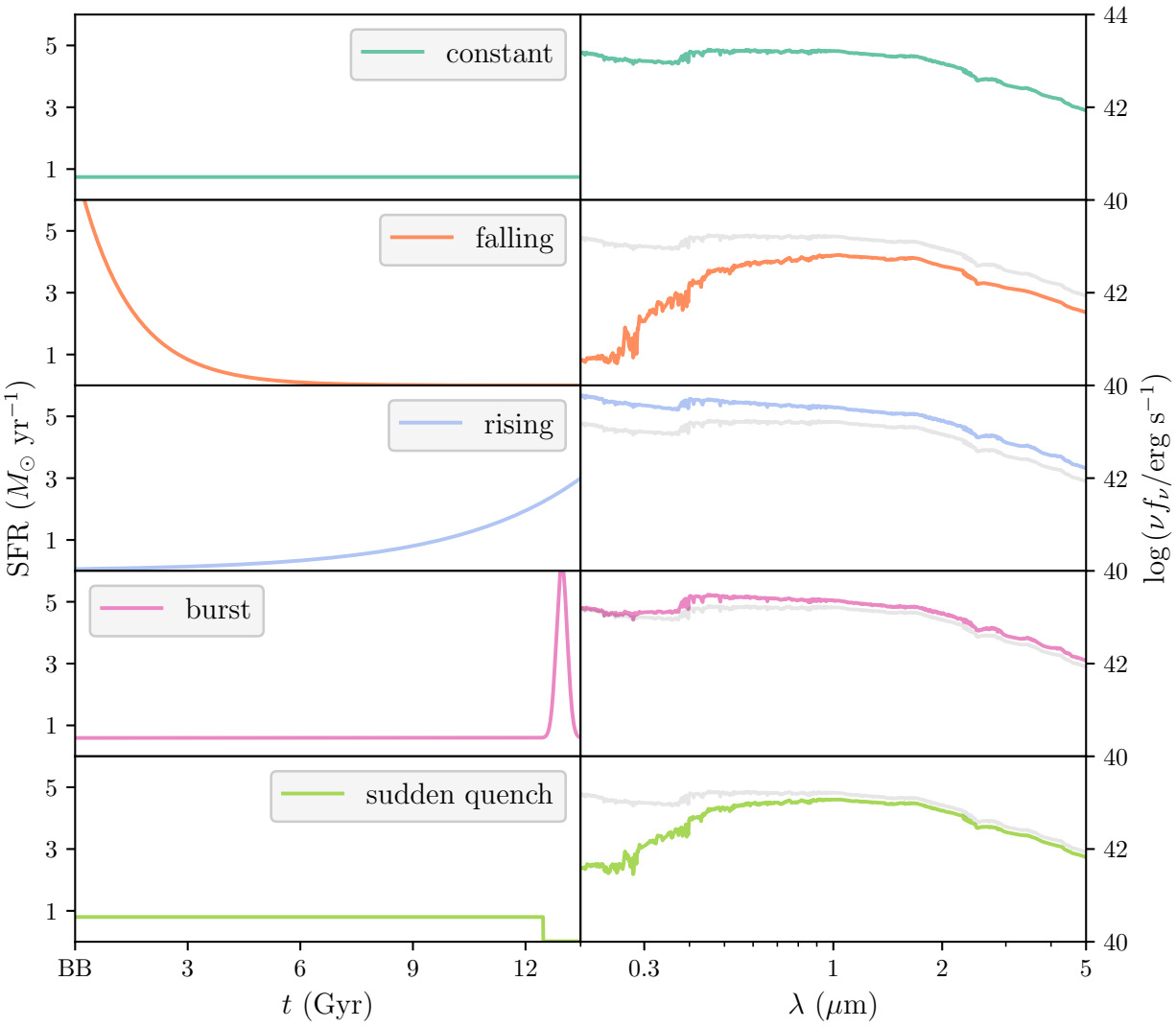


Figure 1.8: Illustrative example star formation histories (left) and corresponding spectral energy distributions (right) for mock galaxies. The example constant (top) and burst (second from bottom) star formation histories produce similar spectral energy distributions. The rising star formation history (middle) also produces a spectral energy distribution with a similar shape, but that has a higher normalization. For reference, the spectral energy distribution for the constant star formation history is shown in gray in the other panels. Based on similar figures in Carnall et al. (2019) and Leja et al. (2019a).

an optional burst or truncation implemented for recent times, where the duration of the burst/truncation is additionally flexible (e.g., Fumagalli et al. 2011; Ciesla et al. 2016, 2018, 2021; Schreiber et al. 2018a). In Figure 1.8, we show example star formation histories (left) and their resulting spectral energy distributions (right), for a number of generic star formation histories. These include a constant SFH (top), an exponentially declining SFH (second from top), and SFHs which incorporate bursts and truncations (bottom two rows). These SFHs and their resulting SEDs show that under certain conditions, differing star formation histories can produce similar spectral energy distributions.

As will be seen in the body of the thesis, we employ a hybrid SFH that is based off a delayed-tau model, where the majority of the SFH is described as such. For the final 100 Myr before observation, we include an additional multiplicative factor, R, which scales the entire SFH over this duration:

$$\mathrm{SFR}(t) \propto \begin{cases} te^{-t/\tau}, & t_{\mathrm{lookback}} > 100 \text{ Myr}, \\ R \times te^{-t/\tau}, & t_{\mathrm{lookback}} \leqslant 100 \text{ Myr}, \end{cases}$$

where t_{lookback} is the lookback time, at the time of observation. This parameterization provides the flexibility for simultaneously modeling the older stellar populations, described via the delayed-tau model, and the younger stellar populations, captured through the scaling coefficient R. In particular, we use the final 100 Myr to determine time-averaged SFRs, as this is the timescale traced by ultraviolet and infrared observations (e.g., Kennicutt 1998b; Calzetti 2013; Madau & Dickinson 2014).

Similar to the many possible choices regarding stellar isochrones, stellar libraries, and simple stellar population packages, there exist many optimized codes under active development for spectral energy distribution fitting (e.g., Iyer & Gawiser 2017; Iyer et al. 2019; Leja et al. 2017, 2019a; Carnall et al. 2018; Boquien et al. 2019; Johnson et al. 2021). Indeed, SED fitting codes have even been developed specifically for probing smaller regions within galaxies (Abdurro'uf et al. 2021). In this thesis, we use the SED fitting code `FAST++` (Kriek et al. 2009; Schreiber et al. 2018b) for our investigations, as will be detailed in the relevant chapters. The above point, of mapping the internal structure of galaxies in order to analyze their spatial properties, will play a major role in the thesis, and will be reviewed in the next section.

1.5 Spatially Resolved Observations

Over the past two decades, progress has been made in mapping the structure of galaxies through spatially resolved observations. These investigations divide a galaxy into several

regions, instead of considering a galaxy as a single monolithic structure. Though they are not resolving individual stars within galaxies, given their extragalactic distances, they are resolving regions of galaxies, and thus the stellar populations which reside in those regions. They critically provide additional information compared with integrated observations, and have become a rapidly growing field within the community.

Early work using spatially resolved observations investigated color distributions and gradients within nearby and intermediate redshift galaxies (e.g., Abraham et al. 1999; Bell & de Jong 2000; Zheng et al. 2004; Wu et al. 2005; Zibetti et al. 2009). These studies then mapped the inferred physical properties of galaxies from the color distributions, like star formation rate, stellar mass, and relative age. Since then, subsequent studies have used newer techniques to study spatially resolved populations, but have built on the foundation that was laid by these early works.

In the intervening years, large integral field unit programs have become operational, and have observed thousands of galaxies (e.g., Croom et al. 2021). Notable integral field unit programs include the Sydney-AAO Multi-object Integral field spectrograph galaxy survey (SAMI; Croom et al. 2012; Bryant et al. 2015) and the Calar Alto Legacy Integral Field Area survey (CALIFA; Sánchez et al. 2012). In particular, the Mapping Nearby Galaxies at Apache Point Observatory (MaNGA; Bundy et al. 2015) survey has provided spatially resolved observations for 10^4 nearby galaxies (Abdurro'uf et al. 2022b), enabling many investigations into the structure of galaxies, specifically the role of quenching (e.g., Belfiore et al. 2018; Ellison et al. 2018; Spindler et al. 2018; Wang et al. 2018; Lin et al. 2019). These investigations will be described in more detail in the body of the thesis.

Beyond these large integral field unit surveys, targeted observations of galaxies and galaxy clusters using integral field units have additionally become increasingly commonplace (e.g., Poggianti et al. 2016, 2025; Neumann et al. 2020). These observations use the latest generation of integral field units (e.g., Bacon et al. 2010; Takada et al. 2014; Morrissey et al. 2018; Jakobsen et al. 2022; Jin et al. 2024) to probe the distribution of star formation and stellar mass, and have likewise examined the physical mechanisms driving quenching (e.g., Poggianti et al. 2017; Vulcani et al. 2020; Roberts et al. 2022).

Further, the use of high-resolution photometry to perform spatially resolved investigations has additionally become more frequent, especially in light of high-resolution observations available from the Hubble Space Telescope, the James Webb Space Telescope (Gardner et al. 2006, 2023), and Euclid (Euclid Collaboration et al. 2025). This trend should continue with the upcoming Nancy Grace Roman Space Telescope (Spergel et al. 2013, 2015; Akeson et al. 2019), and the proposed Cosmological Advanced Survey Telescope for Optical and UV Research (Côté et al. 2025). These types of investigations generally

perform spatially resolved spectral energy distribution fitting like described above, in order to map star formation rates and stellar mass (e.g., Abdurro'uf & Akiyama 2018; Abdurro'uf et al. 2023; Jafariyazani et al. 2019; Morselli et al. 2019; Nelson et al. 2021). With these properties, radial profiles of specific star formation rate, for example, can be constructed to probe different quenching mechanisms.

1.6 Cosmological Simulations

Similarly to spatially resolved observations, the use of large cosmological hydrodynamical simulations for galaxy evolution investigations has accelerated over the past two decades. Indeed, now it is common to find studies comparing observations with simulations. These comparisons highlight areas where simulations excel, in their ability to reproduce the observed galaxy population, and areas where simulations struggle to reproduce observations, suggesting a need for different physical implementations within the simulations. As well, they enable direct investigations into the simulated galaxy population, and are capable of providing large numbers of highly resolved galaxies over cosmological volumes. Given their ubiquity in the current landscape of galaxy evolution studies, we must briefly review such simulations, and in particular, large cosmological hydrodynamical simulations, especially in light of their use in the body of this thesis.

To begin, these simulations start with a cosmological model, like the ΛCDM model described above (e.g., Planck Collaboration et al. 2020), and define a set of initial conditions, typically around $z \sim 100$ (e.g., Crain & van de Voort 2023), which describe the small-scale perturbations on a homogeneous background (e.g., Vogelsberger et al. 2020). They additionally include physical models for gravity and dark energy. They then consider collisionless gravitational dynamics to describe the evolution of dark matter halos (e.g., Crain & van de Voort 2023), which build the scaffolding for galaxies. At this point, if no hydrodynamics have been implemented, these simulations can be followed with the N-body method, and can be described as N-body simulations (e.g., Springel et al. 2005c). Such simulations are a benchmark for clustering studies (e.g., Angulo et al. 2012), and have even used semi-analytic models to populate galaxies within halos (e.g., Springel et al. 2005c).

Next, equations for hydrodynamics are included and solved using different methods. These include Lagrangian, Eulerian, or arbitrary Lagrangian-Eulerian techniques, such as smoothed particle hydrodynamics, adaptive mesh refinements, and moving mesh (e.g., Vogelsberger et al. 2020; Crain & van de Voort 2023; Feldmann & Bieri 2026). Additionally, astrophysical processes are included to produce a realistic galaxy population. The most

important processes consider gas cooling, the interstellar medium, star formation and stellar feedback, the formation and growth of supermassive black holes, active galactic nuclei feedback, magnetic and radiation fields, as well as cosmic rays (e.g., Vogelsberger et al. 2020; Crain & van de Voort 2023; Feldmann & Bieri 2026). These hydrodynamical simulations reproduce the observed galaxy population remarkably well (e.g., Man & Belli 2018), including the star forming main sequence (e.g., Donnari et al. 2019), but there still remain areas of disagreement (e.g., Crain & van de Voort 2023; Feldmann & Bieri 2026), likely owing to the implementation of the subgrid physics model for baryons (e.g., Vogelsberger et al. 2020).

Large cosmological hydrodynamical simulations that have become available over the past decade include Illustris (Genel et al. 2014; Vogelsberger et al. 2014a; Nelson et al. 2015), EAGLE (Crain et al. 2015; Schaye et al. 2015; McAlpine et al. 2016), and COLIBRE (Schaye et al. 2026). In this thesis, we rely on the IllustrisTNG (Nelson et al. 2018, 2019a; Pillepich et al. 2018a; Springel et al. 2018) simulations, specifically the TNG50 run (Nelson et al. 2019b; Pillepich et al. 2019) for our initial investigations. In TNG50, the typical baryonic mass is 8.5×10^4 $M_\odot$, within a simulation box of $L_{\rm box} = 51.7$ cMpc (e.g., Nelson et al. 2019b). This implies that galaxies with $M_* \gtrsim 10^{9.5}$ $M_\odot$ are resolved with $\gtrsim$37,500 particles, enabling us to complete detailed spatially resolved analyses.

Beyond the above mentioned simulations, very large cosmological hydrodynamical simulations ($L_{\rm box} \gtrsim 750$ cMpc) have been completed recently, including MillenniumTNG (Pakmor et al. 2023), FLAMINGO (Schaye et al. 2023), and TNG-Cluster (Nelson et al. 2024). These simulations probe even larger structures, and correspondingly have poorer mass resolution (e.g., Schaye et al. 2026). Though they technically resolve $M_* \approx 10^{9.5}$ $M_\odot$ galaxies with hundreds of particles, this is insufficient for the type of spatially resolved investigations presented in this thesis. However, they remain compelling tests of our understanding of the growth of structure in the Universe, including galaxy clusters, as well as the formation and properties of massive galaxies that they can resolve (e.g., Vogelsberger et al. 2020; Crain & van de Voort 2023).

1.7 This Thesis

This thesis includes several projects that attempt to understand galaxy evolution, specifically the nature of galaxy quenching, through spatially resolved observations of stellar populations. This is undertaken using both simulations, as well as observations. Briefly, the main themes include the mechanisms regulating quenching within galaxies, the environmental dependence of those mechanisms, as well as the mass dependence. These themes

are framed through the lens of the inside-out and outside-in framework described above, as well as adopted throughout the literature. As well, each of these projects successively builds on the previous project(s), thereby providing additional context for the results.

Chapter 2 presents the first project, which investigated the nature of quenching and quenched galaxies in the TNG50 simulation. Critically, this project developed morphological metrics that trace the distribution of star formation within galaxies. These metrics were then used to form populations of inside-out and outside-in quenched galaxies, and their time evolution was considered. As well, we also investigated the typical environments for these different populations, as well as their characteristic masses.

Chapter 3 presents the second project, which investigated the recovery of the morphological metrics when using mock observations. In this project, we produced mock photometry that is consistent with expectations for upcoming and proposed space telescopes, and made adaptations to the metrics for such observations. This mock photometry is additionally consistent with the quality available from the Hubble Space Telescope.

Chapter 4 presents the third project, which investigated the nature of quenching galaxies within the Hubble Frontier Fields (Lotz et al. 2017). Using the morphological metrics and their observational adaptations, we likewise formed populations of galaxies that are consistent with inside-out and outside-in quenching signatures. The environments of these populations, their stellar mass, as well as their distance from the star forming main sequence were all considered.

Chapter 5 then summarizes these projects, and presents the overall conclusions from these works, in particular what they have revealed about the nature of galaxy quenching, and how it can best be studied. As well, we discuss potential future work, including new techniques and observations that will shortly be available with upcoming large-scale galaxy surveys.

Chapter 2

Identifying and Distinguishing Quenching Galaxies with Spatially Resolved Star Formation in TNG50

2.1 Introduction

It has been well known for several decades that galaxies exhibit a strong bimodality in color (e.g., Strateva et al. 2001; Blanton et al. 2003; Baldry et al. 2004; Bell et al. 2004; Driver et al. 2006; Wyder et al. 2007; Brammer et al. 2009; Gavazzi et al. 2010; Peng et al. 2010; Taylor et al. 2015), with a prominent red sequence alongside a blue cloud. Galaxies residing in the red sequence have low rates of star formation (e.g., Blanton & Moustakas 2009; Bluck et al. 2020a,b), and therefore appear "red and dead" (e.g., Brammer et al. 2009; Schawinski et al. 2014), while actively star forming galaxies comprise the blue cloud (e.g., Strateva et al. 2001; Bell et al. 2004; Bluck et al. 2020a,b). Galaxies that have their star formation suppressed or quenched will move from the blue cloud to settle onto the red sequence (e.g., Bell et al. 2004; Faber et al. 2007; Martin et al. 2007). The lack of evolution of the massive end of the star forming stellar mass function with redshift is considered strong supporting evidence for quenching (e.g., Faber et al. 2007; Ilbert et al. 2010, 2013; Pozzetti et al. 2010; Muzzin et al. 2013; Weaver et al. 2023), and there is a corresponding build-up of quiescent galaxies with time (e.g., Drory et al. 2009; Tomczak et al. 2014; Davidzon et al. 2017).

Many physical scenarios have been proposed to explain galaxy quenching. Lack of gas accretion or cooling, the inability of cold gas to form stars, the rapid consumption of

cold gas, and gas outflow or removal are some of the primary considerations for different quenching mechanisms (Man & Belli 2018). For example, active galactic nuclei feedback has long been thought to be an additional energy source that will prevent gas cooling (e.g., Di Matteo et al. 2005; Bower et al. 2006; Croton et al. 2006; McNamara & Nulsen 2007, 2012; Fabian 2012). Similarly, disk or bar instabilities can lead to internal secular quenching (Cole et al. 2000; Martig et al. 2009; Gensior et al. 2020). Environmental effects must also be considered as an independent pathway for quenching (e.g., Peng et al. 2010). The interaction between a galaxy falling into a large structure like a galaxy cluster and its intracluster medium will lead to ram pressure being exerted on the galaxy (Gunn & Gott 1972; Boselli et al. 2022; Dowling & Bradley 2023). Strangulation or starvation (Larson et al. 1980; Kawata & Mulchaey 2008; Peng et al. 2015) prevents galaxies from replenishing their cold gas supply, while gravitational harassment (Moore et al. 1996, 1998, 1999) is due to close galaxy–galaxy interactions in dense environments like clusters.

While these various mechanisms will all eventually quench a galaxy in the absence of gas inflow, it is expected as an ansatz that these mechanisms will present different morphological spatial signatures (Zhang et al. 2019) for young stellar populations that trace star formation. However, it is not clear how the signatures express themselves in the full dynamic environment of galaxies. For instance, it has been proposed that active galactic nuclei feedback in the inner regions of a galaxy will lead to a lack of young stars in these central regions (e.g., Dubois et al. 2013). Environmentally, ram pressure stripping will progressively remove gas from the outer regions of a galaxy (e.g., Gunn & Gott 1972; Abadi et al. 1999; Quilis et al. 2000; Balogh et al. 2000; Vollmer et al. 2001; McCarthy et al. 2008; Boselli et al. 2008; Poggianti et al. 2016, 2017), and it should lead to galaxies with centrally concentrated star formation. Strangulation or starvation is thought to similarly shrink the star forming disk of a galaxy (Finn et al. 2018; Morgan et al. 2024), while gravitational harassment can lead to tidal features (Farouki & Shapiro 1981) and nuclear starbursts (Moore et al. 1996).

Spatially resolved observations are therefore an ideal avenue to best understand the complicated nature of galaxy quenching, given the additional information provided by such observations compared to integrated galaxy properties. Early work utilizing spatially resolved observations focused on color distributions to create maps of relative age, star formation rate, and stellar mass for nearby and intermediate-redshift galaxies (e.g., Abraham et al. 1999; Bell & de Jong 2000; Zheng et al. 2004; Wu et al. 2005; Zibetti et al. 2009). Since then, several large integral field unit programs including the Calar Alto Legacy Integral Field Area survey (CALIFA; Sánchez et al. 2012), the Sydney-AAO Multi-object Integral field spectrograph galaxy survey (SAMI; Croom et al. 2012; Bryant et al. 2015), and the Mapping Nearby Galaxies at Apache Point Observatory (MaNGA; Bundy et al.

2015) have made spatially resolved observations available in large quantities for thousands of nearby galaxies (Croom et al. 2021; Abdurro'uf et al. 2022b). This has enabled substantial progress in studies of active galactic nuclei host galaxies (e.g., Sánchez et al. 2018), age, metallicity, and specific star formation rate gradients (e.g., González Delgado et al. 2014, 2015, 2016; Belfiore et al. 2017b, 2018; Goddard et al. 2017), oxygen abundance gradients (Sánchez et al. 2014; Sánchez-Menguiano et al. 2016), the dynamical state–morphology relation (e.g., Cortese et al. 2016; Brough et al. 2017; Falcón-Barroso et al. 2017; Graham et al. 2018), ionized gas excitation properties (Belfiore et al. 2016; Zhang et al. 2017), the morphology–density relation (e.g., Schaefer et al. 2017, 2019; Owers et al. 2019), the resolved star forming main sequence (e.g., Cano-Díaz et al. 2016; Ellison et al. 2018; Medling et al. 2018), and stellar mass assembly (e.g., Pérez et al. 2013; Ibarra-Medel et al. 2016).

Of particular note is work with integral field unit observations that has been done to understand the nature of inside-out quenching, where star formation is initially suppressed in the central regions of a galaxy and proceeds outward (e.g., González Delgado et al. 2015, 2016; Li et al. 2015; Tacchella et al. 2015, 2016, 2018; Belfiore et al. 2017a, 2018; Goddard et al. 2017; Ellison et al. 2018; Liu et al. 2018; Medling et al. 2018; Sánchez et al. 2018; Spindler et al. 2018; Wang et al. 2018; Guo et al. 2019; Lin et al. 2019; Woo & Ellison 2019; Neumann et al. 2020; Leung et al. 2025). In addition to integral field unit observations, several authors have used high-resolution photometry to understand inside-out quenching through the use of spectral energy distribution fitting (e.g., Morselli et al. 2019; Nelson et al. 2021). Notably, Morselli et al. (2019) find that galaxies that are below the star forming main sequence (e.g., Brinchmann et al. 2004) show a clear suppression of star formation in their central regions, and this suppression becomes stronger with increasing distance below the main sequence. Similarly, Nelson et al. (2021) find, by comparing their high-resolution observations to simulated galaxies from the high-resolution TNG50 (Nelson et al. 2019b; Pillepich et al. 2019) run of IllustrisTNG (e.g., Nelson et al. 2018; Pillepich et al. 2018a; Springel et al. 2018), that massive galaxies below the main sequence likewise display centrally suppressed star formation in both observations and simulations.

In addition to the many studies that have investigated the nature of inside-out quenching, others have examined outside-in quenching, where star formation is initially suppressed in the outer regions of a galaxy and proceeds inward (e.g., Schaefer et al. 2017, 2019; Medling et al. 2018; Chen et al. 2019; Owers et al. 2019; Wang et al. 2022; Cheng et al. 2024b). Considering integral field unit studies and SAMI galaxies, these works have shown that the fraction of star forming galaxies with centrally concentrated star formation increases with increasing environmental density (Schaefer et al. 2017; Wang et al. 2022), and group galaxies display lower levels of specific star formation than field galaxies, along with enhanced centrally concentrated star formation (Schaefer et al. 2019). As well, SAMI

galaxies in denser environments display suppressed specific star formation radial profiles from the outside in (Medling et al. 2018), and galaxies with strong Hδ absorption (indicative of a lack of ongoing star formation; Couch & Sharples 1987; Poggianti et al. 1999) are more often found in clusters than the field. These galaxies have the strongest Hδ absorption in their outskirts (Owers et al. 2019). In addition, Finn et al. (2018) found smaller star forming disks in cluster galaxies using 24 μm Spitzer (Werner et al. 2004) imaging, while Finn et al. (2023) found an excess of star forming galaxies with suppressed star formation rates in clusters. Similar results were found by Morgan et al. (2024) using different techniques in Virgo, as well as by Conger et al. (2025). Furthermore, several studies using integral field unit data have investigated ram pressure stripping in galaxies (e.g., Poggianti et al. 2017, 2019, 2025; Vulcani et al. 2020; Roberts et al. 2022).

Beyond integral field unit programs, the next decade will see continued growth in large galaxy surveys with current, upcoming, and proposed missions that provide high spatial resolution, using facilities like the James Webb Space Telescope (JWST; Gardner et al. 2006, 2023), the Nancy Grace Roman Space Telescope (NGRST; Spergel et al. 2015; Akeson et al. 2019), and the Cosmological Advanced Survey Telescope for Optical and UV Research (CASTOR; Côté et al. 2025). Given the great diversity and complexity of different quenching mechanisms, similar analyses of simulated data will be essential for interpretation. In recent years, many large-scale cosmological simulations have become available (e.g., Genel et al. 2014; Vogelsberger et al. 2014a; Schaye et al. 2015; Nelson et al. 2018; Pillepich et al. 2018a; Springel et al. 2018).

To that end, we aim to use simulations to identify quenching galaxies using simple, observationally motivated metrics that encode information about the physical nature of quenching, through samples of galaxies that end up quenched. These morphological metrics should easily separate quenching galaxies from star forming galaxies based on the distribution of star formation alone, be capable of separating quenching galaxies based on the spatial signature of quenching (e.g., inside-out versus outside-in), provide information on the length of time that quenching takes, and provide insight into how far along the quenching process a galaxy might be. Using simulated galaxies facilitates tracking the evolution of these quenching systems and thus the evolution of these morphological metrics. With the high spatial resolution provided by recent cosmological simulations, we are in a position to better link our findings to what we can observe, and make predictions for the morphological evolution of quenched galaxies in the real Universe.

This chapter is structured as follows: in Section 2.2, we describe the data coming from the high-resolution TNG50 simulation, our analysis procedure to identify quenched galaxies in the simulation, and our metrics that we use to classify galaxies based on morphological evolution. In Section 2.3, we present our results, differences between quenched populations,

show how our metrics evolve with time, and illustrate how machine learning can be used to best separate different populations. In Section 2.4, we discuss our results, in particular focusing on the complementary nature of these morphological metrics when coupled with other environmental measures related to phase space, and the feasibility and implications of using such metrics in upcoming large-scale galaxy surveys. Finally, in Section 2.5, we present our summary and conclusion.

Throughout this chapter, we adopt a flat ΛCDM cosmology that is consistent with the TNG simulation (Weinberger et al. 2017; Pillepich et al. 2018b), based on the Planck intermediate results (Planck Collaboration et al. 2016): $H_0 = 67.74$ km s^{-1} Mpc^{-1}, $\Omega_\mathrm{m} = 0.3089$, $\Omega_\Lambda = 0.6911$, and $\Omega_\mathrm{b} = 0.0486$. Additionally, we frequently use the term "morphology" when referring to the spatial distribution of newly formed stars, in contrast with usage of the term "galaxy morphology" in the literature, which generally describes the visual morphology of the total stellar component.

2.2 Methodology

2.2.1 IllustrisTNG

The simulations that comprise the IllustrisTNG suite[1] (e.g., Nelson et al. 2018, 2019a; Pillepich et al. 2018a; Springel et al. 2018) are state-of-the-art cosmological gravo-magneto-hydrodynamical simulations and feature an updated version of the galaxy formation model (Weinberger et al. 2017; Pillepich et al. 2018b) included in Illustris (Vogelsberger et al. 2013; Torrey et al. 2014). These simulations are the successor to the original Illustris simulation (Genel et al. 2014; Vogelsberger et al. 2014b,a), which uses the moving-mesh code AREPO (Springel 2010; Pakmor et al. 2011, 2016; Weinberger et al. 2020). Various considerations were taken into account when developing the IllustrisTNG model, but chief among these are tuning the model to match observations of the global star formation rate (SFR) density across $z = 8$ to $z = 0$, the galaxy mass function, the stellar mass–halo mass relation, the black hole–stellar mass relation, halo gas fractions, and galaxy sizes, all at $z = 0$ (Rodriguez-Gomez et al. 2019). In the IllustrisTNG simulations, subhalos (i.e. galaxies) are identified from their parent halos using the SUBFIND algorithm (Springel et al. 2001; Dolag et al. 2009), while a cosmology consistent with the Planck Collaboration et al. (2016) results is adopted, and stellar populations are drawn from a Chabrier (2003) initial mass function (Pillepich et al. 2018b). All simulation data from IllustrisTNG are publicly available (Nelson et al. 2019a).

[1] https://www.tng-project.org

In the present work, we use the highest-resolution simulation in the suite, TNG50-1 (hereafter referred to as TNG50), which encompasses a cubic volume of $35h^{-1} \approx 51.7$ Mpc on a side (Nelson et al. 2019b; Pillepich et al. 2019), and follows the evolution of 2×2160^3 resolution elements (dark matter and baryons), where the average mass of a baryonic resolution element is $8.5 \times 10^4\ M_\odot$. The spatial scale of the simulation is essentially set by the gravitational softening length of the dark matter and stellar particles, which is 288 pc at $z = 0$, while the gas softening is adaptive with a minimum of 74 pc (comoving; Nelson et al. 2019b; Pillepich et al. 2019). The average cell size of star forming gas in the interstellar medium of galaxies is ∼100–140 pc (Nelson et al. 2019b; Pillepich et al. 2019). TNG50 has better mass resolution by more than an order of magnitude over the flagship TNG100-1, with two and a half times better spatial resolution (Nelson et al. 2019b), placing TNG50 near modern 'zoom' simulations of individual galaxies in terms of mass resolution, but in a large cosmological volume.

2.2.2 Distinguishing star forming galaxies from quenched galaxies using star formation histories

Selecting a galaxy sample

We begin our analysis by considering fundamental properties of all subhalos (galaxies) present in TNG50 at $z = 0$, including stellar masses and instantaneous star formation rates (SFRs). We limit our analysis to galaxies with a total stellar mass of at least $M_* = 10^{9.5}\ M_\odot$ by $z = 0$, to ensure that specific SFR (sSFR = SFR/$M_\odot$) radial profiles extend to a sufficient distance with adequate sampling (i.e. we essentially require a sufficient number of stellar particles per galaxy; see Section 2.2.3). We find 1666 total galaxies with $M_* \geqslant 10^{9.5}\ M_\odot$ at $z = 0$ which comprise our fiducial sample. We additionally consider masses for the dark matter halos in which the subhalos are embedded, in order to describe their environment.

We consider the merger history and evolution for each galaxy, and track them back through "main progenitor branch" files that encode fundamental information about a galaxy as a function of time through the simulation, similar to what was previously used for all subhalos at $z = 0$. As these files describe the merger history of each galaxy, they link a given galaxy at an arbitrary snapshot with the corresponding progenitor galaxy at the proceeding snapshot, as well as the descendant galaxy at the subsequent snapshot (Nelson et al. 2015). As galaxies will experience many mergers, by considering only the most massive galaxy involved in a merger, the main branch along the progenitor tree can be tracked (e.g., Genel et al. 2018; Nelson et al. 2019a). Within these main progenitor branch files, we

have access to additional information such as the stellar mass history, which describes the stellar mass of the galaxy as a function of time, the instantaneous star formation history, which describes the instantaneous SFR of the galaxy as a function of time, as well as the position of the galaxy within the simulation volume, once again as a function of time. We additionally obtain the radius that encompasses half the stellar mass (which functions as the effective radius, R_e), for the simulated galaxies as a function of time.

For each snapshot along the main progenitor branch for each galaxy, we use three-dimensional "cutouts" of the simulation volume, which encapsulates every bound particle to a given galaxy at that snapshot. We focus on parameters related to the stellar particles (i.e. position, initial birth mass, current mass, and formation time).

Determining star formation histories and the main sequence

We subsequently determine time-averaged total star formation histories (SFHs) for each galaxy in our fiducial sample by employing the results of Donnari et al. (2019) and Pillepich et al. (2019), who produced catalogs[2] of SFRs across various time intervals (e.g., 10, 50, 100, 200, and 1000 Myr) for the simulations in the IllustrisTNG suite. In their work, Donnari et al. (2019) and Pillepich et al. (2019) computed SFRs across the aforementioned timescales by considering all stellar particles formed within the given amounts of time prior to each snapshot (in various physical apertures) through summation of their initial (birth) masses. We use total SFRs, which are computed by including all gravitationally bound stellar particles of a given subhalo, and select 100 Myr as our nominal duration for our time-averaged SFRs. We choose 100 Myr, as it reflects the upper limit of a timescale that is often thought to describe "recent" star formation for an entire galaxy (Calzetti 2013) and is the timescale best traced with ultraviolet and infrared observations (e.g., Kennicutt 1998b; Madau & Dickinson 2014). These time-averaged SFRs are in contrast to the instantaneous SFRs tabulated within the main progenitor branches, which are not observationally motivated. By working through the main progenitor branch for each galaxy and tracking the time-averaged SFRs, we create time-averaged SFHs. When we subsequently refer to the SFR of a galaxy or to attributes or properties related to star formation, we are implicitly using time-averaged values over the above described 100 Myr interval.

While the SFHs are being computed for every galaxy in the sample, we simultaneously determine the star forming main sequence (SFMS, or galaxy main sequence; e.g., Brinchmann et al. 2004; Daddi et al. 2007; Elbaz et al. 2007; Noeske et al. 2007; Peng et al. 2010; Rodighiero et al. 2011; Speagle et al. 2014; Davies et al. 2019; Bluck et al. 2022). We adopt

[2] https://www.tng-project.org/data/docs/specifications/#sec5b

the "ridge line method" (e.g., Pillepich et al. 2019; Donnari et al. 2021b,a; Bottrell et al. 2024) described in Donnari et al. (2019) to determine the SFMS, where galaxies are first binned by snapshot stellar mass and the median (log) SFR is determined for galaxies within a given bin. We use a bin size of 0.2 dex, and only consider galaxies with $M_* \leqslant 10^{10.5}\ M_\odot$, given that this mass scale roughly corresponds with the location where the SFMS deviates from linearity as determined observationally (e.g., Whitaker et al. 2012, 2014) and in TNG (Donnari et al. 2021a). Galaxies with SFRs that are far (>1 dex) from the current estimate of the median SFR within the bin are subsequently removed from further analysis, and the median is recomputed. This procedure is repeated iteratively until the median SFR converges and no further iterations are required. These final median SFRs per bin are used with the bin centers to fit a linear function of the form (Donnari et al. 2019)

$$\langle \log (\mathrm{SFR}/M_\odot\ \mathrm{yr}^{-1}) \rangle = \alpha(z) \log (M_*/M_\odot) + \beta(z),$$

where $\langle \log (\mathrm{SFR}) \rangle$ are the median (log) SFRs, and $\alpha(z)$ and $\beta(z)$ are the slope and intercept of the resulting fits, respectively, as a function of redshift. For $M_* > 10^{10.5}\ M_\odot$, the SFMS is then linearly extrapolated using the fitted values. We take SFMS galaxies to be those with $\Delta \log (\mathrm{SFR}) \geqslant -0.5$, consistent with Pillepich et al. (2019). This procedure is then repeated for every snapshot to determine the SFMS as a function of time.

An example SFH for a normal star forming galaxy can be seen in the top panel of Figure 2.1, along with lines denoting the $\pm 2\sigma$ spread of SFHs for comparison SFMS galaxies that have a similar stellar mass at every snapshot. In addition, we show a plot illustrating the SFMS for $z = 0$ in Figure 2.2.

Identifying quenched galaxies

With the star forming main sequence as a function of time determined, we now aim to find a sample of quenched galaxies at $z = 0$. This sample will act as a sample of quenching galaxies at earlier times. We begin with all galaxies not part of the SFMS at $z = 0$ and consider their SFHs as compared to main-sequence galaxies in a similar mass range (± 0.1 dex, though this range can grow if necessary; see below). We impose an additional requirement that each potential quenching galaxy be compared to at least 50 main-sequence galaxies, in order to reduce the effect of statistical uncertainties. If a given galaxy does not have 50 comparison SFMS galaxies within ± 0.1 dex, the stellar mass bin is increased in increments of ± 0.005 dex, until 50 comparison main-sequence galaxies have been found. This requirement is typically only necessary for the most massive galaxies ($M_* > 10^{11}\ M_\odot$ at $z = 0$), and even then it only increases the size of the stellar mass bin modestly, usually much less than ± 0.05 dex.

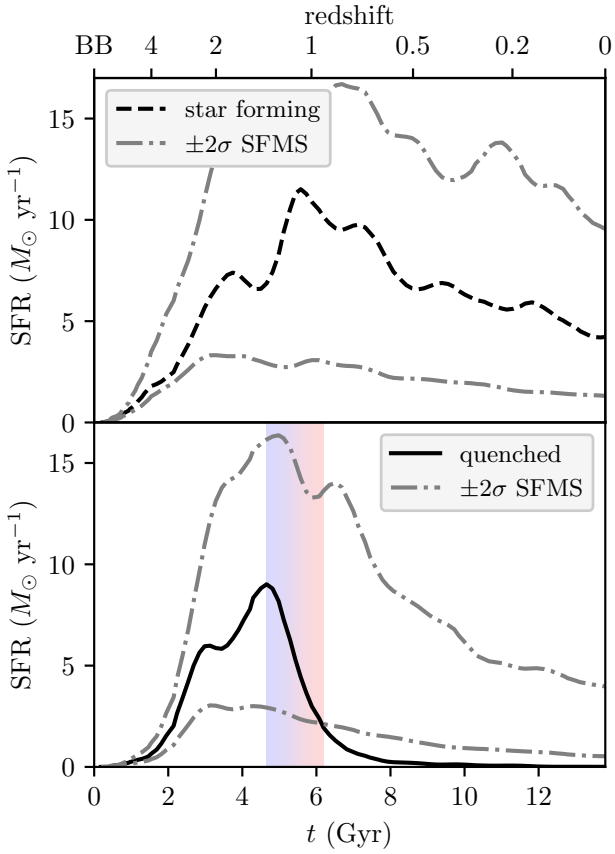


Figure 2.1: Top: An SFH for a normal star forming galaxy ($M_* = 10^{10.72}$ $M_\odot$ at $z = 0$; dashed black line), shown as a function of time (age of the Universe). Additionally shown are the $\pm 2\sigma$ limits from the median SFH of SFMS galaxies in a similar stellar mass range (± 0.1 dex) at every snapshot (dotted–dashed gray lines). Due to the slightly stochastic nature of SFHs over short timescales, we opt to smooth our SFHs with a Gaussian filter, where the smoothing kernel is one snapshot. Bottom: An SFH for a quenched galaxy ($M_* = 10^{10.21}$ $M_\odot$ at $z = 0$; solid black line), where the primary quenching event is highlighted using a vertical colored band. Also shown are the corresponding percentiles (gray dotted–dashed lines) for SFMS galaxies with a similar stellar mass (± 0.1 dex) at every snapshot. Once the SFH for the displayed quenched galaxy drops below the 2.5th percentile, it remains below this threshold, thereby defining this galaxy as quenched. The primary quenching episode for this galaxy lasts <2 Gyr, and by $z = 0$ the galaxy has been quenched for >7 Gyr. The subhalo ID for this quenched galaxy is 198186 at $z = 0$.

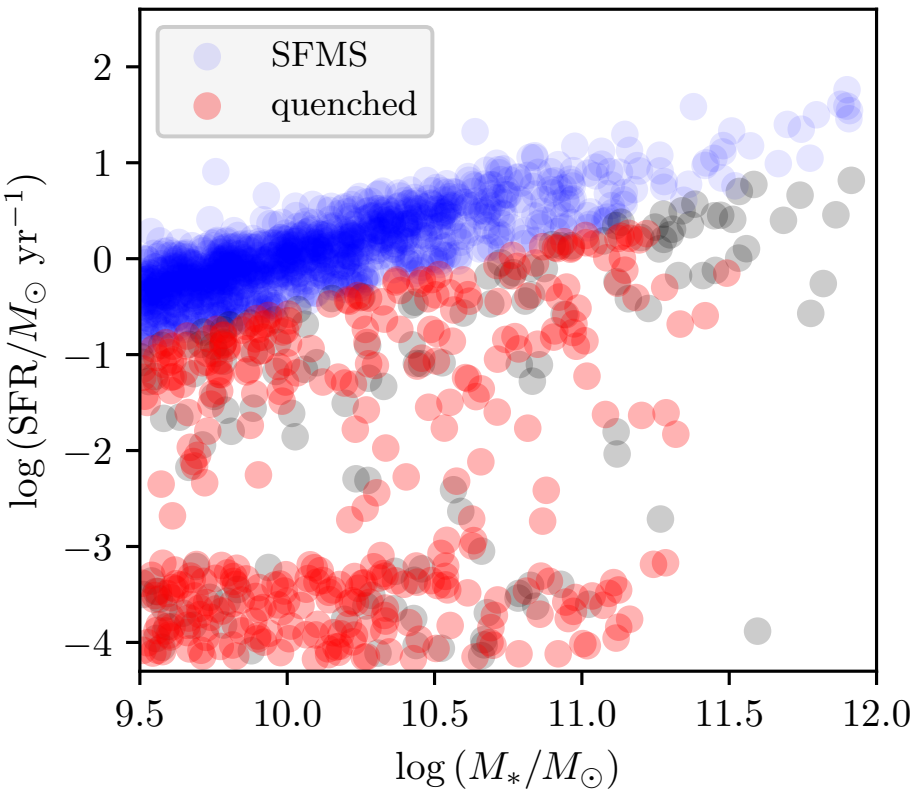


Figure 2.2: Star formation rate as a function of stellar mass for the fiducial sample (1666 galaxies with $M_* \geqslant 10^{9.5}$ $M_\odot$; see Section 2.2.2) at $z = 0$. Galaxies that populate the SFMS are shown in blue. Galaxies with low levels of star formation (SFR ≈ 0) have their SFR set to a small, random nonzero value between $\sim 10^{-3}$ $M_\odot$ yr^{-1} and $\sim 10^{-4}$ $M_\odot$ yr^{-1} for visualization purposes. Galaxies that satisfy our quenched definition (see Section 2.2.2) are shown in red and do not necessarily have SFR $= 0$, while galaxies that do not populate the SFMS (as defined in Section 2.2.2) and that are not quenched are shown in black. These galaxies reside below the SFMS.

For each galaxy, we compare its SFH to the SFHs of its comparison main-sequence galaxies (having a similar stellar mass at each snapshot). Due to the stochastic nature of SFHs in TNG over short timescales, we choose to smooth the selected SFH using a Gaussian filter (smoothing kernel, σ, equal to one snapshot, which is similar to a moving average) to facilitate simpler comparisons with the main-sequence comparison population. Our selected smoothing kernel ensures that broad-scale features remain intact while minimizing large stochastic fluctuations from snapshot to snapshot, especially those where there is a single brief increase (or decrease) in star formation, before returning to the prior level. This smoothing is qualitatively similar to using a slightly longer timescale to measure star formation, but still <200 Myr. Galaxies are considered quenched if

- the galaxy's SFH is above -2σ of the median SFH for the comparison SFMS galaxies for all times prior to falling 2σ below that median and
- the galaxy's SFH subsequently stays at least 2σ below that median SFH for all subsequent times.

This definition is illustrated in the bottom panel of Figure 2.1, where the SFH for the considered galaxy quenches after about six billion years and remains quenched thereafter. This conservative definition of a quenched galaxy ensures that we arrive at a sample that has a single quenching episode for each quenched galaxy, which facilitates a straightforward consideration of the evolution of their quenching attributes (see Section 2.2.4). This definition also minimizes "contamination" in the overall quenching signal from periods of increasing star formation. Therefore, galaxies that satisfy the first criterion above, but which rejuvenate (and subsequently do not satisfy the second criterion) are excluded from our sample.

Using this definition, out of the total 1666 galaxies with $M_* > 10^{9.5}\ M_\odot$ by $z = 0$, we find 361 quenched galaxies, 1160 star forming main-sequence galaxies, and 145 other galaxies below the SFMS (which do not fit our definition of "quenched"; see above). In Figure 2.2, we show the quenched galaxies with red, star forming main-sequence galaxies with blue, and the other galaxies below the star forming main sequence in black. Of the 145 galaxies below the SFMS at $z = 0$, 39 have no star formation, while the remaining 106 have nonzero SFRs, and the majority (109) of both of these populations are comprised of galaxies that experienced rejuvenation at some point. Given our definition above, quenched galaxies will not necessarily have SFR = 0, as evidenced by the red points in Figure 2.2 that have $10^{-3} \lesssim \mathrm{SFR}/M_\odot\ \mathrm{yr}^{-1} \lesssim 10^{-1}$. Henceforth, we refer to galaxies which have completed quenching as "quenched" (generally when discussing populations at $z = 0$),

while we use the term "quenching" to refer to systems that are actively undergoing the quenching process.

We show the derived galaxy stellar mass function for our quenched sample in Figure 2.3 (black points), alongside observed galaxy stellar mass functions (Baldry et al. 2004, 2012) for local red galaxies in the Sloan Digital Sky Survey (SDSS; York et al. 2000) and local red galaxies in the Galaxy And Mass Assembly survey (GAMA; Driver et al. 2011). We find that our quenched sample is a subset of all red or low-SFR galaxies, due to our specific and rather particular definition of what constitutes a quenched galaxy, where our definition is based on a galaxy's SFH in a manner that cannot be reproduced from observations. In Figure 2.3, we similarly show the stellar mass function for passive or quiescent galaxies selected based on a cut in sSFR, where these galaxies have $\log(\mathrm{sSFR}/\mathrm{yr}^{-1}) < -10.5$ (open circles). This broader definition for quiescence is a closer match to the field mass functions of red galaxies (e.g., Baldry et al. 2004), and it again highlights how our definition produces a subset of all quiescent galaxies. As above, galaxies that quench, rejuvenate, and quench again are excluded from our sample.

We additionally define the onset of the primary quenching episode to be the most recent significant peak of star formation (i.e. a local maximum) prior to the galaxy falling 2σ below its comparison SFMS galaxies. We define a significant peak as any peak that has an SFR of at least 40% of the maximum SFR throughout the entire SFH. In the bottom panel of Figure 2.1, the onset of quenching is then the absolute maximum of the SFR across the SFH, and is denoted with the start of the colored vertical band. We find that varying the significance threshold from 40% to 30% or even 50% changes the sample size by at most one galaxy, with slight variations in the extent of the quenching episode on a per-galaxy basis, but does not qualitatively affect our main conclusions. When considering the quenching episode duration across all quenched galaxies, changing the significance threshold by $\pm 10\%$ affects the median quenching duration by $\sim$200 Myr, which is comparable to the length of time between successive snapshots. In addition, for 313 of the quenched galaxies, the onset of quenching began after redshift $z = 1.5$, while only 44 galaxies began quenching during "cosmic noon" ($1.5 \lesssim z \lesssim 2.5$; Madau & Dickinson 2014; Förster Schreiber & Wuyts 2020). Given this, nearly 87% of the sample has begun quenching in the last $\sim$9.5 Gyr of cosmic time. For a small subset ($\sim$8%) of the quenched sample, we find that, after the peak in star formation, certain galaxies being quenching, reach a plateau in their level of star formation, and then begin quenching again, though a steady decline in star formation is overwhelmingly the more common trend. Beyond our chosen definition for the onset of quenching, other considerations include when a galaxy crosses a given sSFR threshold, when a galaxy falls off the main sequence, or when a galaxy is a certain distance away from the main sequence. In testing, we found that our median sSFR value at onset is

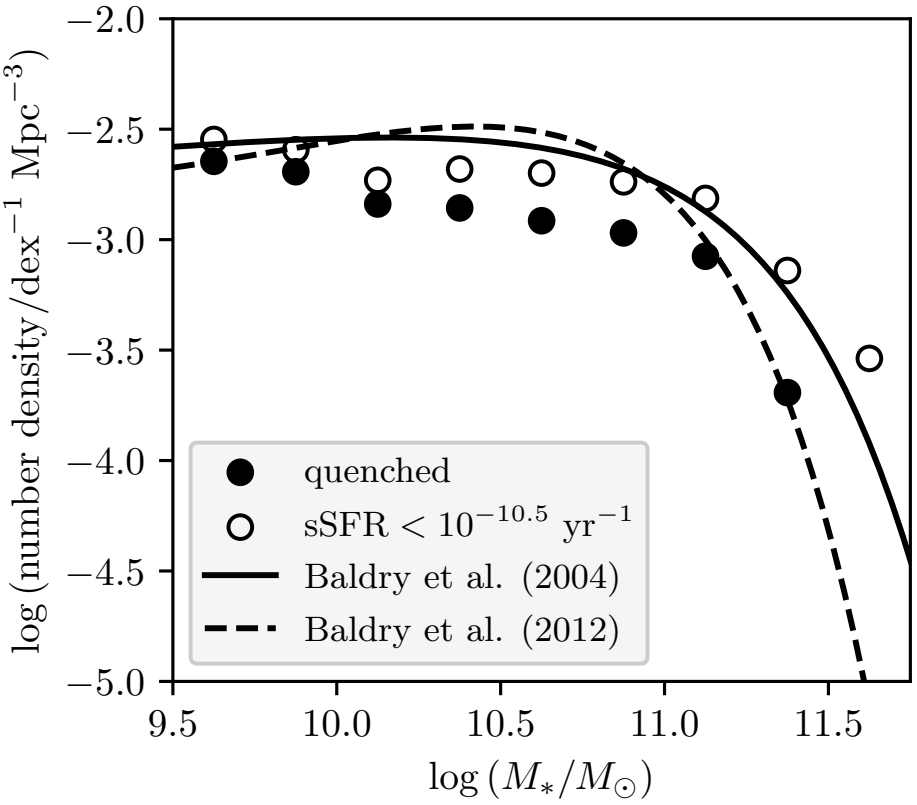


Figure 2.3: The galaxy stellar mass function of our 361 quenched galaxies (black dots; $z = 0$), shown alongside two fitted galaxy stellar mass functions for local ($0.004 < z < 0.08$) red galaxies (dashed line; Baldry et al. 2004, their Figure 10) in SDSS (York et al. 2000), and local ($z < 0.06$) red galaxies (solid line; Baldry et al. 2012, their Figure 15) in GAMA (Driver et al. 2011). Baldry et al. (2004) and Baldry et al. (2012) define red galaxies based on location in the u—r color–magnitude diagram. We additionally show a stellar mass function for TNG50 galaxies based on a cut in sSFR using $\log(\mathrm{sSFR}/\mathrm{yr}^{-1}) < -10.5$ (open circles).

$\sim 10^{-9.5}$ yr^{-1}, and so choosing a threshold value similar to this produces onset times that closely align with our preferred onset times on average ($\pm$200 Myr). As well, we determined that, if we elect to use the time when a galaxy falls off the main sequence, this corresponds to $\sim$130 Myr after our preferred onset times (on average), which is comparable to the time difference between snapshots. Increasing the required distance from the SFMS works to further shorten the length of the quenching episodes. We subsequently define the end of the primary quenching episode as the snapshot when the galaxy first falls 2σ below the median SFR of its comparison SFMS galaxies, which can be seen as the end of the colored vertical band in Figure 2.1. The duration of the quenching episode is given as $\Delta t_{\rm quench} = t_{\rm term} - t_{\rm onset}$.

In addition to the quenched sample, we also create a control sample of normal star forming galaxies. Control galaxies are chosen to have a similar stellar mass ($\Delta \log [M_*/M_\odot] \leqslant 0.1$ dex) to each quenched galaxy, but with the condition that they reside on the SFMS during the entirety of the quenched galaxy's quenching episode. In general, each quenched galaxy has many corresponding control star forming galaxies, and therefore the control sample of normal star forming galaxies is much larger than the quenched sample, where 1607 of the 1666 galaxies in the fiducial sample were considered part of the control sample at some point. We note that this sample is distinct from the comparison SFMS galaxies that were used to define quenched galaxies earlier, as those galaxies must only reside on the main sequence for a given single snapshot to facilitate comparison, while these control star forming galaxies must be on the main sequence throughout the quenched galaxy's entire quenching episode.

2.2.3 Morphological metrics

Before defining metrics that can be of use in observational surveys, we consider 2D histogram "postage stamp" cutouts (based on the distribution of stellar particles) and sSFR radial profiles of quenched galaxies to qualitatively understand morphological features of quenching. Our postage stamp cutouts are projected along the simulation box xy-coordinate axes, thereby acting as random angle projections. In Figure 2.4, we show a time series (Δt = 1.26 Gyr, total) for an example quenched galaxy, which is the same quenched galaxy as in the bottom panel of Figure 2.1. In the top panels of Figure 2.4, we see the young "star forming" stellar particles (with formation ages $\leqslant$100 Myr; see Section 2.2.2) shown in the colored histograms, while the stellar disk is shown with contours. Moving through the time series from left to right, we see that the size of the star forming disk evolves relative to the size of the stellar disk, which remains relatively constant, a feature also seen observationally in Zhang et al. (2021). In the bottom panels of Figure 2.4, we

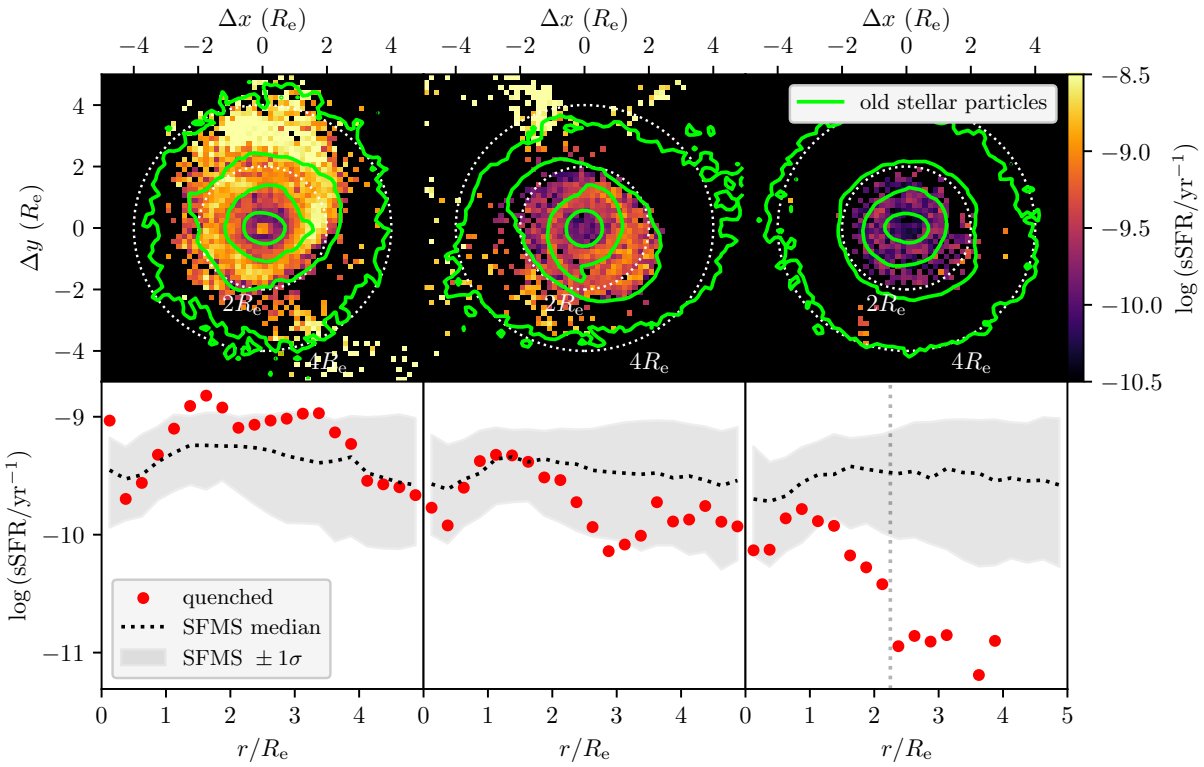


Figure 2.4: Top: projections of an $M_* = 10^{10.21}\ M_\odot$ (at $z = 0$) quenched galaxy (the same galaxy as shown in the bottom panel of Figure 2.1) at three points during its primary quenching episode. From left to right, the time series shows the snapshot at the onset of quenching, ∼38% through the quenching episode, and ∼75% through the quenching episode. The postage stamp cutout images show spatial sSFR values, while the green contours trace the stellar mass distribution, and the white dotted circles describe multiples of the effective radius R_e. The time from the leftmost panel to the middle panel is 615 Myr, while the rightmost panel is an additional 642 Myr after the middle panel. These projections highlight the evolution of the size of the star forming disk relative to the stellar disk, as the star forming disk shows significant outer truncation with increasing time, while the stellar disk remains largely unchanged, in fact shrinking by ∼10%. These panels also display the concentration of star formation. Bottom: sSFR radial profiles for snapshots that correspond to the top panels (red points; bin width of 0.25 R_e). The median sSFR profile for SFMS galaxies at a similar stellar mass is shown with a dotted black line, with the $\pm 1\sigma$ interval shown as a light gray band. The rightmost panel highlights $R_{\rm outer}$ (vertical dotted line), as there is a clear discontinuity in the sSFR profile for this quenched galaxy. In this case, $R_{\rm outer}/R_e \approx 2.3$.

show sSFR radial profiles for the same snapshots as the upper panels, where the example galaxy's profile is shown in red points (bin width of 0.25 R_e out to 5 R_e), while the median $\pm 1\sigma$ band for its comparison SFMS galaxies is shown in gray. We find that this profile also evolves through the quenching episode, and at late times (rightmost panel), this galaxy's sSFR radial profile has a sharp truncation near 2.3 R_e.

Given the features that we have identified from Figure 2.4 and from inspecting similar figures for the quenched sample (see Appendix A.1), we have defined four metrics that encode information about the distribution of star formation within the quenched galaxies during quenching.

The first metric, C_{SF}, describes the concentration of star formation:

$$C_{SF} = SFR_{<1\ kpc}/SFR_{total}, \tag{2.1}$$

where $SFR_{<1\ kpc}$ is the star formation rate in the inner (projected) kiloparsec of the galaxy, and SFR_{total} is the star formation rate over the entirety of the galaxy. The center of the galaxy is taken from the main progenitor branch files and is the stellar center. The second metric, R_{SF}, describes the size of the star forming disk relative to the stellar disk:

$$R_{SF} = \log\left(R_{e,\ SF}/R_e\right), \tag{2.2}$$

where the half-mass radius of the young, star forming particles is $R_{e,\ SF}$, while the half-mass radius (or effective radius) of the stellar disk is R_e. These radii are again taken relative to the stellar center. The third metric, R_{inner}, describes the inner truncation radius of the galaxy, where the sSFR radial profile of the galaxy has a sharp change in slope:

$$R_{inner} = \log[\mathrm{sSFR}(r)] \leqslant -10.5 \cap \mathrm{d}(\mathrm{sSFR})/\mathrm{d}r \geqslant 1, \tag{2.3}$$

where $\mathrm{sSFR}(r)$ is the sSFR radial profile, $\mathrm{d}(\mathrm{sSFR})/\mathrm{d}r$ is its first derivative, and R_{inner} is the outermost radius that satisfies both conditions. For robustness across our considered stellar mass range, we quote R_{inner} values in relation to R_e. We select a threshold sSFR value of $10^{-10.5}$ yr^{-1}, along with a slope of $+1$, as it was found that these values easily identify the inner truncation radius during testing. We confirm that small changes to the values of the threshold sSFR and slope do not significantly affect our results. R_{inner} is found by considering the sSFR radial profile and its first derivative, moving outward from 0 R_e to 5 R_e, which we use as the maximum extent for the profiles. For R_{inner}, if no radius is found that satisfies Equation (2.3), then 0 R_e is used as a lower limit. An illustrative example highlighting R_{inner} is shown in Appendix A.1. The fourth and final metric is similar to the inner truncation radius, but is the outer truncation radius, R_{outer}, defined as

$$R_{outer} = \log[\mathrm{sSFR}(r)] \leqslant -10.5 \cap \mathrm{d}(\mathrm{sSFR})/\mathrm{d}r \leqslant -1. \tag{2.4}$$

This is the innermost radius that satisfies both conditions. The outer truncation radius is similarly measured moving outward from 0 R_e along the sSFR and d(sSFR)/dr radial profiles. We likewise quote R_{outer} values in relation to R_e. The upper limit for R_{outer} is taken to be 5 R_e in the event that no radius is found to satisfy Equation (2.4). We similarly confirm that small changes to the threshold sSFR and slope do not significantly affect our results. We highlight R_{outer} in the final (rightmost) panel of Figure 2.4 for illustration. Finally, as our metrics are defined using two-dimensional projected distances, we confirm that including the full three-dimensional positional information does not significantly change our results. We see only modest changes for C_{SF} and R_{inner} (at $\lesssim$1 R_e), while the remaining metrics do not have increased precision, but instead show a negligible scatter around their two-dimensional values (see Appendix A.2).

2.2.4 Classifying galaxies according to morphological evolution during quenching

With the definitions of our metrics in place, we now determine their values as a function of time for all the quenched galaxies in our sample. We focus on the primary quenching episode, by considering the state of these metrics at the onset of quenching (t_{onset}) until the galaxy has dropped 2σ below the median for the comparison SFMS galaxies, which we describe as the termination of the primary quenching episode (t_{term}). To illustrate this, we show the evolution of the metrics in Figure 2.5 for the same galaxy as was shown in the bottom panel of Figure 2.1, as well as in Figure 2.4.

In Figure 2.5, by considering the left vertical axis, we see that R_{SF} (black dashed line) decreases through the quenching episode, while C_{SF} (solid black line) increases modestly. Additionally, by considering the right vertical axis, we find that R_{inner} stays fixed at low values close to 0 R_e with no evolution, while R_{outer} evolves strongly, sharply decreasing from $t = 5.8$ Gyr to $t = 6.2$ Gyr.

We create plots such as Figure 2.5 for every quenched galaxy in the sample, and together with plots such as Figure 2.4, manually categorize our quenched galaxies into three broad classes. The first contains those that show a morphological evolution that proceeds from the inside out, such that star formation is suppressed in the center of the galaxy and proceeds outward. For this class, C_{SF} will decrease through the quenching episode, R_{SF} increases, and R_{inner} will evolve to higher values of R_e while R_{outer} stays relatively fixed with no strong evolution. We show corresponding figures similar to Figures 2.4 and 2.5 for an example inside-out quenched galaxy in Appendix A.1. The second class is comprised of galaxies whose morphological evolution proceeds from the outside in, where star formation

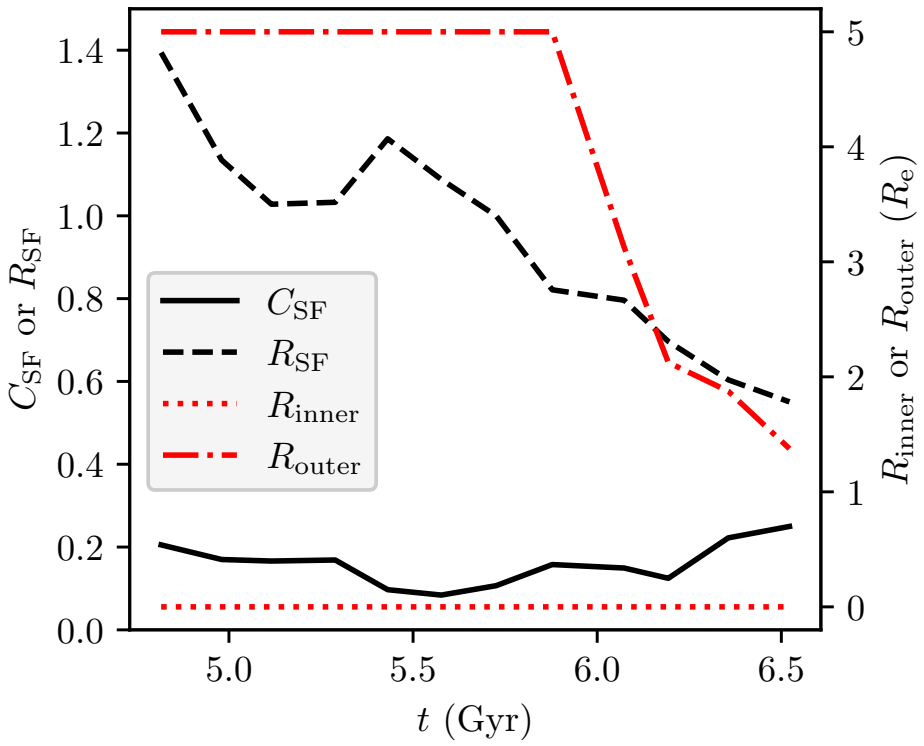


Figure 2.5: Evolution of the morphological metrics for the same galaxy as in the bottom panel of Figure 2.1 and in Figure 2.4, where the vertical axis on the left records the values for $C_{\rm SF}$ (solid black line) and $R_{\rm SF}$ (dashed black line), while the vertical axis on the right records the values for $R_{\rm inner}/R_{\rm e}$ (dotted red line) and $R_{\rm outer}/R_{\rm e}$ (dotted–dashed red line). The extent of the x-axis reflects the primary quenching episode for this galaxy, which lasts <2 Gyr, and is the same as the colored band seen in the bottom panel of Figure 2.1. This galaxy's morphological evolution is consistent with an outside-in signature, seen through the decrease of $R_{\rm SF}$ and $R_{\rm outer}$, along with $C_{\rm SF}$ modestly increasing. This galaxy shows no evolution for $R_{\rm inner}$, a feature commonly noticed for galaxies in the outside-in class in our sample. $R_{\rm e}$ shrinks by ∼10% for this galaxy through the quenching episode.

is suppressed in the outer regions of the galaxy and proceeds inward. The galaxy shown in the bottom panel of Figure 2.1 and in Figures 2.4 and 2.5 is in this second class. These galaxies generally have increasing $C_{\rm SF}$ through the quenching episode with decreasing $R_{\rm SF}$, with relatively constant $R_{\rm inner}$ along with strongly evolving $R_{\rm outer}$. The last class of quenched galaxies are those whose morphological evolution does not clearly match either of the first two classes, and is therefore ambiguous, with aspects that are similar to the inside-out class, but with other aspects that more closely resemble the outside-in class. These galaxies often have modestly increasing $C_{\rm SF}$ through the quenching episode, with relatively constant $R_{\rm SF}$, with evolution of both $R_{\rm inner}$ and $R_{\rm outer}$.

In this classification process, there are situations where the above evolutionary trends are not strictly met for some galaxies, especially when considering the inside-out and outside-in populations. An example is an outside-in quenched galaxy where the evolution of $R_{\rm SF}$ is modest and does not decrease strongly. For these situations, we consider the evolution of the other morphological metrics, in combination with insights gained through visual inspection of the projected postage stamps in order to classify such a galaxy. Regardless, for the majority of the quenched galaxies (>72%), we classify them into either the inside-out or outside-in populations without major difficulty. As well, we initially considered an additional class of quenched galaxy driven by starvation/uniform suppression, where the star formation is uniformly suppressed throughout the galaxy, but we find no conclusive evidence for this additional class based on our metrics. For a galaxy experiencing uniform suppression, we expect that $C_{\rm SF}$ would stay relatively constant through the quenching episode, if the assumption of an unchanging star formation radial profile gradient is valid. This should likewise correspond to a relatively constant $R_{\rm SF}$, and little evolution for $R_{\rm inner}$ and $R_{\rm outer}$. However, this type of uniform suppression would become noticeable once the star formation levels approach the detection limit, where evolution could then be seen.

Through this classification process, we find 78 galaxies have an inside-out morphological evolution signature, while 185 have an outside-in signature. The remaining 98 galaxies have a morphological evolution that is ambiguous.

2.3 Results

2.3.1 Differences between populations

We investigate differences between our quenched populations by considering their environments, and the relation between when a galaxy was accreted as a satellite and the onset

Table 2.1: Environment statistics for each quenched population at $z = 0$, where primary/central galaxies (listed first) are separated from satellite galaxies (listed second in parentheses).

	Inside-out	Outside-in	Ambiguous	Total
Cluster	0 (7)	0 (39)	0 (8)	0 (54)
High-mass group	0 (11)	0 (68)	0 (21)	0 (100)
Low-mass group	0 (10)	1 (36)	0 (20)	1 (66)
Galaxy-scale (field)	38 (12)	30 (11)	36 (13)	104 (36)

of quenching.

We obtain $z = 0$ primary/satellite flags for each galaxy, which indicate if a given galaxy is the primary galaxy in a given halo. These primary flags are set with the SUBFIND (Springel et al. 2001; Dolag et al. 2009) algorithm, and in most cases report the most massive galaxy in the halo. The environments at quenching onset and at $z = 0$ are then determined for every galaxy, based on the mass of the halo that they reside in. At $z = 0$, we define cluster-like environments to be those that have $M_{\rm h}/M_{\odot} \geqslant 10^{14}$, while high-mass groups have halos with $10^{13.5} < M_{\rm h}/M_{\odot} < 10^{14}$, low-mass groups have $10^{13} < M_{\rm h}/M_{\odot} < 10^{13.5}$, and finally galaxy-scale (i.e. field) halos have $M_{\rm h}/M_{\odot} < 10^{13}$.

From our fiducial sample of 1666 total galaxies (361 quenched) with $M_* \geqslant 10^{9.5}\ M_{\odot}$ by $z = 0$, 74 (54) reside in a cluster environment at $z = 0$, while 191 (100) are in high-mass groups and 162 (67) in low-mass groups. This leaves 1239 (140) residing in galaxy-scale halos at $z = 0$, of which 999 (104) are primaries while 240 (36) are satellites. We tabulate these results for the quenched population in the right column of Table 2.1.

To determine the time when a given galaxy was first accreted onto a larger halo, thereby becoming a satellite, we work backward (from $z = 0$) through the main progenitor branch of each quenched galaxy, recording the primary flag at each snapshot. We identify galaxies that have never been a satellite as primary galaxies. For all other cases, to account for minor stochasticity in the primary flags, driven by the "subhalo switching" problem (e.g., Rodriguez-Gomez et al. 2015), where in consecutive snapshots a subhalo is first determined to be a primary, then a satellite, then subsequently a primary again, we identify epochs where a given galaxy is considered a satellite for three consecutive snapshots (generally $\gtrsim$470 Myr). Using these identifications, we determine the length of time that a galaxy is considered a satellite, and compare this duration with the dynamical time at the beginning

of that interval. We adopt the dynamical time scaling relation (e.g., Tinker & Wetzel 2010; Wetzel et al. 2013)

$$t_{\rm dyn} = \frac{1}{H(z)} \approx t_0 \, (1+z)^{-3/2} \, , \tag{2.5}$$

where t_0 is set as 2 Gyr. We require the galaxy to have been a satellite for at least one dynamical time, and use the earliest such valid occurrence as the time when the galaxy was first accreted onto a more massive structure, making it a satellite. We subsequently refer to this as the satellite time.

We next compare the satellite time with the time when the galaxy first began its primary quenching episode. In Figure 2.6, we plot the quenching onset time as a function of satellite time for the inside-out population (left panel) and the outside-in population (right panel). In both panels, the points are scaled by their $z = 0$ stellar mass, and galaxies that have always been primaries are plotted in a separate region beyond the current age of the Universe (gray shaded region), though this is for visualization purposes only. Points are color-coded according to their host halo mass at the onset of quenching. Galaxies below the line of equality begin quenching before being accreted, and those above are first accreted and then begin to quench. From Figure 2.6, it is clear that there are a number of satellites (for both populations) that were accreted many gigayears ago. These satellite galaxies have not been disrupted or have merged into their halo's primary galaxy, as they remain distinct at $z = 0$. Though we might expect that these systems would eventually merge with their primary galaxy over several dynamical times, it has been shown that the merger timescale of satellites depends strongly on the satellite–host mass ratio (e.g., Boylan-Kolchin et al. 2008; Poulton et al. 2020), where for small mass ratios the merger timescale can be many times longer than the dynamical time.

For the inside-out population in the left panel of Figure 2.6, nearly half (38/78) of the population are primary galaxies at $z = 0$ (far right). Many of the inside-out galaxies began quenching in galaxy-scale halos and show no correlation between their respective times (galaxies below the line of equality). However, for a subpopulation (27) that resided in more massive halos ($M_{\rm h} \gtrsim 10^{12.3} \, M_\odot$) when they began quenching, there is some correlation between their satellite time and quenching onset time. For this subpopulation, after being accreted onto a more massive structure, there is an average delay of $\sim$1 Gyr before quenching begins, indicating that the environment may play a role in promoting quenching for these galaxies.

For the outside-in population (right panel), the large majority (154/185) of the population are satellite galaxies, with a subpopulation (31) of primary galaxies (far right). We see that most outside-in quenched galaxies resided in higher-mass halos at quenching

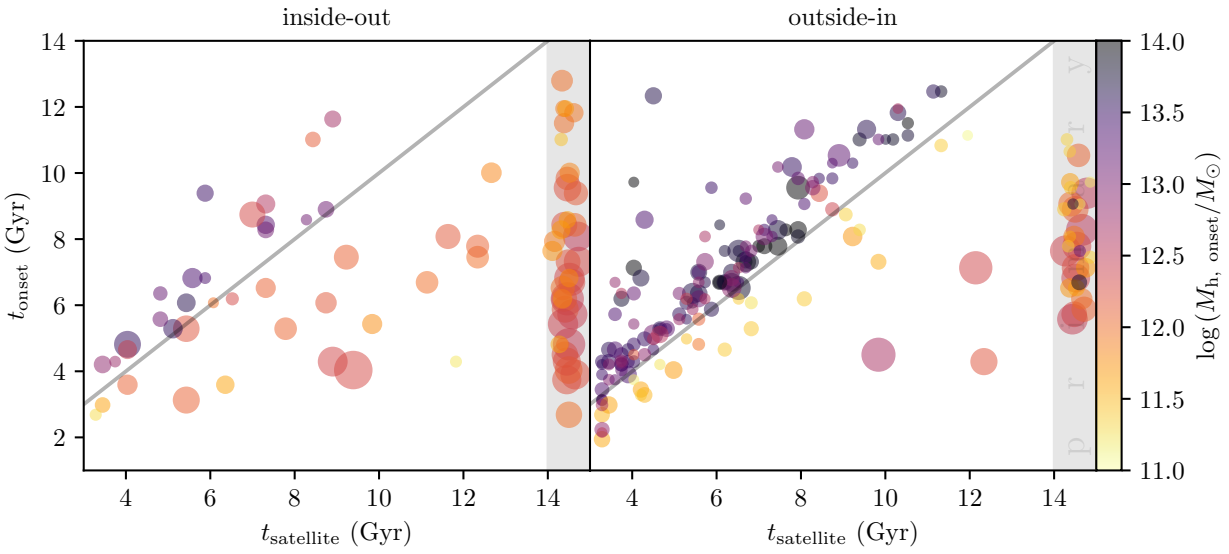


Figure 2.6: The time corresponding to the onset of quenching for our quenched sample, plotted as a function of the time when the galaxy was accreted as a satellite onto a more massive structure, for two of our quenched populations. We plot a line of equality in gray. For galaxies that have always been primary galaxies, by definition the satellite time is set as the current age of the Universe, and we plot these in a separate region with minor perturbations beyond the current age of the Universe for visual clarity (shaded gray region). We separate the inside-out population (left) from the outside-in population (right). We scale our data points by $z = 0$ stellar mass, where more massive galaxies are larger, and we additionally color-code data points by their host halo mass at the onset of quenching. Halo masses have a range from galaxy-scale halos (lighter colors) to cluster/cluster-like mass halos (darker colors). Galaxies below the line of equality have a primary quenching episode that begins before they are accreted as a satellite, while those that sit above equality experience a delay before quenching begins. Galaxies lying along or close to the line of equality have a strong correlation between when they were first accreted and when their primary quenching episode began (e.g., the outside-in population).

onset, with group- and cluster-mass halos being common. Many of the outside-in galaxies in these massive halos show a correlation between their respective times, indicating that the local environment is influencing their evolution through quenching, as expected. For a subpopulation (139) that resided in more massive halos ($M_{\rm h} \gtrsim 10^{12.3}\ M_{\odot}$) at quenching onset, there is an average delay of $\sim$1 Gyr after becoming a satellite before quenching began (galaxies above the line of equality). In general, most galaxies that quench as satellites do so in a manner consistent with an outside-in morphological evolutionary signature, while most primary/central galaxies quench inside-out. As well, outside-in quenched galaxies are more likely to have a delay before quenching after being accreted, while inside-out quenched galaxies are more likely to have begun quenching prior to becoming a satellite, though this is for inside-out quenched galaxies that resided in galaxy-scale halos at quenching onset. For the inside-out population with $M_{\rm h} \gtrsim 10^{12.3}\ M_{\odot}$, there is a similar delay as for the outside-in population.

As an alternative to considering the different quenched populations per environment, we can instead consider the environments and the populations that reside in them. We summarize the above noted points for $z = 0$ in Table 2.1, where we list the number of primary and satellite galaxies for each quenched population as a function of environment. It is clear that most quenched field galaxies quenched inside-out, whereas satellite galaxies in groups and clusters have a mixture of inside-out and outside-in signatures, though most of the inside-out quenched galaxies began quenching in galaxy-scale halos (see above). Additionally, nearly all $z = 0$ quenched galaxies in groups and clusters are satellites, with only a single central/primary quenched galaxy residing in a low-mass group.

We can additionally consider the duration of the quenching episode for each population. In Figure 2.7, we show the duration of the quenching episode as a function of stellar mass, grouped by quenched population, with the inside-out population shown in magenta and the outside-in population in red. We use fixed stellar mass bins of 0.2 dex width from $10^{9.5}\ M_{\odot}$ to $10^{11.5}\ M_{\odot}$ and subsequently require that each stellar mass bin contains a minimum of seven galaxies for reliable statistics. We find that massive ($M_{*} \gtrsim 10^{10.5}\ M_{\odot}$) quenched galaxies overwhelmingly quench inside-out, while for low-mass galaxies ($M_{*} \lesssim 10^{10.3}\ M_{\odot}$) quenching mostly proceeds outside-in. Within each stellar mass bin, we then compute median quenching episode durations (solid lines) along with $\pm 1\sigma$ values (shaded regions), measured in Gyr. We see that the inside-out population has, in general, longer durations for quenching compared to the outside-in population, but with additional scatter at all masses. In particular, at high masses, quenching durations can last for $\sim$3.5 Gyr for the inside-out population, though the average duration is $\sim$2.5 Gyr. The outside-in population shows less scatter and has a characteristic quenching duration of $\sim$1.5 Gyr, which has a weak mass dependence.

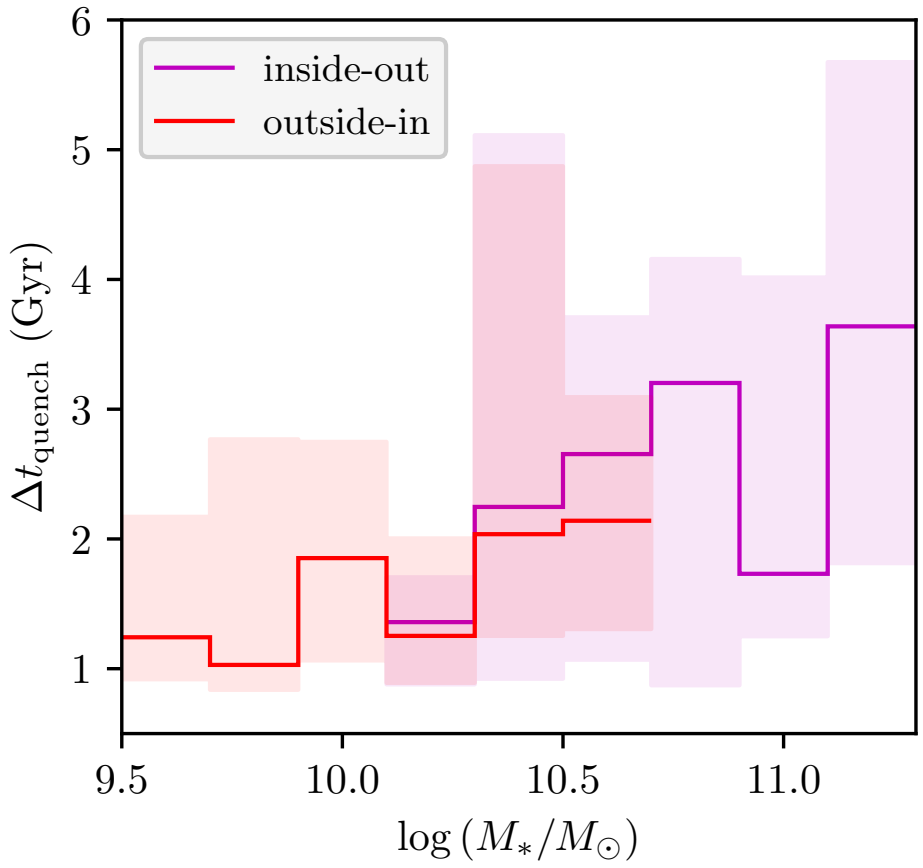


Figure 2.7: The quenching episode duration (see Section 2.2.2) as a function of stellar mass, divided into the inside-out population (magenta) and outside-in population (red). The inside-out population has higher mass overall, compared to the outside-in population, but shows additional scatter in terms of the quenching duration compared to the outside-in population.

In summary, though the scatter is larger than the trend seen in Figure 2.7, with the morphological metrics alone we can estimate the mean quenching duration on a per-population basis, after classifying galaxies into different morphological evolutionary signatures.

2.3.2 Metric evolution per population

With our quenched sample appropriately classified into various morphological quenching signatures (Section 2.2.4), we investigate the evolution of the morphological metrics per population. We bin the metrics by evolutionary signature, and consider characteristic epochs through the quenching episode. In Figure 2.8, we show the distributions of each of the morphological metrics as a separate column, while four characteristic epochs through the quenching episode are displayed as rows. By moving from top to bottom along a column, we see the evolution of a given metric for the populations shown. Given the number of snapshots available for each quenched galaxy along its quenching episode, in combination with the corresponding snapshots for the control star forming galaxies, in total we have 69,493 unique "galaxies" from which we consider the evolution of the different populations. In Appendix A.3, we show similar histograms for the ambiguously quenched population.

As mentioned at the end of Section 2.2.2, we additionally define a sample of control star forming galaxies with which to compare the inside-out and outside-in quenched galaxies. These galaxies remain on the star forming main sequence throughout the entirety of a particular quenched galaxy's quenching episode. Given that these galaxies have no quenching episode themselves, we adopt the corresponding timestamps through the quenching episode for the companion quenched galaxy, in order to facilitate comparisons with the "quenching episode" of the star forming galaxy. Beginning with the control star forming population (shown in gray), we find no evolution of $C_{\rm SF}$ and $R_{\rm SF}$, with $R_{\rm SF}$ peaking around $\sim$0.25, showing that star formation is generally distributed at larger radii beyond the very central regions. Likewise, we see negligible evolution for the star forming population for $R_{\rm inner}$ as well as $R_{\rm outer}$, with both showing no significant cutoff for most galaxies.

Moving next to the inside-out population (shown in magenta), we find this population evolves to low values of $C_{\rm SF}$, starting from a slightly flatter distribution. We expect this flatter distribution at early times is due to a burst of star formation in the core that is preceding quenching, and this is consistent with how we have defined the onset of quenching, which is based on significant peaks of star formation through the SFH. At late times, there is some similarity between the star forming population and the inside-out population for low values of $C_{\rm SF}$, though the inside-out population notably cuts off near $\sim$0.65. For

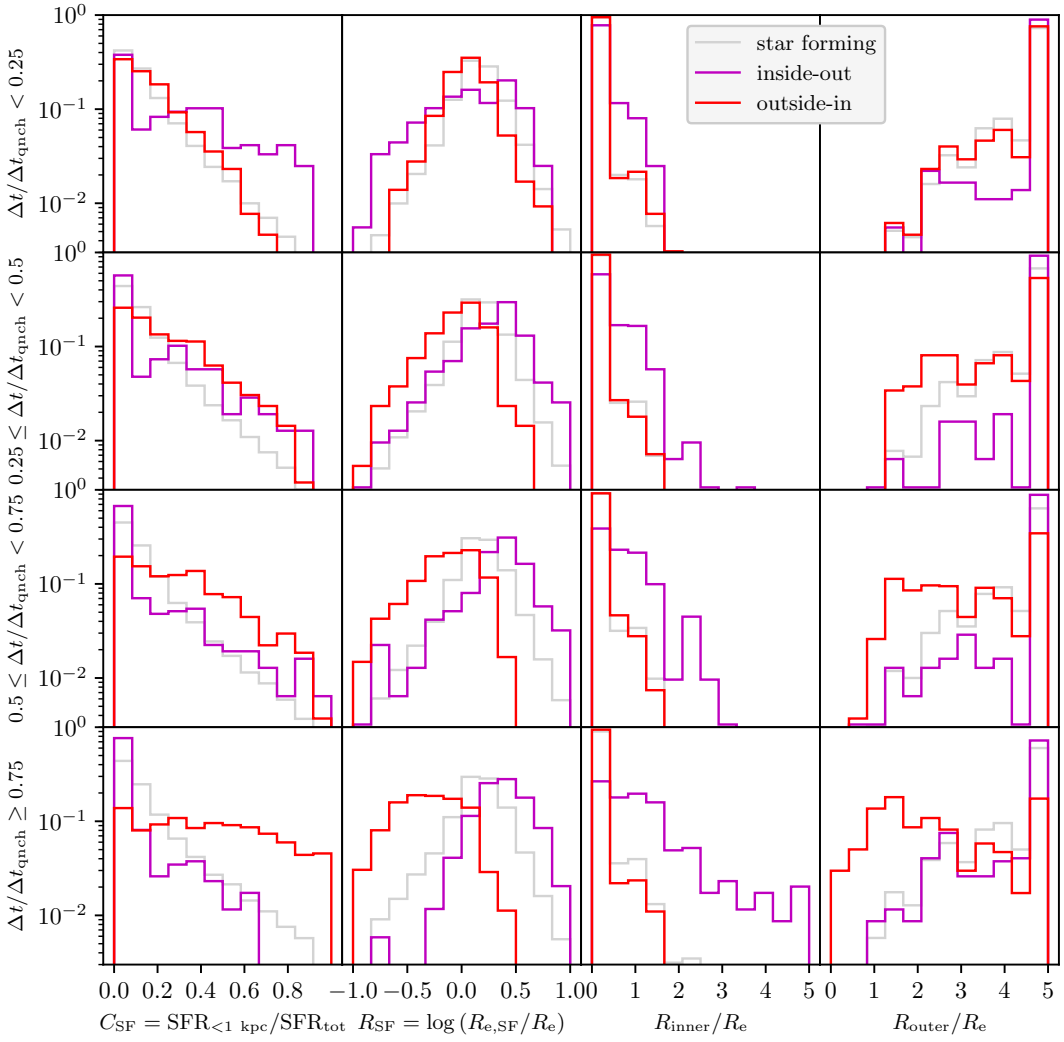


Figure 2.8: Evolution of the morphological metrics for the entire control star forming sample (gray) as well as the inside-out (magenta) and outside-in (red) quenched populations. Each metric is displayed as a separate column, while each row shows a different epoch through the quenching episode, shown on the y-axis. Moving from left to right, the columns show $C_{\rm SF}$, $R_{\rm SF}$, $R_{\rm inner}$, and $R_{\rm outer}$, respectively. The top row corresponds to $\Delta t = t - t_{\rm onset} < 0.25\Delta t_{\rm quench}$, where t is the time through the quenching episode. The remaining rows similarly contain quartiles of the quenching episode, and moving from top to bottom, the evolution of a given metric is visible. We normalize the distributions so that the y-axis in each panel can simply be read as the frequency of that value occurring in the sample.

$R_{\rm SF}$, the inside-out population evolves to higher values of $R_{\rm SF}$, which is expected given the suppression of star formation within the central regions, pushing the subsequent location of the effective radius of the star forming particles to larger radii. This population shows strong evolution of $R_{\rm inner}$, being most similar to the star forming population early in the quenching episode, but evolving to have a flatter distribution late in the quenching episode. This is expected as $R_{\rm inner}$ is sensitive to large suppressions of star formation in the inner regions of our quenched galaxies. Finally, when investigating $R_{\rm outer}$, we find little evolution to lower values for the inside-out population, and they remain largely similar to the star forming population. However, there is a non-negligible subpopulation that has $R_{\rm outer} < 5$ at all times, indicating that even these quenched galaxies, which have been classified as having an inside-out morphological evolutionary signature, may in fact also experience low levels of outside-in evolution, where this outside-in evolution is weak compared to the strong inside-out evolution.

Finally, for the outside-in population (shown in red), we find an evolution of $C_{\rm SF}$ in the opposite direction to the inside-out population, evolving to high values of $C_{\rm SF}$, which is consistent with expectations for this quenching signature, where all the remaining star formation is collected within the central regions. In contrast to the inside-out population, at early times, the outside-in population has a distribution similar to that of the star forming population, indicating that the star formation is more evenly distributed throughout these galaxies prior to quenching. This population also evolves to low values of $R_{\rm SF}$, and as with $C_{\rm SF}$, the two quenched populations have $R_{\rm SF}$ values that evolve in different manners. These low $R_{\rm SF}$ values reflect how the star formation becomes concentrated in the inner regions, in fact becoming more concentrated than the older stellar populations that trace the distribution of stellar mass, leading to $R_{\rm SF}$ values that peak at negative values, given the logarithmic definition of $R_{\rm SF}$. For $R_{\rm inner}$, we see negligible evolution to higher values, with the distributions remaining similar to those of the star forming population at all times. Finally, for $R_{\rm outer}$, the outside-in quenched galaxies display strong evolution, with a significant number having $R_{\rm outer} \approx R_{\rm e}$ by late times, indicating that the star forming disk has shrunk relative to the stellar disk. As before, we expect such behavior, as $R_{\rm outer}$ is sensitive to suppression of star formation in the outer regions of a galaxy, exactly like our outside-in signature galaxies.

Given that $R_{\rm inner}$ and $R_{\rm outer}$ as described above are quoted in relation to $R_{\rm e}$ (in addition to $R_{\rm SF}$), it is important to understand the evolution of $R_{\rm e}$ across the quenched sample. By considering the quenching episodes, we find that $R_{\rm e}$ modestly evolves to lower values on average, with an average reduction of $\sim$10% from the onset of quenching until the termination of quenching, i.e. $R_{\rm e,\ term} \approx 0.9 R_{\rm e,\ onset}$, across the entire quenched sample. When considering the inside-out quenched population alone, we find negligible evolution

(<1%) of R_e on average, while for the outside-in quenched population, we find $R_{e,\,term} \approx 0.84 R_{e,\,onset}$, indicating that the stellar disk is shrinking more strongly for this population than the inside-out population. These findings suggest that, though the stellar disk is shrinking through the quenching episode for most galaxies, this evolution is mild, and so using the effective radii as a comparison point for the morphological metrics is sensible.

To demonstrate the robust distinguishing power of these metrics when used in combination, in Figure 2.9 we show R_{SF} as a function of C_{SF} for our inside-out and outside-in quenched galaxies, along with our control sample of normal star forming galaxies. The characteristic epochs through the quenching episode used here are the same as in Figure 2.8, as is the color scheme. We see that, while the star forming galaxies (gray filled contours) remain relatively fixed from panel to panel, the quenched populations evolve very differently as discussed above. In this space, the inside-out population (magenta contours) begins by largely overlapping with the star forming galaxies, but evolves to the upper left, to low concentrations and high disk ratios. Conversely, the outside-in population (red contours) evolves to the lower right, to high concentrations and low disk ratios. By late times, the populations reside in distinct regions of this parameter space, but with non-negligible overlap with the star forming galaxies. The evolution of these two metrics is not unexpected (see Section 2.2.4 for discussion on an individual galaxy basis), but the amount of ensemble movement throughout the quenching episode is striking.

2.3.3 Recovering quenched populations and progress

We next determine the ability of machine learning–based algorithms to accurately classify the different populations (star forming, inside-out signature, and outside-in signature) as a function of progress through the quenching episode based on the morphological metrics. We additionally investigate the feasibility of recovering the quenching progress when using machine learning.

We use a k-nearest neighbors algorithm (kNN; e.g., Fix & Hodges 1951, 1989; Cover & Hart 1967) available in the package `scikit-learn` (Pedregosa et al. 2011). This algorithm works by finding the k-nearest neighbors to a given point and uses these neighbors as training samples to predict the correct label for the point (Pedregosa et al. 2011). We use the complete set of morphological metrics and the true population labels (i.e. star forming, inside-out, and outside-in) as the training set samples, and use a 70%/30% training/testing split, where the training/testing split is completed such that snapshots from a given galaxy only reside in either the training set or the testing set, but not both, to eliminate bias. Input information related to the progress through the quenching episode is not included,

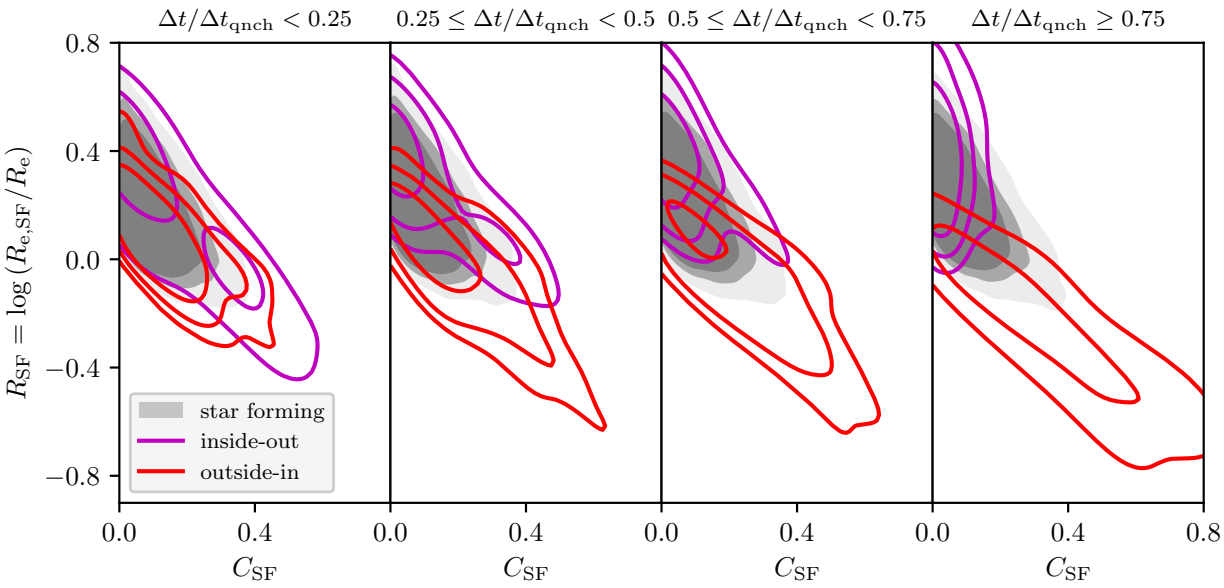


Figure 2.9: The size of the star forming disk relative to the size of the stellar disk, $R_{\rm SF}$, as a function of the concentration of star formation in the central kiloparsec relative to the entire stellar disk, $C_{\rm SF}$. Control star forming galaxies are shown with filled gray contours, where darker colors indicate higher densities. Inside-out quenched galaxies are shown with magenta contours, while outside-in quenched galaxies are shown with red contours. The four panels correspond to quenching episode epoch quartiles, and are the same as in Figure 2.8.

but the progress-binning description below explains how the data are split. We use the three nearest neighbors, and weight the neighbors based on the inverse of their distance. This ensures that closer neighbors of a given point will have a larger influence compared to distant neighbors. Given the distance-based nature of the kNN classifier, we additionally standardize/feature scale the morphological metrics prior to performing any classification, to ensure that metrics with a larger dynamic range (e.g., $R_{\rm inner}$ or $R_{\rm outer}$) do not dominate the distance calculation.

In Figure 2.10, we show the results of applying this machine learning algorithm to our sample, when binned by progress through the quenching episode. For each progress bin, the k-nearest neighbors algorithm provides a predicted class based on the morphological metrics, from which we determine the accuracy of the classification by considering the anticipated population and the true population. For each progress bin, we complete 1000 iterations, where in each iteration a randomly selected number of star forming galaxies is used that closely numbers the total number of inside-out and outside-in quenched galaxies, thereby producing a balanced sample. As well, we take the median (solid lines) and $\pm1\sigma$ range across all iterations (shaded regions). In Figure 2.10, the accuracy of the control star forming population is shown in black, while the inside-out quenched population is shown in magenta, and the outside-in population in red. As above, we are able to discuss the evolution through the "quenching episode" for the star forming population, though this is done by using the corresponding time points for the quenched galaxies' quenching episodes. For the star forming population, we find reasonable levels of accuracy ($\sim$60%) at early times, with an increase in accuracy values to $\sim$70% by intermediate times. At late times, the accuracy further increases, with values exceeding 80% for the star forming population. For the inside-out population, at early times ($\Delta t/\Delta t_{\rm quench} < 0.25$) in the quenching episode, we find lower accuracy values ($\sim$0.5). Moving through the quenching episode, we find increasing accuracy values, until at late times ($\Delta t/\Delta t_{\rm quench} > 0.75$), accuracy values exceed 65%, though they do not approach the levels of the outside-in population or the star forming population, suggesting that inside-out quenched galaxies are slightly more difficult to classify at late times. This is not completely unexpected, given the evolution of the morphological metrics for the inside-out population as described above in Figure 2.8. However, we note that the overall rate of increase in accuracy (i.e. slope) for the inside-out population is similar to that of the star forming population. For the outside-in population, we likewise see a clear increase in accuracy with increasing time through the quenching episode, where at early times low accuracy values are apparent ($\sim$0.45), while at late times ($\Delta t/\Delta t_{\rm quench} > 0.75$), the accuracy of the kNN classification for the outside-in population can exceed 75%. This methodology suggests that applying machine learning algorithms to such morphological metrics enables an accurate population

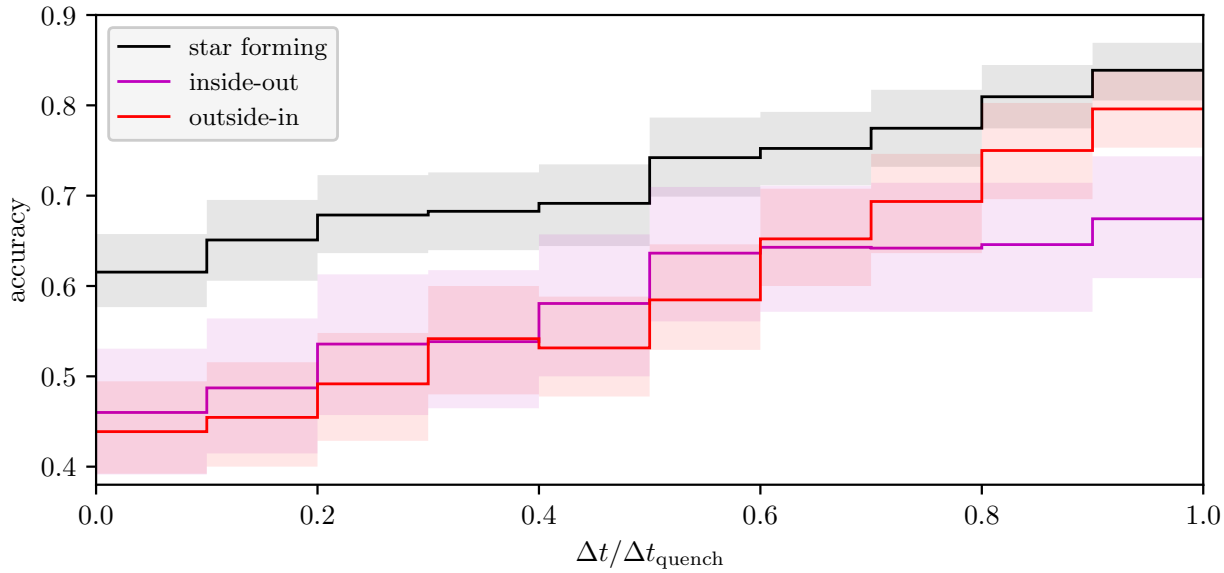


Figure 2.10: The accuracy of the nearest neighbor–based classification as a function of time (progress) through the quenching episode. The accuracy for the control star forming sample is shown in black, while the inside-out and outside-in quenched populations are shown in magenta and red, respectively. For each population, median values are shown as a thick line, while shaded contours denote the $\pm 1\sigma$ range based on 1000 iterations. In these iterations, a randomly selected sample of control star forming galaxies is used, which closely numbers the same amount as the inside-out and outside-in populations.

prediction, especially in the later stages of quenching. In these later stages, as shown above, the morphological differences between populations is most pronounced.

Through testing this classification process, we determined that, by increasing the number of neighbors used, the accuracy of the prediction for the star forming population can be greatly improved. Increasing from three to five or even the 10 nearest neighbors can increase the accuracy beyond 80% for the majority of the quenching episode, and even beyond 90% in some cases when considering many neighbors (e.g., $N_{\rm neighbors} > 25$). However, this increase in the accuracy of the prediction for the star forming population generally produces decreases in the accuracy of the predictions for both quenched populations. At worst, the accuracy values for either population might not exceed 40%, while the accuracy for the star formers is greater than 90%. Because of these considerations, we have opted to use three nearest neighbors for the main classification, as three neighbors is possibly optimal for producing the highest accuracy scores for the quenched populations while still providing high values for the star forming galaxies.

We next explore the ability of machine learning to correctly predict the stage at which a quenching galaxy is (i.e. the progress through the quenching episode) using the same kNN classifier as above. We consider first the inside-out quenched population alone, then subsequently investigate the outside-in population. As before, we use the three nearest neighbors, weighted by the inverse of the distance to the neighbors, along with the full set of standardized morphological metrics and an unbiased training/testing split of 70%/30%. For the training labels, we use the true progress through the quenching episode, but binned into three distinct epochs. These epochs correspond to early ($\Delta t/\Delta t_{\rm quench} \leqslant 0.25$), intermediate ($0.25 < \Delta t/\Delta t_{\rm quench} < 0.75$), and late ($\Delta t/\Delta t_{\rm quench} \geqslant 0.75$). Using the classifier, we predict the progress epoch and repeat 1000 iterations from which we can take median values. We then follow the same procedure for the outside-in quenched population.

In Figure 2.11, we show histograms for the quenching progress of the inside-out quenched galaxies (left panels) and the outside-in quenched galaxies (right panels), binned by epoch through the quenching episode. The distributions have been normalized so that the y-axis can be read as frequency. In the top panels, we show the true distributions for these galaxies, binned (and color-coded) as described above. In the bottom panels, we show the distributions for the predicted epochs after taking the median across the 1000 iterations. Beginning with the inside-out population and the true distributions, we see noticeable peaks at $\Delta t/\Delta t_{\rm quench} = 0$ and $\Delta t/\Delta t_{\rm quench} = 1$ which is a consequence of how we have defined the quenching episode for each quenching galaxy. By construction, every quenching galaxy will have both an onset of quenching as well as a termination of quenching (see near the end of Section 2.2.2). In the bottom panel, we find a larger tail to high quenching episode progress values for the predicted early-episode galaxies, but with a large peak

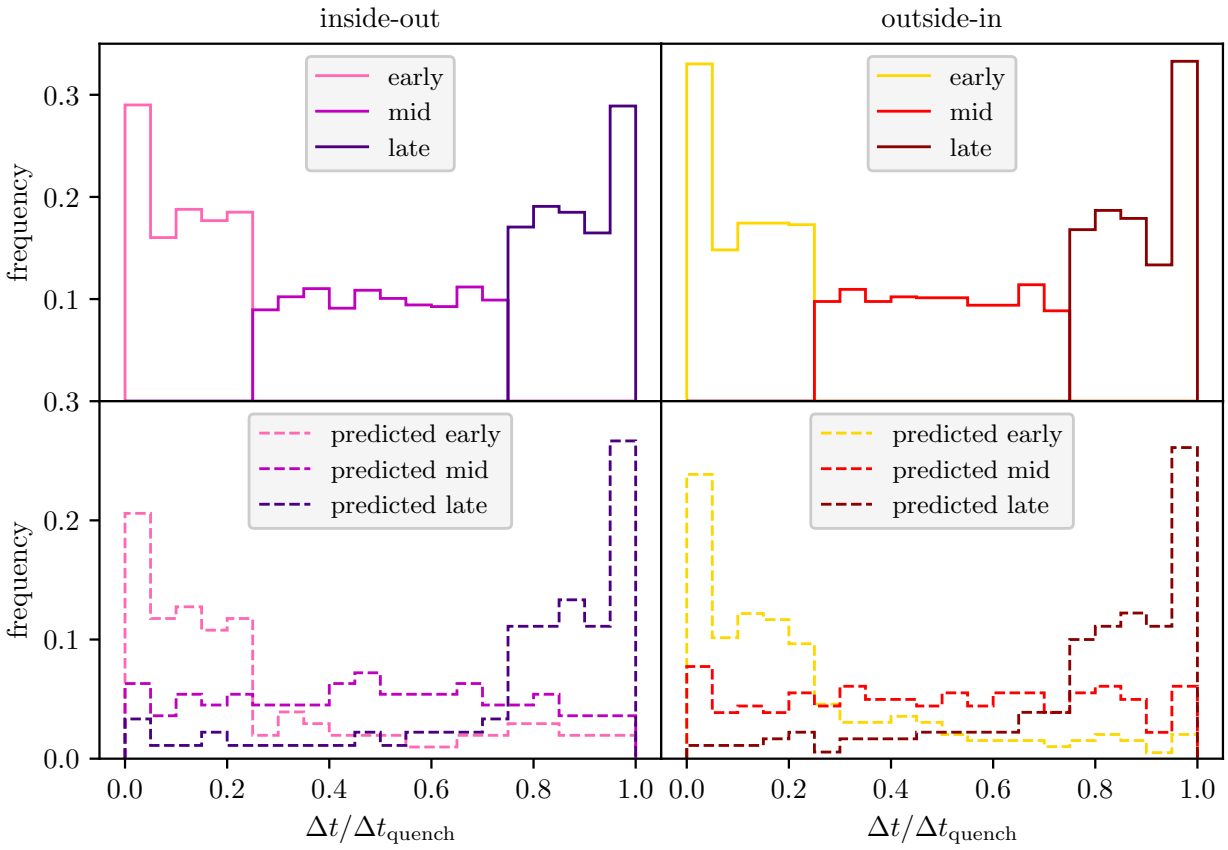


Figure 2.11: Quenching episode progress for inside-out (left) and outside-in (right) quenched galaxies binned by epoch through the quenching episode, with early-episode galaxies shown in lighter colors, while mid- and late-episode galaxies are shown in progressively darker colors. Top: the true distributions for these galaxies, where we normalize the distributions so that the y-axis can simply be read as the frequency of a given value occurring in the sample. The boundary lines that separate the three epochs are easily seen at $\Delta t/\Delta t_{\rm quench} = 0.25$ and 0.75. Bottom: the kNN–based predictions for the episode progress epochs, after running 1000 iterations and taking the median across all iterations. Colors are as in the top panel, and distributions are similarly normalized.

at early values. Similarly, the predicted late-episode galaxies have a quenching episode progress distribution that shows a clear tail to low progress values, mirroring the situation for the predicted early-episode galaxies, with a strong peak at late values. The distribution for the predicted mid-episode galaxies is relatively uniform and lies between the two extreme populations, with tails into both the early and late epochs. This suggests that inside-out galaxies that are at intermediate stages of quenching are more difficult to correctly predict when considering the quenching progress, but that true early-episode galaxies are most commonly classified as early, and similarly true late-episode galaxies are most often classified correctly. Such intermediate-episode galaxies can simultaneously appear as mature early-episode galaxies or as immature late-episode galaxies, producing poor predicted accuracy.

We next consider the outside-in quenched population and largely find a similar situation as for the inside-out population. The k-nearest neighbor classifier correctly predicts the true quenching episode epoch most often for early- and late-episode galaxies, as they seem to be distinct morphologically, but intermediate-episode galaxies are more difficult to distinguish. Nonetheless, these findings suggest that machine learning–based algorithms can properly distinguish the progress through the quenching episode for two distinct populations of quenching galaxies, those with an inside-out evolutionary signature, and those with an outside-in evolutionary signature.

2.4 Discussion

Given the results presented in the current work, simple observationally motivated morphological metrics that are based on the spatial distribution of star formation are capable of being used to identify and distinguish different populations of quenched galaxies within the TNG50 simulation. These quenched populations have different morphological evolutionary signatures, where the two main signatures are consistent with an inside-out evolution and an outside-in evolution. These populations have measurable quenching episodes with differing characteristic durations: that for the inside-out group is $\sim$2.5 Gyr on average, but up to $\sim$3.5 Gyr for massive galaxies. Meanwhile, the timescale for the outside-in population is shorter and less variable, typically $\sim$1.5 Gyr. They also exhibit differing characteristic stellar masses, where the outside-in population is generally lower mass than the inside-out population. We have found that these populations are also found (generally) in different environments, where the inside-out population is more likely to be found in the field while the outside-in population is most often found in denser environments (galaxy groups and clusters). An additional difference is that inside-out quenched galaxies are more likely to

be the most massive galaxies within their respective dark matter halos, while outside-in galaxies are commonly satellites and begin quenching ∼1 Gyr after being accreted onto a more massive structure.

Taken together, these results suggest that the nature of galaxy quenching in these simulations is somewhat binary. The most massive galaxies, which reside in the field (and are themselves primary galaxies), experience inside-out quenching, possibly due to the presence of an active galactic nucleus (AGN). This quenching is somewhat extended over relatively long times (compared to their outside-in counterparts) based on the duration of quenching. Conversely, less massive galaxies, which are generally satellites of more massive structures, are first accreted onto those structures and experience a delay before beginning to quench outside-in. This quenching proceeds quickly, taking a few gigayears or less. As well, this outside-in quenching is possibly driven by the dense environment in which these galaxies live, and it could be a consequence of ram pressure stripping.

When considering how these different populations evolve, especially morphologically, the possibility of distinguishing them from each other and from normal star forming galaxies seems feasible. Indeed, by considering the evolution of the observationally motivated morphological metrics, one can make predictions based on those metrics, finding high accuracy for the predicted population at late times when the populations are most distinct. Further, if one considers a given quenched population alone, predictions for the stage of quenching can be made and are largely capable of distinguishing early-stage quenching galaxies from late-stage quenching galaxies.

These results have implications for the field of galaxy evolution, where large samples of quenching galaxies can be determined based on morphology alone, and those samples can further be divided into different quenching evolutionary signatures. As we discuss below, some considerations must be taken before blindly applying these metrics to real galaxies, as the current work has focused on simulated galaxies.

2.4.1 Comparison with literature results

In the context of studies in the literature, we are not presently aware of any work that has completed a directly similar analysis. However, many authors have investigated quenching timescales as a function of galaxy stellar mass for real galaxies (e.g., Wetzel et al. 2013; Schawinski et al. 2014; Haines et al. 2015; Smethurst et al. 2015; Bremer et al. 2018; Carnall et al. 2018; Rowlands et al. 2018a; Phillipps et al. 2019; Tacchella et al. 2022; Bravo et al. 2023).

Through a combined analysis of SDSS, GALEX (Martin et al. 2005), and Galaxy Zoo (Lintott et al. 2008) data, Schawinski et al. (2014) find that local ($0.02 < z < 0.05$) late-type galaxies ($10^9 < M_*/M_\odot < 10^{11.5}$) experience a gradual shutdown of star formation over several gigayears ($\gtrsim$1 Gyr), while local early-type galaxies in a similar mass range experience a very rapid quenching event ($\lesssim$250 Myr) with a simultaneous morphological transformation. Schawinski et al. (2014) conclude that the slow quenching of their late-type galaxies is due to a stoppage of the comic gas supply followed by an extended exhaustion of the remaining gas, while the early-type galaxies have gas supplies and reservoirs that are destroyed almost instantaneously, possibly by major mergers. In an analysis that leverages similar SDSS/GALEX+Galaxy Zoo data, Smethurst et al. (2015) find that, for local to intermediate-redshift galaxies ($0.01 < z < 0.25$; $10^9 < M_*/M_\odot < 10^{11.2}$), the quenching timescales are clearly different for smooth (i.e. early-type) and disk-like galaxies. Smooth galaxies are found to undergo rapid quenching (<1 Gyr) via major mergers, disk-like galaxies quench over longer periods (>2 Gyr) through secular evolution, and an intermediate population quench over intermediate timescales (between 1 and 2 Gyr) via minor mergers and galaxy interactions (Smethurst et al. 2015). The results of Smethurst et al. (2015) are in qualitative agreement with our results for the quenching timescales ($\sim$1 Gyr to $\sim$2.5 Gyr) over a similar mass range ($M_* \lesssim 10^{11}\ M_\odot$), though we do not separate galaxies based on visual morphology (e.g., smooth or disk-like). At higher masses, we find inside-out quenched galaxies can take up to $\sim$3.5 Gyr to quench (on median), while Smethurst et al. (2015) also find a small percentage of their galaxies can quench over very long timescales (>3 Gyr). However, when we compare our results with those of Schawinski et al. (2014), we do not find any galaxies in our sample that quench as quickly as their rapidly quenching galaxies ($\lesssim$250 Myr), with only two galaxies in our sample quenching in less than 500 Myr. Even if we account for the perturbations in the duration of our quenching episodes due to different peaks in the star formation history or different definitions of the onset of quenching (see Section 2.2.2), which can be up to $\sim$200 Myr when considering the median duration, this would still only influence two galaxies to quenching timescales of <300 Myr. Even so, we find that our results for quenching timescales that take a few gigayears are consistent with the results of Schawinski et al. (2014) for their late-type galaxies.

Considering the nature of quenching timescales for local ($z < 0.06$) galaxies in GAMA, Rowlands et al. (2018a) find a green valley transition timescale of 2.6 Gyr for $M_* > 10^{10.6}\ M_\odot$, which increases with increasing stellar mass. Bremer et al. (2018) find that, for intermediate-mass GAMA galaxies ($10^{10.25} < M_*/M_\odot < 10^{10.75}$) at nearby redshifts ($0.1 < z < 0.2$), the typical green valley traversal timescale is $\sim$1–2 Gyr and is independent of environment. Using the same redshift slice but expanding the considered mass range,

Phillipps et al. (2019) predict that GAMA green valley galaxies have star formation that decreases over 1.5–4 Gyr. As well, Bravo et al. (2023) consider quenching timescales and find values ∼2.5 Gyr for local ($z < 0.06$) low-mass galaxies ($\sim 10^9\ M_\odot$), but find strong mass dependence for the quenching timescale, where by $\sim 10^{11}\ M_\odot$ the timescale has decreased to 1 Gyr. Bravo et al. (2023) additionally find an environmental dependence for galaxies less massive than $\sim 10^{10}\ M_\odot$, where satellites have a shorter quenching timescale compared with central galaxies of ∼0.4 Gyr. We find that our results show good agreement with the predictions of Phillipps et al. (2019) and also the typical timescale of 2.6 Gyr for high-mass galaxies from Rowlands et al. (2018a), in particular the notion that quenching timescale increases with increasing stellar mass. As well, our results are consistent with those of Bremer et al. (2018) over their considered mass range. However, when we investigated the environment of the quenched populations, we found that inside-out quenched galaxies are commonly massive galaxies living in the field, which take a long time to quench (∼2.5 Gyr on average, up to ∼3.5 Gyr at high masses), while the outside-in population are satellites in dense environments and have shorter quenching durations (∼1.5 Gyr), and so we find a clear environmental trend for the quenching timescale. Bremer et al. (2018) finds no environmental dependence for their quenching timescales.

We now discuss studies that consider quenching timescales of simulated galaxies as part of large cosmological simulations (e.g., Trayford et al. 2016; Hahn et al. 2017; Nelson et al. 2018; Rodríguez Montero et al. 2019; Wright et al. 2019, 2022; Park et al. 2022; Walters et al. 2022; Wang et al. 2023b). Trayford et al. (2016) use $10^9 < M_*/M_\odot < 10^{11.3}$ galaxies in the Evolution and Assembly of Galaxies and their Environments (EAGLE) simulation (Crain et al. 2015; Schaye et al. 2015). They conclude that most galaxies spend less than 2 Gyr in the green valley by studying intrinsic u—r colors, and that this timescale is independent of quenching mechanism for satellites and those that host an AGN. Meanwhile, Nelson et al. (2018) investigate the formation of the red sequence and the build-up of the color–mass plane using simulated g—r colors for $10^9 < M_*/M_\odot < 10^{12}$ galaxies within TNG100 and TNG300 (larger simulation boxes using the same models as TNG50, but with lower mass resolution) and find a median green valley transition timescale of ∼1.6 Gyr which decreases as a function of increasing stellar mass (starting at 2–3 Gyr for $M_* < 10^{10}\ M_\odot$ and ending at ∼1 Gyr for $M_* > 10^{11}\ M_\odot$). They find a similar timescale across TNG100 and TNG300, with little difference between central galaxies and satellites (Nelson et al. 2018). In addition, Wright et al. (2019) consider two quenching timescales within EAGLE: the green valley traversal timescale on the color–mass diagram, and the timescale for a galaxy to leave the star forming main sequence and settle onto the passive cloud in sSFR–mass space. They find that low-mass centrals ($M_* < 10^{9.6}\ M_\odot$) take longer to quench than satellites of a similar mass (∼4 Gyr compared to ∼2 Gyr), where the satellite

quenching is driven by strong ram pressure stripping and the central quenching is the result of stellar feedback (Wright et al. 2019). Higher-mass EAGLE galaxies ($M_* > 10^{10.3}$ $M_\odot$) quench more rapidly, $\lesssim$2 Gyr, for both centrals and satellites, as a consequence of galaxy mergers and AGN feedback. In a result similar to that of Nelson et al. (2018), Wright et al. (2019) also find that intermediate-mass galaxies have the longest quenching timescales for centrals and satellites. When we compare our results, we find agreement with Trayford et al. (2016) for our outside-in population, where those galaxies have quenching timescales <2 Gyr, and even some of our low-mass inside-out quenched galaxies also have timescales that are consistent with <2 Gyr. For our high-mass inside-out population, we find longer timescales of up to ∼3.5 Gyr. As above, we find a timescale dependence that is linked with quenching mechanism, a result not found by Trayford et al. (2016). Our result of increasing quenching timescale with increasing stellar mass is not shared by Nelson et al. (2018) or Wright et al. (2019), who found the opposite relationship, nor is our conclusion of different timescales for centrals/satellites when we compare with Nelson et al. (2018), though Wright et al. (2019) find a similar result at low mass. Nonetheless, we agree with Nelson et al. (2018) on the median quenching timescale when we consider our outside-in galaxies (∼1.5 Gyr to their ∼1.6 Gyr).

Besides work that investigates quenching timescales, studies in the literature also examine the nature of both inside-out and outside-in quenching in large cosmological simulations, like that of McDonough et al. (2025). In their work, McDonough et al. (2025) study radial profiles of luminosity-weighted ages for low- and high-mass central and satellite galaxies in TNG100. They find that high-mass ($M_* > 10^{10.5}$ $M_\odot$) central and satellite galaxies experience inside-out quenching that is driven by AGN feedback, with environmental effects only being apparent at extreme halo masses and local overdensities, while low-mass ($M_* < 10^{10}$ $M_\odot$) galaxies experience environmental effects that drive quenching (McDonough et al. 2025). They additionally find that the environmental quenching proceeds outside-in (McDonough et al. 2025). We find very good qualitative agreement between our results and those of McDonough et al. (2025), in particular with regard to the nature of outside-in quenching for low-mass satellites and inside-out quenching for high-mass centrals.

2.4.2 Feasibility with galaxy surveys

Given the results presented in Figure 2.11, we find that we can separate early-episode quenching galaxies from quenching galaxies that are late in their quenching episode. This is true for both populations of quenched galaxies investigated in this work. This result suggests that we can estimate the quenching progress for galaxies with these morphological

evolutionary signatures. Coupled with the total duration of the quenching episode per population (∼2 Gyr for inside-out quenched galaxies below 10^{11} $M_{\odot}$, ∼3.5 Gyr above 10^{11} $M_{\odot}$, and ∼1.5 Gyr for outside-in quenched galaxies; see Figure 2.7), we can make predictions for the elapsed quenching timescale (measured in Gyr) for such galaxies, based only on morphological metrics that trace the evolution of star formation.

In addition, phase-space diagrams of simulated group and cluster galaxies can provide information on the time since infall for galaxies into a massive halo (e.g., Oman et al. 2013; Rhee et al. 2017; de los Rios et al. 2021; Martínez et al. 2023). With appropriate assumptions about the correlation between time since infall and the onset of quenching, these types of investigations can provide insight into the quenching history of such galaxies (e.g., Lotz et al. 2019; Pasquali et al. 2019; Dacunha et al. 2022; Hough et al. 2023). Our methodology as described above can provide an independent estimate for the onset of quenching. Combining this information with phase-space arguments for time since infall could be a powerful way to investigate when quenching occurs as a function of position on phase-space diagrams using observational data, which is otherwise not possible. This process and the diagnostic information it provides is compelling for future large-scale galaxy surveys, which will have sufficient spatial resolution to map the distribution of star formation for galaxies at various redshifts.

In particular, proposed and upcoming missions like CASTOR (Côté et al. 2025) and the Ultraviolet Explorer (UVEX; Kulkarni et al. 2021) aim to image the ultraviolet sky at various resolutions. By combining these observations with other space-based observatories like JWST, NGRST, and Euclid (Euclid Collaboration et al. 2025), all of which will provide longer wavelength coverage to map the distribution of stellar mass, we believe that the morphological metrics described above can be used to distinguish different types of quenching galaxies based on morphological signature. Further, as we have described, these metrics provide great distinguishing power to estimate the duration of quenching for these galaxies, and can place constraints on the quenching progress.

In addition to large photometric galaxy surveys, resolved studies of star formation could prove a compelling testbed for applying our methodology. For example, integral field unit observations can provide high spatial resolution while also collecting spectra. Of the available integral field unit surveys, MaNGA (Bundy et al. 2015) is the largest, having collected observations for 10^4 nearby ($0.01 < z < 0.15$) galaxies (Abdurro'uf et al. 2022b). However, MaNGA splits their sample into a "primary+" and secondary sample, where the primary sample covers two-thirds of the available observations and extends to 1.5 $R_{\rm e}$, while the secondary sample is for the remaining third of the sample, with spatial coverage out to 2.5 $R_{\rm e}$ (Bundy et al. 2015; Yan et al. 2016; Wake et al. 2017). In the current work, we probed the distribution of star formation and stellar mass out to 5 $R_{\rm e}$, and so it is unclear

how well our methodology could perform with such a limited extent, if matching to either the MaNGA primary or secondary radial limits. This type of investigation is outside the scope of the present work.

It has been previously suggested that the active galactic nuclei feedback model in TNG is overly strong compared to observations (e.g., Mitchell et al. 2020; Terrazas et al. 2020; Donnari et al. 2021b; Habouzit et al. 2022; Ma et al. 2022; Voit et al. 2024; Wright et al. 2024). This could result in inside-out quenching that is more dramatic than in real data. As well, there is some evidence that points to the mechanism controlling environmental gas removal in TNG being stronger and happening earlier than what observations imply (e.g., Diemer et al. 2019; Stevens et al. 2019; Chen et al. 2024). However, other studies have found good agreement between TNG galaxies and real data when investigating environmental gas removal (Stevens et al. 2021, 2023), indicating that this situation remains unclear. In either event, when considering applying our methodology to samples of real galaxies, care must be taken regarding the strength of inside-out and outside-in quenching. We expect that the morphological metrics that trace sharp truncations of the star forming disk ($R_{\rm inner}$ and $R_{\rm outer}$) would be most affected, but these metrics were developed with flexibility regarding their definitions, so they could be readily adapted to real galaxies that have gentler specific star formation radial profiles. As well, these morphological metrics have been found to be less important than $C_{\rm SF}$ and $R_{\rm SF}$ for classification purposes (see Appendix A.4). Beyond the strength of the active galactic nuclei feedback model in TNG, AGN in real galaxies produce emission across the electromagnetic spectrum, including in windows commonly used to trace star formation, such as ultraviolet, Hα, and infrared emission (e.g., Baldwin et al. 1981; Veilleux & Osterbrock 1987; Weymann et al. 1991; Elvis et al. 1994; Lacy et al. 2004; Stern et al. 2005). Care must therefore be taken, possibly including the use of molecular gas as a tracer for star formation (e.g., Kennicutt 1998a; Gao & Solomon 2004; Leroy et al. 2008; Bigiel et al. 2008; Bolatto et al. 2013).

Of course, observational data for real galaxies does not simply provide star formation rate maps, but one can use ultraviolet and infrared emission to trace the young stellar populations (e.g., Kennicutt 1998b; Madau & Dickinson 2014) or perform spectral energy distribution fitting to obtain star formation rates and stellar masses. In fact, there have already been works analyzing the morphology of stellar mass and star formation rate maps rather than optical light (e.g., Tan et al. 2024). As an intermediate step before applying the current methodology to real galaxies, testing with synthetic imaging (where the underlying true population is known) must be completed (e.g., Smith & Hayward 2018), and we expect that such testing will reveal additional insights about the feasibility of using morphological metrics like the ones discussed in this work.

2.4.3 Limitations and future directions

When considering the limitations of the current study, we find a few points worth commenting on. The first concerns the definition of the onset of quenching and how this onset is tied to a relative peak in the star formation histories of our sample galaxies. We have found that the distributions of some of our morphological metrics (most obviously $C_{\rm SF}$, but also $R_{\rm SF}$ to a lesser degree; see Figure 2.8) for our inside-out quenched population at early times does not reproduce the distributions for the normal star forming population as expected. As mentioned above, this relative peak in star formation is likely due to a (central) starburst that precedes quenching, leading to the different distributions seen in the top panels of Figure 2.8. In an ideal sense, we could easily identify when a galaxy begins quenching at any point in the star formation history, but in practice, this becomes difficult to do, which is why we have used such a relative peak to define the quenching onset. As a potential remedy, we could have also considered a few additional snapshots prior to this star formation peak, in order to understand how the morphological metrics evolve and compare with other star forming galaxies. However, this introduces another decision regarding how far back to study, as well as the associated durations of central starbursts. In any event, this type of additional analysis is beyond the scope of the current work.

Additionally, in this work, we have considered all valid quenched galaxies within the simulation, regardless of the redshifts that they began quenching at. As an alternative, we could separate galaxies in the early Universe from those at low redshift and repeat our analyses, given how the morphology of galaxies and their star forming disks evolve through cosmic time (e.g., Shibuya et al. 2015; Ferreira et al. 2023; Kartaltepe et al. 2023; Huertas-Company et al. 2024). However, for our sample of 361 quenched galaxies, we find that 313 began quenching after redshift $z = 1.5$, while 44 began quenching between $1.5 < z < 2.5$, with the remaining galaxies representing a small percentage of our sample ($\sim$1%). In addition, we find that ambiguously quenched galaxies make up a larger proportion (than expected) of the sample that began quenching at higher redshifts, and as evidenced above, we do not focus on the ambiguously quenched population in this work. We also find that the median quenching onset redshift is $z \approx 0.73$. With these considerations, we do not expect that separating our sample based on onset redshift should have a large effect on the results presented here, in light of our focus on the inside-out and outside-in quenched populations. Besides, with such a small population that begins quenching at high redshift, statistical comparisons with lower-redshift quenching galaxies might prove difficult.

Regarding future directions, as mentioned above, an appropriate next step is to test this methodology using synthetic imaging or mock observations of these galaxies. In this testing

phase, adaptations appropriate for use with observational datasets must be considered, thereby creating observational proxies of the morphological metrics. These proxies must then be compared to understand their performance in recovering the metrics as described in this work. While beyond the scope of the present study, we will next complete this feasibility investigation in Chapter 3. Beyond these steps, in the event that observational proxies can accurately recover the metrics, then we can look to apply this methodology to datasets of galaxies in the real Universe, to look for samples of inside-out and outside-in quenching galaxies. As discussed above, care must be taken regarding the assumption that the simulated galaxies are representative of the real galaxy population, and additional updates to the definition of the morphological metrics may be necessary. We will aim to use high spatial resolution data that have long integration times, and ideally would use a dataset that includes different environments (e.g., field and dense groups or clusters).

2.5 Summary and Conclusion

In this chapter, we have investigated quenched populations and their evolution by considering subhalos present in the highest-resolution run of the IllustrisTNG suite, TNG50. Using the unprecedented resolution of the simulation over a cosmological volume, we first selected a sample of 361 quenched galaxies based on their star formation histories relative to the star formation histories of star forming main-sequence galaxies with a similar stellar mass. Our main findings are as follows:

1. Four observationally motivated metrics ($C_{\rm SF}$, $R_{\rm SF}$, $R_{\rm inner}$, and $R_{\rm outer}$), which collectively describe the spatial distribution of star formation, evolve as a galaxy quenches (e.g., Figure 2.5), with three main modes being prominent: the first where $C_{\rm SF}$ decreases with time, while $R_{\rm SF}$ increases with time, and where $R_{\rm inner}$ strongly evolves, while $R_{\rm outer}$ is relatively constant. This mode is described as having an inside-out morphological evolutionary signature, and numbers 78 galaxies. The second population has metrics that evolve in the opposite fashion for $C_{\rm SF}$ and $R_{\rm SF}$, while $R_{\rm inner}$ is relatively constant and $R_{\rm outer}$ evolves strongly, and is described with an outside-in evolutionary signature, numbering 185 galaxies. We find evidence for a third population, which lies between the prior two, and is subsequently considered as having an ambiguously evolving morphological signature, comprising the remaining 98 galaxies. We find no conclusive evidence for an additional class of quenched galaxy where the star formation is uniformly suppressed throughout the galaxy. Such a galaxy would show little evolution in the metrics, with $R_{\rm inner}$ and $R_{\rm outer}$ in particular staying essentially constant.

2. Galaxies with an inside-out evolutionary signature are often centrals found in the field, while the environment of outside-in population galaxies tends to be denser regions, like galaxy groups or clusters. Outside-in galaxies are most commonly satellites and experience an average delay of ∼1 Gyr after being accreted onto a massive structure before beginning to quench (Figure 2.6). Inside-out and outside-in galaxies are somewhat bimodal in terms of stellar mass, where inside-out quenched galaxies are generally more massive than their outside-in counterparts.
3. Inside-out and outside-in quenched galaxies have quenching timescales that are a function of stellar mass, with low-mass ($M_* < 10^{11}\ M_\odot$) inside-out galaxies taking ∼2 Gyr, while high-mass ($M_* > 10^{11}\ M_\odot$) inside-out galaxies can take up to ∼3.5 Gyr to quench. Outside-in quenched galaxies have less variability in terms of their quenching timescale, typically taking ∼1.5 Gyr to quench (Figure 2.7).
4. Quenched galaxies evolve in a fundamentally different manner compared to normal star forming galaxies, which do not show significant evolution in their metrics (Figure 2.8). In parameter space, the inside-out population evolves in a different area than the outside-in population, indicating that this combination of metrics can discriminate between different evolutionary signatures for quenched galaxies, and can also separate such quenched populations from normal star forming galaxies (Figure 2.9).
5. k-nearest neighbor algorithms can distinguish galaxies based on their location in the metric parameter space, where the classification process accuracy increases as galaxies continue to quench and become morphologically distinct (Figure 2.10). Machine learning can also separate quenched galaxies based on epoch of progress through the quenching episode (Figure 2.11) for a single population, and combined with estimates for the total duration of the quenching episode, it can provide information on the evolution of these populations and provide testable predictions for observations.

Taken holistically, our results suggest that the nature of galaxy quenching is primarily driven by two main mechanisms within the TNG50 simulation: in the first, feedback from active galactic nuclei or strong central stellar feedback suppresses star formation in the central regions of galaxies, and this suppression evolves from the inside out. This mechanism is most commonly found within massive central galaxies, especially those that live within the field. The second mechanism seems to be a consequence of environmental effects, where low-mass satellites of more massive structures experience an environmental gas removal and corresponding suppression of star formation that proceeds from the outside in, consistent with quenching mechanisms such as ram pressure stripping. However, we have also found low levels of outside-in quenching for predominantly inside-out quenched galaxies, indicating that the nature of quenching for simulated galaxies is not wholly binary. Indeed, we have even found high-mass satellites in dense environments that primarily

quench from the inside out.

Of course, simulations are an idealized scenario from which to undertake such studies, and this is why we caution against blindly adopting and applying such metrics to observational data without first testing with a control sample with known characteristics. To that end, in future work, we are looking to extend our analysis to synthetic observations of galaxies drawn from TNG50 (Chapter 3) before applying those findings to observations of galaxies in the real Universe. We are optimistic that the methodology presented in this work will be a powerful tool for upcoming large galaxy surveys that will cover extended areas of the sky with high spatial resolution, enabling the creation of catalogs of galaxies with different evolutionary signatures.

Chapter 3

Identifying and Distinguishing Quenching Galaxies with Spatially Resolved Star Formation in Mock CASTOR and NGRST Observations

3.1 Introduction

Star formation is the primary regulator of galaxy evolution in the Universe (e.g., Zhang 2018), and is well traced with recombination lines and infrared luminosity (e.g., Kennicutt 1998b; Bell 2003; Burgarella et al. 2005; Calzetti et al. 2007, 2010; Kennicutt & Evans 2012; Calzetti 2013). As well, ultraviolet radiation is one of the most straightforward tracers of star formation, and is mostly dominated by massive stars with short lifetimes (e.g., Vink 2020). Understanding the spatial and temporal evolution of star formation rate across cosmic environments is necessary to understand galaxy evolution and quenching (e.g., Madau & Dickinson 2014). Many mechanisms capable of quenching star formation in galaxies have been proposed including internal processes like active galactic nuclei feedback (e.g., Di Matteo et al. 2005; Bower et al. 2006; Croton et al. 2006; Fabian 2012). This feedback can lead to a lack of young stars in the central regions of galaxies (e.g., Dubois et al. 2013). In addition to internal effects, the environment in which a galaxy resides can also play a role in quenching (e.g., Peng et al. 2010, 2012). Ram pressure stripping (e.g., Gunn & Gott 1972; Abadi et al. 1999; Balogh et al. 2000; Poggianti et al. 2017; Boselli et al. 2022), starvation or strangulation (Larson et al. 1980; Peng et al. 2015), and gravitational

harassment (Moore et al. 1996, 1998) have all been proposed as environmental effects, and can act to suppress star formation in the outskirts of a galaxy. Given these potential internal and external influences, the morphological evolution of a galaxy undergoing a certain kind of quenching will present different spatial signatures (Zhang et al. 2019; Lawlor-Forsyth et al. 2026b), as traced by the evolution of the young stellar population with ultraviolet observations.

Observations that spatially resolve the young stellar populations and can distinguish different quenching evolutionary signatures are clearly ideal, given the additional information included in such observations compared to integrated observations. In addition to large integral field unit surveys such as the Calar Alto Legacy Integral Field Area survey (CALIFA; Sánchez et al. 2012), the Sydney-AAO Multi-object Integral field spectrograph galaxy survey (SAMI; Croom et al. 2012; Bryant et al. 2015), and Mapping Nearby Galaxies at Apache Point Observatory (MaNGA; Bundy et al. 2015), imaging studies using Hα (e.g., Koopmann & Kenney 2004a,b; Gavazzi et al. 2013; Matharu et al. 2021, 2022) and spatially resolved spectral energy distribution fitting have also been completed (e.g., Abdurro'uf & Akiyama 2017, 2018; Jung et al. 2017; Jafariyazani et al. 2019; Morselli et al. 2019; Nelson et al. 2021; Abdurro'uf et al. 2022a, 2023). These studies have found galaxies with suppressed central star formation, indicative of a quenching mechanism that proceeds from the inside to the outskirts, in local (Abdurro'uf & Akiyama 2017; Abdurro'uf et al. 2022a), intermediate (Abdurro'uf & Akiyama 2018; Jafariyazani et al. 2019), and high redshift galaxies (Jung et al. 2017; Abdurro'uf et al. 2023), and galaxies below the star forming main sequence (Morselli et al. 2019). As well, Nelson et al. (2021) found that massive galaxies below the main sequence (e.g., Brinchmann et al. 2004) also show centrally-suppressed star formation in both observations and simulations. Being able to distinguish different quenching signatures is therefore a powerful means of better understanding the shut down of star formation, with the previously mentioned studies all successfully employing spatially resolved spectral energy distribution fitting.

The next decade will be a transformational time in the field of astrophysics. New observatories such as the James Webb Space Telescope (JWST; Gardner et al. 2006, 2023) and Euclid (Euclid Collaboration et al. 2025) have already demonstrated the power of new facilities to probe previously inaccessible times in the history of the Universe (e.g., Castellano et al. 2022; Finkelstein et al. 2022, 2023; Naidu et al. 2022; Adams et al. 2023; Atek et al. 2023; Donnan et al. 2023; Harikane et al. 2023; Labbé et al. 2023, 2025; Kocevski et al. 2023; Bezanson et al. 2024; Greene et al. 2024; Euclid Collaboration et al. 2026a,b,c). With the coming decade, new facilities such as the Vera C. Rubin Observatory (Ivezić et al. 2019), in combination with its Legacy Survey of Space and Time (LSST; e.g., LSST Science Collaboration et al. 2009), as well as the Nancy Grace Roman Space Telescope

(NGRST; Spergel et al. 2013, 2015; Akeson et al. 2019) will similarly have a profound effect on our knowledge of the Universe, enabling large surveys of hundreds of millions of galaxies (e.g., Spergel et al. 2015; Akeson et al. 2019; Ivezić et al. 2019). At the same time, aging facilities like the Hubble Space Telescope (HST) continue to be invaluable given the access to ultraviolet and blue-optical wavelengths (e.g., Côté et al. 2025; Windhorst et al. 2025), but will eventually be decommissioned. This will leave a notable gap in the coverage of the ultraviolet sky that is important for understanding young stellar populations within galaxies (e.g., Kennicutt 1998b; Calzetti 2013; Madau & Dickinson 2014), before the launch of next generation facilities like the Habitable Worlds Observatory (LUVOIR Team 2019; Gaudi et al. 2020).

The Cosmological Advanced Survey Telescope for Optical and UV Research (CASTOR; Côté et al. 2025) is a proposed mission to provide high-resolution imaging and spectroscopy over a $\sim$0.25 deg^2 field of view at ultraviolet and blue-optical wavelengths (0.15–0.55 μm) simultaneously. With a planned launch for the end of the decade (Côté et al. 2023), CASTOR will critically complement both space- and ground-based observatories that observe at longer wavelengths, such as Euclid, NGRST, and Rubin, and will prove instrumental in filling the aforementioned "ultraviolet gap." The combination of these observatories will prove critical for understanding many astrophysical phenomena, including how galaxies have their star formation suppressed or quenched, given the ultraviolet coverage afforded by CASTOR.

In Lawlor-Forsyth et al. (2026b, hereafter Paper I), we showed that observationally motivated metrics that are based on the distribution of star formation can morphologically distinguish simulated quenching galaxies from star forming galaxies in IllustrisTNG (Nelson et al. 2018; Pillepich et al. 2018a; Springel et al. 2018). We found that in many cases (but not all) the quenching population can be further divided into distinct quenching evolutionary signatures: a population where star formation is suppressed inside-out, and an outside-in population. For a minority of the quenching population this classification was not straightforward, as some galaxies showed the effects of both inside-out and outside-in quenching, and thus reside between the two previous populations. We considered this as a third class, that was ambiguously quenching. We found that the inside-out population in the simulation are more often primary/central galaxies found in the field, while outside-in quenched galaxies are commonly satellites in dense environments like galaxy groups and clusters, and begin quenching $\sim$1 Gyr after being accreted onto a larger halo. We found typical timescales associated with the duration of quenching, where the inside-out population can take up to $\sim$3.5 Gyr to quench at higher masses ($M_* \gtrsim 10^{11}$ $M_\odot$), but takes $\sim$2 Gyr to quench at lower masses ($M_* \lesssim 10^{11}$ $M_\odot$). The outside-in population has a typical quenching timescale of $\sim$1.5 Gyr. In Paper I, we additionally found that

the morphological metrics for the quenching populations evolved differently through the quenching episode, and evolve distinctly compared to normal star forming galaxies that do not show evolution (by construction). We found that the morphological metrics can be used to estimate the progress through the quenching episode for the inside-out and outside-in populations.

However, in Paper I, we did not make predictions or testable estimates for galaxies residing in the real Universe (e.g., Smith & Hayward 2018). As such, in this chapter we take a population of simulated quenched galaxies and create mock observations from which we can determine the feasibility of using the metrics introduced in Paper I to find quenched galaxies in upcoming large galaxy surveys. As well, when creating our mock observations, we sample the quenching episode for each galaxy, thereby creating synthetic imaging that tracks the evolution of such systems, to understand the limits of this procedure in real data. Therefore, we artificially place our mock observations at a characteristic redshift that will be accessible to future galaxy surveys. Through this, we will be in a position to make predictions and testable estimates for the proportions of quenched galaxies with different morphological evolution in the real Universe, and provide constraints and suggestions for how to best identify such galaxies.

This chapter is structured as follows: in Section 3.2, we describe the simulated data that we have used previously in Paper I along with the survey strategies for key upcoming large galaxy surveys, our procedure for creating mock observations based on those surveys, as well as the analysis pipeline for extracting physical measurements. In Section 3.3, we present our results and the recoverability of our metrics when using the mock observations as well as considerations for how to best adapt our metrics to real observations. In Section 3.4, we discuss our results and make predictions for upcoming surveys. Finally, in Section 3.5, we present our summary and conclusion.

Throughout this chapter we adopt a flat ΛCDM cosmology that is consistent with the TNG simulation (Weinberger et al. 2017; Pillepich et al. 2018b), based on the Planck intermediate results (Planck Collaboration et al. 2016): $H_0 = 67.74$ km s^{-1} Mpc^{-1}, $\Omega_\mathrm{m} = 0.3089$, $\Omega_\Lambda = 0.6911$, and $\Omega_\mathrm{b} = 0.0486$.

3.2 Methodology

3.2.1 IllustrisTNG and Galaxy Sample

In Paper I, we used the highest resolution run of the IllustrisTNG suite[1] (e.g., Nelson et al. 2018, 2019a; Pillepich et al. 2018a; Springel et al. 2018), TNG50, to select simulated galaxies with $M_* \geqslant 10^{9.5}$ $M_\odot$ by $z = 0$. The IllustrisTNG simulations are cosmological gravo-magneto-hydrodynamical simulations and are the successor to the original Illustris (Genel et al. 2014; Vogelsberger et al. 2014b,a) simulation. They include a revised galaxy formation model (Weinberger et al. 2017; Pillepich et al. 2018b) compared to Illustris (Vogelsberger et al. 2013; Torrey et al. 2014). The moving mesh code AREPO is used (e.g., Springel 2010; Weinberger et al. 2020), alongside the Chabrier (2003) initial mass function (Pillepich et al. 2018b), while a cosmology consistent with the Planck Collaboration et al. (2016) results is employed. The IllustrisTNG model aims to reproduce observations of the global star formation rate density (from $z = 8$ to the present), and galaxy sizes, halo gas fractions, the stellar mass–halo mass relation, the galaxy mass function, and the black hole–stellar mass relation (all at $z = 0$; Rodriguez-Gomez et al. 2019). All simulation data from IllustrisTNG are publicly available (Nelson et al. 2019a).

In Paper I, the TNG50 simulation, that contains a cubic volume of 51.7 Mpc on a side (Nelson et al. 2019b; Pillepich et al. 2019) and follows 2×2160^3 resolution elements (dark matter and baryons) and their evolution, was used as it provides high resolution for the baryonic elements (average mass of 8.5×10^4 $M_\odot$; Nelson et al. 2019b; Pillepich et al. 2019). TNG50 has improved mass resolution by more than an order of magnitude compared to the flagship TNG100 simulation (Nelson et al. 2019b). This improved mass resolution places TNG50 near modern "zoom" simulations but within a large cosmological volume (Nelson et al. 2019b).

In Paper I, we compared the star formation histories (SFHs) of quenched galaxies with those of normal star forming galaxies that reside on the star forming main sequence (e.g., Brinchmann et al. 2004; Daddi et al. 2007; Elbaz et al. 2007; Noeske et al. 2007), and that have a similar ($\leqslant$0.1 dex) stellar mass. We identified the quenched galaxies as those where their SFH was within the $\pm 2\sigma$ limits of the main sequence population but then fell below the 2.5th percentile and stayed below that level. This procedure produced 361 quenched galaxies within TNG50, out of a possible 1666 galaxies with $M_* \geqslant 10^{9.5}$ $M_\odot$ by $z = 0$. We additionally identified the quenching episode for each of these galaxies by noting the last significant peak in star formation (relative to the entire SFH) as the onset, with the

[1] https://www.tng-project.org

termination of quenching occurring when the 2.5th percentile is crossed. Please see Paper I (e.g., their Figure 1) for full details on this procedure.

To summarize the sample used in Paper I, by considering the 361 identified quenched galaxies through their respective quenching episodes, we reach a sample of 5365 quenching galaxies, with an additional 64,128 unique galaxies that represent all possible control star forming galaxies. These control star forming galaxies are similar to the stellar mass ($\leqslant$0.1 dex) of their respective quenching galaxy throughout the quenching galaxy's quenching episode, and so form a mass-matched sample. In total we have some 69,493 unique galaxies that we consider as our fiducial sample.

In order to test the feasibility of the metrics as used in Paper I, we require mock observations against which we can compare our simulation-based results, that trace star formation and stellar mass. We therefore create mock observations with CASTOR and NGRST, as the ultraviolet and blue-optical observations from CASTOR will trace star formation, while the red-optical and near-infrared observations from NGRST will trace stellar mass.

3.2.2 CASTOR Surveys

Before describing the mock observation creation process, we first discuss the proposed CASTOR telescope and accompanying surveys that will provide spatially resolved images for tens of millions of galaxies (Côté et al. 2025). In the following section we provide details for the proposed NGRST High-Latitude Wide-Area Survey (e.g., Doré et al. 2018; Roman Observations Time Allocation Committee & Core Community Survey Definition Committees 2025, hereafter ROTAC et al. 2025).

CASTOR[2] is a proposed 1 m space telescope mission to provide high-resolution imaging and spectroscopy over a 0.247 deg^2 field of view in three ultraviolet to blue-optical bandpasses, simultaneously (Côté et al. 2025). These bandpasses cover the wavelength range from $0.15 - 0.55$ μm, where the image quality will have a point-spread function full width at half maximum of $0\farcs15$ (Côté et al. 2025), comparable to the quality from HST (and more than an order of magnitude better than the Galaxy Evolution Explorer; Martin et al. 2005), with a native pixel size of $0\farcs1$. The design of CASTOR enables nearly diffraction-limited observations (Côté et al. 2025), while additionally having excellent sensitivity (5σ point source detection at >27 AB magnitude in a 1000 s exposure) and a field of view roughly eighty times larger than HST's Advanced Camera for Surveys (Sirianni

[2] https://www.castormission.org

et al. 2005). Compared to other proposed (e.g., Ultraviolet Explorer; Kulkarni et al. 2021) and approved (e.g., ULTRASAT; Sagiv et al. 2014) ultraviolet observatories, CASTOR will have superior image quality and sensitivity (Côté et al. 2025), in addition to having a longer mission duration, making it an excellent discovery mission at ultraviolet and blue-optical wavelengths.

In addition to the main bandpasses[3] (UV, u, g) included in the CASTOR design, a proposed broadband filter is available that will split the UV- and u-channels[4] (Côté et al. 2025), enabling better spectral energy distribution sampling at short wavelengths. Filter transmission curves for the five available CASTOR bands are shown in Figure 3.1.

Of the proposed legacy surveys that CASTOR will complete, there are three notable galaxy surveys of varying depth and area that comprise a tiered "wedding cake" approach (Côté et al. 2025; Marshall et al. 2025). The Wide Survey will image 2227 deg^2 (Côté et al. 2025), exactly overlapping with the NGRST High-Latitude Wide-Area Survey (described below), to a point source depth of ∼27.4 mag (Côté et al. 2025; Marshall et al. 2025). The Deep Survey will image 83 deg^2 over six contiguous regions (Côté et al. 2023) that overlap with LSST/Euclid deep fields (Ivezić et al. 2019; Euclid Collaboration et al. 2022, 2025) and will reach a 5σ point source depth of 29.75 mag in the ultraviolet (Côté et al. 2025). Finally, the Ultradeep Survey will image 1 deg^2 over four pointings for ten times longer than the Deep Survey (Côté et al. 2023, 2025), reaching a depth (5σ, point source) of 31.12 mag (Côté et al. 2025) in the ultraviolet. For all CASTOR surveys, an initial observing sequence of UV, u, and g-band images will be completed, followed by a subsequent sequence employing the broadband filter, producing UV^{L}, u^{S}, and g-band images (Côté et al. 2023). In Table 3.1, we present survey design parameters for the three CASTOR surveys.

[3] https://github.com/castor-telescope/etc/tree/master/castor_etc/data/passbands

[4] https://github.com/castor-telescope/etc_notebooks/tree/master/data

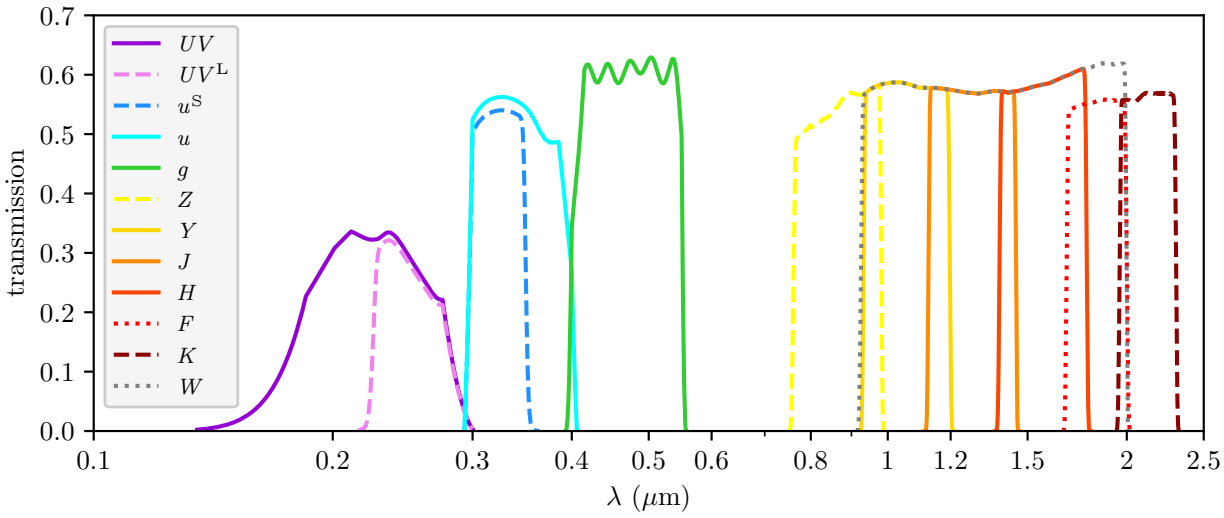


Figure 3.1: Filter transmission curves for the baseline CASTOR bands (UV, u, g), the additional CASTOR bands after using the proposed broadband filter ($UV^{\rm L}$, $u^{\rm S}$), and the bands as part of the NGRST HLWAS Deep tier and Ultradeep component (Z, Y, J, H, F, K, and wide W).

Table 3.1: Survey design parameters for the CASTOR Wide, Deep, and Ultradeep Surveys, and the NGRST HLWAS tiers.

Survey	Bands	Area (deg^2)	Exposure Time (ks)	5σ Point Source Depth (AB mag)	Reference
CASTOR Wide	UV, UV^{L}, u^{S}, u, g	2227	1, 1, 1, 1, 2	27.57, 26.67, 27.03, 27.42, 27.41	1, 2, 3
CASTOR Deep	UV, UV^{L}, u^{S}, u, g	83	18, 18, 18, 18, 36	29.75, 28.90, 29.23, 29.37, 29.11	2, 3
CASTOR Ultradeep	UV, UV^{L}, u^{S}, u, g	1	180, 180, 180, 180, 360	31.12, 30.28, 30.61, 30.69, 30.38	2, 3
HLWAS Wide	H	2702	0.642	26.2	4
HLWAS Medium	Y, J, H	2415	0.642	26.5, 26.4, 26.4	4
HLWAS Deep	Z, Y, J, H, F, K, W	19.2	4.425	27.7, 27.7, 27.6, 27.5, 27.0, 25.9, 28.3	4
HLWAS Ultradeep	Y, J, H	5	8.85	28.2, 28.2, 28.1	4

References. — 1. Côté et al. (2023), 2. Côté et al. (2025), 3. Marshall et al. (2025), 4. ROTAC et al. (2025)

3.2.3 NGRST Surveys

The Nancy Grace Roman Space Telescope[5] (NGRST; Spergel et al. 2013, 2015; Akeson et al. 2019) is an upcoming 2.4 m space telescope that will provide high-resolution imaging and spectroscopy over a 0.28 deg^2 field of view across eight red-optical and near-infrared bands, through its Wide Field Instrument[6] (ROTAC et al. 2025). These bandpasses cover the wavelength range from $0.48 - 2.3$ μm, where the image quality will have a point-spread function full width at half maximum of $0\farcs058 - 0\farcs169$ (band-dependent), comparable to HST (ROTAC et al. 2025), with a pixel size of $0\farcs11$. Only the two bluest bandpasses will not be diffraction-limited. NGRST will additionally have sensitivity comparable to HST, with 5σ point source detection at 26.5 AB magnitude in a $\sim$600 s exposure (ROTAC et al. 2025), and a field of view roughly ninety times larger than HST's Advanced Camera for Surveys (Sirianni et al. 2005).

NGRST will complete three core community surveys using WFI, one of which is the High-Latitude Wide-Area Survey[7,8] (HLWAS; e.g., Doré et al. 2018; ROTAC et al. 2025). The HLWAS is composed of three tiers and an additional component with varying depth and area that similarly comprise a "wedding cake" approach, and includes both imaging and spectroscopy (ROTAC et al. 2025). The Wide tier will cover 2702 deg^2 in H-band[9] imaging alone to a 5σ point source depth of 26.2 mag, while the Medium tier will image 2415 deg^2 complementing the Wide tier in three-band Y, J, H observations to a characteristic depth of 26.5 mag (5σ, point source) in an exposure time of $\sim$600 s (ROTAC et al. 2025). The Deep tier will add Z, F, K, and W-band observations to the Y, J, H imaging over 19.2 deg^2 to reach 1.2 mag deeper across the seven bands, while 5 deg^2 of the Deep tier will finally comprise the Ultradeep component, where Y, J, H imaging is completed for an additional $\sim$0.5 mag deeper compared to the Deep tier (ROTAC et al. 2025). We also note that according to ROTAC et al. (2025), the Deep tier and Ultradeep component are additive to the shallower tiers, enabling exposures of multiple hours for the Y, J, and H-bands. The seven bands[10] that will be used as part of the Deep tier and Ultradeep component have

[5] https://science.nasa.gov/mission/roman-space-telescope

[6] https://science.nasa.gov/mission/roman-space-telescope/wfi-technical

[7] https://science.nasa.gov/mission/roman-space-telescope/high-latitude-wide-area-survey-technical

[8] https://roman-docs.stsci.edu/roman-community-defined-surveys/high-latitude-wide-area-survey

[9] We use Z, Y, J, H, F, K, and W to refer to the NGRST F087, F106, F129, F158, F184, F213, and wide F146 filters, respectively, consistent with ROTAC et al. (2025).

[10] We use the most recent transmission curves from 2024 March 27. For each filter, 18 sensor chip assemblies are available, each with their own respective bandpass quantum efficiencies. We determine a median bandpass across all sensor chip assemblies for each of the available bandpasses.

filter transmission curves shown in Figure 3.1, while the survey design parameters for the three HLWAS survey tiers (and component) are presented in Table 3.1.

3.2.4 Creating Mock Observations

To produce our mock observations, we predict the light distribution as determined using the simulation stellar particles and account for the effects of dust through the use of a spatially-varying foreground screen, given that IllustrisTNG does not account for dust (e.g., Rodriguez-Gomez et al. 2019; Bottrell et al. 2024). While radiative transfer calculations would produce more accurate synthetic images, they are computationally expensive (e.g., Hayek et al. 2010), and the extra precision afforded by radiative transfer is not warranted here. Indeed, we initially pursued using radiative transfer with the code SKIRT (Baes et al. 2011; Camps & Baes 2015), and found that the results of interest (e.g., stellar mass, star formation rate) were not significantly affected. These findings are similar to those of Rodriguez-Gomez et al. (2019) who found that a simplified pipeline (described below) for producing mock observations creates images that are effectively indistinguishable from images produced with SKIRT for IllustrisTNG galaxies with low gas fractions.

Stellar Populations

To begin our analysis we take simulation cutouts (that include all stellar particles) for our sample galaxies and produce noise-free observations using the GALAXEV stellar population synthesis code (Bruzual & Charlot 2003), following the prescription of Rodriguez-Gomez et al. (2019) and their GALAXEV pipeline[11]: every galaxy is observed from a single viewing angle that is perpendicular to the simulation xy-plane, and given the random orientations of the galaxies within the simulation volume, this produces random viewing angles across the sample. The field of view of each observation is ten times the (3D) stellar half-mass (effective) radius for a respective galaxy, ensuring the final images are large enough to facilitate a similar analysis as was completed in Paper I. The number of pixels is chosen to match potential observations from CASTOR and NGRST after dithering (Côté et al. 2025; ROTAC et al. 2025), with a resulting pixel scale of $0\farcs05$. We output our synthetic images at a single characteristic intermediate redshift ($z = 0.5$), that is accessible to current and upcoming/proposed large galaxy surveys (e.g., Euclid, NGRST, LSST, and CASTOR). We discuss surface brightness and physical size effects below (see Section 3.4).

[11] https://github.com/vrodgom/galaxev_pipeline

Following Rodriguez-Gomez et al. (2019), we use the standard and preferred Bruzual & Charlot (2003) simple stellar population models in GALAXEV, that use the "Padova 1994 library" evolutionary tracks (Alongi et al. 1993; Bressan et al. 1993; Fagotto et al. 1994a,b,c; Girardi et al. 1996) with a Chabrier (2003) initial mass function to model the spectra of the stellar particles coming from the simulation. These models describe the rest-frame luminosity per unit wavelength of a simple stellar population as a function of age, wavelength, and metallicity (Bruzual & Charlot 2003). We use an updated version from 2016 of the GALAXEV code that provides better wavelength and metallicity coverage compared to its initial release[12]. These updated models are sampled at 221 unequally spaced ages from 0 to 20 Gyr, at 2023 unequally spaced wavelengths between 91 Å and 36 mm, and at seven unequally spaced metallicities between 10^{-4} and 0.1 (Bruzual & Charlot 2003).

We then calculate the observer-frame flux per unit wavelength for each simple stellar population across all age and metallicity combinations, accounting for cosmological effects at our characteristic redshift (as described above). We use the filter response curves for the CASTOR UV, $UV^{\rm L}$, $u^{\rm S}$, u, g, and NGRST Z, Y, J, H, F, K, and W-bands to determine integrated apparent magnitudes as measured by an observer for each simple stellar population age/metallicity combination. This procedure creates a simple "look-up" table that can be interpolated and normalized using the age, metallicity, and initial birth mass of the stellar particle to produce apparent magnitudes for all stellar particles across all 12 CASTOR and NGRST bands (Rodriguez-Gomez et al. 2019). We then map and add the apparent magnitudes for all stellar particles for a given galaxy onto the final image grid, using the image size and resulting pixel scale as described above.

Dust Modeling

To account for the effects of dust, we employ a simple physically-motivated toy model that describes the spatial variation of a foreground dust screen. To motivate our parametrization for this toy model, we consider the work of Greener et al. (2020). In their work, Greener et al. (2020) produced spatially resolved measurements of dust attenuation obtained from full-spectrum stellar population fits for nearly 140,000 spaxels in 232 star forming galaxies in MaNGA. Based on these fits, Greener et al. (2020) determined the median dust attenuation as a function of radius, binned by galaxy stellar mass and offset from the star forming main sequence (e.g., Brinchmann et al. 2004). They find that galaxies at all stellar masses show more attenuation in the central regions ($\lesssim$0.5 $R_{\rm e}$), compared to outer regions ($\gtrsim$1.5 $R_{\rm e}$), commonly reaching values of $A_{\rm V} \approx 0.2$ mag at large radii (Greener et al. 2020).

[12] https://www.bruzual.org/bc03/Updated_version_2016

These median dust attenuation profiles appear consistent with a radially-declining exponential. In addition, higher-mass galaxies generally have more attenuation than lower-mass galaxies in their central regions, and galaxies closer to the star forming main sequence have attenuation profiles that are enhanced (i.e. a positive offset) compared to galaxies that are farther from the main sequence (Greener et al. 2020).

With these results in mind, we construct our toy model: using the output from TNG50 in Paper I (e.g., their Figure 2) we were able to determine the star forming main sequence as a function of time through all snapshots, where this relationship was described with a simple linear model following Donnari et al. (2019) and Pillepich et al. (2019). Here, we use that model and determine the distance, ΔMS, from the main sequence for every galaxy in our sample based on integrated stellar mass and star formation rate. We parameterize our spatially-varying dust law with a radially-declining exponential that is a function of ΔMS and the integrated stellar mass of the galaxy, M_*, as

$$A_{\rm V}(M_*, \Delta{\rm MS}) = Be^{-x} + C, \tag{3.1}$$

where $A_{\rm V}$ is the V-band dust extinction, the coefficient $B = \max(0.2, \log M_* - 9.5)$, x is the distance from the center of the image to the center of every pixel, and $C = \max(0, 0.2 + 0.1\Delta{\rm MS})$. As suggested above, the factors involved in B and C were determined empirically to produce dust extinction profiles that are qualitatively similar to Greener et al. (2020).

With the above parametrization, massive galaxies will have more dust in their central regions (from B), and galaxies closer to the main sequence will have more dust spread throughout the entirety of the stellar disk (from C). With this approach it is not necessarily critical that we reproduce the actual dust geometry for each galaxy, but rather that we can eventually recover the star formation rate distribution even with a nonuniform dust distribution. Example extinction profiles based on this process are shown in Figure 3.2. With these profiles in hand, we use the dust extinction curves from Calzetti et al. (2000) to determine the extinction as a function of wavelength, A_λ, for each pixel, and use the filter response curves to similarly determine the total extinction per pixel per band, before applying to the noiseless synthetic images.

We show example noiseless unconvolved images for three galaxies in Figure 3.3, using the mock CASTOR and NGRST photometry. In the top row we show the 2D projection of star formation (on a 100 Myr timescale) as seen in TNG along with contours that describe the stellar mass. In the second row we show the example noiseless, unconvolved images using the mock observation process described above without dust, for the same galaxies, where the CASTOR UV-band image is shown with contours from the NGRST H-band. In the third row we show the same images with the effects of dust, that is strongest and

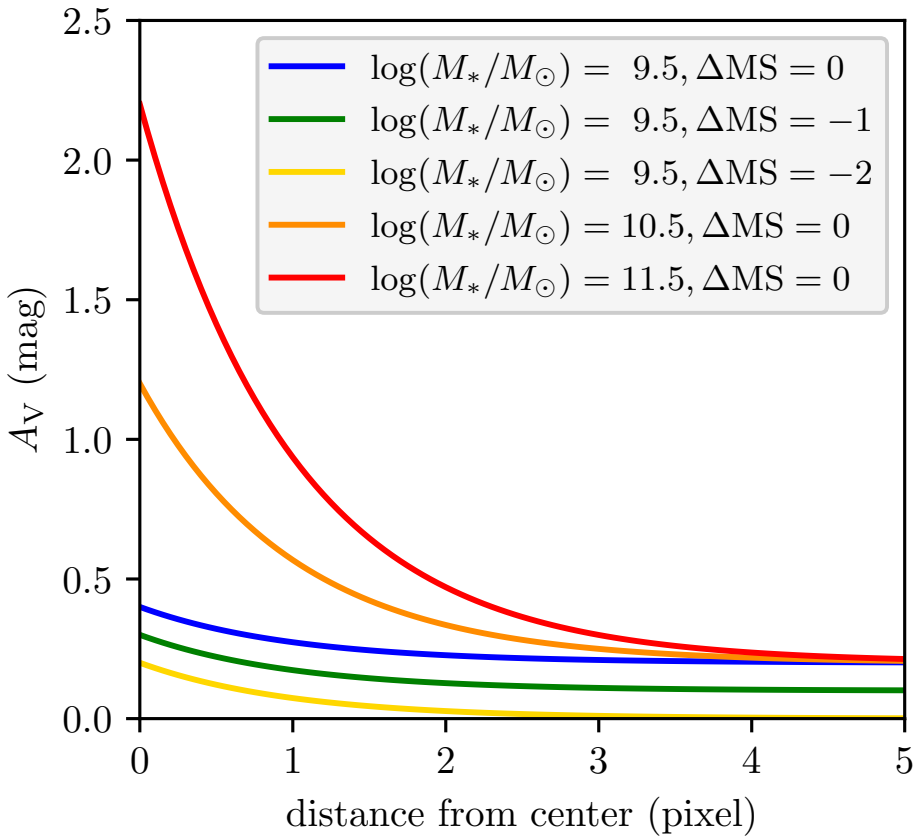


Figure 3.2: Example dust extinction profiles using our toy model from Equation (3.1), shown with different colors. At our chosen characteristic redshift of $z = 0.5$, one pixel corresponds with $\sim$0.31 kpc.

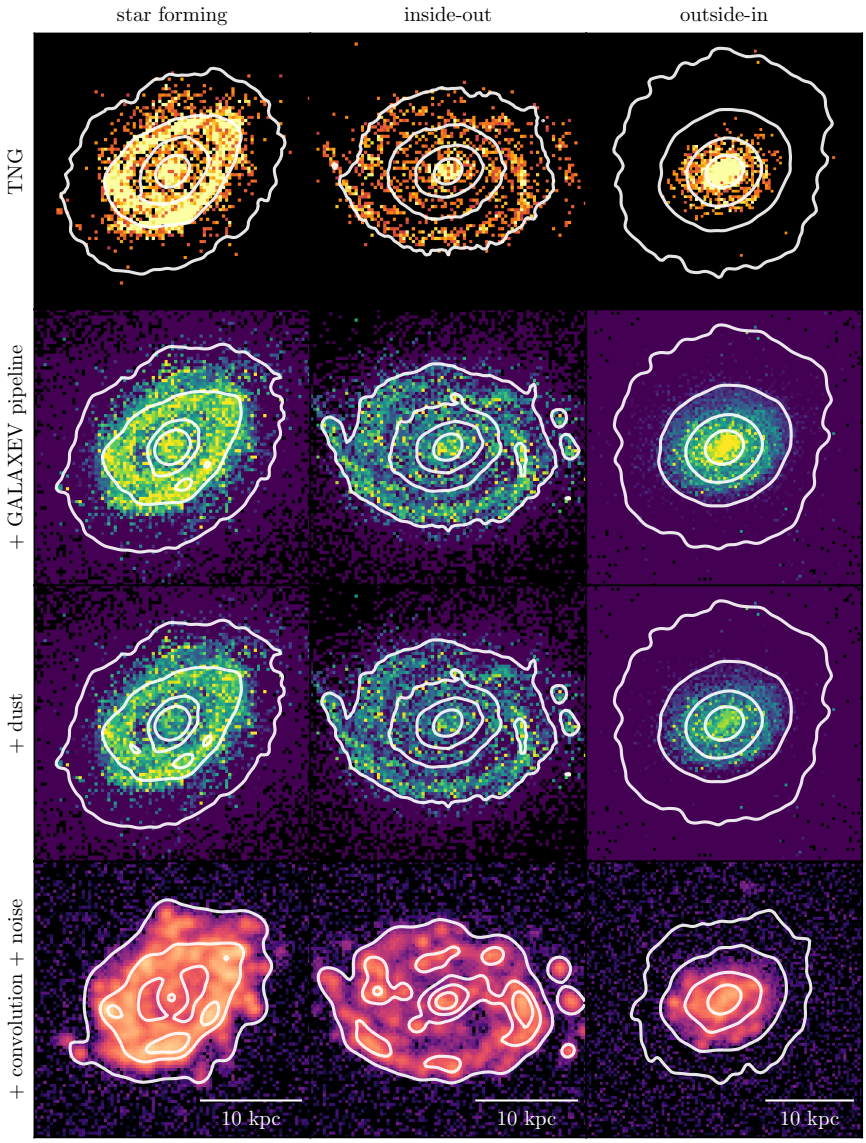


Figure 3.3: The mock observation image creation process for example star forming (left), inside-out (center), and outside-in (right) quenching galaxies, where the quenching galaxies are selected to be in the later stages of quenching. The top row displays a two dimensional projection of star formation as measured within the simulation (100 Myr timescale), with contours shown in white that trace the distribution of stellar mass. The second row shows noiseless, unconvolved CASTOR *UV* images after using the GALAXEV pipeline (see Section 3.2.4), along with contours from the NGRST *H*-band image. The third row shows the effect of our foreground dust treatment (Section 3.2.4). The fourth row shows the final mock observations after convolution and accounting for noise (Sections 3.2.4 and 3.2.4). In the bottom row, we show scale bars that describe the spatial scale of the images at $z = 0.5$.

most noticeable in the central regions of each galaxy. Moving from left to right, we show an example normal star forming galaxy, an inside-out quenching galaxy, and an outside-in quenching galaxy, both in the later stages of quenching ($\sim$75% of the way through the quenching episode).

Telescope Optics

Before we arrive at final mock observations, we must account for the effects of both a point spread function and observing noise.

Astronomical images are affected by the optical system of the telescope carrying out the observations. These effects can be adequately described through convolution with a point spread function (PSF) that matches the resolution of the proposed surveys. For CASTOR, the expected image quality will have a PSF full width at half maximum (FWHM) of $0\farcs15$ for the g-band (Cheng et al. 2024a; Côté et al. 2025), and the NGRST HLWAS will have resolutions of $0\farcs058 - 0\farcs169$ (band-dependent; ROTAC et al. 2025), where only the K-band will have a PSF FWHM larger than $0\farcs15$. In order to produce PSF-matched mock observations, for simplicity we choose an azimuthally-symmetric Gaussian with a FWHM of $0\farcs15$ for all of our synthetic images, thereby matching the expected CASTOR image quality. In the fourth row of Figure 3.3, we show our images after convolution with the PSF.

Noise Modeling

We next add appropriate noise (background, detector, and read) to our synthetic images. Following Cheng et al. (2024a), background values for CASTOR were based on the HST exposure time calculator[13], and include contributions from earthshine, zodiacal light, and geocoronal emission lines in the ultraviolet. We adopt the background values for CASTOR from the CASTOR exposure time calculator[14] (Cheng et al. 2024a) for average earthshine and low zodiacal background, as the CASTOR exposure time calculator does not account for positional variations in zodiacal light. Background values for the CASTOR filters are listed in Table 3.2.

Background values for NGRST were based on JWST backgrounds, and include contributions from zodiacal light and the galactic interstellar medium, where the zodiacal light model was based on the model of Wright (1998) and Gorjian et al. (2000), and is consistent

[13] https://etc.stsci.edu
[14] https://github.com/CASTOR-telescope/ETC

Table 3.2: Noise parameters for the CASTOR and NGRST filters.

Filter	λ (μm)	Background (mag asec^{-2})	Read (e$^-$ px^{-1})	Dark (e$^-$ s^{-1} px^{-1})	Reference
UV	0.226	26.09	3.0	0.0001	1, 2
$UV^{\rm L}$	0.252	25.32	3.0	0.0001	1, 2
$u^{\rm S}$	0.323	24.96	3.0	0.0001	1, 2
u	0.345	24.53	3.0	0.0001	1, 2
g	0.475	22.96	3.0	0.0001	1, 2
Z	0.872	21.88	13.81	0.018	3
Y	1.062	21.98	13.81	0.018	3
J	1.284	22.15	13.81	0.018	3
H	1.580	22.32	13.81	0.018	3
F	1.838	22.47	13.81	0.018	3
K	2.131	22.64	13.81	0.018	3
W	1.434	22.19	13.81	0.018	3

References. — 1. Cheng et al. (2024a), 2. Côté et al. (2025),
3. https://roman.gsfc.nasa.gov/science/wfi_technical.html

with the model of Reach et al. (1997) and Kelsall et al. (1998) at the wavelengths under consideration. Emission from the diffuse galactic interstellar medium was based on the models of Schlegel et al. (1998) and Arendt et al. (1998). These two components have been in use since the Spitzer Space Telescope (Werner et al. 2004) and Herschel Space Observatory (Pilbratt et al. 2010), and continue with Euclid[15]. The output backgrounds are also consistent with that from the JWST Backgrounds Tool[16] v1.3.0 (e.g., Rigby et al. 2023). We produce background estimates for two Rubin Deep Drilling Fields[17] (e.g., Ivezić et al. 2019) that are the locations of the NGRST HLWAS Deep tier (ROTAC et al. 2025): COSMOS (Scoville et al. 2007) and XMM-LSS (Pierre et al. 2004). These fields are additionally

[15] https://irsa.ipac.caltech.edu/applications/BackgroundModel
[16] https://jwst-docs.stsci.edu/jwst-other-tools/jwst-backgrounds-tool
[17] https://survey-strategy.lsst.io/baseline/ddf.html

proposed locations for the CASTOR Deep and Ultradeep surveys (Côté et al. 2023). For each field we take the median zodiacal value over the times of the year where the field is in a characteristic spacecraft viewing zone. We then average the output backgrounds for the two fields, producing a final background estimate as a function of wavelength. Background values for the NGRST filters are listed in Table 3.2.

For both CASTOR and NGRST, we adopt projections for read noise and dark current from Cheng et al. (2024a) and Côté et al. (2025) for CASTOR, and from the WFI Technical page for NGRST[18]. These values are listed in Table 3.2. We similarly adopt the respective survey strategies for CASTOR (Côté et al. 2023, 2025; Marshall et al. 2025) and the HLWAS (ROTAC et al. 2025), to determine the number of CCD reads for each survey. We use exposure times equivalent to the Ultradeep survey for CASTOR, and the Ultradeep component within the Deep tier for the NGRST HLWAS (see Table 3.1). The exposure times and depths listed in Table 3.1 for the CASTOR Ultradeep survey are the formal limits. A careful assessment of the in-orbit performance of the telescope will determine systematic factors, but we nonetheless use the exposure times as listed in Table 3.1 for simplicity. For each CASTOR filter this is an exposure time of 50 hr, except the g-band that has a total exposure of 100 hr (Côté et al. 2023, 2025; Marshall et al. 2025). The improved depth of the Ultradeep survey enables us to probe galaxies with levels of star formation that could prove difficult to detect with the Wide survey alone. For the HLWAS filters in the Deep tier this is 4.425 ks for the Z, F, K, and wide W-bands, while the Y, J, and H-bands in the Ultradeep component have total exposure times of 13.917 ks due to the extra (additive) Medium and Deep tiers (ROTAC et al. 2025).

For each filter, we add the contributions from the background and dark current to our PSF-convolved noiseless synthetic images before sampling from a Poisson distribution. We next add the RMS noise values by sampling from a Gaussian where the standard deviation is determined by the number of reads and the read noise. We finally subtract the background to produce mock observations that include the effects of the telescope optical system and noise. We also produce images that describe the uncertainty in these images, from which we can easily compute signal-to-noise ratios. In the bottom row of Figure 3.3, we show our final mock observations after accounting for noise, assuming the exposure times as discussed above.

[18]See footnote 6.

3.2.5 Spectral Energy Distribution Fitting

With our final mock observations produced for our sample of star forming and quenching/quenched galaxies, we produce photometric tables for use with stellar population synthesis fitting software to fit spectral energy distributions (SEDs). To best reproduce the radial profiles used in Paper I, we measure the photometry in 20 equally-spaced (in radius) concentric circular annuli out to five times the effective radius (or half mass radius, as measured in TNG) for each galaxy. We then fit this photometry using the SED fitting code `FAST++`[19] (e.g., Schreiber et al. 2018b), which is an updated C++ version of the original code presented in Kriek et al. (2009).

In our fitting we use the same GALAXEV stellar population synthesis model (Bruzual & Charlot 2003) as was used to produce the mock observations with the updates described above, namely, the standard Padova 1994 evolutionary tracks with the better wavelength (91 Å to 36 mm) and metallicity (0.008 to 0.05) coverage. We use a Chabrier (2003) initial mass function and a Calzetti et al. (2000) dust attenuation law, once again matching the process used when producing the mock observations. We likewise use the characteristic redshift described above to produce the mock observations as a spectroscopic redshift. For our star formation history (SFH), we use a flexible hybrid SFH that is based on a delayed-tau star formation history (e.g., Moustakas et al. 2013; Speagle et al. 2014; Ciesla et al. 2017; Carnall et al. 2019; Johnson et al. 2021) until 100 Myr ago (in lookback time). In the final 100 Myr we assume the same delayed-tau model, but with a multiplicative coefficient, R, that controls the overall scaling (e.g., Fumagalli et al. 2011; Ciesla et al. 2016, 2018, 2021; Schreiber et al. 2018a). Mathematically, this SFH is described as

$$\mathrm{SFR}(t) \propto \begin{cases} R \times (t - t_\mathrm{f}) e^{-(t-t_\mathrm{f})/\tau}, & t_\mathrm{lb} \leqslant \Delta t_\mathrm{SF}, \\ (t - t_\mathrm{f}) e^{-(t-t_\mathrm{f})/\tau}, & t_\mathrm{lb} > \Delta t_\mathrm{SF} \cap t \geqslant t_\mathrm{f}, \\ 0, & t < t_\mathrm{f}, \end{cases} \tag{3.2}$$

where t is time, t_f is the time when the first stars were formed, τ is the e-folding time of the stellar population, t_lb is the lookback time, and $\Delta t_\mathrm{SF} = 100$ Myr. The respective times are related by $t + t_\mathrm{lb} = t_\mathrm{age}$, where t_age is the age of the stellar population, and is related to the formation time by $t_\mathrm{f} + t_\mathrm{age} = t_0$, where t_0 is the current age of the Universe.

We find that this SFH can capture both the broad scale evolution of long-lived stellar populations over long timescales, and also provide the flexibility necessary to describe rapid bursts or truncations in star formation over the most recent 100 Myr epoch, similar to Ciesla et al. (2016, 2018). We list the parameter space investigated by the components

[19] https://github.com/cschreib/fastpp

Table 3.3: Spectral energy distribution fitting model parameters.

Parameter	Minimum	Maximum	Step	$N_{\rm steps}$
$\log(t_{\rm age}/{\rm yr})$	8.8	9.9	0.1	12
$\log(\tau/{\rm yr})$	8	10.5	0.1	26
$\log(R)$	-3	2	0.1	51
$A_{\rm V}$ (mag)	0	1.8	0.1	19
Z	0.008	0.05	irr.	3
z	0.5	0.5		1
stellar populations	Bruzual & Charlot (2003)			
initial mass function	Chabrier (2003)			
dust attenuation	Calzetti et al. (2000)			

of the SED fitting procedure in Table 3.3, while in Figure 3.4, we show example SFHs and resulting SEDs for different combinations of τ and R, where the ultraviolet to near infrared coverage afforded by CASTOR and NGRST enables us to distinguish SEDs with high confidence.

In Figure 3.5, we show two dimensional histograms that compare our SED-fitted parameters with similar values either available directly in TNG, or derivable from TNG. The key parameters (per annulus) we consider are stellar mass, star formation rate, metallicity, and dust. For the metallicity per annulus in TNG, we take the median metallicity across all relevant stellar particles, while for the expected dust used for TNG, we use the average dust value across all pixels that comprise an annulus, using the foreground dust methodology described above. In the following, we take the difference of the fitted values from the expected (i.e. TNG) values, and describe the "recovery" of fitted values using the median difference and the standard deviation (scatter, σ) of the differences.

We find very good recovery when considering stellar mass, where the median difference and scatter are 0.19 dex and 0.23 dex, respectively, when considering all masses, and 0.18 dex and 0.14 dex for $M_* \geqslant 10^9\ M_\odot$. We next find very good recovery for star formation rate, with generally low scatter at higher values of star formation, and increasing scatter as star formation decreases, as expected. The median difference and scatter are -0.13 dex and 0.46 dex across all star formation rates, and -0.11 dex and 0.31 dex above

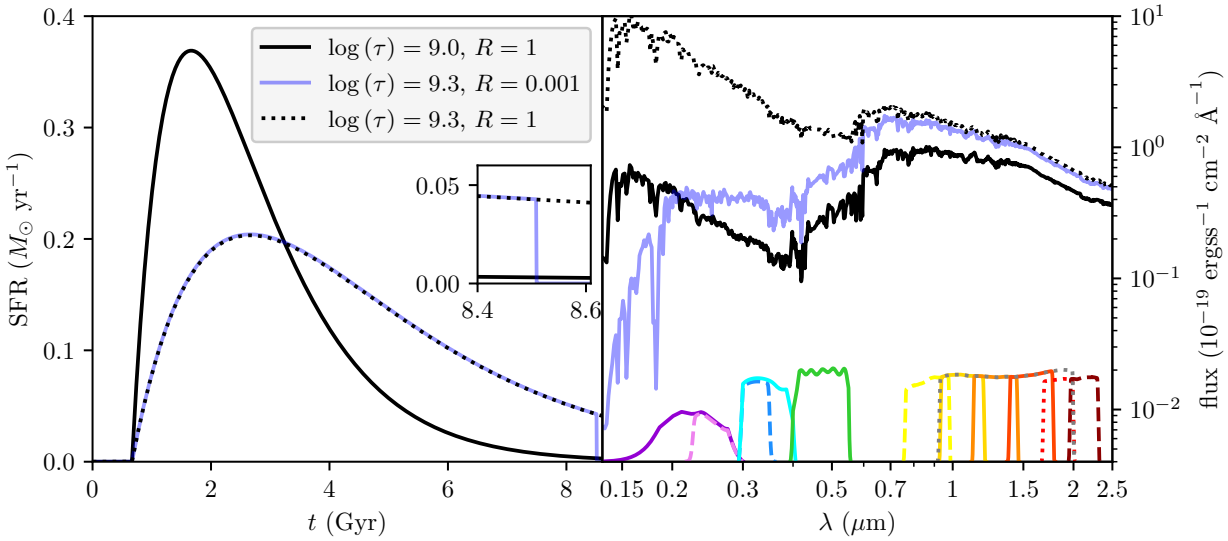


Figure 3.4: Left: example star formation histories for galaxies at $z = 0.5$ showing different combinations of the e-folding time τ and the suppression/burst coefficient R, using the star formation history as described in Equation (3.2). The inset shows a zoom into the last ∼200 Myr, where the final 100 Myr suppression for the star formation history with $\log(\tau/\mathrm{yr}) = 9.3, R = 10^{-3}$ is evident. Right: the resulting spectral energy distributions, color-matched to the star formation histories on the left, shown without the dimming effects of a foreground dust screen. Also shown in the lower part of the panel are the filter transmission curves for CASTOR and NGRST, color-coded the same as in Figure 3.1.

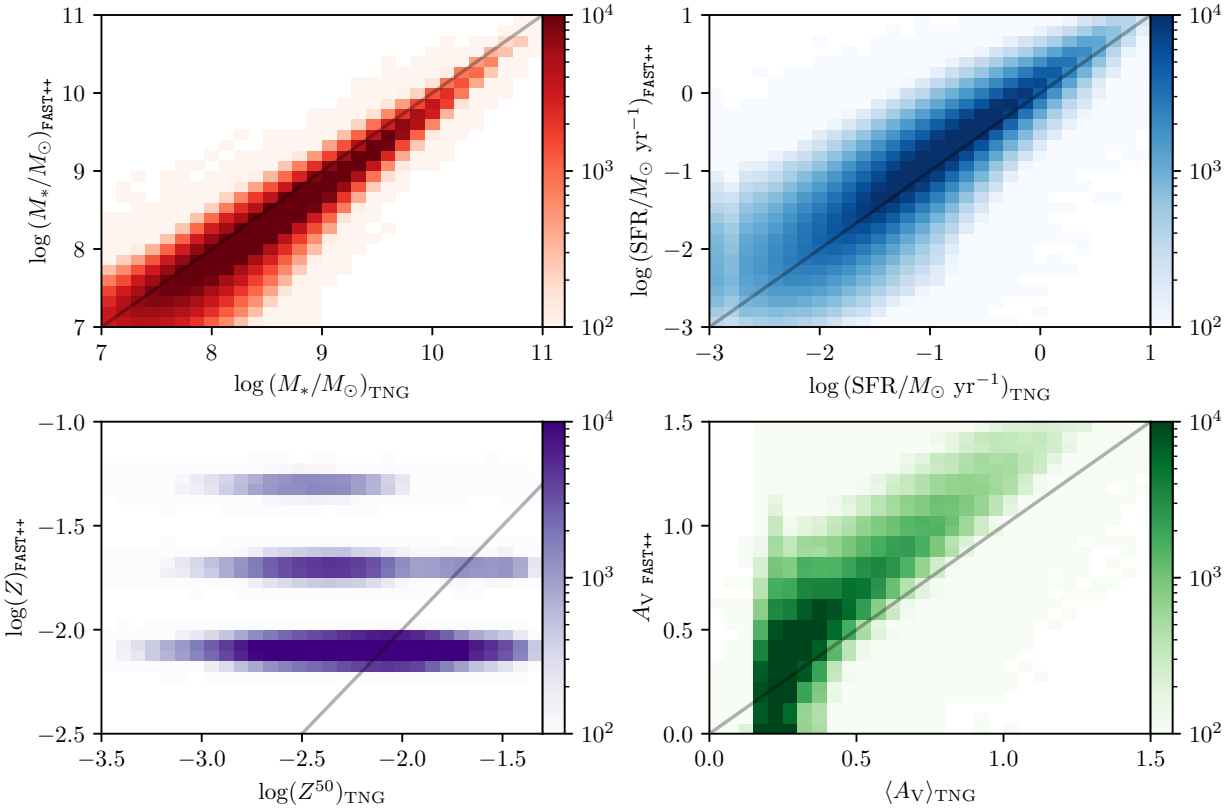


Figure 3.5: Comparisons of the fitted results from `FAST++` as a function of the simulated properties from TNG. Where relevant we show the logarithm for the given quantities, as noted in the axes labels. In all panels, we show a line of equality (gray). For the fitted metallicity and dust from `FAST++`, we perturb the values slightly for visualization purposes.

SFR $\geqslant 0.1\ M_{\odot}\ \mathrm{yr}^{-1}$. These results are encouraging as these parameters are critical for our next steps (see below). For the metallicity, we find poorer recovery of the expected metallicity: median difference and scatter of -0.10 dex and 0.37 dex, respectively, for all metallicities, and 0.21 dex and 0.15 dex above $Z = 0.01$. In general, `FAST++` finds best fit solutions with higher levels of metallicity compared to the median metallicity in TNG. This is partly due to the limited metallicities available in GALAXEV that we use within `FAST++`. We find that small changes in metallicity (i.e. changing from $Z = 0.008$ to $Z = 0.02$, or from $Z = 0.02$ to $Z = 0.05$, etc.) do not produce significant changes in the recovered SED, and additionally, the differences in metallicity are typically compensated with differences in dust. As a consequence, small changes in metallicity produce small variations in the recovered star formation rate at the level of $\leqslant$0.3 dex for >85% of cases. Finally, for the strength of the foreground dust screen, we additionally find good recovery of the average dust screen (as described above), where the median difference and scatter are -0.08 mag and 0.19 mag across all dust values, with a feature at $\langle A_{\mathrm{V}} \rangle_{\mathrm{TNG}} \approx 0.2$ mag where `FAST++` can find a best fit solution that has additional dust. This feature is not seen anywhere else, and is a bias that is apparent at low signal-to-noise ratio (SNR). The nature of our constructed dust profiles mean they often reach $\sim$0.2 mag in the outer regions of a galaxy where signal-to-noise ratio is low. When restricting to annuli with H-band SNR $\geqslant 3$, we find that this feature is significantly diminished and there is reduced scatter as well: 0.16 mag, along with a median difference of -0.09 mag. Further increasing the lower limit on allowed H-band SNR results in decreasing scatter.

As a sanity check, we additionally investigate the integrated values for stellar mass and star formation rate. When comparing the values from the simulation to the fitted results, we find median offsets of 0.18 dex and -0.12 dex, along with $\pm 1\sigma$ ranges of 0.05 dex and 0.07 dex for stellar mass and star formation rate, respectively. These integrated values also function as a consistency check for the fits from the annuli, given that the annuli are fitted independently from the other annuli that comprise a galaxy. If the individual annular fits showed systematically different results we would expect to find larger differences and scatter between the integrated stellar masses and star formation rates.

We use the SED fitting results to produce radial profiles for star formation rate (SFR) and stellar mass, from which we can compute specific star formation rate (sSFR = SFR/M_*) radial profiles. For all galaxies we compute χ^2 by comparing the fitted profiles to the profiles from the simulation for both the (log) stellar mass and star formation rate. These χ^2 distributions are log-normal, with a median χ^2 of $0.13^{+0.30}_{-0.08}$ and $3.1^{+14.0}_{-2.3}$ for stellar mass and star formation rate, respectively. By considering both values simultaneously, we determine an ideal case with optimal recovery (i.e. $\chi^2 \approx 0$) and a typical case where the recovery is close to the median χ^2 value. We show example radial profiles in Figure 3.6, for an ideal

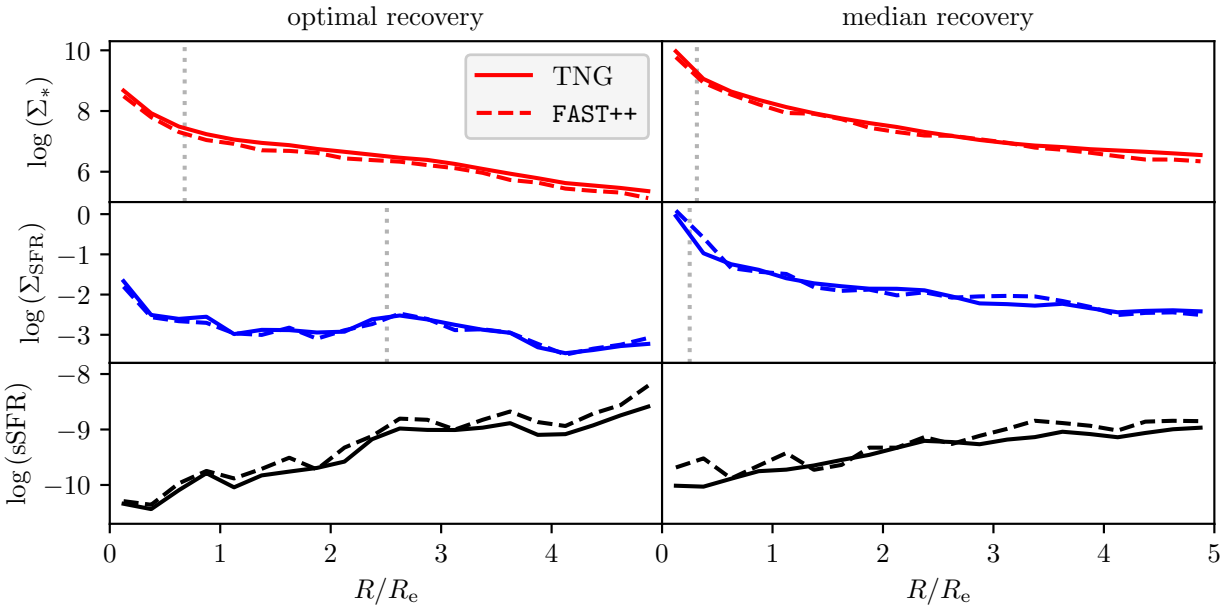


Figure 3.6: Example radial profiles showing recovered properties (dashed lines) when compared to the simulation (solid lines). Moving from top to bottom, we show the stellar mass radial profile (red, units of $M_\odot$ kpc^{-2}), the star formation rate radial profile (blue, units of $M_\odot$ yr^{-1} kpc^{-2}), and the specific star formation rate radial profile (black, units of yr^{-1}). The galaxy on the left illustrates an ideal case where the respective radial profiles have optimal recovery when compared to their simulation counterparts, while the galaxy on the right shows a typical case, where the recovered profiles demonstrate what the median recovery is like. For the stellar mass and star formation rate profiles, we show the radius that encloses half of the stellar mass, or young stellar mass (see Section 3.2.6), respectively, as dotted vertical gray lines.

case (left), and a typical case (right).

3.2.6 Morphological Metrics

In Paper I we showed that the concentration of star formation, the size of the star forming disk relative to the stellar mass disk, and characteristic radii that trace sharp truncations of star formation can effectively discriminate various quenching mechanisms for galaxies undergoing a shut down of star formation, while also distinguishing these galaxies from a control sample of normal star forming galaxies. We refer the reader to Paper I for full details. We include the formulations and brief descriptions for these parameters as used on the simulated galaxies below for completeness:

$$C_{\rm SF}^{\rm TNG} = {\rm SFR}_{<1\ {\rm kpc}}/{\rm SFR}_{\rm total}, \tag{3.3}$$

$$R_{\rm SF}^{\rm TNG} = \log\left(R_{\rm e,\ SF}/R_{\rm e}\right), \tag{3.4}$$

$$R_{\rm inner}^{\rm TNG} = \log[{\rm sSFR}(r)] \leqslant -10.5 \cap {\rm d}({\rm sSFR})/{\rm d}r \geqslant 1, \tag{3.5}$$

$$R_{\rm outer}^{\rm TNG} = \log[{\rm sSFR}(r)] \leqslant -10.5 \cap {\rm d}({\rm sSFR})/{\rm d}r \leqslant -1. \tag{3.6}$$

The concentration of star formation, $C_{\rm SF}^{\rm TNG}$, is measured by comparing the star formation rate within the central 1 kpc relative to the total star formation rate integrated over the entire galaxy, while the size of the star forming disk relative to the stellar mass disk, $R_{\rm SF}^{\rm TNG}$, is determined by comparing the half mass radius (or effective radius) of young (<100 Myr) stellar particles with the effective radius of all stellar particles. The subsequent morphological metrics, the inner and outer truncation radii, $R_{\rm inner}^{\rm TNG}$ and $R_{\rm outer}^{\rm TNG}$, describe sharp truncations or abrupt changes in slope in the specific star formation rate radial profile, and are determined by moving outward from 0 $R_{\rm e}$ to 5 $R_{\rm e}$ for both. The metrics are then the outermost and innermost such radii that satisfy Equation (3.5) and (3.6), respectively.

As described previously, with the above metrics, in Paper I we showed that quenching galaxies in TNG50 have spatial signatures that are consistent with an inside-out quenching signature, an outside-in quenching signature, and an ambiguous signature, for some 361 quenched galaxies out of a possible 1666 galaxies with $M_* \geqslant 10^{9.5}\ M_\odot$.

Metric Adaptations

To best recover observational proxies for these same metrics, we find that we must make adaptations for the metrics. For the concentration of star formation, $C_{\rm SF}^{\texttt{FAST++}}$, we use

the star formation rate radial profile and multiply with the characteristic timescale of 100 Myr to produce a young stellar mass profile. With this young mass profile, we then produce a cumulative young mass profile and interpolate to the radius corresponding to 1 kpc (projected), and compare with the final point (i.e. the outermost; $R \approx 5\ R_{\rm e}$) in the cumulative profile, taking the ratio as the observational proxy $C_{\rm SF}^{\texttt{FAST++}}$. We describe alternative adaptations that we previously explored in Appendix B.1.

For the size of the star forming disk relative to the stellar mass disk, $R_{\rm SF}^{\texttt{FAST++}}$, we similarly produce a cumulative young mass profile following the steps described above, and additionally produce a cumulative stellar mass profile. For both cumulative profiles we interpolate to the point containing fifty percent of the profile, producing proxies for the effective radii for the star formation and stellar mass. For visualization purposes we show examples of these radii as vertical dotted gray lines for the two example galaxies in Figure 3.6. Finally we take the logarithm of the ratio of these radii to determine the observational proxy $R_{\rm SF}^{\texttt{FAST++}}$. We again describe alternative adaptations in Appendix B.1. For both the inner and outer truncation radii, we adopt no adaptations as the specific star formation radial profiles are appropriate for use with the same formulation as used in the simulation, and as described in Paper I.

With the fitted values and uncertainties, we draw 100 realizations for each radial profile (star formation, stellar mass, specific star formation) on a per-galaxy basis, where we assume the fitted values and corresponding uncertainties describe Gaussians. From the realizations of each profile, we compute the relevant observational morphological metrics for every realization, forming a distribution for each morphological metric per galaxy. We take the median across these values as the final value for the morphological metric, in order to incorporate information related to the uncertainties on the fitted values (stellar mass and star formation rate radial profiles). This process creates uncertainties for each metric for each galaxy that are similar to bootstrap errors.

3.3 Results

In Figure 3.7, we show two dimensional histograms that compare the morphological metric observational proxies with the morphological metrics as used in the simulation. As above we take the difference of the observational proxies from the expected (simulation-based) values to describe the recovery using the median difference and scatter.

We find the best recovery when considering the concentration of star formation, $C_{\rm SF}^{\texttt{FAST++}}$, with low scatter at all values. The median difference and scatter are 0.01 and 0.05, respectively, when considering all values, and $<$0.01 and 0.05 when considering $C_{\rm SF} \geqslant 0.5$. We

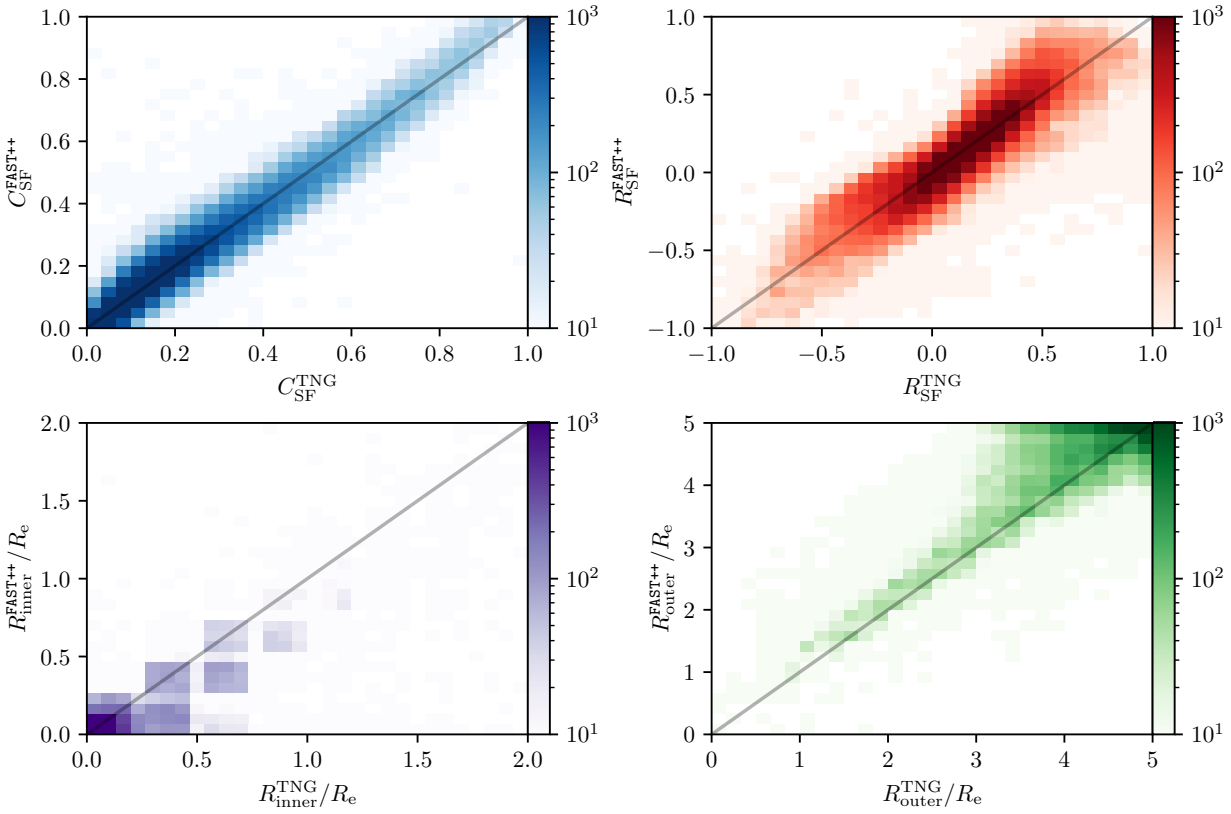


Figure 3.7: Comparisons of the observational proxies of the morphological metrics using the fitted results from `FAST++` as a function of the morphological metrics as computed using TNG. In all panels, we show 2D histograms where the color scale describes the density of points, and we additionally show a line of equality (gray). For the inner truncation radius, we zoom the panel into the relevant region for clarity purposes.

likewise find excellent recovery when considering the size of the star forming disk relative to the stellar mass disk, $R_{\rm SF}^{\texttt{FAST++}}$, with similarly low scatter at all values. The median difference and scatter are 0.01 dex and 0.14 dex, respectively, for all values of $R_{\rm SF}$, and <0.01 dex and 0.13 dex for $R_{\rm SF} \geqslant 0$. For the characteristic radii that trace sharp truncations of star formation, we find, in general, good recovery for both the inner truncation radius $R_{\rm inner}^{\texttt{FAST++}}$, and the outer truncation radius $R_{\rm outer}^{\texttt{FAST++}}$. For the inner truncation radius, away from the line of equality we can find small offsets, particularly at $R_{\rm inner}^{\texttt{FAST++}}/R_{\rm e} \approx 0$, that is commonly found for galaxies with $R_{\rm inner}^{\rm TNG}/R_{\rm e} \lesssim 1$. We do not consider this small offset to be significant, as variations in the recovery of the radial profiles can directly impact the recoverability of the truncation radii. As well, we find that $|R_{\rm inner}^{\rm TNG} - R_{\rm inner}^{\texttt{FAST++}}| \leqslant 0.2\ R_{\rm e}$ for 94% of our sample galaxies. The median difference and scatter are 0.01 and 0.13 for all values of $R_{\rm inner}$, and 0.06 and 0.15 for $R_{\rm inner}/R_{\rm e} > 0$. For the outer truncation radius, we find increasing scatter with increasing radii. This is not unexpected, as the outer regions of every galaxy will, in general, have lower signal-to-noise ratio data, and the recovered fitted radial profiles can be less accurate compared with the inner regions. Nonetheless, we find that our recovered outer truncation radii are accurate to within $\pm 1\ R_{\rm e}$ of $R_{\rm outer}^{\rm TNG}$ for 84% of the sample, where this is largely driven by the scatter at large $R_{\rm outer}$. The median difference and scatter are -0.05 and 0.58, respectively, across all values of $R_{\rm outer}$, but -0.14 and 0.49 for $R_{\rm outer} < 5$.

We next reproduce the analysis as completed in Paper I that considers the feasibility of recovery the quenching population using machine learning classification. Specifically, we use a k-nearest neighbors algorithm (kNN; e.g., Fix & Hodges 1951, 1989; Cover & Hart 1967) that is available in the package `scikit-learn` (Pedregosa et al. 2011), and that uses the k-nearest neighbors to a point in some hyperdimensional parameter space as samples to use for training. From these samples, a prediction can be made on the class or label for the given point of interest (Pedregosa et al. 2011). We use our fitted observational proxies for the four morphological metrics and the true population labels (from Paper I; i.e. star forming, inside-out, and outside-in) as the training set samples, and use the same 70%/30% training/testing split as in Paper I. Following Paper I, we use the three nearest neighbors, weighting the contribution of each neighbor based on their inverse distance, thereby ensuring that closer neighbors will have more influence compared to neighbors that are more distant. We additionally standardize/feature-scale the morphological metric proxies before classification.

In Figure 3.8, we show the results of this analysis, where the progress through the quenching episode is binned into deciles. For each bin, we determine the accuracy of the predicted classification by comparison with the true population, adopted from the simulation and from Paper I. The star forming population (black) is shown alongside the two quenching populations: inside-out (magenta) and outside-in (red). As each star forming

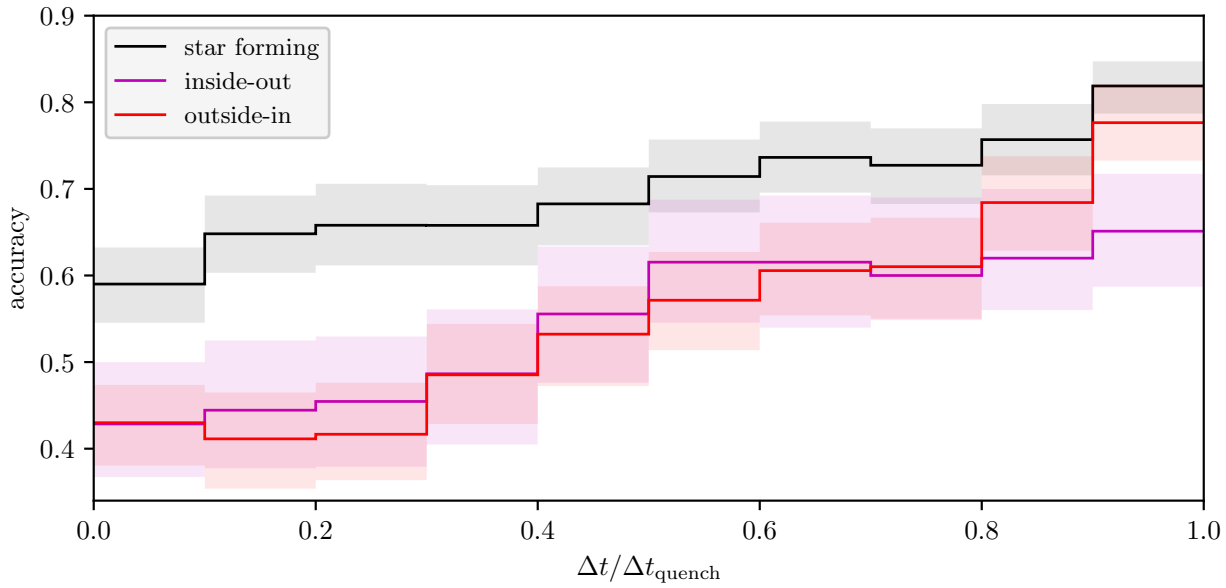


Figure 3.8: The accuracy of the machine learning-based nearest neighbor classification as a function of progress (time) through the quenching episode. For each population (star forming, black; inside-out quenching, magenta; outside-in quenching, red), we show median values across 1000 iterations as solid lines, with the corresponding shaded contours denoting the $\pm 1\sigma$ range. For each iteration, a randomly selected sample of star forming galaxies is chosen to closely number the same number of quenching galaxies (inside-out + outside-in).

galaxy has no quenching episode itself, we adopt the timestamps through the quenching episode from the corresponding quenching galaxy, and refer to this as the "quenching episode" for the star forming galaxy. For each progress bin/decile, we compute 1000 iterations where for each iteration we randomly select a number of star forming galaxies that closely numbers the same number of quenching (inside-out + outside-in) galaxies, and determine the correctly predicted classifications, forming an accuracy value. From these iterations, we then compute a median accuracy (solid lines) along with the corresponding $\pm 1\sigma$ range for each population (shaded regions). In Figure 3.8, we find that the accuracy for the star forming population increases throughout the quenching episode, starting from reasonable levels ($\sim$60%) at early times. Late in the quenching episode, the accuracy for the star forming population increases, exceeding 80%. For the inside-out and outside-in populations, at early times the accuracy is low ($<$0.5), but by moving through the quenching episode, we see a general rise in the accuracy values, where at late times accuracies can exceed $\sim$75% for the outside-in population. These results are similar to those found in Paper I, though slightly lower at all times for all populations. This is not unexpected, given the degradation of the "truth" involved in producing the mock observations. However, even with slightly lower accuracy values at all epochs for the different populations, these results are encouraging and suggest that this methodology can properly classify the different populations, especially at later stages of quenching when the morphological differences are most pronounced.

Finally, we likewise reproduce the analysis as in Paper I that examines the ability for a machine learning classification algorithm to correctly determine the stage at which a quenching galaxy is, when considering a given quenching population alone. In this scheme, we use the same k-nearest neighbors classifier as employed above, and similarly use the three nearest neighbors, once again weighted by inverse distance. We first consider the inside-out population, and use the observational proxies for the morphological metrics and the corresponding values for the progress through the quenching episode as input to the classifier, where we bin the progress through the quenching episode into three epochs: early ($\Delta t/\Delta t_{\rm quench} \leqslant 0.25$), mid-episode ($0.25 < \Delta t/\Delta t_{\rm quench} < 0.75$), and late ($\Delta t/\Delta t_{\rm quench} \geqslant 0.75$). We then predict the progress epoch, and repeat this analysis across 1000 iterations to produce distributions, from which we take the median. We then repeat this analysis considering only the outside-in population.

In Figure 3.9, we show the results of this analysis as histograms where the progress through the quenching episode is binned and the y-axis can be read as frequency. On the left, we show the results for the inside-out population, while on the right, we show the situation for the outside-in quenching galaxies. In the top row, we show the true distributions, while in the bottom row, we show the resulting predicted distributions.

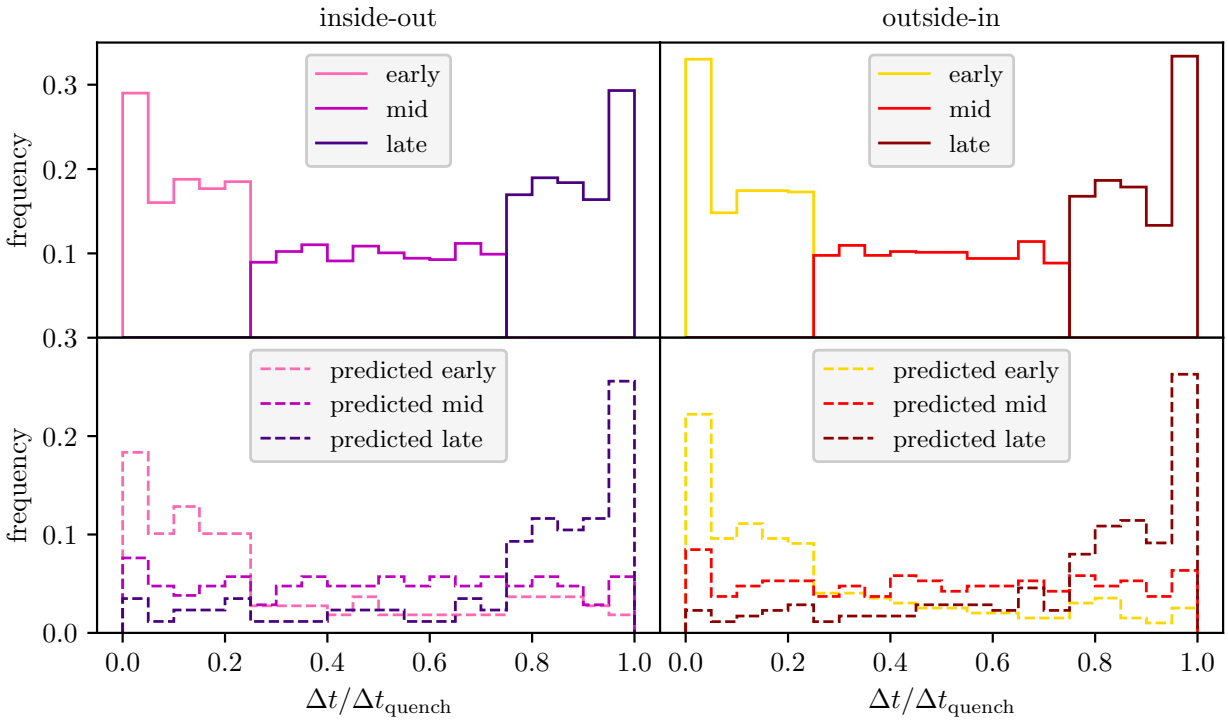


Figure 3.9: True (top) and predicted (bottom) quenching episode progress values for inside-out quenching galaxies (left) and outside-in quenching galaxies (right) using a machine learning-based k-nearest neighbors classifier after 1000 iterations. For each panel, the histograms have been normalized so that the y-axis can be read as frequency of occurrence. In each panel, populations are color coded by quenching episode progress epoch, where lighter colors correspond with earlier epochs and darker colors with later epochs. In the top panels, the boundaries that separate early-episode from mid-episode, and mid-episode from late-episode, are clearly seen at $\Delta t/\Delta t_{\rm quench} = 0.25$ and 0.75, respectively.

Considering first the top panel for the inside-out population, by construction the different epochs are perfectly separated. The true early galaxies have a peak at $\Delta t/\Delta t_{\rm quench} = 0$, and the true late galaxies have a corresponding peak at $\Delta t/\Delta t_{\rm quench} = 1$, where both features are due to the nature of the quenching episode progress definition, and all unique quenching galaxies will have both points by construction. We refer to Paper I, from where we adopt the definition for this episode. In the bottom row we see that the predicted early episode galaxies are peaked at early values with a long tail to later values. Likewise, the predicted late episode galaxies are strongly peaked at late values with a tail to earlier values. The mid-episode galaxies reside in an intermediary space where they show no clear peak, though the mid-episode distribution shows tails into the early- and late-episode epochs as well. From this panel, it is clear that inside-out quenching galaxies that are truly early in their quenching episode are most commonly classified as early, while true late-episode galaxies are most often classified as late. Inside-out galaxies that are in the middle of their quenching episode are most difficult to distinguish, as they can appear similar to mature early-episode galaxies or to immature late-episode galaxies. When next considering the outside-in quenching population, we find an extremely analogous situation as for the inside-out population, where early- and late-episode galaxies are clearly morphologically distinct, but are closer to mid-episode galaxies, as expected. These results strongly resemble those found in Paper I, and once again suggest that this methodology can be successfully applied to mock observations of simulated galaxies to predict the progress through the quenching episode for both inside-out and outside-in quenching galaxies.

3.4 Discussion

We now discuss and interpret our results in the context of other studies presented in the literature, address our research questions as outlined above, and acknowledge limitations of the present work and future directions for follow-up.

By considering our results from the previous section, we are able to arrive at a number of fundamental conclusions based on the current study. The results have shown that by using mock CASTOR and NGRST imaging we are able to recover spatially resolved star formation rates and stellar masses, from which we construct radial profiles. These radial profiles can then be used to distinguish different modes of quenching, using the simple observational metrics introduced in Paper I. When using machine learning classification algorithms on the observational proxies for the morphological metrics, we are able to accurately predict the true population (coming from the simulation) when considering normal star forming galaxies, inside-out quenching galaxies, and outside-in quenching galaxies, es-

pecially at late times. At early times, the quenching galaxies closely resemble star forming galaxies, and the morphological distinction is less clear. Finally, by considering a given quenching population alone, we can accurately distinguish galaxies that are in the early stages of their quenching episode from those that are in the late stages of quenching. Galaxies that are at intermediate stages are more difficult to accurately classify and can be misclassified as either early or late.

As presented in Paper I, these morphological metrics evolve through the quenching episode, which we have recovered here. This evolution has strong distinguishing power, and can be used to well separate these populations. These findings suggest that this methodology is capable of capturing the true underlying population for star forming galaxies and galaxies that are in the stages of quenching, especially at later stages. This result has broad implications for the field of galaxy evolution, where studies can adopt these metrics and apply similar analyses to not only identify quenching galaxies based on morphology alone, but to identify galaxies that likely belong to a given quenching population.

3.4.1 Comparison with Literature Results

In the broader context of studies presented in the literature, we are not aware of any such study that completes a directly similar analysis as presented here. However, there has been much work done on investigating the morphology of quenching galaxies, particularly on how transition galaxies have morphologies intermediate between star forming galaxies and quiescent galaxies (e.g., Mendez et al. 2011; Fang et al. 2013; Almaini et al. 2017; Rodriguez-Gomez et al. 2019; Matharu et al. 2020). In addition, many works in the literature use morphological metrics to identify merging or interacting systems (e.g., Conselice et al. 2000; Conselice 2003; Lotz et al. 2004, 2008; Pawlik et al. 2016; Powell et al. 2017; Sazonova et al. 2024), or even ram pressure-stripped systems, that are a clear sign of environmental factors that can quench galaxies in such dense environments (e.g., Holwerda et al. 2011; Roberts & Parker 2020; Roberts et al. 2021; Roman-Oliveira et al. 2021; Krabbe et al. 2024). Further, studies investigating the morphology of the emitting gas or dust emission have been used to probe the effect of the environment (e.g., Koopmann & Kenney 2004a) and distribution of star formation (e.g., Hall et al. 2018; Díaz-García et al. 2020; Shen et al. 2023) on quenching.

The studies most similar to the work presented here are investigations into the relationship and effect of quenching on galaxy morphology or the correlation between morphology and star formation activity as a function of redshift, to understand the morphological evolution of quenching galaxies (e.g., Wuyts et al. 2011; Bell et al. 2012; Lang et al. 2014;

Bluck et al. 2022). Even still, these investigations consider large populations of quenching galaxies, and often explore the ensemble changes in morphology, given that they are unable to track the evolution of single galaxies given their observational nature.

3.4.2 Surface Brightness Effects

Before considering any applications, we discuss the effects of signal-to-noise ratio (SNR) as well as redshift dependence on the results. As mentioned above (Section 3.2.5), we generally find that with SNR $\gtrsim 3$ for a given annulus, that the stellar mass, star formation rate, metallicity, and dust are close in value to their counterparts as measurable or derivable from the simulation. In particular, we take the difference of the fitted values from the expected TNG values, and use the median difference and scatter for stellar mass (described above, see Section 3.2.5; 0.19 dex and 0.23 dex) and star formation rate (-0.13 dex and 0.46 dex, respectively) as baseline values. Limiting our annuli to those with an H-band SNR $\geqslant 10$, we find that the median difference and scatter for these values decrease: 0.17 dex and 0.20 dex for stellar mass, and -0.12 dex and 0.38 dex for star formation rate, respectively. When further increasing the limiting H-band SNR beyond ten, we find that the median stellar mass difference continues to decrease, as does the scatter. However, arbitrarily increasing the H-band SNR does not oblige the UV-band SNR to likewise increase, and we find no further improvements regarding the median star formation rate difference or scatter with increasing the H-band SNR. However, if we instead consider limiting to UV-band SNR $\geqslant 10$, then we find a median SFR difference of the same -0.12 dex, with a smaller scatter of 0.23 dex. Further increasing the UV-band SNR produces negligible improvements for the median difference, with only small improvements to the scatter.

Beyond individual annular values, the signal-to-noise ratio of the imaging has a direct impact on the quality of the recovered radial profiles. We again consider the H-band SNR, but now investigate the number of annuli with SNR $\geqslant 10$ per galaxy, recalling that each profile has 20 annular bins. We split the entire sample by stellar mass, considering a low-mass population ($M_* < 10^{9.95}\ M_\odot$) and a high-mass population ($M_* \geqslant 10^{9.95}\ M_\odot$). The dividing stellar mass is arbitrary but was chosen to perfectly divide the sample in two. The average and median number of annuli with H-band SNR $\geqslant 10$ for the low-mass sample are 14 and 13, respectively, while the corresponding number of annuli for the high-mass sample are 17.5 and 20, respectively. As expected, the higher mass galaxies have more high SNR annuli than their lower mass counterparts. If we instead consider a threshold SNR cut at $\mathrm{SNR}_{H\text{-band}} \geqslant 3$ to explore this lower SNR regime, we find that the average (median) number of annuli meeting the SNR threshold are 17 (18) and 18.8 (20) for the low- and high-mass populations, respectively. Taken together, these findings suggest that galaxies

that do not have H-band SNR $\geqslant 10$ for all of their annular bins are likely to have SNR $\geqslant 3$ for almost all of their annuli. This is especially true for the high-mass population, and remains true even for the low-mass population as well. This is reassuring given the desire to apply this methodology to different, particularly higher, redshifts.

For the current work, we produced mock CASTOR and NGRST images at a single characteristic intermediate redshift of $z = 0.5$, that is accessible to current and upcoming/ proposed large galaxy surveys (e.g., Euclid, NGRST, LSST, and CASTOR). We additionally produced our mock images assuming the CASTOR Ultradeep survey and the NGRST HLWAS Deep tier and Ultradeep component. Given the effects of surface brightness dimming (e.g., Tolman 1930, 1934; Hubble & Tolman 1935), moving to higher redshift will reduce the signal-to-noise ratio by a factor of $(1 + z)^3$, given the flux density per unit frequency units (i.e. janskys) used here (Whitney et al. 2020). When applied to our existing results at $z = 0.5$ and investigating $z = 1$ as an example case, we find that the average and median number of annuli for the low-mass sample (as described above) with SNR$_{H\text{-band}} \geqslant 3$ are 15 and 15, respectively. The high-mass sample has an average (median) number of annuli with SNR$_{H\text{-band}} \geqslant 3$ of 18 (20). Compared with the situation at $z = 0.5$, this is a modest decrease and mostly strongly affects the low-mass sample, where the number of annuli with SNR$_{H\text{-band}} \geqslant 3$ decreases by two on average/median. Using SNR$_{H\text{-band}} \geqslant 10$ we find average (median) values of 11.3 (11) for the low-mass sample, and 15.8 (16) for the high-mass sample. This represents an inward shift to 4 R_e for the high-mass sample, while being limited to nearly $\sim$3 R_e for the low-mass galaxies. When additionally considering the redshift dependence of angular size, we find that by moving to $z = 1$ from $z = 0.5$, we would obtain mock observations that are 76.4% the size of our fiducial images. Given the size-mass relation (e.g., Shen et al. 2003; van der Wel et al. 2014; Lange et al. 2015; Mowla et al. 2019), this effect would be most detrimental to the lowest mass galaxies, making their mock observations even smaller than presently. Though we expect that the blurring effect of the point spread function is small (see below), images that are comparable in size to the point spread function would become problematic for accurately recovering their stellar mass and star formation rate radial profiles. However, when considering galaxies in our sample with $10^{9.5} \leqslant M_*/M_\odot < 10^{9.75}$, we find that the median mock image size is 101 pixels square at $z = 0.5$, resulting in $z = 1$ images of median size $\sim$77 pixels square, which is sufficient to complete the analysis as described in this work.

These findings suggest that the methodology presented in the current work should be suitable for large galaxy surveys, but that care must be taken when adapting the technique, as lower mass galaxies at higher redshift may not have sufficient signal-to-noise extending to $\sim$5 R_e. However, these findings also indicate that even intermediate mass galaxies ($M_* \approx 10^{10}$ $M_\odot$) should have profiles with sufficient signal-to-noise to carry out the kind

of analysis described above.

3.4.3 Application to Future CASTOR and NGRST Surveys

We now discuss the feasibility of applying our methodology to samples of galaxies in the real Universe, by first considering the expected number of galaxies in the proposed CASTOR surveys and the upcoming NGRST surveys.

In Paper I, we calculated the galaxy stellar mass function for our simulated sample of quenched galaxies, given the total simulation volume of TNG50 ($35/h$ Mpc on a side, where $h = 0.6774$). We additionally compared our calculated stellar mass function with stellar mass functions for local ($0.004 < z < 0.08$) red galaxies (Baldry et al. 2004) in the Sloan Digital Sky Survey (SDSS; York et al. 2000), and local ($z < 0.06$) red galaxies (Baldry et al. 2012) in the Galaxy And Mass Assembly survey (GAMA; Driver et al. 2011). We note that Baldry et al. (2004, 2012) define red galaxies via location in $u - r$ color–magnitude space. In Paper I, we found good agreement between the shapes of our measured galaxy stellar mass function and those of Baldry et al. (2004, 2012), but with a noticeable shift to lower values for all stellar masses for our empirical function, reflecting the more restrictive definition of quenched galaxy. Following this, by fitting a Schechter function (Schechter 1976) to our results from Paper I, we can make predictions on the abundances of quenched galaxies that satisfy our (conservative) definition of a quenched galaxy (see Section 3.2.1).

In the present work we used a single Schechter function of the form (Weigel et al. 2016):

$$\begin{aligned} n_{\rm galaxies} &= \Phi(M) \mathrm{d} \log M \\ &= \ln(10)\ \Phi^*\ e^{-10^{\log M - \log \mathcal{M}^*}} \\ &\quad \times \left(10^{\log M - \log \mathcal{M}^*}\right)^{\alpha+1} \mathrm{d} \log M, \end{aligned} \tag{3.7}$$

where $n_{\rm galaxies}$ is the number density of galaxies in a mass bin of $\mathrm{d} \log M$, M is the stellar mass, $\mathcal{M}^*$ is the characteristic mass that describes the "knee" of the Schechter function, α is the power law slope for masses smaller than $\mathcal{M}^*$, and Φ^* describes the overall normalization and is the number density at $\mathcal{M}^*$. We fit our calculated stellar mass function for galaxies with $9.5 \leqslant \log(M_*/M_\odot) \leqslant 11.75$ with the above, and find best fit values of $\log(\mathcal{M}^*/M_\odot) = 11.22$, $\alpha = -1.21$, and $\Phi^*/10^{-3} = 0.47$. We next consider the area of the CASTOR Ultradeep survey (1 deg^2, that should overlap with the deep NGRST surveys; see above) and representative low- and intermediate-redshifts that will be accessible to CASTOR/NGRST and determine the total volume of space within these redshift shells.

We then calculate expected galaxy counts based on our fitted stellar mass function for our quenched population, and show our findings in Figure 3.10.

Considering Figure 3.10, we expect that more than 99,000 ($\pm$4800) galaxies with $M_* > 10^{9.5}\ M_\odot$ should be within the survey footprint at $z < 1$ assuming a bin width of 0.1 dex, while there should be more than 27,000 ($\pm$2500) galaxies with $M_* > 10^{10.5}\ M_\odot$. This amounts to a large sample of quenching galaxies to investigate and is bolstered by the number of galaxies at higher redshifts, given the large corresponding volume. Indeed, when considering the highest redshift bin in Figure 3.10, we expect to find more than 69,000 ($\pm$3000) of the $M_* > 10^{9.5}\ M_\odot$ galaxies between $z = 0.6$ and $z = 1$, while there should be some 19,000 ($\pm$1500) galaxies with $M_* > 10^{10.5}\ M_\odot$. This subpopulation may prove critical in applying this type of morphological investigation to higher redshift galaxies, given the discussion of signal-to-noise and surface brightness dimming in the proceeding section. At intermediate redshifts like the one considered in this work ($z \approx 0.5$), we anticipate some 22,000 ($\pm$1000) galaxies with $M_* > 10^{9.5}\ M_\odot$, and more than 6000 ($\pm$500) quenching galaxies with $M_* > 10^{10.5}\ M_\odot$. Below $z \approx 0.4$, we expect some 7800 ($\pm$400) galaxies above $M_* = 10^{9.5}\ M_\odot$, and even 2100 ($\pm$200) galaxies at higher stellar masses ($M_* > 10^{10.5}\ M_\odot$). These findings indicate that with surveys such as the CASTOR Ultradeep survey alongside the Ultradeep component of the NGRST HLWAS, many thousands of these types of quenching galaxies should be visible, and should be ideal candidates for applying the type of methodology and morphological study as presented in this work.

Beyond the expected number of galaxies, there should also be several massive ($M > 10^{14}\ M_\odot$) galaxy clusters at the redshifts under consideration. Using similar redshift slices as above and the area of the NGRST HLWAS Deep tier (19.2 deg^2), we expect $\sim$10, $\sim$10, and $\sim$3 clusters for $0 \leqslant z \leqslant 0.2$, $0.2 \leqslant z \leqslant 0.4$, and $0.4 \leqslant z \leqslant 0.6$, respectively (Mak et al. 2011). The cluster galaxies will prove invaluable for understanding the effect of the environment.

In addition to the many thousands of galaxies and handful of massive galaxy clusters that should be within such fields, we also consider the locations of such galaxies in color–color space, a popular technique for separating star forming galaxies from quiescent galaxies (e.g., Strateva et al. 2001; Daddi et al. 2004; Williams et al. 2009; Ilbert et al. 2013). We use the standard UVJ diagram (e.g., Williams et al. 2009) as well as the $FUV{-}V{-}J$ diagram (e.g., Leja et al. 2019b).

In Figure 3.11, we show our findings for the inside-out (left) and outside-in (right) quenching populations, where the top panels show the $FUV{-}V{-}J$ diagrams and the bottom panels show the UVJ diagrams. We bin galaxies by location in color–color space, and bins are color-coded according to the median progress through the quenching episode for

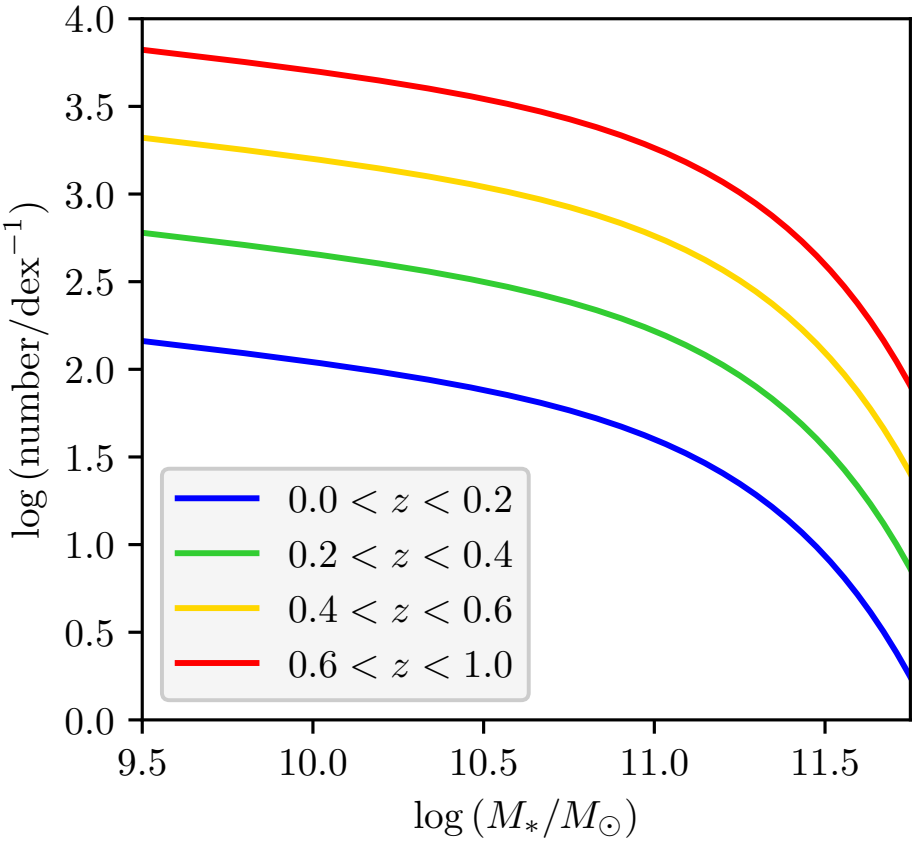


Figure 3.10: Expected number of galaxies per stellar mass bin for different redshift shells, determined using the fitted Schechter function as shown in Equation (3.7) and the total volume of space within each redshift shell. Each redshift shell is shown with distinct colors.

galaxies within that bin. Using the mean progress as compared to the median progress produces negligible differences. Lighter colors correspond to earlier times, and darker colors to later. In the FUV–V–J diagrams we show the division (black dashed line) of Leja et al. (2019b) that best separates star forming galaxies from quiescent galaxies based on a cut in sSFR for galaxies in 3D-HST (Brammer et al. 2012), while in the UVJ diagrams we show similar divisions from Muzzin et al. (2013) for $z < 1$ galaxies from COSMOS/UltraVISTA (McCracken et al. 2012). In all panels, we show unfilled contours that describe the density and location of the respective quenching population with silver. Though we do not show contours that describe the density and location of normal star forming galaxies for visual clarity, these populations peak in density close to the densest region for the quenching populations, but generally with an offset to lower values of V–J and FUV–V (upper panels) or U–V (lower panels), and additionally do not occupy the quiescent region in any panel. Considering Figure 3.11, as we expect, we see that quenching galaxies that are in the early stages of quenching (light colors) generally reside within the locus of the star forming region, but as galaxies begin to, and continue to quench, they move to the quiescent region for each respective diagram (dark colors). These findings indicate that by carefully using such color–color diagrams, one can select quenching galaxies that are further along in their quenching process on the basis of synthesized colors (especially in the passive regions), though we discuss limitations below.

Taken together, these findings demonstrate the feasibility of first finding, then correctly identifying such quenching galaxies within fields such as the CASTOR Ultradeep field and the deep fields of NGRST's HLWAS. We expect that when applied to such datasets, the methodology outlined in this chapter will prove useful for identifying and distinguishing different populations of quenching galaxies to great success, using morphological considerations alone. With such samples available, additional follow-up can focus on various aspects of each population, such as environment (both local and large-scale), interactions and mergers, prevalence and strength of active galactic nucleus feedback, and kinematics, for example.

3.4.4 Limitations and Future Directions

When considering the limitations of the present work, we find a few points worth commenting on, and discuss each as it arises chronologically in the methodology presented above.

The first concerns how representative simulated galaxies are of real galaxies. Previous studies have proposed that the active galactic nuclei feedback model is strong in TNG

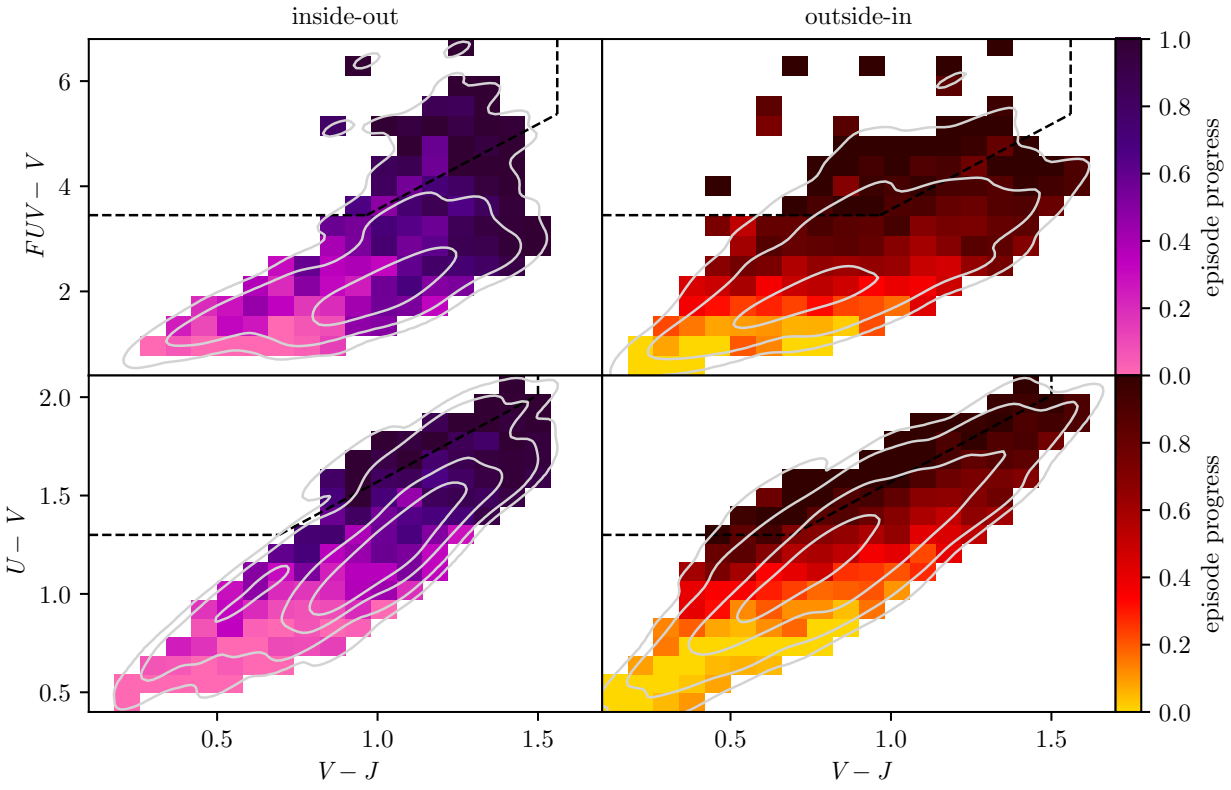


Figure 3.11: Color–color diagrams showing the median progress through the quenching episode per bin for inside-out (left) and outside-in (right) quenching galaxies, color-coded by progress through the quenching episode. Earlier times in the quenching episode are colored more lightly (pink and gold, respectively), while those later in the quenching episode are darker (dark magenta and dark red, respectively). The upper panels show the location of galaxies in $FUV-V$, $V-J$ color space, while the lower panels show the standard UVJ diagram. In the upper panels, we additionally show the division of Leja et al. (2019b) for star forming and quiescent galaxies (black dashed line) while the lower panels show the division of Muzzin et al. (2013). In all panels, contours that denote the location and density of the respective quenching population are shown in silver.

when compared to observations (e.g., Terrazas et al. 2020; Donnari et al. 2021b; Voit et al. 2024; Wright et al. 2024), resulting in inside-out quenching that is pronounced compared to observations. Additional work has suggested that environmental gas removal may be overly strong (e.g., Diemer et al. 2019; Stevens et al. 2019, 2021, 2023), resulting in dramatic outside-in quenching. Therefore applying the morphological metrics to real galaxies must be done carefully, especially when considering $R_{\rm inner}$ and $R_{\rm outer}$. However, these metrics are less important compared to $C_{\rm SF}$ and $R_{\rm SF}$ when identifying quenching galaxies (see Appendix D of Paper I).

The next concern is the similarity between the prescription for generating the mock observations, the GALAXEV pipeline described above, and the setup for the SED fitting process, as both the GALAXEV pipeline and the SED fitting code `FAST++` rely on the models of Bruzual & Charlot (2003). In reality, galaxies have complex star formation histories and metallicity and dust distributions, which means that our ability to recover star formation rates here is a best-case scenario. Even so, one could instead generate the mock observations using different libraries such as Starburst99 (Leitherer et al. 1999), those of Maraston (2005), FSPS (Conroy et al. 2009; Conroy & Gunn 2010), or BPASS (Eldridge et al. 2017), or using different pipelines (e.g., Fortuni et al. 2023; Janulewicz & Cui 2025; Lovell et al. 2025; Zhou et al. 2025; Roper et al. 2026), though the use of these alternative libraries or pipelines is outside the scope of this work.

Beyond these initial considerations, the next principle consideration is an improvement regarding a more physically realistic dust setup. A natural approach is to use a full radiative transfer code such as SKIRT (Baes et al. 2003, 2011; Baes & Camps 2015; Camps & Baes 2015, 2020) or POWDERDAY (Narayanan et al. 2021). Indeed, many papers in the literature have used SKIRT with TNG galaxies for various investigations (e.g., Huertas-Company et al. 2019; Whitney et al. 2021; Trčka et al. 2022; Costantin et al. 2023; Baes et al. 2024; Bottrell et al. 2024). However, following Rodriguez-Gomez et al. (2019) and their considerations, in this work we took a simpler approach by using a foreground dust screen based on Calzetti et al. (2000). As mentioned above, we did initially pursue using SKIRT but found for our purposes that the results were not sufficiently different to warrant the extra computation. In either event, the effect of dust will most strongly affect young stellar populations, and when considering galaxies in the later stages of quenching this effect should be small. An additional minor consideration is the blurring effect of the point spread function when producing our mock observations. Given the PSF used above (FWHM of $0\farcs15$), we expect the effect of the PSF should be small but non-negligible (see, for example, the last row of Figure 3.3). Indeed, when we compared our SED-fitted values for stellar mass and star formation rate that are based on the PSF-convolved mock observations with their simulation-based counterparts (Figure 3.5), we found small differences that are not

systematic, further supporting our conclusion that the effect of the PSF is small. However, this is based on the PSF used in the current work, and similar conclusions may not hold for observations with a much larger point spread function.

Alternative approaches or implementations in the current work could include using a sophisticated SED fitter with Bayesian inference (like BAGPIPES; Carnall et al. 2018, 2019), or even a fitter that can use or uses fully non-parametric star formation histories, like PROSPECTOR (Leja et al. 2017, 2019a; Johnson et al. 2021) or Dense Basis (Iyer & Gawiser 2017; Iyer et al. 2019), respectively. In the present work, we have opted to use the relatively simpler and more straight forward grid fitter `FAST++`, and we do not anticipate that using an alternative SED fitter should have a large effect on our presented results. In fact, though we have used a relatively simpler fitter, we have still recovered key parameters such as stellar mass, star formation rate, metallicity, and dust, when comparing the fitted results with similar properties within the simulation (see Figure 3.5 and surrounding discussion).

An additional approach is to do full pixel-by-pixel SED fitting and subsequently bin the fitted results together to recover the annular bins. We briefly explored this option but issues with low surface brightness and low signal-to-noise ratio data (especially in the outskirts of many galaxies) prevented this approach from accurately recovering the expected star formation history parameters like stellar mass and star formation rate. Beyond pixel-by-pixel fitting, one could also first perform voronoi tesselation using such software (e.g., VorBin; Cappellari & Copin 2003), and subsequently complete SED fitting on the voronoi-binned photometry, or alternatively use a fitter that accounts for the similarity in the shapes of the SEDs when binning pixels together (e.g., `piXedfit`; Abdurro'uf et al. 2021). Both of these latter approaches hold promise, though the issue with the low signal-to-noise data in outer regions will still provide some difficulties. In either event, such approaches are outside the scope of this work.

When considering the ability to identify quenching galaxies in a representative sample from a large galaxy survey, we face challenges due to the dominant star forming population. The ability to find "needles in a haystack" using our approach needs further refinement, and may require additional information beyond the morphological metrics alone. For instance, including the integrated star formation rate or the distance from the star forming main sequence could prove vital for properly identifying quenching galaxies. Indeed, in the above analysis where we showed we can distinguish different populations of quenching galaxies from normal star forming galaxies, we used a balanced sample of star forming galaxies and quenching (inside-out + outside-in) galaxies. We note that in the star forming region of the UVJ diagrams above (Figure 3.11), the star forming population will be heavily dominant, so we expect that our recovery would have many false positives, thus proving difficult to truly identify early quenching galaxies. However, Figure 3.11 does show that among a

UVJ-passive sample there is minimal contamination from star forming galaxies, and we can therefore apply this technique to identify later inside-out and outside-in quenching galaxies.

Regarding future directions, the next step is to apply the methodology outlined here to populations of galaxies in the real Universe. To facilitate this, we will aim to use high spatial resolution data with deep integration times. In order to make additional comparisons across various cosmic environments, the ideal dataset would include observations of both field and cluster galaxies, as well as those in intermediate density environments between these two extremes. Promising datasets to consider include large campaigns completed with HST, given the excellent spatial resolution and wavelength coverage afforded by such observations. Programs such as the Cosmic Assembly Near-infrared Deep Extragalactic Legacy Survey (CANDELS; Grogin et al. 2011; Koekemoer et al. 2011), the Cluster Lensing And Supernova Survey with Hubble (CLASH; Postman et al. 2012), the Hubble Frontier Fields (HFF; Lotz et al. 2017), the Reionization Lensing Cluster Survey (RELICS; Coe et al. 2019), or the COSMOS Legacy UV-Optical Treasury Campaign with Hubble (CLUTCH; HST program ID 17802; PI: J. Kartaltepe) would satisfy some or all of the above desirable criteria. This is the scope of our next investigation in Chapter 4.

3.5 Summary and Conclusion

In this chapter, we have investigated the feasibility of recovering morphological metrics for mock observations of galaxies present in the high resolution simulation TNG50. We first adopt the sample of 361 quenched galaxies from TNG50 as initially determined in Paper I, and consider all time points within each galaxies' respective quenching episode, alongside normal star forming galaxies that have a similar stellar mass as the quenching galaxies. We arrive at a sample of 5365 quenching galaxies and 64,128 unique star forming galaxies. For each galaxy, we produce mock images that are based on proposed or upcoming galaxy surveys with CASTOR (Côté et al. 2025) and NGRST (ROTAC et al. 2025), and bin the photometry into concentric annuli. Our main findings are as follows:

1. By employing a hybridized parametric star formation history (e.g., Figure 3.4) that can capture both the broad scale evolution of long-lived stellar populations and provide flexibility for bursts or truncations of star formation over short timescales (100 Myr), we are able to accurately recover key parameters like stellar mass and star formation rate when compared to the corresponding simulation parameters (Figure 3.5).

2. By reconstructing radial profiles of stellar mass and star formation rate through the use of the annular fits, we are able to produce radial profiles that are close matches to their simulation counterparts, where the accuracy of the recovered profile depends on surface brightness and signal-to-noise ratio (Figure 3.6).
3. Using the recovered radial profiles and the adapted observational proxies for the morphological metrics, the concentration of star formation and the ratio of disk sizes are most accurately recovered, while the characteristic radii that trace sharp truncations in star formation are slightly more difficult to recover, especially $R_{\rm outer}$ (Figure 3.7).
4. Machine learning classification algorithms can separate star forming galaxies from quenching galaxies, and further, can separate inside-out quenching galaxies from outside-in quenching galaxies, especially at later times in the quenching episode, when the morphology of these different populations of galaxies is most distinct (Figure 3.8).
5. Machine learning classifications can also be used well to predict the epoch of progress through the quenching episode for the two main populations of quenching galaxies, when each is considered independently. Early-episode galaxies are most easily distinguished from late-episode galaxies, while mid-episode galaxies can be more difficult to distinguish given their resemblance to mature early galaxies and immature late galaxies (Figure 3.9).

These findings as described above suggest that the observational adaptations of the morphological metrics can be successfully applied to mock observations of simulated galaxies, and can be used to recover information about the intrinsic state of quenching galaxies based only on morphology alone. Caution must be taken when applying such metrics to galaxies with properties (e.g., surface brightness, angular size, etc.) that differ from those in the simulated images considered here. Our next step in this series of investigations is to apply our findings to observations of galaxies in the real Universe, using high spatial resolution observations with deep integration times. We will consider galaxies in dense environments and those residing in the field to enable comparisons between different populations, thereby investigating the effect of the environment.

Chapter 4

Identifying and Distinguishing Quenching Galaxies with Spatially Resolved Star Formation in the Hubble Frontier Fields

4.1 Introduction

Galaxy quenching is a central unsolved problem in the field of astrophysics (e.g., Tumlinson et al. 2017), given the complex physical mechanisms and associated length- and timescales involved. Understanding how galaxies quench, or have their star formation suppressed, is key to understanding galaxy evolution, as quenching is the primary driver for galaxies moving from the star forming blue cloud to the red sequence (Bell et al. 2004; Faber et al. 2007; Martin et al. 2007). Much progress has been made in our understanding of quenching, including considerations related to the roles of mass and environment for low-mass and high-mass galaxies (e.g., Peng et al. 2010; Zhang et al. 2021), for central and satellite galaxies (e.g., Peng et al. 2012; Davies et al. 2019; Bluck et al. 2020b), as well as at low- (e.g., Gómez et al. 2003; Peng et al. 2010; Wetzel et al. 2012) and high-redshift (e.g., Muzzin et al. 2012; Balogh et al. 2016; Nantais et al. 2017; van der Burg et al. 2020). However, there remain results that are currently unexplained by formation and evolutionary paradigms, including the large body of evidence of massive quenched galaxies at early cosmic times ($z > 3$; e.g., Carnall et al. 2023, 2024; Alberts et al. 2024; Bluck et al. 2024; Nanayakkara et al. 2024) as discovered with the James Webb Space Telescope

(JWST; Gardner et al. 2006, 2023), for example. Other poorly constrained phenomena include timescales associated with quenching (e.g., Schawinski et al. 2014; Smethurst et al. 2015; Bremer et al. 2018; Phillipps et al. 2019), as well as the role of mergers (e.g., Birnboim et al. 2007; Peng et al. 2014; Ellison et al. 2022) and the circumgalactic medium (e.g., Davies et al. 2020). Though large cosmological simulations have recently proved integral in better understanding and testing different quenching mechanisms (e.g., Donnari et al. 2019, 2021b,a; Wright et al. 2019; Nelson et al. 2021; Wang et al. 2023b; Lawlor-Forsyth et al. 2026b), large observational samples of quenched galaxies remain crucial as input for subsequent generations of simulations (e.g., Vogelsberger et al. 2020; Crain & van de Voort 2023; Feldmann & Bieri 2026), as well as for studying quenching in the real Universe.

Quenching mechanisms in the literature are commonly divided into internal and external regimes (e.g., Peng et al. 2010, 2012), where the internal mechanisms are driven by the galaxy itself, while the external mechanisms consider the environment and surroundings in which a galaxy is embedded. Internal mechanisms include the effects of active galactic nucleus feedback (e.g., Di Matteo et al. 2005; Bower et al. 2006; Croton et al. 2006; McNamara & Nulsen 2007, 2012; Fabian 2012), stellar feedback (e.g., Cole et al. 2000; Su et al. 2019), and secular evolution from disk and bar instabilities (e.g., Martig et al. 2009; Gensior et al. 2020). External quenching mechanisms driven by the environment include ram pressure stripping (e.g., Gunn & Gott 1972; Abadi et al. 1999; Poggianti et al. 2017; Boselli et al. 2022) and starvation/strangulation (e.g., Larson et al. 1980; Kawata & Mulchaey 2008; Peng et al. 2015). Gravitational harassment is also a potential driver for environmental quenching (e.g., Moore et al. 1996, 1998, 1999), in addition to mergers (e.g., Ellison et al. 2022, 2024), though the extent to which mergers are important for galaxy quenching remains debated (e.g., Birnboim et al. 2007; Moustakas et al. 2013; Weigel et al. 2017; Quai et al. 2021).

As well, it has been suggested that quenching can partially be described using a model where high-mass central galaxies quench first in the center, before this quenching proceeds outward, producing an "inside-out" signature (e.g., Tacchella et al. 2015, 2016, 2018; González Delgado et al. 2016; Abdurro'uf & Akiyama 2018; Belfiore et al. 2018; Rowlands et al. 2018b; Guo et al. 2019; Lin et al. 2019; Bluck et al. 2020b; Nelson et al. 2021; McDonough et al. 2023, 2025; Lawlor-Forsyth et al. 2026b). Conversely, for low-mass satellite galaxies, quenching first occurs on the outskirts of the galaxy and proceeds inward, producing an "outside-in" signature (e.g., Bluck et al. 2020b; Wang et al. 2023b; McDonough et al. 2025; Lawlor-Forsyth et al. 2026b). These inside-out and outside-in explanations chiefly consider feedback from an active galactic nucleus for the former, and environmental effects such as ram pressure stripping and starvation/strangulation for the latter (e.g., Bluck et al. 2020b; Nelson et al. 2021; McDonough et al. 2025). However, such a model

does not account for other objects such as high-mass satellites, though it has been suggested that these objects are predominantly quenching inside-out, with minor outside-in effects (e.g., Bluck et al. 2020b; McDonough et al. 2025).

In addition, many of the physical mechanisms that quench galaxies act over a range of length- (e.g., Peng et al. 2010; Bluck et al. 2020a) and timescales (e.g., Wetzel et al. 2013; Schawinski et al. 2014; Wright et al. 2019), highlighting the need for detailed observations that can spatially resolve the young stellar populations that are suppressed through the act of quenching. Naturally, integral field unit observations have therefore been used to study quenching phenomena (e.g., González Delgado et al. 2015; Tacchella et al. 2015; Goddard et al. 2017; Schaefer et al. 2017; Sánchez et al. 2018; Lin et al. 2019). As well, studies using Hα to directly probe the extent of star formation over short timescales have been completed (e.g., Koopmann & Kenney 2004a,b; Gavazzi et al. 2013; Matharu et al. 2021, 2022). Beyond these investigations, studies leveraging high-resolution photometry with spectral energy distribution fitting have been completed (e.g., Abdurro'uf & Akiyama 2018; Morselli et al. 2019; Nelson et al. 2021; Abdurro'uf et al. 2022a, 2023; Tan et al. 2022). These spatially resolved photometric studies are compelling, given their scalability and the number of galaxies that will be observed in large-scale surveys in the coming years (e.g., LSST Science Collaboration et al. 2009; Euclid Collaboration et al. 2022; Roman Observations Time Allocation Committee & Core Community Survey Definition Committees 2025).

Thus, to better understand the nature of quenching, the various physical mechanisms, evolutionary pathways, and associated length- and timescales, samples of spatially resolved galaxies are critical. We then require a way to efficiently identify different quenching modes in such observations, to first facilitate direct investigations, and secondly to highlight cases for future follow-up. In Lawlor-Forsyth et al. (2026b, hereafter Paper I), we used the highest resolution run of the IllustrisTNG simulation (Nelson et al. 2018; Pillepich et al. 2018a; Springel et al. 2018), TNG50 (Nelson et al. 2019b; Pillepich et al. 2019), to develop observationally motivated metrics that are based on the spatial distribution and morphology of star formation in the simulated galaxies. We showed that these metrics can be used to distinguish simulated quenching galaxies from simulated star forming galaxies on the basis of morphology alone. Further, we showed that simulated quenching galaxies can be additionally separated into different quenching evolutionary signatures, including an inside-out morphological signature, and an outside-in signature. We found that the inside-out population was often higher mass field galaxies, while the outside-in population was commonly lower mass satellite galaxies. These populations additionally experienced different quenching timescales, where the outside-in population took $\sim$ 1.5 Gyr to quench, while the inside-out class took $\sim$2.5 Gyr.

In Paper I, we limited our analysis to simulated galaxies, leaving an application to real galaxies for future work. However, it was still necessary to evaluate how these metrics, as developed for simulated galaxies, would perform on real data. As an intermediate step, in Lawlor-Forsyth et al. (2026a, hereafter Paper II), we created mock observations of the simulated galaxies from Paper I. These mock observations were designed to mimic data from upcoming galaxy surveys (Côté et al. 2025; Roman Observations Time Allocation Committee & Core Community Survey Definition Committees 2025), but are comparable in quality and wavelength coverage to those available with the Hubble Space Telescope (HST). By performing spatially resolved spectral energy distribution fitting, we found that we were able to recover key parameters like stellar mass and star formation rate. Using these physical quantities, we were then able to recover the morphological metrics as determined in Paper I to high fidelity, suggesting that this methodology was mature for application to samples of real galaxies. Therefore, we now look to apply our procedure to galaxies in the Hubble Frontier Fields (Lotz et al. 2017) to identify and investigate different quenching signatures.

This chapter is structured as follows: in Section 4.2, we describe the available high-resolution processed data, and data preparation and reduction steps. In Section 4.3, we describe our analysis procedure for extracting physical measurements, as well as the morphological metrics as introduced in Paper I and Paper II for classifying our sample into different quenching evolutionary signatures. In Section 4.4, we present our results, in particular focusing on the differences between the quenching populations when considering stellar mass and environmental influences like location in phase space and phase space-inferred infall time. In Section 4.5, we discuss our results, the implications of our findings for upcoming large-scale galaxy surveys, and next steps. Finally, in Section 4.6, we present our summary and conclusion.

Throughout this chapter we adopt a flat ΛCDM cosmology that is consistent with the TNG simulation (Weinberger et al. 2017; Pillepich et al. 2018b), based on the Planck intermediate results (Planck Collaboration et al. 2016): $H_0 = 67.74$ km s^{-1} Mpc^{-1}, $\Omega_\mathrm{m} = 0.3089$, $\Omega_\Lambda = 0.6911$, and $\Omega_\mathrm{b} = 0.0486$.

4.2 Data

4.2.1 Hubble Frontier Fields

The Hubble Frontier Fields[1,2] (Lotz et al. 2017) are a sample of six massive lensing clusters drawn from the Abell catalog (Abell 1958; Abell et al. 1989) and the Massive Cluster Survey (Ebeling et al. 2001, 2007): Abell 2744, Abell S1063 (also known as RXC J2248.7−4431), Abell 370, MACS J0416.1−2403 (hereafter MACS J0416), MACS J0717.5+3745 (hereafter MACS J0717), and MACS J1149.5+2223 (hereafter MACS J1149). The survey includes imaging of each cluster along with adjacent (or parallel) fields offset from the clusters (Lotz et al. 2017). Properties of the clusters and their parallel fields, including the cluster redshifts, velocity dispersions, and radii within which the mean density of the cluster halo is 200 times the critical density of the Universe at the time of observation, R_{200}, are tabulated in Table 4.1.

[1] https://frontierfields.org
[2] https://archive.stsci.edu/prepds/frontier

Table 4.1: The Hubble Frontier Fields.

Cluster	RA[a] (h m s)	Dec[a] (d m s)	$z_{\rm clus}$	σ (km s^{-1})	R_{200} (Mpc)	Parallel RA[a] (h m s)	Parallel Dec[a] (d m s)	Reference
Abell 2744	00:14:21.2	−30:23:50.1	0.308	1497	2.35	00:13:53.6	−30:22:54.3	z [1], σ [2], R_{200} [3]
Abell S1063[b]	22:48:44.4	−44:31:48.5	0.348	1840	2.38	22:49:17.7	−44:32:43.8	z [4, 5], σ [6], R_{200} [7]
Abell 370	02:39:52.9	−01:34:36.5	0.375	1170	2.66	02:40:13.4	−01:37:32.8	z [8, 9], σ [10], R_{200} [11]
MACS J0416.1−2403	04:16:08.9	−24:04:28.7	0.396	955	1.89	04:16:33.1	−24:06:48.7	z [12, 13], σ [14], R_{200} [7]
MACS J1149.5+2223	11:49:36.3	+22:23:58.1	0.543	1840	2.35	11:49:40.5	+22:18:02.3	z [15], σ [15], R_{200} [7]
MACS J0717.5+3745	07:17:34.0	+37:44:49.0	0.545	1660	2.36	07:17:17.0	+37:49:47.3	z [15, 16], σ [15], R_{200} [7]

References. — 1. Couch & Newell (1984); 2. Owers et al. (2011); 3. Medezinski et al. (2016); 4. Böhringer et al. (2004); 5. Gómez et al. (2012); 6. Gómez et al. (2012); 7. Umetsu et al. (2016); 8. Kristian et al. (1978); 9. Struble & Rood (1991); 10. Dressler et al. (1999); 11. Umetsu et al. (2011); 12. Mann & Ebeling (2012); 13. Ebeling et al. (2014); 14. Jauzac et al. (2014); 15. Ebeling et al. (2007); 16. Edge et al. (2003)

[a] Cluster and parallel positions taken from Lotz et al. (2017).

[b] Also known as RXC J2248.7−4431.

The Frontier Fields program builds on the success of the Cluster Lensing And Supernova Survey with Hubble (CLASH; Postman et al. 2012), that included four of the six selected clusters. At the time of their completion, the Frontier Fields represented some of the deepest observations ever conducted with HST, totaling more than 840 orbits across the six clusters and their parallel fields, reaching 5σ point source depths of $\sim$29 $\mathrm{mag_{AB}}$ in the parallel fields (Lotz et al. 2017). Over small portions of the cluster pointings, the imaging reaches depths of $\sim$30–33 $\mathrm{mag_{AB}}$ given the lensing nature of the clusters (Lotz et al. 2017). As part of the original survey design, each of the clusters and their parallel fields were imaged with seven filters using the Advanced Camera for Surveys Wide Field Channel (ACS/WFC; e.g., Stark et al. 2025) and the Wide Field Camera 3 near-infrared channel (WFC3/IR; e.g., Marinelli et al. 2025). In addition to this, imaging in up to ten other filters[3] exists from the Wide Field Camera 3 ultraviolet channel (WFC3/UVIS; e.g., Postman et al. 2012) and other ACS/WFC and WFC3/IR observations (e.g., Shipley et al. 2018). Filter transmission curves for the complete filter set are shown in Figure 4.1. In Appendix C.1 we tabulate the filter set available per cluster/parallel field.

Following the work completed by Lotz et al. (2017), several groups including the AstroDeep team[4,5,6] (Castellano et al. 2016; Merlin et al. 2016; Di Criscienzo et al. 2017; Bradač et al. 2019), the DeepSpace team (Shipley et al. 2018; Nedkova et al. 2021), and those involved in the Beyond Ultra-deep Frontier Fields and Legacy Observations[7] (BUFFALO; Steinhardt et al. 2020; Niemiec et al. 2023; Pagul et al. 2024) have produced extended photometric and redshift catalogs for the Frontier Fields. More recently, several groups have completed large programs targeting the Frontier Fields with JWST (e.g., Treu et al. 2022; Willott et al. 2022; Windhorst et al. 2023; Bezanson et al. 2024; Suess et al. 2024; Atek et al. 2025; Sarrouh et al. 2026); we discuss these additional data in Section 4.5.

[3]We use *UV*, *UV'*, *u*, *C*, *B*, *g*, *V*, V^{W}, *r*, *i*, *I*, *z*, *Y*, Y^{W}, *J*, *JH*, and *H* to refer to the HST F225W, F275W, F336W, F390W, F435W, F475W, F555W, F606W, F625W, F775W, F814W, F850LP, F105W, F110W, F125W, F140W, and F160W filters, respectively, consistent with Marinelli et al. (2025) and Stark et al. (2025).

[4]http://www.astrodeep.eu/frontier-fields

[5]http://www.astrodeep.eu/ff34

[6]https://archive.stsci.edu/hlsp/hffcatalogs

[7]https://archive.stsci.edu/hlsp/buffalo

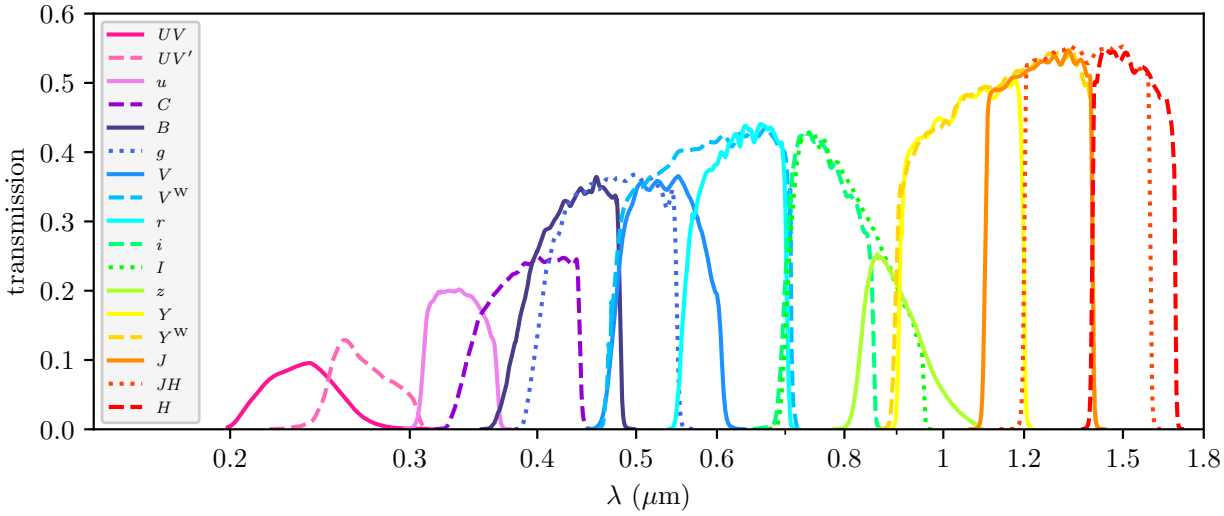


Figure 4.1: HST filter transmission curves for the Frontier Fields bands across all clusters and parallel fields. Not every band is available for every pointing (i.e. cluster or parallel field). See Appendix C.1 for full details regarding which filters are available per pointing.

DeepSpace Catalogs and Data

The DeepSpace team[8] (Shipley et al. 2018; Nedkova et al. 2021) have produced science-ready mosaics for the Frontier Fields, including the clusters and their parallel fields, and associated multi-wavelength photometric, redshift, and stellar population synthesis catalogs. This dataset is described fully in Shipley et al. (2018). These catalogs include photometric fluxes and uncertainties, photometric redshifts determined with EAzY (Brammer et al. 2008), spectroscopic redshifts from the literature when available, flux radii that describe circular apertures that enclose half the total flux (determined with SExtractor; Bertin & Arnouts 1996), and various quality flags. These catalogs also include physical parameters like integrated stellar mass and star formation rate (SFR) derived through spectral energy distribution (SED) fitting using FAST (Kriek et al. 2009). In their SED fitting, Shipley et al. (2018) employed a simple delayed exponential (or "tau") model for their star formation history along with a fixed solar metallicity ($Z = 0.02$).

The imaging available from Shipley et al. (2018) includes science-ready images from the rest-frame ultraviolet to the near-infrared in up to 17 filters, as noted above, where bright cluster galaxies have been modeled and removed. These bright cluster galaxies (bCGs) are distinct from the traditional use of the term "brightest cluster galaxy" in the literature to describe the brightest galaxy (commonly a massive elliptical; e.g., De Lucia & Blaizot 2007; Von Der Linden et al. 2007; Lauer et al. 2014) within a cluster. In practice, these bright cluster galaxies all have extended profiles that dominate the majority of light and that will contaminate other nearby galaxies (Shipley et al. 2018). The bCG-subtracted science-ready imaging has been point spread function (PSF) matched to the H-band imaging, as the H-band photometry is the longest wavelength imaging available in the dataset and has the largest PSF (full width at half maximum $\sim 0\farcs147$[9]) of the available filters. We show cutouts of the bCG-subtracted PSF-matched science-ready imaging for an example galaxy in Figure 4.2. In addition, weight maps, bCG models, point spread functions, and segmentation maps are also available (Shipley et al. 2018). However, though the bCG-subtracted images are science-ready for non-bCG galaxies, science-ready images including the bCGs are not available, and so must be prepared separately. As well, the weight maps and bCG model images are not PSF-matched. Further, the segmentation maps were similarly produced after the bCGs had been removed (Shipley et al. 2018), and so bCG-only segmentation maps must also be generated.

[8] https://cosmos.phy.tufts.edu/~danilo/HFF/Home.html

[9] https://hst-docs.stsci.edu/wfc3ihb/chapter-7-ir-imaging-with-wfc3/7-6-ir-optical-performance

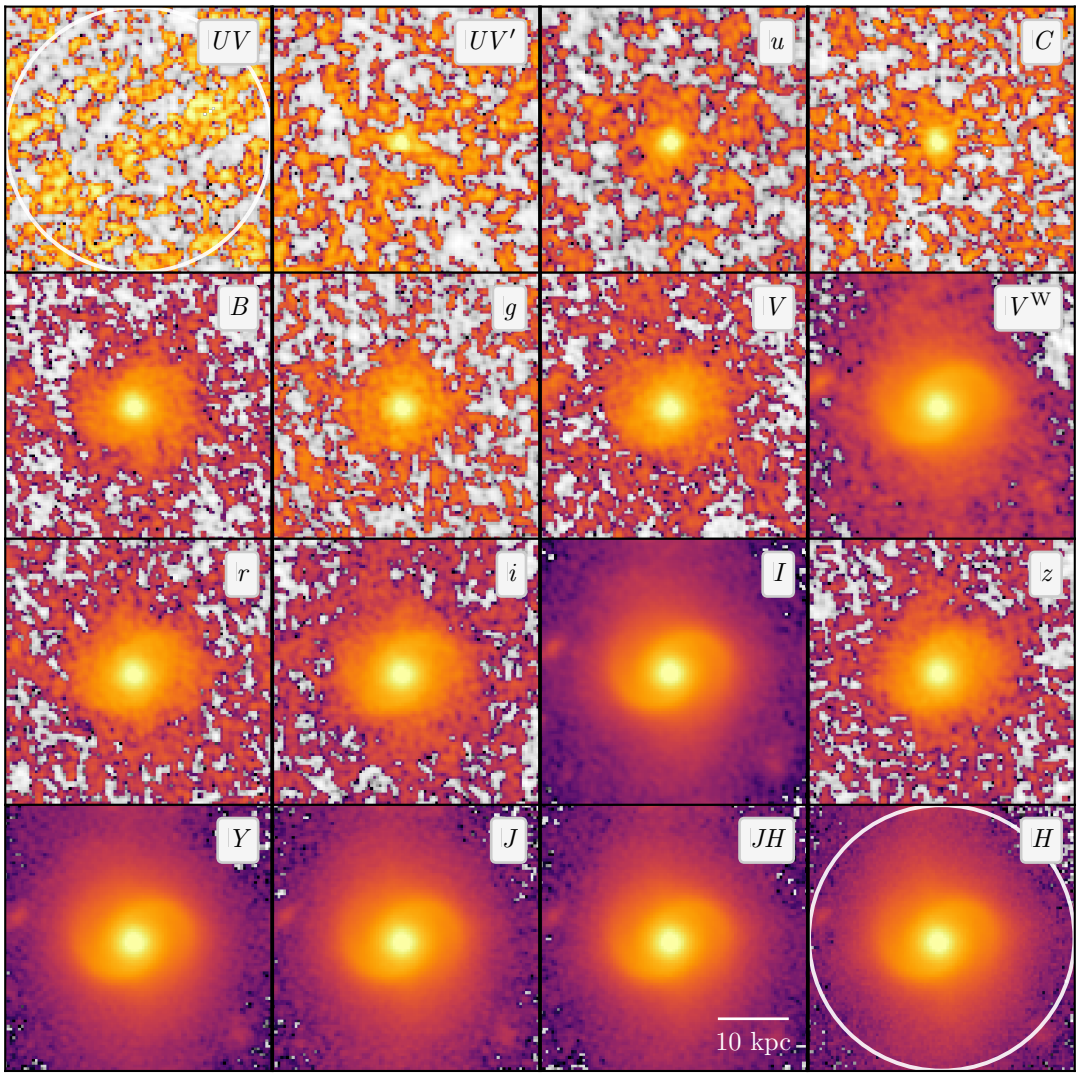


Figure 4.2: Example cutouts for galaxy ID 5809 in MACS J0717 ($z_{\rm spec} = 0.546$, $M_* = 10^{10.44}\ M_\odot$, SFR $= 0.36\ M_\odot\ {\rm yr}^{-1}$). In each cutout, pixels with negative values are shown in a log-grayscale, while positive pixels are shown in color with a log scale. Each cutout uses a per-cutout scaling, meaning a universal scaling for all cutouts has not been applied. Cutouts are arranged according to increasing wavelength, from left to right and top to bottom. Each cutout is labeled in the top right corner with the corresponding filter. Inscribed within the *UV*- and *H*-band cutouts are circles denoting the extent of 5 $R_{\rm e}$ (see Section 4.3.1), for visual reference. A scale bar is additionally shown in the *JH*-band image. This galaxy does not have any quality flag issues per band (Section 4.3.1).

4.2.2 Data Preparation

In order to prepare the data for analysis, we begin by PSF-matching the weight (inverse variance) maps and model images through convolution with the available point spread function images, as described earlier (i.e., Shipley et al. 2018). As above, we PSF-match to the H-band image per pointing. We additionally determine dimensionless correction/calibration factors for subsequent use when determining the per-pixel noise with the variance maps. We determine these correction factors by calculating the empirically-measured root mean square (RMS) value of blank sky regions in the science images and the predicted RMS from the PSF-matched variance maps for the same pixels. The ratio of the empirical RMS to the predicted RMS provides the global correction factor that will be used subsequently to rescale the variance maps on a per filter, per pointing basis.

Given that the imaging produced by Shipley et al. (2018) includes bCG-subtracted science-ready images for the non-bCGs, we must account for the bCGs themselves, as they are not present in the existing segmentation maps. We therefore generate segmentation maps for the bCGs from the model fits to these galaxies, in order to maintain consistency with how the photometry of fainter galaxies is defined. Since detection and segmentation algorithms require a noise threshold, we add random Gaussian noise based on the median RMS from the inverse weight map to the model images.

With these noisy model images, we next create co-added bCG-only detection images for segmentation mapping. We follow Shipley et al. (2018) and use the I-, Y-, J-, JH-, and H-bands to create the bCG-only detection image by first combining the model images into a mean mosaic, weighted by the corresponding weight images. We additionally create a total weight image by combining the weight images (Shipley et al. 2018). We produce a final bCG model detection image by dividing the weighted mean mosaic with the total error image, which is the square root of the total weight image, consistent with Shipley et al. (2018). Using these detection images we then produce bCG-only segmentation maps with `Photutils` (Bradley et al. 2025).

When creating photometric cutouts, we start with the PSF-matched bCG-subtracted science imaging for non-bCGs, and add the PSF-matched noiseless bCG models for bCGs. We create noise cutouts from the science images and PSF-matched variance images according to

$$\text{noise} = \sqrt{\text{var} \times \text{corr}^2 + \text{sci}/t_{\text{exp}}},$$

where "var" is the variance map, "corr" is the correction/calibration as determined above, "sci" is the science image, and t_{exp} is the exposure time, in seconds. We additionally

create segmentation map cutouts for all galaxies and bCG-segmentation map cutouts for the bCGs.

4.2.3 Sample Selection

We next determine a galaxy sample, including bCGs, based on the existing catalogs from Shipley et al. (2018). We begin by creating a single catalog that includes every source in the Shipley et al. (2018) catalogs, numbering 81,315 sources. We additionally adopt select attributes from the catalogs of Pagul et al. (2024), who produced photometric and redshift catalogs for the Frontier Fields through the BUFFALO survey (Steinhardt et al. 2020). We adopt the spectroscopic redshifts as tabulated by Pagul et al. (2024), collected from the literature (Lagattuta et al. 2019; Treu et al. 2022) and the NASA/IPAC Extragalactic Database[10].

We then form an initial sample based on redshift, integrated stellar mass, and quality flags, as described further below. Given our analysis requirements, forming a final galaxy sample requires multiple steps that will be outlined below. Where available, we use spectroscopic redshifts in place of photometric redshifts, but use photometric redshifts otherwise. We select galaxies with $M_* \geqslant 10^8\ M_\odot$, $z \geqslant 0.14$, and $z \leqslant 0.67$ from the Shipley et al. (2018) catalogs. The redshift limits are chosen to span the range of redshifts for cluster members, as defined in Section 4.2.3. We additionally require $\delta z < 0.2$ for the sources that only have photometric redshifts. Further, we require that all sources have `use_phot = 1` (as introduced by Skelton et al. 2014), that selects "OK" sources in a consistent fashion (Shipley et al. 2018). We also require that the sources are extended (`star_flag` $\neq$ `1`) and that there are no problematic H-band flags (`flag_F160W` $\geqslant$ `0`), that ensures that the H-band photometry is not aligned with a region where the weight map is negative (Shipley et al. 2018). These combined cuts produce a catalog of 3643 sources.

Next, we impose an H-band signal-to-noise ratio (SNR) floor for the sources. Our analysis is based on photometry in 20 circular annuli, as described in Section 4.3.1. We require H-band SNR $\geqslant 3$ for all annuli to ensure that reliable stellar mass estimates can be determined when completing SED fitting (see below), resulting in 1987 sources. Furthermore, we conservatively exclude another 48 sources that are partially masked (Shipley et al. 2018) or have other visually identified artifacts (as described in Section 4.3.1), resulting in a sample of 1939 galaxies. We also exclude 502 galaxies with low integrated SFR as determined from SED fits to the total photometry (see Section 4.3.2), and thus have a sample of 1437

[10] https://ned.ipac.caltech.edu

galaxies. We consider these 1437 galaxies to be our non-quenched "primary" sample, while the 502 galaxies with low global SFR forms our quenched extended sample (see below).

Redshift Limits

We seek global limits on redshift, informed by redshift limits for each cluster. In their work, Shipley et al. (2018) compared the scatter (σ) of photometric redshifts with known spectroscopic redshifts on a per pointing (i.e. cluster/parallel field) basis, producing normalized median absolute deviations ($\sigma_{\rm NMAD}$; Beers et al. 1990) per cluster. Motivated by Morishita et al. (2017), we follow Nedkova et al. (2021) and adopt the normalized median absolute deviations for the Frontier Fields, and use these as redshift limits to determine the global upper and lower limits for the sample. These limits are defined as (Nedkova et al. 2021):

$$3 \times \sigma_{\rm NMAD} \geqslant \frac{z \pm z_{\rm clus}}{1 + z_{\rm clus}},$$

where z represents the global upper/lower redshifts of the sample, depending on the sign in the numerator. Using the lowest redshift cluster and its associated normalized median absolute deviation (Abell 2744; $z_{\rm clus} = 0.308$, $\sigma_{\rm NMAD} = 0.043$), we find $z_{\rm min} = 0.14$. Following a similar procedure for the highest redshift cluster/normalized median absolute deviation combination (MACS J1149; $z_{\rm clus} = 0.543$, $\sigma_{\rm NMAD} = 0.027$), we find $z_{\rm max} = 0.67$. We use these redshift limits to select our sample as described above. For galaxies beyond the extent of each respective cluster (see Section 4.2.3), these limits additionally define a foreground and background field sample.

Phase Space-inferred Infall Time

Recently, Dou & Yu (2025) completed an investigation evaluating the performance of caustics (Regos & Geller 1989; Diaferio & Geller 1997; Diaferio 1999) and relations from the literature (e.g., Rhee et al. 2017; Pasquali et al. 2019), in order to accurately estimate the infall times for simulated galaxies into clusters at $z = 0$. They used the TNG300 simulation (Nelson et al. 2019a) of the IllustrisTNG simulation suite (.e.g, Nelson et al. 2018; Pillepich et al. 2018a; Springel et al. 2018), and created phase space diagrams (e.g., Diaferio 1999; Mahajan et al. 2011) in order to determine the infall time (e.g., Oman et al. 2013; Oman & Hudson 2016; Rhee et al. 2017; Pasquali et al. 2019) for cluster galaxies based on location in phase space by considering their orbital histories (Dou & Yu 2025). We adopt the method of Dou & Yu (2025), but extend their analysis to all snapshots with

redshifts similar to the Frontier Fields ($0.14 < z < 0.67$), and additionally use the TNG-Cluster simulation (Nelson et al. 2024) in combination with the TNG300 simulation. We provide an overview of the Dou & Yu (2025) method in Appendix C.2 for completeness. We follow a similar procedure to determine infall times for our Frontier Fields cluster galaxies, based on redshift and location in phase space.

With these considerations, we separate our Frontier Fields galaxies into a cluster and field sample based on position in phase space. We define cluster galaxies to be those with $R_{2D} \leqslant 0.5R_{200}$ and $|V_{LoS}| \leqslant 3.5\sigma_{LoS}$. Of the 1437 galaxies that comprise the non-quenched sample (those with $SFR_{total} \geqslant 10^{-3}\ M_{\odot}\ yr^{-1}$), we find that 723 galaxies reside in clusters, while the remaining 714 reside in the field. Of the 502 galaxies that make up the quenched extended sample, 338 reside in clusters and 164 reside in the field.

4.3 Methodology

4.3.1 Annular Photometry and Visual Inspection

Following Paper II, for all galaxies in the sample, we bin the photometry into 20 equally spaced (linearly in radius) concentric circular annuli out to five times the effective radius (also known as the half flux radius), R_e (as tabulated by Shipley et al. 2018), for each galaxy. When determining the flux and noise for each annulus, we use the segmentation maps as a mask, where only pixels associated with the galaxy of interest or the background are included in the flux/noise determination. For bCGs, the bCG-only segmentation maps are similarly used as a mask. Total noise per annulus is determined by considering the individual noise contributions per pixel, added in quadrature.

We inspect every cutout and compare with the tabulated quality flags from the Shipley et al. (2018) catalogs to ensure that our annular bins do not overlap with masked regions and that there are no remaining artifacts. The masked regions in the science-ready images come directly from Shipley et al. (2018), where they masked regions associated with bright stars causing halos and diffraction spikes, bCG model residuals, satellite trails, cosmic rays, and pixels with negative weights (Shipley et al. 2018). Where our cutout photometry does overlap with a masked region, we record flags for the affected filters in such cases, to ensure that these bands are not used subsequently when performing SED fitting. After visually inspecting every cutout and recording "use" flags for the sources, we find that 48 sources have partially masked regions on their H-band cutouts, such that performing our analysis is not possible for these sources. We remove these and subsequently follow the procedure

as described above to determine the annular photometry across the 20 radial bins for each source. As stated in Section 4.2.3, our final sample satisfying all our requirements is 1939 galaxies.

4.3.2 Spectral Energy Distribution Fitting

We are ultimately interested in applying the morphological metrics introduced in Paper I and refined in Paper II to our sample of galaxies. We will discuss our morphological metrics in further detail below (Section 4.3.4), but for now, this requirement means that our sample galaxies must have non-negligible levels of star formation. To determine this, we perform SED fitting on the integrated photometry. Further, we require SED-fitted physical parameters for the annuli in order to calculate our morphological metrics. We now describe our SED fitting procedure.

We perform spectral energy distribution (SED) fitting using the SED fitting code `FAST++`[11] (e.g., Schreiber et al. 2018b,a). `FAST++` is an updated C++ version of the original SED fitting code `FAST`, as introduced in Kriek et al. (2009). Each parameter involved in describing the star formation history for a target galaxy, from which the spectral energy distribution is derived, is defined on a fixed grid (Schreiber et al. 2018b). Adopting the core characteristics of the SED fitting setup from Paper II, we use the standard and preferred GALAXEV simple stellar population synthesis model (Bruzual & Charlot 2003), that employ the "Padova 1994 library" evolutionary tracks (Alongi et al. 1993; Bressan et al. 1993; Fagotto et al. 1994a,b,c; Girardi et al. 1996). We use the updated 2016[12] version of the GALAXEV code to achieve better wavelength and metallicity coverage compared to earlier releases: 221 unequally spaced ages from 0 to 20 Gyr; 2023 unequally spaced wavelengths from 91 Å to 36 mm; and a total of seven unequally spaced metallicities between 10^{-4} and 0.1 (Bruzual & Charlot 2003). We additionally use a Chabrier (2003) initial mass function along with the dust attenuation law from Calzetti et al. (2000).

We adopt the star formation history as described in Paper II: a flexible hybrid star formation history that builds on a delayed-tau model (e.g., Moustakas et al. 2013; Speagle et al. 2014; Ciesla et al. 2017; Carnall et al. 2019; Johnson et al. 2021) until the final 100 Myr. At this point, a multiplicative factor, R, is introduced, that controls the overall scaling of the star formation history over those final 100 Myr (e.g., Fumagalli et al. 2011; Ciesla et al. 2016, 2018, 2021; Schreiber et al. 2018a). This star formation history has the

[11] https://github.com/cschreib/fastpp
[12] https://www.bruzual.org/bc03/Updated_version_2016

Table 4.2: Spectral energy distribution fitting model parameters.

Parameter	Minimum	Maximum	Step	$N_{\rm steps}$
$\log(t_{\rm age}/{\rm yr})$	8.5	10.0	0.1	16
$\log(\tau/{\rm yr})$	8.0	9.9	0.1	20
$\log(R)$	-3.0	2.0	0.1	51
$A_{\rm V}$ (mag)	0.0	1.8	0.1	19
Z	0.008	0.05	irr.	3
z	0.1	0.73	0.01	64
stellar populations	Bruzual & Charlot (2003)			
initial mass function	Chabrier (2003)			
dust attenuation	Calzetti et al. (2000)			

form (Paper II)

$$\mathrm{SFR}(t) \propto \begin{cases} R \times (t - t_{\rm f}) e^{-(t-t_{\rm f})/\tau}, & t_{\rm lb} \leqslant \Delta t_{\rm SF}, \\ (t - t_{\rm f}) e^{-(t-t_{\rm f})/\tau}, & t_{\rm lb} > \Delta t_{\rm SF} \cap t \geqslant t_{\rm f}, \\ 0, & t < t_{\rm f}, \end{cases} \tag{4.1}$$

where t is time, $t_{\rm f}$ is the formation time of the first stars, τ is the e-folding time of the stellar population, $t_{\rm lb}$ is the lookback time, and $\Delta t_{\rm SF} = 100$ Myr. The various times included in the star formation history are related: $t + t_{\rm lb} = t_{\rm age}$, where $t_{\rm age}$ is the age of the stellar population. Further, $t_{\rm f} + t_{\rm age} = t_0$, where t_0 is the current age of the Universe (Paper II). As was described in Paper II, this star formation history can capture broad evolution of old stellar populations over long timescales while also being capable of describing rapid truncations or bursts of star formation over the defined 100 Myr timescale. We list the parameter grid for all components of the SED fitting procedure in Table 4.2, noting that the entire parameter space encompasses 59,535,360 possible combinations. We additionally show example star formation histories and their resulting SEDs for specific values available in our fitting prescription in Figure 4.3.

We then perform SED fitting on the integrated photometry for the non-quenched+ quenched sample of 1939 galaxies, ensuring that we use the results of our visual inspection and the corresponding "use" flags to properly mask any requisite filters from the SED

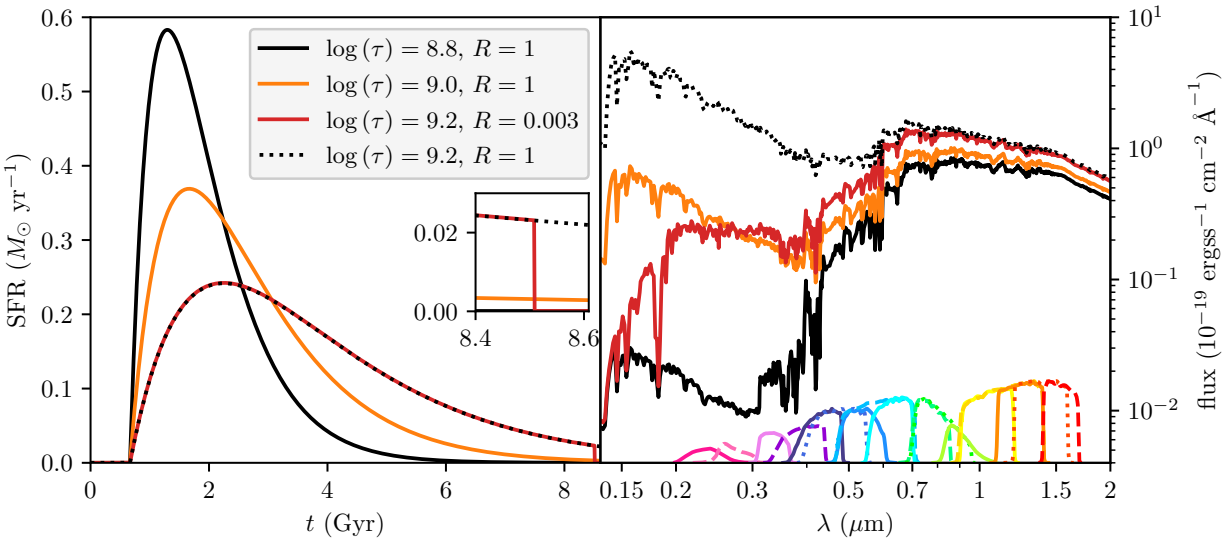


Figure 4.3: Left: example star formation histories drawn from the parameter space investigated during the integrated fits. These star formation histories show different combinations of the multiplicative factor R (that controls the overall scaling of the star formation history in the final 100 Myr) and the e-folding time τ. The inset shows a zoom into the last 200 Myr to better highlight the effect of R. Right: the resulting spectral energy distributions for the star formation histories on the left, using the same color scheme, without the effect of any foreground dust (i.e. $A_V = 0$). We also show the filter transmission curves for the filter set available in the Frontier Fields.

fitting analysis. Consistently with Paper I and Paper II, we choose to define SFR as the star formation rate averaged over the final 100 Myr, as it is the timescale that is well traced by ultraviolet and infrared observations (Kennicutt 1998a; Madau & Dickinson 2014), and is the duration associated with "recent" galaxy-wide star formation (Calzetti 2013).

After completing the integrated SED fitting, we find that 502 of the 1939 galaxies have integrated $\mathrm{SFR}_{\mathrm{total}} < 10^{-3}\ M_{\odot}\ \mathrm{yr}^{-1}$. Based on findings from Paper II, integrated star formation rates below this level become unreliable for subsequent annular analysis, and so we set a threshold requirement at $10^{-3}\ M_{\odot}\ \mathrm{yr}^{-1}$ for our galaxies. Removing these 502 galaxies, we arrive at a sample of 1437 galaxies with $M_{*} \geqslant 10^{8}\ M_{\odot}$ and $\mathrm{SFR} \geqslant 10^{-3}\ M_{\odot}\ \mathrm{yr}^{-1}$ that we apply our morphological metrics to (Section 4.3.4). We additionally find that we recover well the stellar mass estimates from the integrated fitting of Shipley et al. (2018), where the median difference and scatter between their integrated stellar masses and our estimates are 0.01 dex and 0.16 dex, respectively.

We next complete SED fitting on the annular photometry (from Section 4.3.1), producing physical properties for the 20 radial bins per galaxy, specifically stellar mass and SFR radial profiles. We show an example set of these profiles in Figure 4.4. As well, we sum across our stellar mass and SFR profiles on a per galaxy basis, and compare with the integrated fits determined above. With the summed annular properties, we recover well the integrated stellar masses and SFRs. The median difference and scatter between the integrated stellar masses and the annular sums are -0.01 dex and 0.10 dex, respectively, while the difference and scatter for SFR are -0.05 dex and 0.30 dex, respectively.

4.3.3 Star Forming Main Sequence Determination

We determine each galaxy's location relative to the star forming main sequence (SFMS; e.g., Brinchmann et al. 2004; Peng et al. 2010; Speagle et al. 2014). Given our sample size, as well as how the Frontier Fields target clusters that host galaxies with lower specific star formation rates (e.g., Balogh et al. 1997, 1998, 1999, 2000; Lewis et al. 2002; Gómez et al. 2003; Kauffmann et al. 2004), in order to better sample and define the SFMS for normal star forming galaxies at these redshifts, we use the results from the recent data release of the Cosmic Evolution Survey (COSMOS; Scoville et al. 2007), that includes JWST data: COSMOS-Web[13] (Casey et al. 2023; Shuntov et al. 2025). We describe the data and SED fitting procedure employed by the COSMOS-Web team (Arango-Toro et al. 2025; Shuntov et al. 2025) in Appendix C.3.

[13] https://cosmos2025.iap.fr

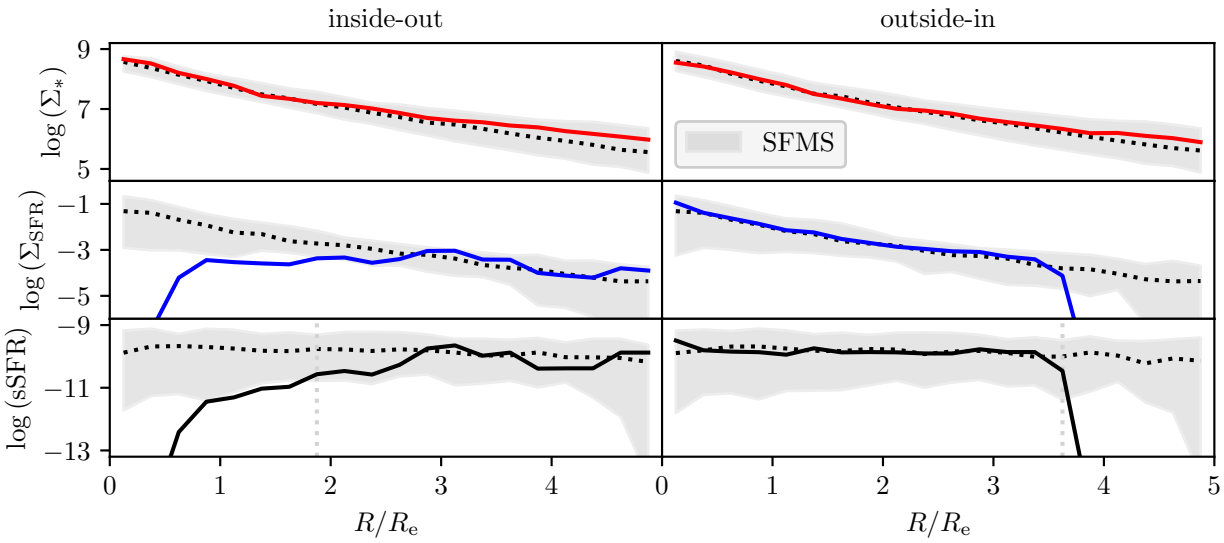


Figure 4.4: Example radial profiles for different types of galaxies using the classification scheme from Section 4.3.4. An inside-out quenching galaxy (left) is shown along with an outside-in quenching galaxy (right). Moving from top to bottom, these panels show the stellar mass radial profile (red, units of $M_\odot$ kpc^{-2}), the SFR radial profile (blue, units of $M_\odot$ yr^{-1} kpc^{-2}), and finally the sSFR radial profile (black, units of yr^{-1}). In all panels we show the median (black dotted line) and $\pm 1\sigma$ spread (gray shaded region) for the radial profiles, based on using comparison SFMS galaxies (Section 4.3.3) that are close in stellar mass: $\Delta \log (M_*/M_\odot) \leqslant 0.1$ dex. In the bottom panels, we denote the location of $R_{\rm inner}$ (left) and $R_{\rm outer}$ (right) with a vertical light gray dotted line, respectively.

As in Paper I, we adopt the "ridge line method" (e.g., Pillepich et al. 2019; Donnari et al. 2021b,a; Bottrell et al. 2024) introduced in Donnari et al. (2019) to determine the location of the SFMS. In this method, the COSMOS-Web galaxies are binned by stellar mass and the median (log) SFR is then calculated for each bin (Donnari et al. 2019). We use a bin width of 0.2 dex, and limit our analysis to galaxies with $M_* \leqslant 10^{10.1}\ M_\odot$, the mass scale where, roughly, the star forming main sequence deviates from linearity (e.g., Whitaker et al. 2012, 2014). Based on their star formation rates, COSMOS-Web galaxies that are >1 dex away from the current median SFR are removed from the bin and from further analysis, and the median is then recalculated. This iterative procedure is then complete when the median SFR converges, and these median SFRs (across all bins) are used, along with the bin centers, to perform a linear fit (Donnari et al. 2019):

$$\langle \log\left(\mathrm{SFR}/M_\odot\ \mathrm{yr}^{-1}\right)\rangle = \alpha \log\left(M_*/M_\odot\right) + \beta,$$

where $\langle \log(\mathrm{SFR})\rangle$ are the median (log) SFRs, and α and β are the slope and intercept, respectively. For higher masses, $M_* > 10^{10.1}\ M_\odot$, the star forming main sequence is linearly extrapolated using the fitted α and β, consistent with Donnari et al. (2021a). We then use the fitted relation from the COSMOS-Web galaxies to classify our Frontier Fields galaxies as being part of the star forming main sequence or the green valley. Motivated by Pillepich et al. (2019), we define SFMS galaxies as those with $\Delta \log(\mathrm{SFR}) \geqslant -0.5$, consistent with our procedure in Paper I. Galaxies below this threshold we define as green valley galaxies, as we have already excluded galaxies with very low global star formation rates ($\mathrm{SFR}_{\mathrm{total}} < 10^{-3}\ M_\odot\ \mathrm{yr}^{-1}$, as above). With the fit and accompanying threshold (as described above) applied to our galaxies, we find 681 star forming main sequence galaxies, along with 756 green valley galaxies.

4.3.4 Quenching Process Classification

In Paper I, using a machine learning classification algorithm, we showed that observationally motivated morphological metrics can first separate simulated quenching galaxies from star forming galaxies, and further, that quenching galaxies can be additionally separated into two evolutionary signatures: a pathway where the star formation is initially quenched in the interior regions of a galaxy, and subsequently proceeds outward, creating an "inside-out" signature. The second pathway evolves in the opposite fashion, where star formation is first suppressed in the outer regions of a galaxy, before proceeding inward, defining an "outside-in" signature. We now apply the same scheme to our Frontier Fields galaxies, in order to classify them as quenching inside out or outside in.

We adopt the observationally motivated morphological metrics first introduced in Paper I, and further refined in Paper II, that are based on the spatial distribution of star formation. The morphological metrics consider the concentration of star formation, the size of the star forming disk relative to the stellar disk, and radii that describe abrupt changes or truncations of star formation (Paper I):

$$C_{\rm SF} = {\rm SFR}_{<1\ {\rm kpc}}/{\rm SFR}_{\rm total}, \tag{4.2}$$

$$R_{\rm SF} = \log\left(R_{\rm e,\ SF}/R_{\rm e}\right), \tag{4.3}$$

$$R_{\rm inner} = \log[{\rm sSFR}(r)] \leqslant -10.5 \cap {\rm d}({\rm sSFR})/{\rm d}r \geqslant 1, \tag{4.4}$$

$$R_{\rm outer} = \log[{\rm sSFR}(r)] \leqslant -10.5 \cap {\rm d}({\rm sSFR})/{\rm d}r \leqslant -1, \tag{4.5}$$

where $C_{\rm SF}$ is the concentration of star formation, measured via the SFR in the inner 1 kpc of the galaxy relative to the total SFR. The size of the star forming disk, $R_{\rm e,\ SF}$ is next compared to the stellar disk, $R_{\rm e}$, to define $R_{\rm SF}$. $R_{\rm inner}$ and $R_{\rm outer}$ are then the inner and outer truncation radii, respectively, and are determined using the specific star formation radial profile, sSFR(r), along with its first derivative, d(sSFR)/dr.

Though these metrics were initially designed for use when considering simulated galaxies from IllustrisTNG (Nelson et al. 2018; Pillepich et al. 2018a; Springel et al. 2018) as was done in Paper I, in Paper II we adapted the metrics for use with mock observations of the same simulated galaxies. We determined that 20 radial bins (extending out to 5 $R_{\rm e}$) were sufficient to properly recover the stellar mass and SFR radial profiles after SED fitting, and with these SED fits we could likewise recover the morphological metrics with high precision, using data of quality/coverage comparable to the Frontier Fields data. For this reason we adopt the morphological metrics from Paper II, using the same adaptations as described there: we interpolate the SFR profile to find the value at 1 kpc (projected) and compare with the integrated profile for $C_{\rm SF}$. For $R_{\rm SF}$, we likewise interpolate the SFR and stellar mass profiles to find the radius containing fifty percent of the profile, and subsequently take the logarithm of the ratio. Both truncation radii require no observational adaptations (Paper II). We calculate these quantities for all 1437 galaxies in our non-quenched primary sample with ${\rm SFR}_{\rm total} \geqslant 10^{-3}\ M_{\odot}\ {\rm yr}^{-1}$.

We next employ a k-nearest neighbor algorithm (kNN; e.g., Fix & Hodges 1951, 1989; Cover & Hart 1967), from the `scikit-learn` package (Pedregosa et al. 2011), in order to classify our galaxies as quenching from the inside out or the outside in. The kNN algorithm uses the k-nearest neighbors to a point in a given parameter space as training samples, to infer the class or label of the point under consideration, with optional weighting based on distance (Pedregosa et al. 2011). For the training set, we use the simulated galaxies (drawn from IllustrisTNG, from Paper I), but employ the observational proxies of the four

morphological metrics (from Paper II), along with the distance from the SFMS, ΔSFMS (measured in dex), that compares the expected (log) SFR for a galaxy based on its (log) stellar mass if it was on the SFMS, to its actual (log) SFR. We additionally use the true population labels (from Paper I; i.e. star forming, inside-out, and outside-in). For the observed target sample, we use the morphological metrics and ΔSFMS for the 1437 galaxies in the non-quenched primary sample.

For both the training set and target sample, we standardize/feature-scale the respective morphological metrics prior to performing the classification. This ensures that metrics with large dynamic range are not dominant when classifying (Pedregosa et al. 2011). Similarly to Paper I and Paper II, we use the five nearest neighbors, and weight the contribution of the neighbors using the inverse of their distance. We use the complete set of galaxies available from Paper I and Paper II, some 69,493 unique galaxies with which we have morphological metrics, to complete the classification. After applying the kNN classification, we find 129 inside-out quenching galaxies, along with 70 outside-in quenching galaxies. In Figure 4.4, we show example radial profiles for an inside-out quenching galaxy on the left, and those for an outside-in quenching galaxy on the right. In all panels we compare with galaxies close in stellar mass, $\Delta \log (M_*/M_\odot) \leqslant 0.1$ dex, that lie on the SFMS, where the $\pm 1\sigma$ region is shown with a gray band, while the the median is shown with a dotted black line. In the bottom row, we denote the location of $R_{\rm inner}$ for the inside-out quenching galaxy (left), and $R_{\rm outer}$ for the outside-in quenching galaxy (right), with a vertical light gray dotted line, respectively.

4.4 Results

In Figure 4.5, we show the distributions of the morphological metrics for the classified galaxies, compared to similarly classified simulated galaxies, where the metrics are taken from Paper I. In the top row, we show inside-out quenching galaxies (magenta), while in the bottom row we show outside-in quenching galaxies (red). The distributions for the simulated galaxies from Paper I are shown with dashed lines, while the Frontier Fields galaxies investigated here are shown with solid lines. In each panel, we normalize the distributions so that the y-axis can be read as frequency. We show similar plots for star forming galaxies in Appendix C.4, where the distributions shown there are consistent between the simulated galaxies and the Frontier Fields galaxies.

We first consider the inside-out quenching population in Figure 4.5, and compare the distributions between the simulated galaxies (that form the training set,) and the Frontier

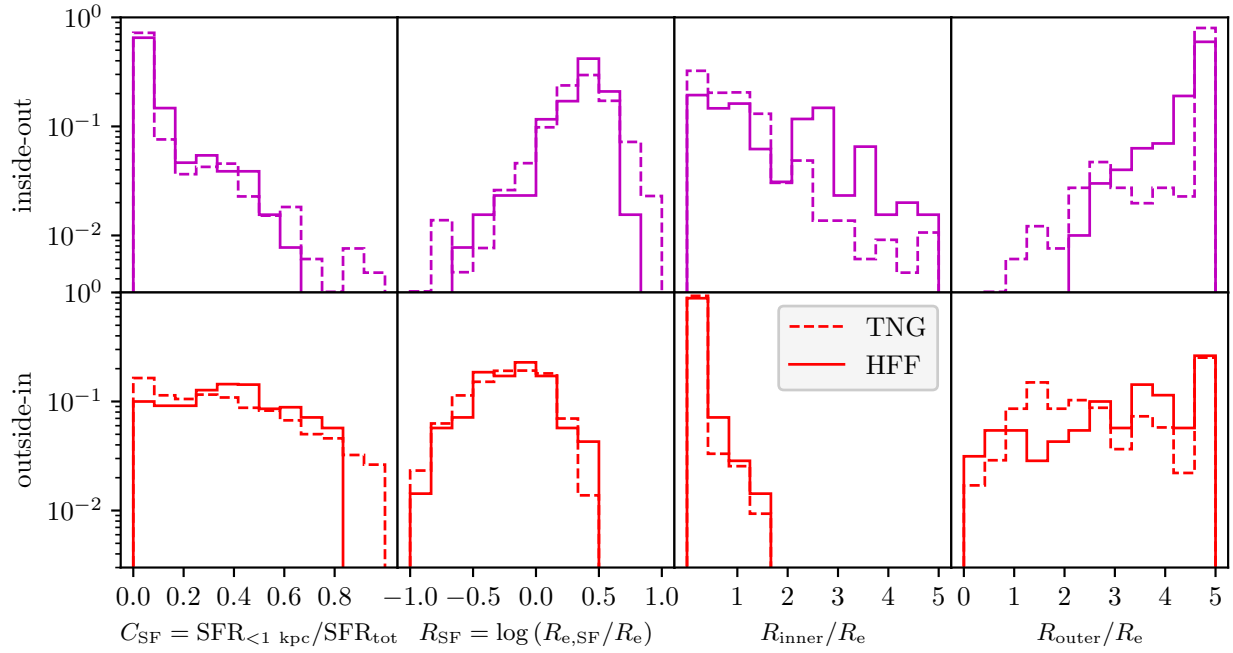


Figure 4.5: Distributions for each morphological metric (columns), separating inside-out quenching galaxies (top, magenta), from outside-in quenching galaxies (bottom, red), after classification (solid lines). Comparison distributions for the corresponding population of simulated quenching galaxies from Paper I are shown with dashed lines, respectively. These simulated galaxies formed the training set during classification (see Section 4.3.4). Moving from left to right, the columns show $C_{\rm SF}$, $R_{\rm SF}$, $R_{\rm inner}$, and $R_{\rm outer}$, respectively. Each distribution has been normalized such that the y-axis can simply be read as the frequency of a given value occurring in the sample.

Fields galaxies (that form the observed target sample) using a two-sample Kolmogorov-Smirnov (KS) test for goodness of fit (e.g., Hodges 1958). We find good agreement, where for each of the morphological metrics, the distribution for the sample galaxies is consistent with being drawn from the same distribution as the simulated galaxies. The p-values are 0.54, 0.87, 0.10, and 0.54 for $C_{\rm SF}$, $R_{\rm SF}$, $R_{\rm inner}$, and $R_{\rm outer}$, respectively. Notably, the distributions for $C_{\rm SF}$ and $R_{\rm SF}$ are quite similar, while $R_{\rm inner}$ shows a higher fraction of galaxies with large values when compared with the simulation. For $R_{\rm outer}$, we again find very good agreement, though Frontier Fields galaxies generally take larger values of $R_{\rm outer}$ compared to their simulated counterparts from Paper I.

For the outside-in quenching galaxies in the bottom row of Figure 4.5, we likewise find very good agreement between our sample galaxies and the simulated galaxies. Employing a two-sample KS test as before, for each metric for the outside-in quenching Frontier Fields galaxies, we find no significant differences when compared with the simulated galaxies. The p-values are 0.99, 0.99, 0.99, and 0.54, for $C_{\rm SF}$, $R_{\rm SF}$, $R_{\rm inner}$, and $R_{\rm outer}$, respectively. In particular, the distributions for $R_{\rm SF}$, and $R_{\rm inner}$ show excellent agreement. The distributions for $C_{\rm SF}$ show that our outside-in quenching sample galaxies are less likely to take very high concentration values ($\sim$1) when compared with the simulated galaxies, and that they similarly show a relatively uniform distribution in $R_{\rm outer}$. Of course, by construction these distributions should be similar, as in Section 4.3.4 we used the simulated galaxies as the training set, in order to classify the sample galaxies according to their morphological metrics. Given this, the kNN classification should only classify galaxies that have morphological metrics similar to simulated galaxies as inside-out or outside-in, for example. Nonetheless, it is encouraging to find broad similarities between the simulated and observed galaxies when considering the suite of morphological metrics simultaneously, for a given population.

We next consider the phase space distribution of our non-quenched+quenched samples in Figure 4.6, following the analysis completed in Section 4.2.3. The cluster-normalized line-of-sight velocity is plotted as a function of projected 2D distance from the respective cluster center, where we take the logarithm of the projected 2D distance for visual clarity. Galaxies without phase space-inferred infall times are plotted in white, otherwise galaxies are color-coded by their infall time: galaxies with recent infall times ($t_{\rm infall} \lesssim 1$ Gyr) are plotted with blue, while galaxies with ancient infall times ($t_{\rm infall} \sim 6$ Gyr) are plotted with red, for example. Inside-out quenching galaxies are plotted with squares, while outside-in quenching galaxies are plotted with triangles. We additionally denote the boundary (light gray line) that separates the field from the cluster, where the boundary is $R_{\rm 2D} < 0.5R_{200} \cap |V_{\rm LoS}| < 3.5\sigma_{\rm LoS}$. Galaxies that make up the quenched extended sample (SFR$_{\rm total} < 10^{-3}$ $M_{\odot}$ yr^{-1}, numbering 502), and galaxies from the non-quenched primary

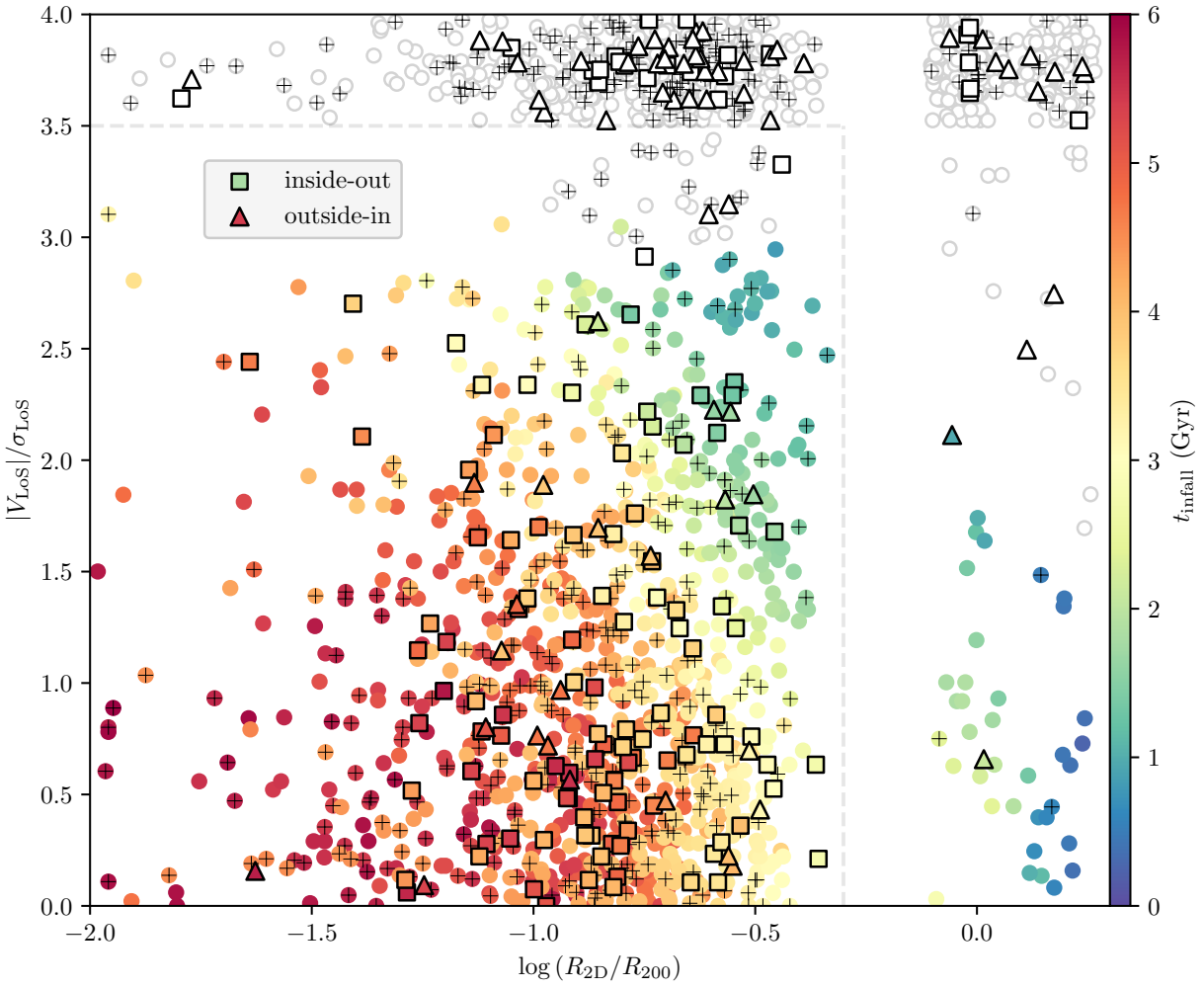


Figure 4.6: Phase space locations for the non-quenched+quenched sample of 1939 galaxies. Here we plot galaxies that do not have infall time estimates with white, while inside-out and outside-in quenching galaxies are plotted with squares and triangles, respectively. We plot galaxies that are part of the non-quenched sample but not classified as inside-out or outside-in with circles, and color-code these galaxies, along with the inside-out and outside-in populations, by infall time. Galaxies that are part of the quenched extended sample are additionally color-coded by infall time when possible, and are highlighted with small crosses. We denote the boundary that separates the field from the cluster ($R_{\rm 2D}/R_{200} < 0.5 \cap |V_{\rm LoS}|/\sigma_{\rm LoS} < 3.5$) with a dashed light gray line. Field galaxies with large line-of-sight velocities beyond $|V_{\rm LoS}|/\sigma_{\rm LoS} = 3.5$ are plotted between this value and $|V_{\rm LoS}|/\sigma_{\rm LoS} = 4$ for visualization purposes.

sample that were not classified as either inside-out or outside-in quenching (numbering 682, excluding 556 kNN-classified star forming galaxies), are plotted with circles and are color-coded according to infall time. Both of these latter subpopulations (quenched+unclassified) are predominantly found within the cluster. Quenched extended sample galaxies are further denoted with small crosses. Field galaxies with large line-of-sight velocities beyond the plot boundaries are plotted at random y-values between $|V_{\rm LoS}|/\sigma_{\rm LoS} = 3.5$ and $|V_{\rm LoS}|/\sigma_{\rm LoS} = 4$ for visualization purposes.

We first consider the cluster galaxies in Figure 4.6, and will discuss the field population below. Of the 129 inside-out quenching galaxies we classified, 106 are in clusters. For the outside-in population, 25 of the 70 galaxies reside in clusters. Figure 4.6 shows that both populations of cluster quenching galaxies reside in similar regions of the phase space, commonly with $-1.3 < \log(R_{\rm 2D}/R_{200}) < -0.5$ and $0 < |V_{\rm LoS}|/\sigma_{\rm LoS} < 2.5$. Further, the inside-out and outside-in populations have a similar distribution to the unclassified galaxies (colored circles) along the line-of-sight velocity, but are somewhat more centrally concentrated radially. Given these locations in phase space, these galaxies tend to have old infall times. The median infall time (and spread) for the inside-out quenching population is $4.0^{+1.1}_{-1.0}$ Gyr, while it is $4.0^{+0.9}_{-2.1}$ Gyr for the outside-in quenching population.

Beyond the two main quenching populations, there exist many galaxies at small distances from the cluster core with correspondingly ancient infall times ($t_{\rm infall} \sim 6$ Gyr). A large proportion of these galaxies populate the quenched extended sample (denoted with small crosses), the 502 galaxies with global SFR $< 10^{-3}$ $M_\odot$ yr^{-1} that we were unable to determine morphological metrics for, consistent with observations of clusters with high fractions of quenched galaxies (e.g., Wetzel et al. 2013; Davies et al. 2019; Hewitt et al. 2025).

In Figure 4.7, we show the total star formation rates for our non-quenched+quenched sample as a function of stellar mass. In the background we show contours (light gray) that describe the location and density of the COSMOS-Web (Casey et al. 2023) galaxies we used to determine the SFMS. Our best fit to the SFMS is shown with a solid dark gray line, while the SFMS $-$ 0.5 dex boundary for classification as green valley is shown with a dotted gray line. In the foreground we show all galaxies from our non-quenched+quenched samples as colored symbols and white dots. The 502 galaxies with SFR $< 10^{-3}$ $M_\odot$ yr^{-1} that make up the quenched extended sample are plotted with white dots at random SFRs between 10^{-3} $M_\odot$ yr^{-1} and 10^{-4} $M_\odot$ yr^{-1} for visualization purposes. Galaxies that are part of the non-quenched primary sample that were not classified as either inside-out or outside-in quenching, numbering 682 galaxies and excluding classified star forming galaxies (556), are likewise plotted with white dots. The inside-out quenching galaxies are plotted with squares, and are color-coded by infall time, based on the phase space analysis completed in

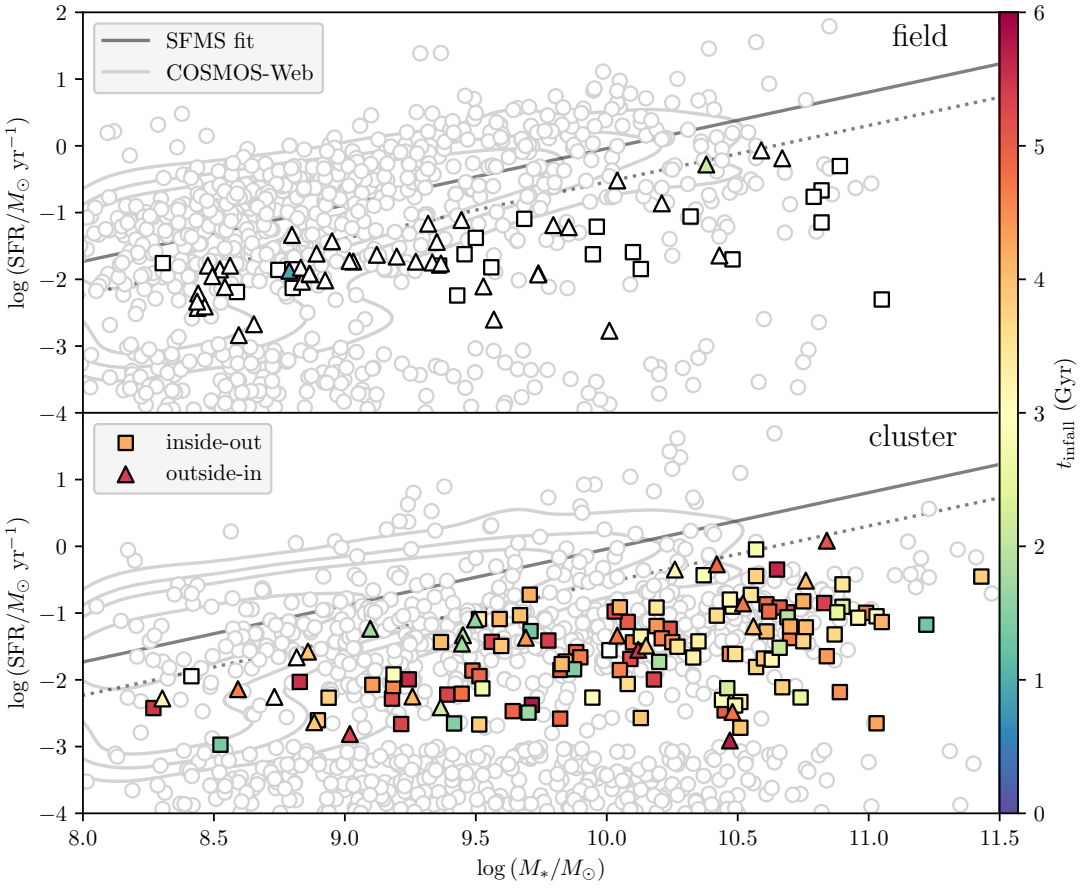


Figure 4.7: Global star formation rate as a function of stellar mass for the non-quenched+quenched sample of 1939 galaxies. In the background we show unfilled contours (light gray) that denote the location and density of galaxies drawn from COSMOS-Web (Casey et al. 2023) from which we determine the star forming main sequence (dark gray solid line). Galaxies >0.5 dex below the fit for the star forming main sequence (dark gray dotted line) are classified as green valley galaxies, while those above this line are classified as star forming main sequence galaxies. Galaxies with very low levels of star formation from the quenched extended sample, that we cannot apply our morphological metrics to, are plotted at small, random nonzero star formation rates from 10^{-3} $M_\odot$ yr^{-1} to 10^{-4} $M_\odot$ yr^{-1} for visualization purposes. Inside-out and outside-in quenching galaxies are plotted with squares and triangles, respectively, and are color-coded according to infall time. Galaxies that are part of the non-quenched sample not classified as inside-out or outside-in quenching are plotted with white dots, as are galaxies from the quenched extended sample. We separate galaxies that reside in the field (top) from those present in the cluster (bottom).

Section 4.2.3. Outside-in quenching galaxies are plotted with triangles, and are similarly color-coded. We separate galaxies that reside in the field (top), from those that live in clusters (bottom).

In both the field and cluster, inside-out and outside-in quenching galaxies are almost exclusively found in the green valley (also see Appendix C.5), which is likely a consequence of including the distance from the SFMS, ΔSFMS, in the kNN classification above. However, we investigated the distributions of ΔSFMS for the star forming, inside-out, and outside-in populations drawn from the simulation, and found that there was significant overlap between the quenching populations ($\mu = -0.27$ dex, $\sigma = 0.30$ dex, when combined) and the star forming population ($\mu = 0.01$ dex, $\sigma = 0.20$ dex). Further, we additionally used a random forest classifier (from `scikit-learn`; Pedregosa et al. 2011), which uses a collection of 100 randomized decision trees to determine the relative importance (or mean decrease in impurity, or Gini impurity; Pedregosa et al. 2011) of each morphological metric and ΔSFMS when training. We find that ΔSFMS has an importance of 0.25, which is less than, or comparable to, the importance values for $C_{\rm SF}$ (0.24) and $R_{\rm SF}$ (0.31), but more than the importance values for $R_{\rm inner}$ (0.07) and $R_{\rm outer}$ (0.13), consistent with findings from Paper I. This indicates that while ΔSFMS is helpful when classifying, ∼75% of the classification is driven by the morphological metrics alone.

Considering the field and cluster together, inside-out quenching galaxies are more massive, with a median stellar mass of $\log(M_*/M_\odot) = 10.1^{+0.6}_{-0.7}$, compared with $\log(M_*/M_\odot) = 9.3^{+0.9}_{-0.7}$ for outside-in quenching galaxies, representing a higher median stellar mass of $\Delta\log(M_*/M_\odot) = 0.8^{+0.2}_{-0.1}$ dex, where the 68% confidence interval was found through bootstrap resampling. The inside-out population is also found more commonly in clusters (106/129), compared to the outside-in population (25/70), which is most often found in the field. As shown above, the two populations have similar median infall times ($4.0^{+1.1}_{-1.0}$ Gyr for inside-out, and $4.0^{+0.9}_{-2.1}$ Gyr for outside-in) when considering the field and cluster populations simultaneously. We find some evidence that the field population of inside-out+outside-in quenching galaxies has higher specific star formation rates, with a median sSFR of $\log(\mathrm{sSFR}/\mathrm{yr}^{-1}) = -10.9^{+0.3}_{-0.7}$, compared with $\log(\mathrm{sSFR}/\mathrm{yr}^{-1}) = -11.6^{+0.6}_{-0.6}$ for the cluster population of these quenching galaxies. However, these differences are comparable to the spread for each population per environment.

In the top panel of Figure 4.7, we see that there are 23 inside-out and 45 outside-in quenching galaxies present in the field. The inside-out quenching galaxies span the range of stellar masses under investigation, with a median stellar mass of $\log(M_*/M_\odot) = 9.7^{+1.1}_{-0.9}$. Considering the outside-in quenching galaxies in the field, we find that they are generally less massive than the inside-out quenching galaxies, with a median stellar mass of $\log(M_*/M_\odot) = 9.0^{+0.8}_{-0.5}$. In the bottom (cluster) panel, considering first the inside-out

population, we find that these galaxies (106) are generally more massive than their field counterparts, with a median stellar mass of $\log(M_*/M_\odot) = 10.2^{+0.5}_{-0.7}$. In a similar fashion, the outside-in quenching galaxies in the cluster (25) are more massive than outside-in quenching galaxies in the field, with a median stellar mass of $\log(M_*/M_\odot) = 9.5^{+0.9}_{-0.6}$. Taken together, the inside-out+outside-in population in the cluster is $\Delta \log(M_*/M_\odot) = 0.8^{+0.3}_{-0.1}$ dex more massive than in the field, with 68% bootstrapped confidence intervals.

We next look to understand the prevalence of these different quenching processes as a function of stellar mass, binned by environment, and additionally separated by star forming+green valley versus green valley only. The results of this investigation are shown in Figure 4.8. Galaxies present in the cluster (left) are separated from those in the field (right), while green valley galaxies in the non-quenched primary sample (bottom, solid lines) are also considered distinct from all galaxies in the non-quenched sample (top, dashed lines; i.e. star forming+green valley). In all panels, fractions are relative to the non-quenched sample: those galaxies with $\mathrm{SFR}_{\mathrm{total}} \geqslant 10^{-3}\ M_\odot\ \mathrm{yr}^{-1}$ that we were able to compute morphological metrics for. Binomial errors are used to convey the uncertainty for each fraction, while the range of each mass bin is illustrated with x-axis error bars.

In Figure 4.8, by first considering the evolution for all galaxies (top row), we see that the fraction of cluster inside-out quenching galaxies (dashed magenta line) increases with increasing stellar mass, where at high masses ($M_* \gtrsim 10^{10.5}\ M_\odot$), the inside-out population makes up ∼30% of the galaxy population with $\mathrm{SFR} > 10^{-3}\ M_\odot\ \mathrm{yr}^{-1}$. By fitting a linear function, we find a slope of $m = 0.08 \pm 0.02$. Conversely, the fraction of outside-in galaxies (dashed red line) is relatively independent of stellar mass ($m = -0.01 \pm 0.01$). Moving next to the field while still considering all galaxies with $\mathrm{SFR} > 10^{-3}\ M_\odot\ \mathrm{yr}^{-1}$, we find a similar situation for the inside-out galaxies but less pronounced: the fraction of inside-out galaxies (dashed pink line) increases with stellar mass ($m = 0.02 \pm 0.01$), amounting to ∼15% of the galaxy population at high stellar mass ($M_* \gtrsim 10^{10.5}\ M_\odot$). By comparing the trends for the inside-out population in the cluster and the field, we find that the difference in slopes is statistically significant, with $p = 0.024$ from a t-test. In the field, the fraction of outside-in quenching galaxies is again relatively uniform with stellar mass ($m = 0.01 \pm 0.01$), as was found in the cluster. Given that there is no statistically significant difference between the linear relations (slopes or intercepts) for the outside-in populations in the cluster and field, the rate of finding an outside-in quenching galaxy in the field is the same as in the cluster, when considering all galaxies.

We expect, and find (see above), quenching galaxies to be primarily located in the green valley. Therefore it may be more appropriate to consider the green valley as the parent population, though this of course depends on the relative timescales of morphologically-identifiable transition signatures with green valley lifetime. We consider only the green

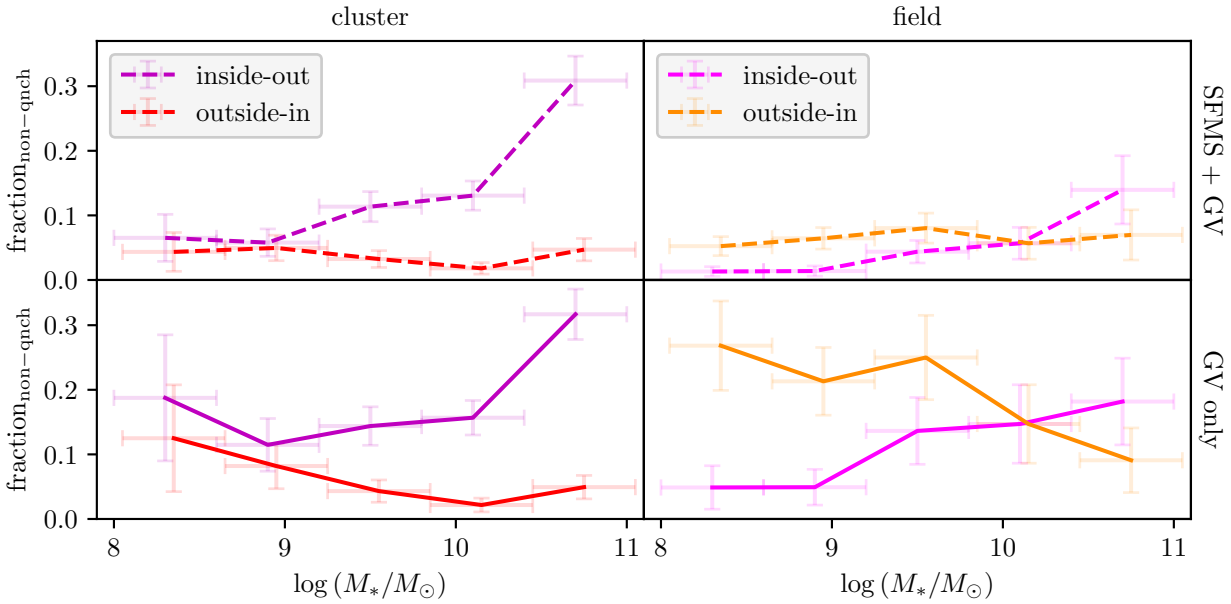


Figure 4.8: Fraction of non-quenched galaxies with SFR $> 10^{-3}$ $M_\odot$ yr^{-1} experiencing either inside-out (pink–magenta) or outside-in (orange–red) quenching, as a function of stellar mass. We bin galaxies by environment, separating cluster galaxies (left) from those in the field (right). We additionally separate all galaxies in the non-quenched primary sample (top, dashed lines), from green valley-only galaxies in the non-quenched sample (bottom, solid lines). In all panels, we show binomial errors for each fraction (y-axis error bars), and use x-axis error bars to illustrate the considered mass range for each mass bin. The results for the outside-in population are slightly offset horizontally from the inside-out populations for visual clarity.

valley population, numbering 756 galaxies, in the bottom row of Figure 4.8. By simultaneously considering both quenching populations, we find that the fraction of all green valley galaxies in the cluster (543 galaxies) is made up of ∼30% inside-out+outside-in quenching galaxies for $M_* \lesssim 10^9\ M_\odot$, where this fraction decreases at intermediate masses ($M_* \sim 10^{9.5}\ M_\odot$) to ∼20%, before increasing at high stellar mass ($M_* \sim 10^{10.5}\ M_\odot$), reaching ∼40%. For the green valley galaxies in the field (213 galaxies), by again considering both quenching populations simultaneously, we find that the fraction of inside-out+outside-in quenching galaxies is ∼30%, where this fraction is relatively constant with stellar mass, showing a modest increase at intermediate stellar masses to ∼40%. The similarity between the cluster and field proportions is then worth considering, given that the green valley itself represents a much larger fraction of the total population in clusters (∼72%). Conversely, when considering all galaxies in the field (top right panel; 714 galaxies), these mostly reside on the SFMS (501 galaxies), as shown above. Therefore, the fraction of field inside-out+outside-in quenching galaxies in the green valley is much higher than the fraction for all galaxies, which is not the case for cluster galaxies.

Given the large population of galaxies that we find in clusters (723 galaxies), we next explore the fraction of inside-out and outside-in quenching galaxies as a function of stellar mass, but now binned by phase space-inferred infall time. We consider three infall time bins: recent infall galaxies ($t_{\rm infall} < 2$ Gyr), intermediate infall galaxies ($2 < t_{\rm infall}/{\rm Gyr} < 4$), and ancient infall galaxies ($t_{\rm infall} > 4$ Gyr). We show the results of this investigation in Figure 4.9, where error bars are as in Figure 4.8.

In Figure 4.9, we see that the trends noticed in Figure 4.8 for the general cluster population are largely recovered across the three infall time bins as well. The strong mass dependence of the inside-out quenching population noted in Figure 4.8 is fairly robust, seen in almost all panels. As above, these panels show that the fraction of inside-out quenching galaxies increases as a function of stellar mass. The exception is the recent infall panel, $t_{\rm infall} < 2$ Gyr, for green valley galaxies, which has large uncertainties. As well, the outside-in quenching population is likewise mass independent given the uncertainties. This mimics the situation for this population noted above in Figure 4.8. Given the large uncertainties, especially in the green valley only panels (bottom row), there is no strong dependence on infall time for any population, except perhaps the most massive ($M_* \gtrsim 10^{10.5}\ M_\odot$) inside-out population. At these masses, the fraction of inside-out quenching galaxies increases with increasing infall time. This is seen when considering all galaxies (top row), as well as green valley-only galaxies (bottom row). It is somewhat surprising, in particular, that the outside-in quenching population shows no dependence on infall time. However, this is possibly a consequence of the small sample size, where only 25 outside-in quenching galaxies reside in the cluster.

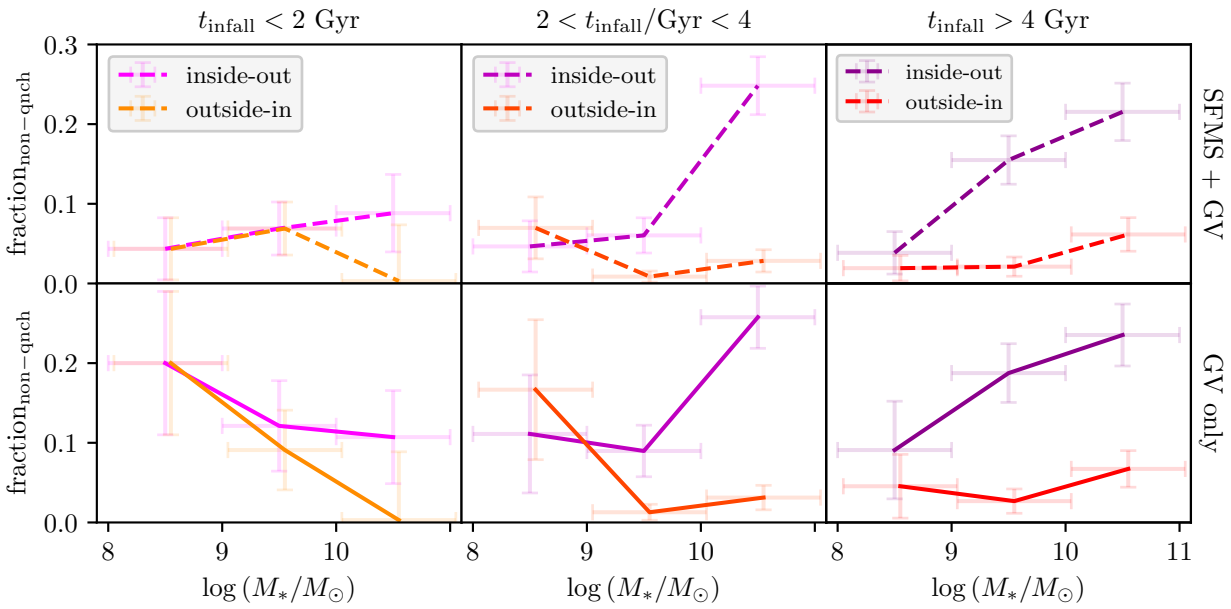


Figure 4.9: Fraction of non-quenched galaxies with SFR $> 10^{-3}$ $M_\odot$ yr^{-1} experiencing either inside-out (pink–dark magenta) or outside-in (orange–red) quenching, as a function of stellar mass. We bin galaxies by phase space-based estimated infall time, $t_{\rm infall}$, separating recent infall galaxies (left, $t_{\rm infall} < 2$ Gyr), from intermediate infall galaxies (middle, $2 < t_{\rm infall}/{\rm Gyr} < 4$), and ancient infall galaxies (right, $t_{\rm infall} > 4$ Gyr). We additionally separate all galaxies in the non-quenched primary sample (top, dashed lines), from green valley-only galaxies in the non-quenched sample (bottom, solid lines). As in Figure 4.8, we use binomial errors to describe uncertainties on the fractions (y-axis error bars), while the range for each mass bin is given by the x-axis error bars. Fractions for the outside-in population are slightly offset horizontally for clarity.

4.5 Discussion

Given the results presented above, we have found that using the observationally motivated morphological metrics introduced in Paper I and refined in Paper II, that trace the distribution of star formation within galaxies, we can identify galaxies in the Hubble Frontier Fields that have morphological metrics consistent with those predicted from the TNG simulation to have resulted from different quenching pathways. For these quenching pathways, the first is consistent with a scenario in which star formation is suppressed in the interior of a galaxy, and proceeds outward. The other pathway has star formation that is quenched initially on the outskirts, and proceeds inward. Considering their mass and environmental dependence, the inside-out quenching population in the Frontier Fields is more massive than the outside-in quenching population, and is commonly found in cluster galaxies. Outside-in quenching galaxies are commonly found in the field. This suggests that the high-mass galaxies, regardless of environment and central/satellite status, are quenching inside-out, while the low mass satellites are quenching outside-in.

When viewed together, these results suggest that the nature of galaxy quenching, as inferred here, is more complicated than our previous investigations would suggest. In particular, we find a high rate of inside-out quenching galaxies present in the cluster, and indeed that have resided in the cluster over extended periods. In Paper I, and as followed-up in Paper II, when we investigated simulated galaxies, we found inside-out quenching galaxies to largely reside in the field. Further, in Paper I, we did find that inside-out galaxies have quenching that is extended over several gigayears, on the order of the infall times we found above, so perhaps some environmental effect is promoting the funneling of material down onto the active galactic nuclei (AGN) in these systems, thereby producing the expected inside-out signature. This physical scenario seems plausible, but will require additional work (see below).

Concerning the outside-in population, we find fewer galaxies, especially in the cluster, when viewed in the context of Paper I. In that work, we found that outside-in galaxies make up the majority of the quenching population and are dominant in clusters, while above we showed that the fraction of outside-in quenching galaxies in the Frontier Fields sample is higher in the field ($\sim$6.3%), compared with the cluster ($\sim$3.5%). As well, in Paper I, we found that simulated outside-in quenching galaxies in TNG had a quenching timescale of the order of $\sim$1.5 Gyr, while above we found outside-in galaxies residing in the cluster with infall time estimates of $>$3 Gyr. This situation is puzzling, as we might expect quenching driven by environmental processes to act in a more efficient manner (e.g., Balogh et al. 2000; Quilis et al. 2000). However, we did find that the outside-in quenching galaxies have a mild preference towards more recent infall times. As above, this scenario

requires additional work, as described below.

From these considerations, we find that the quenching of simulated galaxies as investigated in Paper I is somewhat simplified compared to what we have inferred about quenching using observations of real galaxies. Specifically, in Paper I, we could summarize the quenching pathways as thus: high-mass central galaxies in the field quench inside out, likely driven by AGN feedback, while low-mass satellites quench outside in, as a consequence of environment, consistent with expectations for ram pressure stripping. Here, for the Frontier Fields, we find that high-mass satellites additionally quench inside out, in a similar manner to their high-mass central counterparts. This result agrees well with the findings of Bluck et al. (2020b) and McDonough et al. (2025), and suggests that the quenching prescription in the TNG simulations does not completely capture the various quenching pathways experienced by real galaxies.

4.5.1 Comparison with Literature Results

In the context of studies in the literature, we are not currently aware of any such work that has completed a directly similar analysis as presented above. However, there have been a number of recent investigations using spatially resolved SED fitting to investigate quenching in different environments (e.g., Nelson et al. 2021; Abdurro'uf et al. 2022a, 2023; Olsen et al. 2026), and other works have investigated the fraction of quenching galaxies at various redshifts (e.g., Schawinski et al. 2014; McNab et al. 2021).

Using imaging and slitless spectroscopy from the 3D-HST survey (Brammer et al. 2012; Skelton et al. 2014; Momcheva et al. 2016), Nelson et al. (2021) completed spatially resolved spectral energy distribution fitting for 3200 star forming main sequence galaxies at $0.7 < z < 1.5$ with $10^9 < M_*/M_\odot < 10^{11}$. In their work, Nelson et al. (2021) used spatially resolved near-infrared spectra to create Hα emission line maps, which trace the distribution of star formation for short timescales ($\sim$10 Myr; e.g., Kennicutt 1998b; Kennicutt & Evans 2012), and *JH*-band imaging to trace the distribution of stellar mass. Nelson et al. (2021) additionally complete spatially resolved SED fitting using existing rest frame ultraviolet to near-infrared imaging in eight bands from the Cosmic Assembly Near-infrared Deep Extragalactic Legacy Survey (CANDELS; Grogin et al. 2011; Koekemoer et al. 2011) to correct their SFR maps for dust. They then bin galaxies by stellar mass, and create sSFR radial profiles for galaxies below, on, and above the star forming main sequence by stacking galaxies with a mass bin. Nelson et al. (2021) find that at high stellar masses ($10^{10.5} < M_*/M_\odot < 10^{11}$), galaxies below the main sequence are strongly centrally suppressed, indicative of inside-out quenching. Indeed, they even find evidence of inside-out

quenching for massive 3D-HST galaxies that reside on the main sequence (Nelson et al. 2021). For less massive galaxies ($M_* < 10^{10.5}\ M_\odot$), Nelson et al. (2021) find no evidence for inside-out or outside-in quenching for any galaxies across the main sequence, finding flat sSFR profiles on average. In our work, we found evidence of inside-out quenching for massive green valley galaxies in the field, consistent with the findings of Nelson et al. (2021) at $M_* > 10^{10.5}\ M_\odot$. However, Nelson et al. (2021) do not find any evidence for outside-in quenching within their sample of 3D-HST galaxies, while we find a smaller population of outside-in quenching galaxies in the Frontier Fields.

Abdurro'uf et al. (2022a) completed spatially resolved panchromatic SED fitting for 10 nearby (<20 Mpc) spiral galaxies with $10^{9.7} < M_*/M_\odot < 10^{11.2}$ on a pixel-by-pixel basis, using 24 broad band filters covering the rest frame far-ultraviolet to the far-infrared. Using maps of physical properties including SFR and stellar mass, along with archival high-resolution maps of atomic and molecular gas, they investigate radial variations, and find central SFR suppressions for many of their galaxies, which correlate with reduced molecular gas fractions (Abdurro'uf et al. 2022a). They additionally find that with increasing distance from the star forming main sequence, the central suppressions seen in their sSFR radial profiles become more pronounced (Abdurro'uf et al. 2022a). They conclude that these features are consistent with inside-out quenching, where this quenching started a few gigayears prior to observation (Abdurro'uf et al. 2022a). We find good agreement with the results of Abdurro'uf et al. (2022a) when considering the intermediate-to-high mass population in the field, where we found inside-out quenching. In particular, the finding of Abdurro'uf et al. (2022a), for an increasing central suppression of SFR with increasing distance from the SFMS, is complementary to our results above. We found a higher fraction of inside-out quenching galaxies (at high masses) in the green valley, when compared with the combined SFMS+green valley population. In a similar fashion to Nelson et al. (2021), Abdurro'uf et al. (2022a) do not comment on outside-in quenching in their sample, though their radial sSFR profiles for galaxies away from the SFMS ($\gtrsim$0.5 dex) do show evidence for a negative sSFR profile at $R > 1.5\ R_e$, especially at $\Delta\text{SFMS} < -1$ (their Figure 11).

As well, Abdurro'uf et al. (2023) investigated quenching in 444 galaxies with $10^{7.5} < M_*/M_\odot \lesssim 10^{11.8}$ at $0.3 < z < 6.0$ present in two intermediate redshift clusters, along with a corresponding field sample. Abdurro'uf et al. (2023) complete spatially resolved SED fitting using high-resolution HST and JWST imaging covering the rest frame blue-optical to the near-infrared. As above, they create maps of physical properties, from which they form radial profiles, including sSFR radial profiles (Abdurro'uf et al. 2023). They bin their galaxies by distance from the SFMS and by stellar mass, from which they produce average radial profiles (Abdurro'uf et al. 2023). Here, we focus on their results for $0.3 < z < 0.8$ galaxies, which is the redshift range most comparable with our analysis of the Frontier

Fields. They find that $M_* < 10^{11}$ $M_\odot$ green valley ($-1 <$ ΔSFMS < -0.4) galaxies have suppressed central star formation with active star formation in their disks, while quiescent galaxies (ΔSFMS < -1) show similar profiles for $M_* > 10^{9.5}$ $M_\odot$ (their Figure 8; Abdurro'uf et al. 2023). Abdurro'uf et al. (2023) conclude that their results point toward inside-out quenching. We find that our findings are consistent with those of Abdurro'uf et al. (2023), where we have likewise found inside-out quenching across similar mass scales as those investigated by Abdurro'uf et al. (2023), for galaxies in clusters. Indeed, we found that inside-out quenching galaxies are more often found in the cluster, compared to other quenching modes.

Recently, Olsen et al. (2026) completed spatially resolved spectral energy distribution fitting for eight $z < 0.3$ well-resolved star forming galaxies with $10^{9.5} < M_*/M_\odot \lesssim 10^{11}$ in the UltraViolet Imaging of the Cosmic Assembly Near-infrared Deep Extragalactic Legacy Survey (UVCANDELS; Wang et al. 2025), an extension to CANDELS (Grogin et al. 2011; Koekemoer et al. 2011). The sample of Olsen et al. (2026) is comprised mostly of face-on galaxies, but is supplemented with edge-on disks, with some showing signatures of tidal interactions. Olsen et al. (2026) used ten-band HST observations from the rest-frame ultraviolet to the near-infrared and fit voronoi-binned photometry (e.g., Cappellari & Copin 2003) to produce maps of stellar mass, star formation rate, dust attenuation, and the time at which half the stellar mass was formed, t_{50}. Using these maps, Olsen et al. (2026) additionally produce radial profiles of (logarithmic) sSFR at the time of observation and at 1 Gyr lookback time to investigate the evolution of star formation, in the context of galaxy quenching. They find evidence for different quenching pathways in their sample by comparing the slopes of the resolved SFR–M_* relation: an inside-out pathway, and an outside-in pathway (Olsen et al. 2026). They further find that the sSFR profiles show an overall decrease over the past 1 Gyr, where five of the eight galaxies in particular show a larger change in the outskirts than in the centers (Olsen et al. 2026). They conclude that the evolution for these five systems indicates a possible early onset of quenching in these galaxies (Olsen et al. 2026). The results of Olsen et al. (2026) are in very good qualitative agreement with the results we found above over a broader mass range ($10^8 < M_*/M_\odot < 10^{11.5}$), specifically the identification of quenching pathways suggestive of an inside-out mechanism, as well as an outside-in mechanism. In our work, we found that the outside-in quenching population makes up a smaller overall fraction of the identified quenching pathways (70 galaxies, compared to 129 for inside-out), while Olsen et al. (2026) find that five of their eight galaxies show early signs of outside-in quenching. However, due to the smaller sample size investigated by Olsen et al. (2026), it is difficult to drawn firm conclusions on the prevalence of different quenching mechanisms in their sample.

Regarding the fraction of quenching galaxies, Schawinski et al. (2014) used a com-

bined analysis of Sloan Digital Sky Survey (York et al. 2000), Galaxy Evolution Explorer (GALEX; Martin et al. 2005), and Galaxy Zoo (Lintott et al. 2008, 2011) data to investigate the green valley for local ($0.02 < z < 0.05$) galaxies with $10^9 < M_*/M_\odot < 10^{11.5}$. Schawinski et al. (2014) define the green valley based on cuts in the u–r color–mass diagram, and find ∼17% of early- and late-type galaxies populate the green valley. At higher redshifts, McNab et al. (2021) investigated the fraction of green valley galaxies with $10^{9.5} < M_*/M_\odot < 10^{11.5}$ in $1.0 < z < 1.4$ clusters. McNab et al. (2021) define the green valley with respect to cuts in the NUV–V–J color–color diagram, and find that the fraction of their green valley galaxies is relatively independent of stellar mass, representing ∼13% of their sample in the cluster, and ∼14% in the field, where the field galaxies are photometric members that are >1.5 Mpc from their cluster centers. The results of Schawinski et al. (2014) and McNab et al. (2021) at first seem inconsistent with the results we described above, where we found ∼30% of the cluster and field populations (with SFR $> 10^{-3}$ $M_\odot$ yr^{-1}) to consist of our combined inside-out+outside-in quenching populations in the green valley (see Figure 4.8). However, above we were investigating the fraction of inside-out and outside-in quenching galaxies relative to the green valley, not the fraction of green valley galaxies itself. As well, we defined the green valley with respect to the star forming main sequence, where green valley galaxies have $\Delta\text{SFMS} < -0.5$, and we did not enforce a lower threshold, unlike both Schawinski et al. (2014) and McNab et al. (2021). If we instead defined green valley galaxies in the Frontier Fields to be those with $-1 < \Delta\text{SFMS} < -0.5$, similar to Abdurro'uf et al. (2023), we find fractions similar to those of Schawinski et al. (2014) for their mixed field sample and McNab et al. (2021) for their cluster and field samples, of ∼12% and ∼14%, respectively. In Figure 4.10, we repeat the analysis from above, as shown in Figure 4.8, using this narrower definition of the green valley. We find results that are consistent with those presented above, given the large uncertainties.

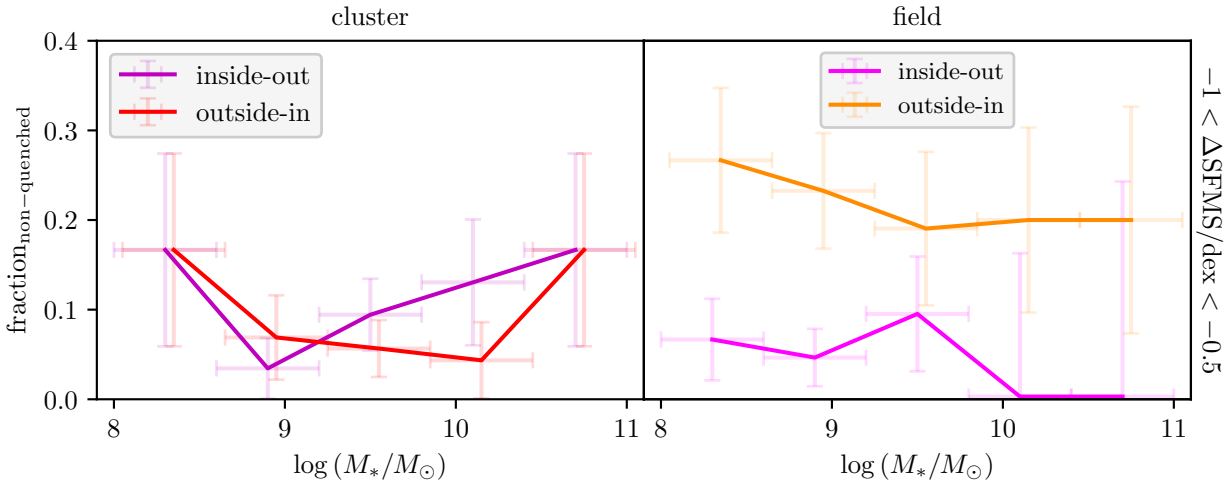


Figure 4.10: Fraction of non-quenched galaxies, per population and environment, as a function of stellar mass, that reside in a narrower definition of the green valley, similar to Abdurro'uf et al. (2023). We separate the cluster (left) from the field (right). Populations are color-coded, and error bars are determined as in Figure 4.8, with the outside-in population slightly offset horizontally from the inside-out population for visual clarity.

4.5.2 Feasibility with Galaxy Surveys

With the results presented above in mind, we are confident that the methodology as shown can be adapted to large samples of galaxies, in order to collect samples of quenching galaxies for further analysis. Specifically, current, upcoming, and proposed large-scale galaxy surveys with high spatial resolution will be able to map the distribution of star formation for galaxies across a range of redshifts. As described in Paper II, the Cosmological Advanced Survey Telescope for Optical and UV Research (CASTOR; Côté et al. 2025), a proposed far ultraviolet–blue-optical space telescope, will complete a number of community-driven surveys to image the ultraviolet/blue-optical sky. The resulting image quality will be comparable to HST, where the PSF full width at half maximum (FWHM) is $0\farcs15$ (Cheng et al. 2024a; Côté et al. 2025). Of the proposed surveys, the Wide, Deep, and Ultradeep surveys will form a tiered "wedding cake" approach, where the Wide survey will image 2227 deg^2 to a 5σ point source depth of $\sim$27.2 AB mag (Côté et al. 2025; Marshall et al. 2025). The Deep and Ultradeep surveys image smaller areas to greater depths, with the Ultradeep survey in particular imaging 1 deg^2 to a depth of $\sim$30.6 AB mag across the available filters. As shown in Paper II, the Ultradeep survey alone will provide tens of thousands of intermediate-to-massive galaxies ($M_* > 10^{9.5}$ $M_\odot$) at intermediate redshifts, from which our methodology can be applied. Beyond CASTOR, the Ultraviolet Explorer (UVEX; Kulkarni et al. 2021) will additionally provide imaging of the ultraviolet sky, though at lower resolution.

Aside from the critical ultraviolet observations for probing star formation (e.g., Vink 2020), upcoming missions like the Nancy Grace Roman Space Telescope (NGRST; Spergel et al. 2013, 2015; Akeson et al. 2019) will provide the complementary red-optical–near-infrared observations to trace the distribution of stellar mass. The imaging from NGRST will likewise be comparable in quality to HST, with a PSF FWHM less than $0\farcs15$ for all filters but the $K_{\rm F213}$-band (FWHM of $0\farcs169$; Roman Observations Time Allocation Committee & Core Community Survey Definition Committees 2025, hereafter ROTAC et al. 2025). NGRST will complete a High-Latitude Wide-Area Survey (HLWAS; e.g., Doré et al. 2018; ROTAC et al. 2025), which will similarly be comprised of wedding cake-style tiers, where the Medium tier will image 2415 deg^2 to a point source depth of $\sim$26.4 AB mag across the $Y_{\rm F106}$-, $J_{\rm F129}$-, and $H_{\rm F158}$-bands. The Deep and Ultra deep tiers add additional filters and depth, at the expense of area, where the Ultradeep tier will image 5 deg^2 to a depth of $\sim$28.1 AB mag (ROTAC et al. 2025). As well, as shown in Paper II, we expect that the NGRST HLWAS Deep tier will include on the order of tens of massive ($M > 10^{14}$ $M_\odot$) galaxy clusters at intermediate redshifts similar to the Frontier Fields, which will enable a complementary environmental analysis, similar to the one presented here. In addition to

NGRST, Euclid (Euclid Collaboration et al. 2025) and its Wide Survey (>14,600 deg^2 to a depth of 24.4 AB mag; Euclid Collaboration et al. 2022, 2025) could also provide imaging to determine stellar mass distributions, but care would need to be taken given the larger PSF (∼0.″34; Euclid Collaboration et al. 2025).

4.5.3 Limitations and Future Directions

When considering the limitations of the current work, we find a few points that merit commentary. The first concerns our required SNR threshold and extent, in order to include prospective galaxies in our sample. Above, we required H-band SNR $\geqslant 3$ for all annuli extending out to 5 R_e, to ensure that reliable stellar mass estimates can be determined when fitting spectral energy distributions. Prior to this step, we had 3643 potential galaxies, while after we had the aforementioned 1987 galaxies. This represents a loss of ∼45% of the initial sample of 3643 galaxies. If instead we could limit our analysis to 3 R_e, then we would arrive at a sample of 3001 galaxies with H-band SNR $\geqslant 3$ out to 3 R_e. This potential sample of 3001 galaxies would then represent a loss of only ∼18% of the initial sample. While this appears as an attractive option to increase the sample size, we do not seriously consider this, given the methodology presented in Paper I and refined in Paper II. In particular, as an initial consideration, we have shown above that the radial profiles for normal star forming galaxies clearly encode information out to 5 R_e (see Figure 4.4). Further, much of the differing morphological information encoded by the metrics is captured beyond 3 R_e, as seen in Figure 4.5, for the inside-out and outside-in quenching populations with R_{inner} and R_{outer}. For these reasons, we believe that simply "trimming down" to an arbitrarily smaller radial extent is seriously detrimental to the methodology presented above, where it remains unclear what value that adds to the physical investigation, beyond merely increasing the size of the sample. There clearly remain superior methods for increasing the sample size, including using large galaxy surveys as detailed above.

An additional concern is the similarity between the simulated galaxies found in TNG50, that were used to form the training set during classification (see Section 4.3.4), and the real galaxies found in the Frontier Fields. When comparing observations to simulated galaxies, it has been suggested that the AGN feedback model in TNG is overly strong (e.g., Mitchell et al. 2020; Terrazas et al. 2020; Donnari et al. 2021b; Habouzit et al. 2022; Ma et al. 2022; Voit et al. 2024; Wright et al. 2024). This could result in dramatic inside-out quenching that is not representative of real data. Indeed, in Paper I we found examples of inside-out quenching galaxies with large central suppressions of star formation, though we did not compare with observations in that work. In addition, previous studies have proposed that the process regulating environmental gas removal may be overly efficient in TNG compared

to observations (e.g., Diemer et al. 2019; Starkenburg et al. 2019; Stevens et al. 2019; Chen et al. 2024), though other studies have found good agreement (Stevens et al. 2021, 2023). This could possibly result in outside-in quenching for TNG galaxies that is pronounced compared to real galaxies.

In the context of the work presented here, we find that while there is strong similarity on a morphological basis between corresponding populations of galaxies in TNG and the Frontier Fields (i.e. star forming, inside-out, and outside-in; see Figure 4.5), populations are not directly representative of one another. Therefore, as detailed in Section 4.3.4, we opted to use the distance from the star forming main sequence, ΔSFMS, as an additional input to the kNN algorithm when classifying. We view this addition as an appropriate adaptation in order to leverage the results from the simulation, as presented in Paper I, for classification purposes. Furthermore, as discussed in Section 4.4, the distributions for ΔSFMS in TNG show significant overlap. Given this, in addition to the results of the random forest classification (completed to understand the importance of ΔSFMS; see Section 4.4), we conclude that by including ΔSFMS, we are not introducing biases toward expected results. Instead, we are using the available information to best adapt parameters that were designed for use with simulated galaxies, for use with real galaxies.

Finally, an additional limitation we face in the current work is the inability to predict quenching progress values for the quenching populations, based on the morphological metrics. In Paper I, once again using a kNN classifier, we were able to make predictions for the elapsed normalized duration of quenching, based on the overall evolution of the metrics seen there. In the current work, we attempted to apply this analysis to the Frontier Fields quenching populations using a kNN regressor, comparing it with the phase space-inferred infall time estimates. We found no strong correlation between the values for either population, which may suggest that there truly exists no correlation. However, performing a kNN regression is inherently more difficult than a more straightforward classification, as while the classification only needs broad boundaries, regression requires the fine structure of the mapping, from metrics to quenching progress, to be more robust. This analysis thus requires additional consideration, and is one of the aspects that we will revisit in future work.

Regarding future directions, a logical next step is to apply the methodology outlined here to larger samples of galaxies. As discussed above, the next decade will provide observations of many tens of thousands of galaxies that we can test on, especially when considering CASTOR and NGRST. However, in the immediate future, we can look to existing high spatial resolution datasets including COSMOS (Scoville et al. 2007) and CANDELS (Grogin et al. 2011; Koekemoer et al. 2011) to investigate field environments. We can additionally employ data from the Cluster Lensing And Supernova Survey with

Hubble[14] (CLASH; Postman et al. 2012) and the Reionization Lensing Cluster Survey[15] (RELICS; Coe et al. 2019) to investigate dense cluster environments. Compelling programs which incorporate HST data with new JWST data include the Canadian NIRISS Unbiased Cluster Survey[16] (CANUCS; Willott et al. 2022; Sarrouh et al. 2026), the JWST Advanced Deep Extragalactic Survey[17] (JADES; Rieke et al. 2023a; Eisenstein et al. 2026), the JWST Extragalactic Medium-band Survey (JEMS; Williams et al. 2023), the Prime Extragalactic Areas for Reionization and Lensing Science[18] (PEARLS; Windhorst et al. 2023) program, the Ultradeep NIRSpec and NIRCam Observations before the Epoch of Reionization[19] (UNCOVER; Bezanson et al. 2024; Suess et al. 2024) program, and the Gravitational Lensing & NIRCam Imaging to Probe Early Galaxy Formation and Sources of Reionization (GLIMPSE; Atek et al. 2025) program. As mentioned above, and as found in Paper II, the SNR requirements to accurately estimate stellar mass radial profiles are somewhat conservative (e.g., H-band SNR $\geqslant 3$), but the limiting factor when using additional datasets is the availability of ultraviolet or blue-optical imaging, as is available in the Frontier Fields.

However, instead of relying on ultraviolet imaging to determine spatially resolved SFRs after SED fitting, one could alternatively probe the distribution of star formation using Hα imaging. Such observations, specifically for the Frontier Fields and parallels, have been produced (Vulcani et al. 2015, 2016, 2017) from grating prism spectroscopy with HST in the Grism Lens-Amplified Survey from Space[20] (GLASS; Treu et al. 2015). Integral field unit observations have also been undertaken for the Frontier Fields clusters (Caminha et al. 2017; Karman et al. 2017; Lagattuta et al. 2017; Mahler et al. 2018) and field galaxies (e.g., Poggianti et al. 2017), additionally providing spatially resolved Hα imaging. Besides the programs mentioned above, other works have completed narrow band Hα imaging for intermediate redshift clusters (e.g., Kodama et al. 2004; Koyama et al. 2010, 2011, 2018), and the field (e.g., Sobral et al. 2013; Matharu et al. 2022).

Finally, future work could additionally apply the morphological metrics to observations of galaxies known to be experiencing inside-out or outside-in quenching. For instance, Type 1 AGN, particularly Type 1 Seyferts (e.g., Seyfert 1943; Antonucci 1993; Urry & Padovani 1995), as well as ram pressure stripped galaxies (e.g., Poggianti et al. 2017, 2025; Roberts & Parker 2020), are attractive classes for application. In addition to providing

[14] https://www.stsci.edu/~postman/CLASH
[15] https://relics.stsci.edu
[16] https://niriss.github.io
[17] https://jades-survey.github.io
[18] https://sites.google.com/view/jwstpearls
[19] https://jwst-uncover.github.io
[20] https://archive.stsci.edu/prepds/glass

direct measurements of the metrics on such systems, this would help to further refine the metrics for use with real galaxies.

4.6 Summary and Conclusion

In this chapter, we have investigated quenching populations of galaxies present in the Hubble Frontier Fields. Using the high quality data available for the clusters and their parallel fields, we first selected a non-quenched primary sample of 1437 galaxies with $\mathrm{SFR}_{\mathrm{total}} \geqslant 10^{-3}\ M_{\odot}\ \mathrm{yr}^{-1}$ at $0.14 < z < 0.67$, along with a quenched extended sample of 502 galaxies with lower SFRs from the same redshifts. We then applied the morphological metrics introduced in Paper I and refined in Paper II to our sample, where the morphological metrics collectively describe the spatial distribution of star formation. Through comparison with the simulated galaxies from Paper I, we classified quenching galaxies in the Frontier Fields into two main quenching pathways, which are described with different morphological signatures. The first is consistent with an inside-out quenching mechanism, where star formation is first suppressed in the interior of the galaxy, before proceeding outward. The second evolves in the opposite direction, where star formation is initially suppressed on the outskirts, and is consistent with outside-in quenching. Our main findings are as follows:

1. We find 129 galaxies have quenching consistent with an inside-out pathway, and an additional 70 galaxies have quenching consistent with an outside-in pathway. We find good agreement between the distributions of the metrics for our classified sample galaxies and their simulated counterparts (Figure 4.5). Inside-out quenching galaxies are more massive ($\log[M_*/M_{\odot}] = 10.1^{+0.6}_{-0.7}$) than outside-in quenching galaxies ($\log[M_*/M_{\odot}] = 9.3^{+0.9}_{-0.7}$) by $\Delta \log(M_*/M_{\odot}) = 0.8^{+0.2}_{-0.1}$ dex, and both populations almost exclusively populate the green valley.
2. Inside-out quenching galaxies are found more often in clusters, while the outside-in population predominantly reside in the field (Figure 4.7). In the cluster, the two populations reside in similar regions of phase space (Figure 4.6). These populations have the same median infall time, 4.0 Gyr, but the inside-out population has a smaller spread in values ($\sim$1.1 Gyr) compared to the outside-in population ($\sim$1.4 Gyr), which may have a mild preference for more recent infall times. Galaxies present in clusters are additionally more massive than those in the field, by $\sim$0.5 dex on a per-population basis.
3. Considering the prevalence of finding these systems in the cluster and the field relative to the entire non-quenched primary sample, we find that the fraction of inside-out

quenching galaxies is strongly a function of stellar mass in the cluster (Figure 4.8). This population represents ∼30% of the non-quenched sample at high masses ($M_* \gtrsim 10^{10.5}\ M_\odot$), and also increases with mass in the field, but to a lesser degree. In both environments, the outside-in population shows no mass dependence, representing $\lesssim$10% of the non-quenched sample at all masses. When considering the green valley, the combined quenching populations make up ∼30% of the overall cluster population at all stellar masses, with a similar fraction found across all masses in the field.

4. For cluster galaxies, when binned by infall time, the prevalence of these systems is similar to the overall cluster situation, where inside-out quenching galaxies similarly show a strong mass dependence (Figure 4.9). The high mass end ($M_* \gtrsim 10^{10.5}\ M_\odot$) shows mild infall time dependence as well, where these galaxies make up a larger fraction of the non-quenched sample at intermediate and ancient infall times, compared to recent infall times. The outside-in population shows no dependence on infall time, and is once again mass independent.

Viewed holistically, our results suggest that, for a subset of green valley galaxies present in the Frontier Fields, the spatial distribution of their star formation shows quenching morphologies consistent with the two pathways identified in Paper I, where galaxies experience inside-out and outside-in quenching. When comparing our results from the simulation to real data, the inside-out population is similarly more massive than the outside-in population. However, observed inside-out quenching is more common in clusters, and further, observed high-mass satellites experience inside-out quenching in clusters. This mode additionally dominates over outside-in quenching in clusters, and is not what is expected from simple environmental quenching models (e.g., Abadi et al. 1999; Roediger & Hensler 2005; Hester 2006).

These results demonstrate that star formation quenching is more complicated in real life compared to simulations, but that simulations can be readily used to help infer quenching pathways for observed samples of galaxies. Current surveys and existing datasets offer many avenues for follow-up, and with upcoming large-scale galaxy surveys, the number of galaxies that can be investigated using this methodology will number in the millions. We are thus optimistic that our procedure will be a powerful tool for the future of galaxy evolution studies.

Chapter 5

Conclusion and Future

We now summarize the work presented in this thesis, before considering the broader context and implications of the combined works. We conclude with a discussion of future directions and additional datasets that would be complementary for the type of investigations presented here.

5.1 Summary

In this thesis, we have investigated the nature of quenching galaxies in both simulations and observations. For both the simulations and observations, a priority was placed on using spatially resolved measures of star formation in particular, in order to resolve the effects of different quenching mechanisms which will suppress star formation. As described in Chapter 1, we expect that different quenching mechanisms will present different spatial signatures. These signatures can roughly be grouped into a framework that considers an inside-out quenching signature, as well as an outside-in quenching signature. As described there, inside-out quenching signatures should be found in the presence of internal mechanisms, including active galactic nuclei (AGN) feedback, as well as those driven by bar instabilities. Conversely, outside-in quenching signatures should be found for external mechanisms that are driven by the environment. Here, such external mechanisms include the stripping of gas through ram pressure stripping, in addition to mechanisms that slow, limit, or prevent gas accretion onto the halo, like starvation/strangulation. Clearly, the use of spatially resolved observations is necessary in order to distinguish these diverse pathways to quenching.

In Chapter 2, we investigated quenched galaxies in the cosmological hydrodynamical simulation TNG50 (Nelson et al. 2019b; Pillepich et al. 2019). Given the high-resolution of TNG50, we were able to probe spatially resolved quantities starting from a representative sample of 1666 galaxies with $M_* \geqslant 10^{9.5}\ M_\odot$ by $z = 0$. By comparing the star formation histories of galaxies that resided on the star forming main sequence with those that did not, we selected a sample of 361 quenched galaxies. We then investigated the spatial distribution of star formation within these 361 galaxies, and determined that four morphological metrics are adequate to describe this distribution. These metrics are based on the concentration of star formation, $C_{\rm SF}$, the size of the star forming disk relative to the stellar disk, $R_{\rm SF}$, and radii that describe sharp truncations of the star forming disk, $R_{\rm inner}$ and $R_{\rm outer}$, when viewing specific star formation rate radial profiles.

We additionally considered the evolution of these metrics for the sample of 361 quenched galaxies, through their quenching episodes. We found three prominent modes which describe their collective evolution. In the first, $C_{\rm SF}$ decreases with time, $R_{\rm SF}$ and $R_{\rm inner}$ increase with time, and $R_{\rm outer}$ is relatively constant. In the second, $C_{\rm SF}$ increases with time, $R_{\rm SF}$ and $R_{\rm outer}$ decrease with time, and $R_{\rm inner}$ is relatively constant. The first mode is describe as having an evolutionary spatial morphological signature that is consistent with an inside-out quenching mechanism, while the second is consistent with an outside-in quenching mechanism. The third mode is an intermediary mode, showing features of the previous modes, which we consider as ambiguously quenched. With these classifications, we found 78 inside-out quenched galaxies, and 185 outside-in quenched galaxies. The remaining 98 galaxies populate the ambiguous class. Further, normal star forming galaxies do not show evolution in their morphological metrics. Using a k-nearest neighbor analysis, we found that we can additionally separate these galaxies based on their morphological metrics, where this process becomes easier as galaxies become more morphologically distinct.

We found that the inside-out quenched galaxies are generally centrals in the field, and are more massive than outside-in quenched galaxies, which tend to be satellites in denser environments like groups and clusters. Outside-in galaxies experience a delay of $\sim$1 Gyr after being accreted onto a more massive structure before they begin quenching, and have quenching timescales that increase with increasing stellar mass, with an average timescale of $\sim$1.5 Gyr. Inside-out quenched galaxies likewise have quenching timescales that increase with mass, but take longer to quench on average ($\sim$2.5 Gyr).

In Chapter 3, we investigated the feasibility of recovering the morphological metrics for the above described sample of simulated galaxies, using mock observations. We used every time point along each quenched galaxy's respective quenching episode, as well as comparison star forming galaxies from the star forming main sequence with a similar stellar

mass. Through this, we arrived at a sample of 5365 quenching galaxies, and 64,128 unique star forming galaxies, for a total of nearly 70,000 galaxies. For each galaxy, we produced mock observations consistent with those that should be available from the upcoming Nancy Grace Roman Space Telescope (NGRST; Spergel et al. 2013, 2015; Akeson et al. 2019), and the proposed Cosmological Advanced Survey Telescope for Optical and UV Research (CASTOR; Côté et al. 2025), at a characteristic redshift of $z = 0.5$. Specifically, the mock observations from CASTOR cover ultraviolet and blue-optical wavelengths, providing constraints for recent star formation activity, while the NGRST mock observations cover red-optical and near-infrared wavelengths, which trace the bulk of the stellar mass. These observations are also consistent with the quality available from the Hubble Space Telescope over similar wavelengths.

We then fit the spectral energy distributions of these mock observations with a flexible hybrid star formation history that captures both recent star formation activity, as well as the evolution of the long-lived stellar populations. We found that this parameterization is able to accurately recover the key quantities of interest, star formation rate and stellar mass, in a spatially resolved sense via accurate radial profiles. With adaptations to the morphological metrics (from above) as appropriate for observations, we found that we could likewise recover these parameters to high fidelity. Using a k-nearest neighbor analysis as before, we could similarly distinguish the populations of star forming galaxies and inside-out and outside-in quenching galaxies. As was previously found, the quality of this separation improved with increasingly morphologically distinct populations.

In Chapter 4, we investigated quenching galaxies in the Hubble Frontier Fields (Lotz et al. 2017), a collection of six massive lensing clusters at intermediate redshifts ($z \approx 0.4$). Critically, the Frontier Fields additionally includes observations of a set of parallel/flanking fields, which are offset from the clusters, and which provide a comparison field sample. We first selected a sample of 1437 galaxies with $M_* \geqslant 10^8\ M_\odot$ and $\mathrm{SFR}_{\mathrm{total}} \geqslant 10^{-3}\ M_\odot\ \mathrm{yr}^{-1}$. Then, building on the previous investigations, we fit their spatially resolved spectral energy distributions to determine star formation and stellar mass radial profiles. With these radial profiles, we constructed the morphological metrics using the adaptations appropriate for observations. We then used the simulated galaxy sample from TNG50 as a training set, and using a k-nearest neighbors algorithm, classified our Frontier Fields sample galaxies into those that are consistent with an inside-out quenching signature, and an outside-in quenching signature. We additionally formed a sample that was consistent with the simulated star forming galaxies, as a consistency check.

With these classifications, we found 129 inside-out quenching galaxies, and 70 outside-in quenching galaxies. We did not specifically investigate a corresponding ambiguously quenching class, as was found in the simulation, though in principle this could be completed

as well. We additionally considered the dependence on environment and mass for these populations, and distance from the star forming main sequence.

We found that the inside-out quenching galaxies are more massive than the outside-in quenching galaxies, by $\Delta \log (M_*/M_\odot) = 0.8^{+0.2}_{-0.1}$ dex, and that the cluster galaxies are more massive than field galaxies, by $\sim$0.5 dex on average. Both populations almost exclusively populate the green valley, with very few galaxies populating the star forming main sequence. However, this result may be influenced by how we compared the simulated galaxies to the observed galaxies, and the adaptations that were adopted. The inside-out quenching population are found more often in clusters, while the outside-in population commonly reside in the field. Within clusters, the two populations reside in similar regions of phase space, and have the same median cluster infall time of 4.0 Gyr. Inside-out quenching galaxies make up $\sim$30% of the sample in the cluster at high stellar mass ($M_* \gtrsim 10^{10.5}\ M_\odot$), while outside-in quenching galaxies are equally likely to be found at all stellar masses in the cluster and in the field. The two populations of quenching galaxies additionally show little dependence on cluster infall time, except the most massive inside-out quenching galaxies, which is more commonly found for intermediate and ancient infall times.

5.2 Synthesis of Results

As demonstrated in this thesis, using spatially resolved measures of star formation is a powerful way to investigate the nature of quenching in galaxies present in simulations, as well as observations. By resolving the stellar populations and considering the spatial distribution of star formation, new insight can be gained on the prevalence and strength of different quenching mechanisms, in addition to providing constraints on their associated timescales.

Based on our findings for quenching galaxies in the simulations, we concluded that the quenching prescription within TNG was consistent with two primary mechanisms. The first was strong active galactic nuclei feedback powered by the infall of matter on to the simulated central supermassive black holes (e.g., Weinberger et al. 2017, 2018; Nelson et al. 2019b; Zinger et al. 2020). This mechanism produced a strong inside-out signature, seen through inspecting postage stamp cutouts of the simulated galaxies, as well as their morphological metrics. This mechanism was most strongly found for central galaxies residing in the field. The other mechanism is a consequence of environment, where the conditions suitable for star formation are being disrupted in the outer regions of a galaxy before the inner regions. We concluded that this is consistent with ram pressure stripping, where the gas that is fuel for star formation is effectively stripped away (e.g., Steinhauser et al. 2016;

Yun et al. 2019; Rohr et al. 2023), and found this to be common for low-mass satellite galaxies residing in dense environments. Thus, the quenching modes found within the simulation can be concisely summarized as consistent with AGN feedback for high-mass centrals in the field, and ram pressure stripping for low-mass satellites.

When we subsequently investigated the nature of quenching in observations, we found results that shared some similarities with those of the simulation, but others that differ. As noted in the body of the thesis, other works have likewise found differences between observations and simulations of quenching galaxies, specifically when discussing the TNG simulations (e.g., Diemer et al. 2019; Stevens et al. 2019; Terrazas et al. 2020; Donnari et al. 2021b). Regarding agreement, we found that inside-out quenching galaxies are more massive on average compared to outside-in quenching galaxies. If we assume that AGN feedback is the dominant quenching mechanism for high-mass galaxies, this agrees well with our findings from the simulation, and is well supported in the literature (e.g., Nelson et al. 2021; Abdurro'uf et al. 2022a, 2023; Bluck et al. 2022). However, we found that inside-out quenching galaxies in the Frontier Fields mostly reside in clusters, which is at odds with our findings from TNG. When we additionally consider similar types of analyses from the community (e.g., Tacchella et al. 2015; González Delgado et al. 2016; Abdurro'uf & Akiyama 2018; Belfiore et al. 2018; Bluck et al. 2020b), we found that while high-mass centrals experience inside-out quenching, and low-mass satellites experience environmental quenching, the current understanding is that high-mass satellites experience inside-out quenching as well (e.g., Bluck et al. 2020b; McDonough et al. 2025), making them distinct from their lower-mass counterparts.

Given these considerations, we concluded that our findings from the Frontier Fields are in agreement with those in the literature. Inside-out quenching is dominant at high stellar mass, regardless of central/satellite status, while environmental effects dominate for low-mass satellites. Therefore, the relatively simpler quenching scenario we found in the simulation does not represent the full breadth of quenching scenarios as found observationally.

However, for our work in the Frontier Fields, we relied on the morphological metrics that were first developed for use with the simulated galaxies. Therefore, while the distributions for the metrics show good agreement between observations and simulations, and thus indicate that the quenching galaxies identified as quenching inside-out and outside-in are in fact doing so, an independent verification on their quenching state is ideal. As detailed in the thesis, this could include observations which trace AGN activity, or those which are well suited for identifying signs of ram pressure stripping, such as high-resolution radio observations.

Nonetheless, we are encouraged by the success we have found in developing morphological metrics which can identify and distinguish different populations of quenching galaxies, based on their spatially resolved star formation distribution. Though additional refinement is necessary, and independent verification would support the conclusions we have drawn here, this methodology is an attractive framework for upcoming large-scale galaxy surveys. We will describe these types of surveys below.

5.3 Future Directions

As described above, independent verification of our morphological metrics is ideal for observations. This would ensure that our inside-out quenching galaxies are experiencing AGN feedback, while the outside-in quenching galaxies are experiencing ram pressure stripping, for instance.

However, in light of our findings in the Frontier Fields and how they compare to the physical scenario presented in TNG, we could also pursue additional analyses using different large, cosmological hydrodynamical simulations. In particular, the EAGLE simulation (Schaye et al. 2015) has been used in quenching investigations, especially those comparing the physical models with other simulations, including TNG. As well, the recent COLIBRE simulations (Schaye et al. 2026) could provide an additional comparison point. Importantly, COLIBRE likewise provides a different subgrid physics model than the one used in TNG, and is additionally different than the one used in EAGLE. This type of study could contrast the strength of the feedback and gas removal processes in TNG with other simulations, and again compare with expectations from observations, including like those presented above for the Frontier Fields.

Regarding existing observations, there exist many high-quality datasets that are currently archived and are publicly available. These include programs like the Cosmic Evolution Survey (COSMOS; Scoville et al. 2007) and the Cosmic Assembly Near-infrared Deep Extragalactic Survey (CANDELS; Grogin et al. 2011; Koekemoer et al. 2011), from which a robust field sample could be formed. Specifically, there is additional ultraviolet imaging that is being completed for the COSMOS field, in the COSMOS Legacy UV-Optical Treasury Campaign with Hubble (HST program ID 17802; PI: J. Kartaltepe), which would help constrain the star formation rates for galaxies present in COSMOS. As well, to form a robust cluster sample we could similarly look to other existing programs, such as the Cluster Lensing And Supernova Survey with Hubble (CLASH; Postman et al. 2012), and the Reionization Lensing Cluster Survey (RELICS; Coe et al. 2019). Observations from CLASH already include ultraviolet imaging with Hubble, using a nearly identical set of

filters as was presented in the analysis of the Frontier Fields, and while RELICS does not include any ultraviolet imaging, it does include blue-optical coverage, that probes the rest frame ultraviolet for clusters at intermediate redshifts. CLASH has imaged 25 clusters with an average redshift of $z \approx 0.4$, while RELICS has imaged 42 clusters with an average redshift of $z \approx 0.4$ as well, and they are therefore comparable to the Frontier Fields in terms of redshift coverage. For these above listed programs, given that they mostly rely on high spatial resolution imaging from Hubble, they are therefore well positioned to enable spatially resolved analyses like we have completed here.

5.3.1 Future Surveys

Beyond existing datasets, there are a number of upcoming large-scale galaxy surveys in the next decade. These surveys will provide high spatial resolution imaging for millions of galaxies, enabling the kinds of spatially resolved analyses presented here.

As discussed in detail in the thesis, the upcoming NGRST observatory will complete a High-Latitude Wide-Area Survey (HLWAS; Doré et al. 2018; Roman Observations Time Allocation Committee & Core Community Survey Definition Committees 2025) which will image $\sim$2400 deg^2 of the sky in three-band near-infrared observations, with further imaging in additional bandpasses over smaller areas. This will provide deep near-infrared data at high spatial resolution, enabling a robust determination of the spatially resolved stellar mass distribution for millions of local and intermediate redshift galaxies with $z \lesssim 0.5$. At higher redshifts like $z \approx 1$, this imaging will probe rest frame green-optical wavelengths and the near-infrared, likewise enabling a determination of stellar mass, while also providing constraints for star formation rate distributions. However, NGRST and its HLWAS would be best complemented with additional imaging at shorter wavelengths, to probe observer frame near-ultraviolet to blue-optical wavelengths, which are necessary for determining the spatial extent of star formation within galaxies. Fortunately, CASTOR is a proposed space telescope to complete such a mission, with its Wide survey designed to overlap with the HLWAS (Côté et al. 2025). This survey will obtain imaging in five bands from the ultraviolet to the blue-optical, to depths of $\sim$27.2 AB mag (5σ point source). The combination of CASTOR and NGRST will therefore cover the ultraviolet to near-infrared for millions of galaxies, enabling the kinds of spatially resolved analyses like were conducted for the Frontier Fields. In particular, large datasets like these will accelerate our understanding of galaxy evolution through sheer volume and quality.

Beyond space telescopes, the Vera C. Rubin Observatory (Ivezić et al. 2019) will complete a decade-long survey, the Legacy Survey of Space and Time (LSST; LSST Science Collaboration et al. 2009; Bianco et al. 2022). LSST will reach 10 year depths of $\sim$26.5 AB mag

across its six near-ultraviolet to near-infrared filters, imaging $\gtrsim 18,000$ deg^2 in the main survey (Bianco et al. 2022), providing a sample of billions of galaxies. In addition, Rubin will image smaller areas, about 60 deg^2 total, to greater depth, in their Deep Drilling Fields, which will be $\sim$1 mag deeper (Bianco et al. 2022). LSST, in combination with the Deep Drilling Fields, will therefore be very complementary for spatially resolved analyses of local galaxies in the next decade.

In addition to upcoming and proposed galaxy surveys, the Euclid space telescope (Euclid Collaboration et al. 2025) has already released 63.1 deg^2 of imaging in the Euclid Quick Data Release 1 (Euclid Collaboration et al. 2026d). This imaging is at the depth of the in-progress Wide Survey (Euclid Collaboration et al. 2022, 2025), which will ultimately image $>14,600$ deg^2 to a depth of 24.4 AB mag using its wide red-optical filter, along with three near-infrared bands. Aside from the Wide Survey, Euclid will also complete a Deep Survey via imaging its three Deep Fields, which will cover an area of $\sim$53 deg^2 once complete, to depths $\sim$2 mag deeper than the Wide Survey (Euclid Collaboration et al. 2022). The Euclid Deep Fields additionally have synergy with the Rubin Deep Drilling Fields, having two deep fields in common. Further, Euclid will observe six legacy fields, totaling 6.5 deg^2, via their Auxiliary Fields to greater depth ($\geqslant 4\times$) than the Wide Survey (Euclid Collaboration et al. 2022). These Auxiliary Fields include CANDELS and COSMOS (Euclid Collaboration et al. 2022). As above, the wealth of imaging available from the Wide Survey, the Auxiliary Fields, and the Deep Survey is crucial for determining the distribution of stellar mass. Though Euclid has a larger point spread function ($\sim 0\farcs34$; Euclid Collaboration et al. 2025) than NGRST or CASTOR, the observations that it is providing, and will continue to provide, are compelling for such spatially resolved analyses at lower redshift. In particular, the large area that the Euclid Wide Survey will image upon completion will provide observations for billions of galaxies, providing an extensive dataset, ripe for investigations of this nature.

From the above surveys, it is clear that the next few years will be an exciting time for spatially resolved investigations into quenching galaxies. These large-scale surveys will usher in a new age of galaxy observations, and will help to illuminate the complex mechanisms controlling galaxy evolution.

References

Abadi, M. G., Moore, B., & Bower, R. G. 1999, MNRAS, 308, 947

Abazajian, K. N., Adelman-McCarthy, J. K., Agüeros, M. A., et al. 2009, ApJS, 182, 543

Abdurro'uf, & Akiyama, M. 2017, MNRAS, 469, 2806

Abdurro'uf, & Akiyama, M. 2018, MNRAS, 479, 5083

Abdurro'uf, Lin, Y.-T., Hirashita, H., et al. 2022a, ApJ, 926, 81

Abdurro'uf, Lin, Y.-T., Wu, P.-F., & Akiyama, M. 2021, ApJS, 254, 15

Abdurro'uf, Accetta, K., Aerts, C., et al. 2022b, ApJS, 259, 35

Abdurro'uf, Coe, D., Jung, I., et al. 2023, ApJ, 945, 117

Abell, G. O. 1958, ApJS, 3, 211

Abell, G. O., Corwin, Jr., H. G., & Olowin, R. P. 1989, ApJS, 70, 1

Abraham, R. G., Ellis, R. S., Fabian, A. C., Tanvir, N. R., & Glazebrook, K. 1999, MNRAS, 303, 641

Adame, A. G., Aguilar, J., Ahlen, S., et al. 2025, JCAP, 2025, 008

Adams, N. J., Conselice, C. J., Ferreira, L., et al. 2023, MNRAS, 518, 4755

Akeson, R., Armus, L., Bachelet, E., et al. 2019, arXiv:1902.05569

Alam, S., Aubert, M., Avila, S., et al. 2021, PhRvD, 103, 083533

Alberts, S., Williams, C. C., Helton, J. M., et al. 2024, ApJ, 975, 85

Almaini, O., Wild, V., Maltby, D. T., et al. 2017, MNRAS, 472, 1401

Alongi, M., Bertelli, G., Bressan, A., et al. 1993, A&AS, 97, 851

Angulo, R. E., Springel, V., White, S. D. M., et al. 2012, MNRAS, 426, 2046

Antonucci, R. 1993, ARA&A, 31, 473

Arango-Toro, R. C., Ilbert, O., Ciesla, L., et al. 2025, A&A, 696, A159

Arendt, R. G., Odegard, N., Weiland, J. L., et al. 1998, ApJ, 508, 74

Arnouts, S., Cristiani, S., Moscardini, L., et al. 1999, MNRAS, 310, 540

Arnouts, S., Moscardini, L., Vanzella, E., et al. 2002, MNRAS, 329, 355

Astropy Collaboration, Robitaille, T. P., Tollerud, E. J., et al. 2013, A&A, 558, A33

Astropy Collaboration, Price-Whelan, A. M., Sipőcz, B. M., et al. 2018, AJ, 156, 123

Astropy Collaboration, Price-Whelan, A. M., Lim, P. L., et al. 2022, ApJ, 935, 167

Atek, H., Shuntov, M., Furtak, L. J., et al. 2023, MNRAS, 519, 1201

Atek, H., Chisholm, J., Kokorev, V., et al. 2025, arXiv:2511.07542

Baade, W., & Minkowski, R. 1954, ApJ, 119, 206

Bacon, R., Accardo, M., Adjali, L., et al. 2010, SPIE, 7735, 773508

Baes, M., & Camps, P. 2015, A&C, 12, 33

Baes, M., Verstappen, J., De Looze, I., et al. 2011, ApJS, 196, 22

Baes, M., Davies, J. I., Dejonghe, H., et al. 2003, MNRAS, 343, 1081

Baes, M., Gebek, A., Trčka, A., et al. 2024, A&A, 683, A181

Baldry, I. K., Glazebrook, K., Brinkmann, J., et al. 2004, ApJ, 600, 681

Baldry, I. K., Driver, S. P., Loveday, J., et al. 2012, MNRAS, 421, 621

Baldwin, J. A., Phillips, M. M., & Terlevich, R. 1981, PASP, 93, 5

Balogh, M. L., Morris, S. L., Yee, H. K. C., Carlberg, R. G., & Ellingson, E. 1997, ApJL, 488, L75

Balogh, M. L., Morris, S. L., Yee, H. K. C., Carlberg, R. G., & Ellingson, E. 1999, ApJ, 527, 54

Balogh, M. L., Navarro, J. F., & Morris, S. L. 2000, ApJ, 540, 113

Balogh, M. L., Schade, D., Morris, S. L., et al. 1998, ApJL, 504, L75

Balogh, M. L., McGee, S. L., Mok, A., et al. 2016, MNRAS, 456, 4364

Barnes, J. E. 1989, Natur, 338, 123

Barnes, J. E., & Hernquist, L. 1992, ARA&A, 30, 705

Beers, T. C., Flynn, K., & Gebhardt, K. 1990, AJ, 100, 32

Belfiore, F., Maiolino, R., Maraston, C., et al. 2016, MNRAS, 461, 3111

Belfiore, F., Maiolino, R., Maraston, C., et al. 2017a, MNRAS, 466, 2570

Belfiore, F., Maiolino, R., Tremonti, C., et al. 2017b, MNRAS, 469, 151

Belfiore, F., Maiolino, R., Bundy, K., et al. 2018, MNRAS, 477, 3014

Bell, E. F. 2003, ApJ, 586, 794

Bell, E. F., & de Jong, R. S. 2000, MNRAS, 312, 497

Bell, E. F., McIntosh, D. H., Katz, N., & Weinberg, M. D. 2003, ApJS, 149, 289

Bell, E. F., Wolf, C., Meisenheimer, K., et al. 2004, ApJ, 608, 752

Bell, E. F., van der Wel, A., Papovich, C., et al. 2012, ApJ, 753, 167

Bennett, A. S. 1962, MmRAS, 68, 163

Benson, A. J. 2010, PhR, 495, 33

Bertin, E., & Arnouts, S. 1996, A&AS, 117, 393

Bertone, G., & Hooper, D. 2018, RvMP, 90, 045002

Bertone, G., Hooper, D., & Silk, J. 2005, PhR, 405, 279

Bethe, H. A. 1990, RvMP, 62, 801

Bezanson, R., Labbe, I., Whitaker, K. E., et al. 2024, ApJ, 974, 92

Bianco, F. B., Ivezić, Ž., Jones, R. L., et al. 2022, ApJS, 258, 1

Bigiel, F., Leroy, A., Walter, F., et al. 2008, AJ, 136, 2846

Binney, J., & Merrifield, M. 1998, Galactic Astronomy (Princeton Univ. Press)

Binney, J., & Tremaine, S. 1987, Galactic Dynamics (Princeton Univ. Press)

Binney, J., & Tremaine, S. 2008, Galactic Dynamics, Second Edition (Princeton Univ. Press)

Birnboim, Y., & Dekel, A. 2003, MNRAS, 345, 349

Birnboim, Y., Dekel, A., & Neistein, E. 2007, MNRAS, 380, 339

Blanton, M. R., & Moustakas, J. 2009, ARA&A, 47, 159

Blanton, M. R., Hogg, D. W., Bahcall, N. A., et al. 2003, ApJ, 594, 186

Bluck, A. F. L., Maiolino, R., Brownson, S., et al. 2022, A&A, 659, A160

Bluck, A. F. L., Maiolino, R., Sánchez, S. F., et al. 2020a, MNRAS, 492, 96

Bluck, A. F. L., Maiolino, R., Piotrowska, J. M., et al. 2020b, MNRAS, 499, 230

Bluck, A. F. L., Conselice, C. J., Ormerod, K., et al. 2024, ApJ, 961, 163

Blumenthal, G. R., Faber, S. M., Primack, J. R., & Rees, M. J. 1984, Natur, 311, 517

Böhringer, H., Schuecker, P., Guzzo, L., et al. 2004, A&A, 425, 367

Bolatto, A. D., Wolfire, M., & Leroy, A. K. 2013, ARA&A, 51, 207

Bond, J. R., Cole, S., Efstathiou, G., & Kaiser, N. 1991, ApJ, 379, 440

Bond, J. R., Kofman, L., & Pogosyan, D. 1996, Natur, 380, 603

Boquien, M., Burgarella, D., Roehlly, Y., et al. 2019, A&A, 622, A103

Boselli, A., Boissier, S., Cortese, L., & Gavazzi, G. 2008, ApJ, 674, 742

Boselli, A., Fossati, M., & Sun, M. 2022, A&ARv, 30, 3

Bottrell, C., Yesuf, H. M., Popping, G., et al. 2024, MNRAS, 527, 6506

Bovy, J. 2026, Dynamics and Astrophysics of Galaxies (Princeton Univ. Press)

Bower, R. G., Benson, A. J., Malbon, R., et al. 2006, MNRAS, 370, 645

Boylan-Kolchin, M., Ma, C.-P., & Quataert, E. 2008, MNRAS, 383, 93

Bradač, M., Huang, K.-H., Fontana, A., et al. 2019, MNRAS, 489, 99

Bradley, L., Sipőcz, B., Robitaille, T., et al. 2025, astropy/photutils: 2.3.0, 2.3.0, Zenodo, doi: 10.5281/zenodo.17129028

Brammer, G. B., van Dokkum, P. G., & Coppi, P. 2008, ApJ, 686, 1503

Brammer, G. B., Whitaker, K. E., van Dokkum, P. G., et al. 2009, ApJL, 706, L173

Brammer, G. B., van Dokkum, P. G., Franx, M., et al. 2012, ApJS, 200, 13

Bravo, M., Robotham, A. S. G., Lagos, C. d. P., et al. 2023, MNRAS, 522, 4481

Breiman, L. 2001, MachL, 45, 5

Bremer, M. N., Phillipps, S., Kelvin, L. S., et al. 2018, MNRAS, 476, 12

Bressan, A., Fagotto, F., Bertelli, G., & Chiosi, C. 1993, A&AS, 100, 647

Bressan, A., Marigo, P., Girardi, L., et al. 2012, MNRAS, 427, 127

Brinchmann, J., Charlot, S., White, S. D. M., et al. 2004, MNRAS, 351, 1151

Brough, S., van de Sande, J., Owers, M. S., et al. 2017, ApJ, 844, 59

Bruzual, G., & Charlot, S. 2003, MNRAS, 344, 1000

Bryant, J. J., Owers, M. S., Robotham, A. S. G., et al. 2015, MNRAS, 447, 2857

Bundy, K., Bershady, M. A., Law, D. R., et al. 2015, ApJ, 798, 7

Burgarella, D., Buat, V., & Iglesias-Páramo, J. 2005, MNRAS, 360, 1413

Butcher, H., & Oemler, Jr., A. 1984, ApJ, 285, 426

Calzetti, D. 2013, in Secular Evolution of Galaxies, ed. J. Falcón-Barroso & J. H. Knapen, Vol. 419 (Cambridge Univ. Press)

Calzetti, D., Armus, L., Bohlin, R. C., et al. 2000, ApJ, 533, 682

Calzetti, D., Kennicutt, R. C., Engelbracht, C. W., et al. 2007, ApJ, 666, 870

Calzetti, D., Wu, S.-Y., Hong, S., et al. 2010, ApJ, 714, 1256

Caminha, G. B., Grillo, C., Rosati, P., et al. 2017, A&A, 600, A90

Camps, P., & Baes, M. 2015, A&C, 9, 20

Camps, P., & Baes, M. 2020, A&C, 31, 100381

Cannon, A. J., & Pickering, E. C. 1918, AnHar, 91, 1

Cano-Díaz, M., Sánchez, S. F., Zibetti, S., et al. 2016, ApJL, 821, L26

Cappellari, M., & Copin, Y. 2003, MNRAS, 342, 345

Cardelli, J. A., Clayton, G. C., & Mathis, J. S. 1989, ApJ, 345, 245

Carnall, A. C., Leja, J., Johnson, B. D., et al. 2019, ApJ, 873, 44

Carnall, A. C., McLure, R. J., Dunlop, J. S., & Davé, R. 2018, MNRAS, 480, 4379

Carnall, A. C., McLeod, D. J., McLure, R. J., et al. 2023, MNRAS, 520, 3974

Carnall, A. C., Cullen, F., McLure, R. J., et al. 2024, MNRAS, 534, 325

Casey, C. M., Kartaltepe, J. S., Drakos, N. E., et al. 2023, ApJ, 954, 31

Castellano, M., Amorín, R., Merlin, E., et al. 2016, A&A, 590, A31

Castellano, M., Fontana, A., Treu, T., et al. 2022, ApJL, 938, L15

Cavaliere, A., & Fusco-Femiano, R. 1976, A&A, 49, 137

Ceverino, D., Sánchez Almeida, J., Muñoz Tuñón, C., et al. 2016, MNRAS, 457, 2605

Chabrier, G. 2003, PASP, 115, 763

Charlot, S., & Fall, S. M. 2000, ApJ, 539, 718

Chen, H., Xie, L., Wang, J., et al. 2024, MNRAS, 528, 2451

Chen, Y.-M., Shi, Y., Wild, V., et al. 2019, MNRAS, 489, 5709

Cheng, I., Woods, T. E., Côté, P., et al. 2024a, AJ, 167, 178

Cheng, Z., Li, C., Li, N., Yan, R., & Mo, H. 2024b, ApJ, 961, 216

Choi, J., Dotter, A., Conroy, C., et al. 2016, ApJ, 823, 102

Ciesla, L., Buat, V., Boquien, M., et al. 2021, A&A, 653, A6

Ciesla, L., Elbaz, D., & Fensch, J. 2017, A&A, 608, A41

Ciesla, L., Elbaz, D., Schreiber, C., Daddi, E., & Wang, T. 2018, A&A, 615, A61

Ciesla, L., Boselli, A., Elbaz, D., et al. 2016, A&A, 585, A43

Ciesla, L., Gómez-Guijarro, C., Buat, V., et al. 2023, A&A, 672, A191

Ciesla, L., Elbaz, D., Ilbert, O., et al. 2024, A&A, 686, A128

Coe, D., Salmon, B., Bradač, M., et al. 2019, ApJ, 884, 85

Cole, S., Lacey, C. G., Baugh, C. M., & Frenk, C. S. 2000, MNRAS, 319, 168

Conger, K., Rudnick, G., Finn, R. A., et al. 2025, ApJ, 978, 113

Conroy, C. 2013, ARA&A, 51, 393

Conroy, C., & Gunn, J. E. 2010, ApJ, 712, 833

Conroy, C., Gunn, J. E., & White, M. 2009, ApJ, 699, 486

Conselice, C. J. 2003, ApJS, 147, 1

Conselice, C. J., Bershady, M. A., & Jangren, A. 2000, ApJ, 529, 886

Cortese, L., Fogarty, L. M. R., Bekki, K., et al. 2016, MNRAS, 463, 170

Cortijo-Ferrero, C., González Delgado, R. M., Pérez, E., et al. 2017, A&A, 607, A70

Costantin, L., Pérez-González, P. G., Vega-Ferrero, J., et al. 2023, ApJ, 946, 71

Côté, P., Woods, T. E., Hutchings, J. B., et al. 2023, Phase 0 Science Development Report for CASTOR, Tech. rep., Canadian Space Agency, Longueuil, QC

Côté, P., Woods, T. E., Hutchings, J. B., et al. 2025, JATIS, 11, 042202

Couch, W. J., & Newell, E. B. 1984, ApJS, 56, 143

Couch, W. J., & Sharples, R. M. 1987, MNRAS, 229, 423

Cover, T., & Hart, P. 1967, ITIT, 13, 21

Crain, R. A., & van de Voort, F. 2023, ARA&A, 61, 473

Crain, R. A., Schaye, J., Bower, R. G., et al. 2015, MNRAS, 450, 1937

Croom, S. M., Lawrence, J. S., Bland-Hawthorn, J., et al. 2012, MNRAS, 421, 872

Croom, S. M., Owers, M. S., Scott, N., et al. 2021, MNRAS, 505, 991

Croton, D. J., Springel, V., White, S. D. M., et al. 2006, MNRAS, 365, 11

Curtis, H. D. 1918, PLicO, 13, 9

da Cunha, E., Charmandaris, V., Díaz-Santos, T., et al. 2010, A&A, 523, A78

Dacunha, T., Belyakov, M., Adhikari, S., et al. 2022, MNRAS, 512, 4378

Daddi, E., Cimatti, A., Renzini, A., et al. 2004, ApJ, 617, 746

Daddi, E., Dickinson, M., Morrison, G., et al. 2007, ApJ, 670, 156

Dale, D. A., Helou, G., Magdis, G. E., et al. 2014, ApJ, 784, 83

Davidzon, I., Ilbert, O., Laigle, C., et al. 2017, A&A, 605, A70

Davies, J. J., Crain, R. A., Oppenheimer, B. D., & Schaye, J. 2020, MNRAS, 491, 4462

Davies, L. J. M., Robotham, A. S. G., Lagos, C. d. P., et al. 2019, MNRAS, 483, 5444

Dayal, P., & Ferrara, A. 2018, PhR, 780, 1

de Jager, C., Nieuwenhuijzen, H., & van der Hucht, K. A. 1988, A&AS, 72, 259

de los Rios, M., Martínez, H. J., Coenda, V., et al. 2021, MNRAS, 500, 1784

De Lucia, G., & Blaizot, J. 2007, MNRAS, 375, 2

Di Criscienzo, M., Merlin, E., Castellano, M., et al. 2017, A&A, 607, A30

Di Matteo, T., Springel, V., & Hernquist, L. 2005, Natur, 433, 604

Diaferio, A. 1999, MNRAS, 309, 610

Diaferio, A., & Geller, M. J. 1997, ApJ, 481, 633

Díaz-García, S., Moyano, F. D., Comerón, S., et al. 2020, A&A, 644, A38

Diemer, B., Stevens, A. R. H., Lagos, C. d. P., et al. 2019, MNRAS, 487, 1529

Dolag, K., Borgani, S., Murante, G., & Springel, V. 2009, MNRAS, 399, 497

Donnan, C. T., McLeod, D. J., Dunlop, J. S., et al. 2023, MNRAS, 518, 6011

Donnari, M., Pillepich, A., Nelson, D., et al. 2021a, MNRAS, 506, 4760

Donnari, M., Pillepich, A., Nelson, D., et al. 2019, MNRAS, 485, 4817

Donnari, M., Pillepich, A., Joshi, G. D., et al. 2021b, MNRAS, 500, 4004

Doré, O., Hirata, C., Wang, Y., et al. 2018, arXiv:1804.03628

Dotter, A. 2016, ApJS, 222, 8

Dou, H., & Yu, H. 2025, A&A, 699, A95

Dowling, T. E., & Bradley, M. E. 2023, RSPSA, 479, 20220504

Draine, B. T., & Li, A. 2007, ApJ, 657, 810

Dressler, A. 1980, ApJ, 236, 351

Dressler, A., Smail, I., Poggianti, B. M., et al. 1999, ApJS, 122, 51

Driver, S. P., Allen, P. D., Graham, A. W., et al. 2006, MNRAS, 368, 414

Driver, S. P., Hill, D. T., Kelvin, L. S., et al. 2011, MNRAS, 413, 971

Drory, N., Bundy, K., Leauthaud, A., et al. 2009, ApJ, 707, 1595

Dubois, Y., Gavazzi, R., Peirani, S., & Silk, J. 2013, MNRAS, 433, 3297

Ebeling, H., Barrett, E., Donovan, D., et al. 2007, ApJL, 661, L33

Ebeling, H., Edge, A. C., & Henry, J. P. 2001, ApJ, 553, 668

Ebeling, H., Stephenson, L. N., & Edge, A. C. 2014, ApJL, 781, L40

Edge, A. C., Ebeling, H., Bremer, M., et al. 2003, MNRAS, 339, 913

Einstein, A. 1916, AnP, 354, 769

Eisenstein, D. J., Willott, C., Alberts, S., et al. 2026, ApJS, 283, 6

Elbaz, D., Daddi, E., Le Borgne, D., et al. 2007, A&A, 468, 33

Eldridge, J. J., Stanway, E. R., Xiao, L., et al. 2017, PASA, 34, e058

Ellison, S., Ferreira, L., Wild, V., et al. 2024, OJAp, 7, 121

Ellison, S. L., Sánchez, S. F., Ibarra-Medel, H., et al. 2018, MNRAS, 474, 2039

Ellison, S. L., Wilkinson, S., Woo, J., et al. 2022, MNRAS, 517, L92

Elvis, M., Wilkes, B. J., McDowell, J. C., et al. 1994, ApJS, 95, 1

Euclid Collaboration, Scaramella, R., Amiaux, J., et al. 2022, A&A, 662, A112

Euclid Collaboration, Mellier, Y., Abdurro'uf, et al. 2025, A&A, 697, A1

Euclid Collaboration, Enia, A., Pozzetti, L., et al. 2026a, A&A, 711, A14

Euclid Collaboration, Girardi, G., Rodighiero, G., et al. 2026b, A&A, 711, A22

Euclid Collaboration, Bisigello, L., Rodighiero, G., et al. 2026c, A&A, 711, A24

Euclid Collaboration, Aussel, H., Tereno, I., et al. 2026d, A&A, 711, A1

Faber, S. M., Willmer, C. N. A., Wolf, C., et al. 2007, ApJ, 665, 265

Fabian, A. C. 2012, ARA&A, 50, 455

Fagotto, F., Bressan, A., Bertelli, G., & Chiosi, C. 1994a, A&AS, 104, 365

Fagotto, F., Bressan, A., Bertelli, G., & Chiosi, C. 1994b, A&AS, 105, 29

Fagotto, F., Bressan, A., Bertelli, G., & Chiosi, C. 1994c, A&AS, 105, 39

Falcón-Barroso, J., Lyubenova, M., van de Ven, G., et al. 2017, A&A, 597, A48

Fall, S. M., & Efstathiou, G. 1980, MNRAS, 193, 189

Fang, J. J., Faber, S. M., Koo, D. C., & Dekel, A. 2013, ApJ, 776, 63

Farouki, R., & Shapiro, S. L. 1981, ApJ, 243, 32

Fath, E. A. 1909, LicOB, 149, 71

Feldmann, R., & Bieri, R. 2026, in Encyclopedia of Astrophysics, ed. S. L. McGee, Vol. 4 (Elsevier), 576

Feldmann, R., & Mayer, L. 2015, MNRAS, 446, 1939

Ferland, G. J., Chatzikos, M., Guzmán, F., et al. 2017, RMxAA, 53, 385

Ferrarese, L., & Merritt, D. 2000, ApJL, 539, L9

Ferreira, L., Conselice, C. J., Sazonova, E., et al. 2023, ApJ, 955, 94

Finkelstein, S. L., Bagley, M. B., Arrabal Haro, P., et al. 2022, ApJL, 940, L55

Finkelstein, S. L., Bagley, M. B., Ferguson, H. C., et al. 2023, ApJL, 946, L13

Finn, R. A., Vulcani, B., Rudnick, G., et al. 2023, MNRAS, 521, 4614

Finn, R. A., Desai, V., Rudnick, G., et al. 2018, ApJ, 862, 149

Fioc, M., & Rocca-Volmerange, B. 1997, A&A, 326, 950

Fix, E., & Hodges, J. L. 1951, Discriminatory Analysis—Nonparametric Discrimination: Consistency Properties, Tech. Rep. 4: 21-49-004, USAF School of Aviation Medicine, Randolph Field, TX

Fix, E., & Hodges, J. L. 1989, International Statistical Review, 57, 238

Fontanot, F., De Lucia, G., Monaco, P., Somerville, R. S., & Santini, P. 2009, MNRAS, 397, 1776

Förster Schreiber, N. M., & Wuyts, S. 2020, ARA&A, 58, 661

Fortuni, F., Merlin, E., Fontana, A., et al. 2023, A&A, 677, A102

Fraser-McKelvie, A., Aragón-Salamanca, A., Merrifield, M., et al. 2020, MNRAS, 495, 4158

Friel, E. D. 1995, ARA&A, 33, 381

Frieman, J. A., Turner, M. S., & Huterer, D. 2008, ARA&A, 46, 385

Fujita, Y. 2004, PASJ, 56, 29

Fumagalli, M., Gavazzi, G., Scaramella, R., & Franzetti, P. 2011, A&A, 528, A46

Gao, Y., & Solomon, P. M. 2004, ApJ, 606, 271

Gardner, J. P., Mather, J. C., Clampin, M., et al. 2006, SSRv, 123, 485

Gardner, J. P., Mather, J. C., Abbott, R., et al. 2023, PASP, 135, 068001

Gaudi, B. S., Seager, S., Mennesson, B., et al. 2020, arXiv:2001.06683

Gavazzi, G., Fumagalli, M., Cucciati, O., & Boselli, A. 2010, A&A, 517, A73

Gavazzi, G., Fumagalli, M., Fossati, M., et al. 2013, A&A, 553, A89

Geller, M. J., & Huchra, J. P. 1989, Sci, 246, 897

Genel, S., Vogelsberger, M., Springel, V., et al. 2014, MNRAS, 445, 175

Genel, S., Nelson, D., Pillepich, A., et al. 2018, MNRAS, 474, 3976

Gensior, J., Kruijssen, J. M. D., & Keller, B. W. 2020, MNRAS, 495, 199

Girardi, L., Bressan, A., Bertelli, G., & Chiosi, C. 2000, A&AS, 141, 371

Girardi, L., Bressan, A., Chiosi, C., Bertelli, G., & Nasi, E. 1996, A&AS, 117, 113

Goddard, D., Thomas, D., Maraston, C., et al. 2017, MNRAS, 466, 4731

Gómez, P. L., Nichol, R. C., Miller, C. J., et al. 2003, ApJ, 584, 210

Gómez, P. L., Valkonen, L. E., Romer, A. K., et al. 2012, AJ, 144, 79

González Delgado, R. M., Pérez, E., Cid Fernandes, R., et al. 2014, A&A, 562, A47

González Delgado, R. M., García-Benito, R., Pérez, E., et al. 2015, A&A, 581, A103

González Delgado, R. M., Cid Fernandes, R., Pérez, E., et al. 2016, A&A, 590, A44

Gordon, K. D., Clayton, G. C., Misselt, K. A., Landolt, A. U., & Wolff, M. J. 2003, ApJ, 594, 279

Gorjian, V., Wright, E. L., & Chary, R. R. 2000, ApJ, 536, 550

Gott, III, J. R., Jurić, M., Schlegel, D., et al. 2005, ApJ, 624, 463

Graham, M. T., Cappellari, M., Li, H., et al. 2018, MNRAS, 477, 4711

Greene, J. E., Labbe, I., Goulding, A. D., et al. 2024, ApJ, 964, 39

Greener, M. J., Aragón-Salamanca, A., Merrifield, M. R., et al. 2020, MNRAS, 495, 2305

Grogin, N. A., Kocevski, D. D., Faber, S. M., et al. 2011, ApJS, 197, 35

Gunn, J. E., & Gott, III, J. R. 1972, ApJ, 176, 1

Guo, K., Peng, Y., Shao, L., et al. 2019, ApJ, 870, 19

Habouzit, M., Somerville, R. S., Li, Y., et al. 2022, MNRAS, 509, 3015

Hahn, C., Tinker, J. L., & Wetzel, A. 2017, ApJ, 841, 6

Haines, C. P., Pereira, M. J., Smith, G. P., et al. 2015, ApJ, 806, 101

Hall, C., Courteau, S., Jarrett, T., et al. 2018, ApJ, 865, 154

Harikane, Y., Ouchi, M., Oguri, M., et al. 2023, ApJS, 265, 5

Hayek, W., Asplund, M., Carlsson, M., et al. 2010, A&A, 517, A49

Hester, J. A. 2006, ApJ, 647, 910

Hewitt, G., Sarron, F., Balogh, M. L., et al. 2025, MNRAS, 541, 409

Ho, Z.-H., Lin, L., Jian, H.-Y., et al. 2026, arXiv:2606.01297

Hodges, J. L. 1958, ArM, 3, 469

Holwerda, B. W., Pirzkal, N., de Blok, W. J. G., & van Driel, W. 2011, MNRAS, 416, 2447

Hopkins, P. F., Hernquist, L., Cox, T. J., et al. 2006, ApJS, 163, 1

Hough, T., Cora, S. A., Haggar, R., et al. 2023, MNRAS, 518, 2398

Hubble, E. 1926, ApJ, 64, 321

Hubble, E. 1929, PNAS, 15, 168

Hubble, E., & Tolman, R. C. 1935, ApJ, 82, 302

Huertas-Company, M., Rodriguez-Gomez, V., Nelson, D., et al. 2019, MNRAS, 489, 1859

Huertas-Company, M., Iyer, K. G., Angeloudi, E., et al. 2024, A&A, 685, A48

Husser, T.-O., Wende-von Berg, S., Dreizler, S., et al. 2013, A&A, 553, A6

Ibarra-Medel, H. J., Sánchez, S. F., Avila-Reese, V., et al. 2016, MNRAS, 463, 2799

Ilbert, O., Arnouts, S., McCracken, H. J., et al. 2006, A&A, 457, 841

Ilbert, O., Salvato, M., Le Floc'h, E., et al. 2010, ApJ, 709, 644

Ilbert, O., McCracken, H. J., Le Fèvre, O., et al. 2013, A&A, 556, A55

Inoue, A. K., Shimizu, I., Iwata, I., & Tanaka, M. 2014, MNRAS, 442, 1805

Ivezić, Ž., Kahn, S. M., Tyson, J. A., et al. 2019, ApJ, 873, 111

Iyer, K., & Gawiser, E. 2017, ApJ, 838, 127

Iyer, K. G., Gawiser, E., Faber, S. M., et al. 2019, ApJ, 879, 116

Jafariyazani, M., Mobasher, B., Hemmati, S., et al. 2019, ApJ, 887, 204

Jakobsen, P., Ferruit, P., Alves de Oliveira, C., et al. 2022, A&A, 661, A80

Janulewicz, P., & Cui, W. 2025, RASTI, 4, rzaf027

Jauzac, M., Clément, B., Limousin, M., et al. 2014, MNRAS, 443, 1549

Jian, H.-Y., Lin, L., Bottrell, C., et al. 2025, ApJ, 995, 187

Jin, S., Trager, S. C., Dalton, G. B., et al. 2024, MNRAS, 530, 2688

Johnson, B. D., Leja, J., Conroy, C., & Speagle, J. S. 2021, ApJS, 254, 22

Jones, A. P., Köhler, M., Ysard, N., Bocchio, M., & Verstraete, L. 2017, A&A, 602, A46

Jones, C., & Forman, W. 1984, ApJ, 276, 38

Jørgensen, B. R., & Lindegren, L. 2005, A&A, 436, 127

Jung, I., Finkelstein, S. L., Song, M., et al. 2017, ApJ, 834, 81

Karman, W., Caputi, K. I., Caminha, G. B., et al. 2017, A&A, 599, A28

Kartaltepe, J. S., Rose, C., Vanderhoof, B. N., et al. 2023, ApJL, 946, L15

Kauffmann, G., White, S. D. M., & Guiderdoni, B. 1993, MNRAS, 264, 201

Kauffmann, G., White, S. D. M., Heckman, T. M., et al. 2004, MNRAS, 353, 713

Kauffmann, G., Heckman, T. M., Tremonti, C., et al. 2003a, MNRAS, 346, 1055

Kauffmann, G., Heckman, T. M., White, S. D. M., et al. 2003b, MNRAS, 341, 33

Kawata, D., & Mulchaey, J. S. 2008, ApJL, 672, L103

Kelsall, T., Weiland, J. L., Franz, B. A., et al. 1998, ApJ, 508, 44

Kennicutt, Jr., R. C. 1989, ApJ, 344, 685

Kennicutt, Jr., R. C. 1998a, ApJ, 498, 541

Kennicutt, Jr., R. C. 1998b, ARA&A, 36, 189

Kennicutt, Jr., R. C., & Evans, N. J. 2012, ARA&A, 50, 531

Kewley, L. J., Dopita, M. A., Sutherland, R. S., Heisler, C. A., & Trevena, J. 2001, ApJ, 556, 121

King, A., & Pounds, K. 2015, ARA&A, 53, 115

Kocevski, D. D., Onoue, M., Inayoshi, K., et al. 2023, ApJL, 954, L4

Kodama, T., Balogh, M. L., Smail, I., Bower, R. G., & Nakata, F. 2004, MNRAS, 354, 1103

Koekemoer, A. M., Faber, S. M., Ferguson, H. C., et al. 2011, ApJS, 197, 36

Koopmann, R. A., & Kenney, J. D. P. 2004a, ApJ, 613, 851

Koopmann, R. A., & Kenney, J. D. P. 2004b, ApJ, 613, 866

Koyama, Y., Kodama, T., Nakata, F., Shimasaku, K., & Okamura, S. 2011, ApJ, 734, 66

Koyama, Y., Kodama, T., Shimasaku, K., et al. 2010, MNRAS, 403, 1611

Koyama, Y., Hayashi, M., Tanaka, M., et al. 2018, PASJ, 70, S21

Krabbe, A. C., Hernandez-Jimenez, J. A., Mendes de Oliveira, C., et al. 2024, MNRAS, 528, 1125

Kravtsov, A. V., & Borgani, S. 2012, ARA&A, 50, 353

Kriek, M., & Conroy, C. 2013, ApJL, 775, L16

Kriek, M., van Dokkum, P. G., Labbé, I., et al. 2009, ApJ, 700, 221

Kristian, J., Sandage, A., & Westphal, J. A. 1978, ApJ, 221, 383

Kroupa, P. 2001, MNRAS, 322, 231

Kulkarni, S. R., Harrison, F. A., Grefenstette, B. W., et al. 2021, arXiv:2111.15608

Labbé, I., van Dokkum, P., Nelson, E., et al. 2023, Natur, 616, 266

Labbé, I., Greene, J. E., Bezanson, R., et al. 2025, ApJ, 978, 92

Lacy, M., Storrie-Lombardi, L. J., Sajina, A., et al. 2004, ApJS, 154, 166

Lada, C. J., & Lada, E. A. 2003, ARA&A, 41, 57

Lagattuta, D. J., Richard, J., Clément, B., et al. 2017, MNRAS, 469, 3946

Lagattuta, D. J., Richard, J., Bauer, F. E., et al. 2019, MNRAS, 485, 3738

Lang, P., Wuyts, S., Somerville, R. S., et al. 2014, ApJ, 788, 11

Lange, R., Driver, S. P., Robotham, A. S. G., et al. 2015, MNRAS, 447, 2603

Larson, R. B. 1969, MNRAS, 145, 271

Larson, R. B. 1981, MNRAS, 194, 809

Larson, R. B., Tinsley, B. M., & Caldwell, C. N. 1980, ApJ, 237, 692

Lauer, T. R., Postman, M., Strauss, M. A., Graves, G. J., & Chisari, N. E. 2014, ApJ, 797, 82

Lawlor-Forsyth, C., Balogh, M. L., McGee, S. L., & Rudnick, G. H. 2026a, arXiv:2607.15638

Lawlor-Forsyth, C., Balogh, M. L., Sazonova, E., et al. 2026b, ApJ, 1000, 61

Le Borgne, J.-F., Bruzual, G., Pelló, R., et al. 2003, A&A, 402, 433

Leavitt, H. S. 1907, AnHar, 60, 87

Leavitt, H. S., & Pickering, E. C. 1912, HarCi, 173, 1

Leitherer, C., Schaerer, D., Goldader, J. D., et al. 1999, ApJS, 123, 3

Leja, J., Carnall, A. C., Johnson, B. D., Conroy, C., & Speagle, J. S. 2019a, ApJ, 876, 3

Leja, J., Johnson, B. D., Conroy, C., van Dokkum, P. G., & Byler, N. 2017, ApJ, 837, 170

Leja, J., Tacchella, S., & Conroy, C. 2019b, ApJL, 880, L9

Lejeune, T., Cuisinier, F., & Buser, R. 1997, A&AS, 125, 229

Lemaître, G. 1927, ASSB, 47, 49

Lemaître, G. 1931, MNRAS, 91, 483

Lemaître, G. 1933, ASSB, 53, 51

Lemaître, G. A., & MacCallum, M. A. H. 1997, GReGr, 29, 641

Leroy, A. K., Walter, F., Brinks, E., et al. 2008, AJ, 136, 2782

Leung, H.-H., Wild, V., Papathomas, M., Carnall, A. C., & Chen, Y. 2025, MNRAS, 543, 738

Lewis, I., Balogh, M., De Propris, R., et al. 2002, MNRAS, 334, 673

Li, C., Wang, E., Lin, L., et al. 2015, ApJ, 804, 125

Libeskind, N. I., van de Weygaert, R., Cautun, M., et al. 2018, MNRAS, 473, 1195

Lin, L., Hsieh, B.-C., Pan, H.-A., et al. 2019, ApJ, 872, 50

Lintott, C., Schawinski, K., Bamford, S., et al. 2011, MNRAS, 410, 166

Lintott, C. J., Schawinski, K., Slosar, A., et al. 2008, MNRAS, 389, 1179

Liu, Q., Wang, E., Lin, Z., et al. 2018, ApJ, 857, 17

Lotz, J. M., Primack, J., & Madau, P. 2004, AJ, 128, 163

Lotz, J. M., Davis, M., Faber, S. M., et al. 2008, ApJ, 672, 177

Lotz, J. M., Koekemoer, A., Coe, D., et al. 2017, ApJ, 837, 97

Lotz, M., Remus, R.-S., Dolag, K., Biviano, A., & Burkert, A. 2019, MNRAS, 488, 5370

Lovell, C. C., Roper, W. J., Vijayan, A. P., et al. 2025, OJAp, 8, 152

LSST Science Collaboration, Abell, P. A., Allison, J., et al. 2009, arXiv:0912.0201

LUVOIR Team. 2019, arXiv:1912.06219

Lynden-Bell, D. 1969, Natur, 223, 690

Ma, W., Liu, K., Guo, H., et al. 2022, ApJ, 941, 205

Madau, P. 1995, ApJ, 441, 18

Madau, P., & Dickinson, M. 2014, ARA&A, 52, 415

Mahajan, S., Mamon, G. A., & Raychaudhury, S. 2011, MNRAS, 416, 2882

Mahler, G., Richard, J., Clément, B., et al. 2018, MNRAS, 473, 663

Maio, U., Dolag, K., Ciardi, B., & Tornatore, L. 2007, MNRAS, 379, 963

Mak, D. S. Y., Pierpaoli, E., & Osborne, S. J. 2011, ApJ, 736, 116

Man, A., & Belli, S. 2018, NatAs, 2, 695

Mann, A. W., & Ebeling, H. 2012, MNRAS, 420, 2120

Maraston, C. 2005, MNRAS, 362, 799

Marigo, P., Girardi, L., Bressan, A., et al. 2017, ApJ, 835, 77

Marinelli, M., Green, J., et al. 2025, in Wide Field Camera 3 Instrument Handbook, Version 18.0 (Baltimore: STScI)

Marshall, M. A., Amen, L., Woods, T. E., et al. 2025, MNRAS, 537, 1703

Martig, M., Bournaud, F., Teyssier, R., & Dekel, A. 2009, ApJ, 707, 250

Martin, D. C., Fanson, J., Schiminovich, D., et al. 2005, ApJL, 619, L1

Martin, D. C., Wyder, T. K., Schiminovich, D., et al. 2007, ApJS, 173, 342

Martínez, H. J., Coenda, V., Muriel, H., de los Rios, M., & Ruiz, A. N. 2023, MNRAS, 519, 4360

Matharu, J., Muzzin, A., Brammer, G. B., et al. 2020, MNRAS, 493, 6011

Matharu, J., Muzzin, A., Brammer, G. B., et al. 2021, ApJ, 923, 222

Matharu, J., Papovich, C., Simons, R. C., et al. 2022, ApJ, 937, 16

Matthews, T. A., & Sandage, A. R. 1963, ApJ, 138, 30

McAlpine, S., Helly, J. C., Schaller, M., et al. 2016, A&C, 15, 72

McCarthy, I. G., Frenk, C. S., Font, A. S., et al. 2008, MNRAS, 383, 593

McCracken, H. J., Milvang-Jensen, B., Dunlop, J., et al. 2012, A&A, 544, A156

McDonough, B., Curtis, O., & Brainerd, T. G. 2023, ApJ, 958, 19

McDonough, B., Curtis, O., & Brainerd, T. G. 2025, ApJ, 978, 67

McGee, S. L., Balogh, M. L., Bower, R. G., Font, A. S., & McCarthy, I. G. 2009, MNRAS, 400, 937

McGee, S. L., Bower, R. G., & Balogh, M. L. 2014, MNRAS, 442, L105

McNab, K., Balogh, M. L., van der Burg, R. F. J., et al. 2021, MNRAS, 508, 157

McNamara, B. R., & Nulsen, P. E. J. 2007, ARA&A, 45, 117

McNamara, B. R., & Nulsen, P. E. J. 2012, NJPh, 14, 055023

Medezinski, E., Umetsu, K., Okabe, N., et al. 2016, ApJ, 817, 24

Medling, A. M., Cortese, L., Croom, S. M., et al. 2018, MNRAS, 475, 5194

Mendez, A. J., Coil, A. L., Lotz, J., et al. 2011, ApJ, 736, 110

Merlin, E., Amorín, R., Castellano, M., et al. 2016, A&A, 590, A30

Miller, G. E., & Scalo, J. M. 1979, ApJS, 41, 513

Mitchell, P. D., Schaye, J., Bower, R. G., & Crain, R. A. 2020, MNRAS, 494, 3971

Mo, H., van den Bosch, F. C., & White, S. 2010, Galaxy Formation and Evolution (Cambridge Univ. Press)

Momcheva, I. G., Brammer, G. B., van Dokkum, P. G., et al. 2016, ApJS, 225, 27

Moore, B., Katz, N., Lake, G., Dressler, A., & Oemler, A. 1996, Natur, 379, 613

Moore, B., Lake, G., & Katz, N. 1998, ApJ, 495, 139

Moore, B., Lake, G., Quinn, T., & Stadel, J. 1999, MNRAS, 304, 465

Morgan, C. R., Balogh, M. L., Boselli, A., et al. 2024, A&A, 691, A20

Morishita, T., Abramson, L. E., Treu, T., et al. 2017, ApJ, 835, 254

Morrissey, P., Matuszewski, M., Martin, D. C., et al. 2018, ApJ, 864, 93

Morselli, L., Popesso, P., Cibinel, A., et al. 2019, A&A, 626, A61

Moustakas, J., Coil, A. L., Aird, J., et al. 2013, ApJ, 767, 50

Mowla, L., van der Wel, A., van Dokkum, P., & Miller, T. B. 2019, ApJL, 872, L13

Muzzin, A., Wilson, G., Yee, H. K. C., et al. 2012, ApJ, 746, 188

Muzzin, A., Marchesini, D., Stefanon, M., et al. 2013, ApJ, 777, 18

Naab, T., & Burkert, A. 2003, ApJ, 597, 893

Naab, T., & Ostriker, J. P. 2017, ARA&A, 55, 59

Naidu, R. P., Oesch, P. A., van Dokkum, P., et al. 2022, ApJL, 940, L14

Nanayakkara, T., Glazebrook, K., Jacobs, C., et al. 2024, NatSR, 14, 3724

Nantais, J. B., Muzzin, A., van der Burg, R. F. J., et al. 2017, MNRAS, 465, L104

Narayanan, D., Turk, M. J., Robitaille, T., et al. 2021, ApJS, 252, 12

Nedkova, K. V., Häußler, B., Marchesini, D., et al. 2021, MNRAS, 506, 928

Neistein, E., van den Bosch, F. C., & Dekel, A. 2006, MNRAS, 372, 933

Nelson, D., Pillepich, A., Ayromlou, M., et al. 2024, A&A, 686, A157

Nelson, D., Pillepich, A., Genel, S., et al. 2015, A&C, 13, 12

Nelson, D., Pillepich, A., Springel, V., et al. 2018, MNRAS, 475, 624

Nelson, D., Springel, V., Pillepich, A., et al. 2019a, ComAC, 6, 2

Nelson, D., Pillepich, A., Springel, V., et al. 2019b, MNRAS, 490, 3234

Nelson, E. J., Tacchella, S., Diemer, B., et al. 2021, MNRAS, 508, 219

Neumann, J., Fragkoudi, F., Pérez, I., et al. 2020, A&A, 637, A56

Niemiec, A., Jauzac, M., Eckert, D., et al. 2023, MNRAS, 524, 2883

Noeske, K. G., Weiner, B. J., Faber, S. M., et al. 2007, ApJL, 660, L43

Oemler, Jr., A. 1974, ApJ, 194, 1

Olsen, C., Gawiser, E., Welker, C., et al. 2026, ApJ, 1001, 82

Oman, K. A., & Hudson, M. J. 2016, MNRAS, 463, 3083

Oman, K. A., Hudson, M. J., & Behroozi, P. S. 2013, MNRAS, 431, 2307

Owers, M. S., Randall, S. W., Nulsen, P. E. J., et al. 2011, ApJ, 728, 27

Owers, M. S., Hudson, M. J., Oman, K. A., et al. 2019, ApJ, 873, 52

Oxland, M., Parker, L. C., de Carvalho, R. R., & Sampaio, V. M. 2024, MNRAS, 529, 3651

Padovani, P., Alexander, D. M., Assef, R. J., et al. 2017, A&ARv, 25, 2

Pagul, A., Sánchez, F. J., Davidzon, I., et al. 2024, ApJS, 273, 10

Pakmor, R., Bauer, A., & Springel, V. 2011, MNRAS, 418, 1392

Pakmor, R., Springel, V., Bauer, A., et al. 2016, MNRAS, 455, 1134

Pakmor, R., Springel, V., Coles, J. P., et al. 2023, MNRAS, 524, 2539

Papaderos, P., Breda, I., Humphrey, A., et al. 2022, A&A, 658, A74

Park, C., & Hwang, H. S. 2009, ApJ, 699, 1595

Park, M., Tacchella, S., Nelson, E. J., et al. 2022, MNRAS, 515, 213

Pasquali, A., Smith, R., Gallazzi, A., et al. 2019, MNRAS, 484, 1702

Pawlik, M. M., Wild, V., Walcher, C. J., et al. 2016, MNRAS, 456, 3032

Pedregosa, F., Varoquaux, G., Gramfort, A., et al. 2011, JMLR, 12, 2825

Peebles, P. J., & Ratra, B. 2003, RvMP, 75, 559

Peng, Y., Lilly, S. J., Renzini, A., & Carollo, M. 2012, ApJ, 757, 4

Peng, Y., Lilly, S. J., Renzini, A., & Carollo, M. 2014, ApJ, 790, 95

Peng, Y., Maiolino, R., & Cochrane, R. 2015, Natur, 521, 192

Peng, Y., Lilly, S. J., Kovač, K., et al. 2010, ApJ, 721, 193

Pérez, E., Cid Fernandes, R., González Delgado, R. M., et al. 2013, ApJL, 764, L1

Perlmutter, S., Aldering, G., Goldhaber, G., et al. 1999, ApJ, 517, 565

Peterson, J. R., & Fabian, A. C. 2006, PhR, 427, 1

Phillipps, S., Bremer, M. N., Hopkins, A. M., et al. 2019, MNRAS, 485, 5559

Pickles, A. J. 1998, PASP, 110, 863

Pierre, M., Valtchanov, I., Altieri, B., et al. 2004, JCAP, 2004, 011

Pietrinferni, A., Cassisi, S., Salaris, M., & Castelli, F. 2004, ApJ, 612, 168

Pilbratt, G. L., Riedinger, J. R., Passvogel, T., et al. 2010, A&A, 518, L1

Pillepich, A., Nelson, D., Hernquist, L., et al. 2018a, MNRAS, 475, 648

Pillepich, A., Springel, V., Nelson, D., et al. 2018b, MNRAS, 473, 4077

Pillepich, A., Nelson, D., Springel, V., et al. 2019, MNRAS, 490, 3196

Planck Collaboration, Ade, P. A. R., Aghanim, N., et al. 2016, A&A, 594, A13

Planck Collaboration, Aghanim, N., Akrami, Y., et al. 2020, A&A, 641, A6

Poggianti, B. M., Smail, I., Dressler, A., et al. 1999, ApJ, 518, 576

Poggianti, B. M., Fasano, G., Omizzolo, A., et al. 2016, AJ, 151, 78

Poggianti, B. M., Moretti, A., Gullieuszik, M., et al. 2017, ApJ, 844, 48

Poggianti, B. M., Gullieuszik, M., Tonnesen, S., et al. 2019, MNRAS, 482, 4466

Poggianti, B. M., Vulcani, B., Tomicic, N., et al. 2025, A&A, 699, A357

Popesso, P., Concas, A., Cresci, G., et al. 2023, MNRAS, 519, 1526

Popper, D. M. 1980, ARA&A, 18, 115

Postman, M., & Geller, M. J. 1984, ApJ, 281, 95

Postman, M., Coe, D., Benítez, N., et al. 2012, ApJS, 199, 25

Poulton, R. J. J., Power, C., Robotham, A. S. G., & Elahi, P. J. 2020, MNRAS, 491, 3820

Powell, M. C., Urry, C. M., Cardamone, C. N., et al. 2017, ApJ, 835, 22

Pozzetti, L., Bolzonella, M., Zucca, E., et al. 2010, A&A, 523, A13

Press, W. H., & Schechter, P. 1974, ApJ, 187, 425

Prugniel, P., & Soubiran, C. 2001, A&A, 369, 1048

Quai, S., Hani, M. H., Ellison, S. L., Patton, D. R., & Woo, J. 2021, MNRAS, 504, 1888

Quilis, V., Moore, B., & Bower, R. 2000, Sci, 288, 1617

Reach, W. T., Franz, B. A., & Weiland, J. L. 1997, Icar, 127, 461

Rees, M. J., & Ostriker, J. P. 1977, MNRAS, 179, 541

Regos, E., & Geller, M. J. 1989, AJ, 98, 755

Renzini, A., & Peng, Y.-j. 2015, ApJL, 801, L29

Rhee, J., Smith, R., Choi, H., et al. 2017, ApJ, 843, 128

Rieke, M. J., Robertson, B., Tacchella, S., et al. 2023a, ApJS, 269, 16

Rieke, M. J., Kelly, D. M., Misselt, K., et al. 2023b, PASP, 135, 028001

Riess, A. G., Filippenko, A. V., Challis, P., et al. 1998, AJ, 116, 1009

Rigby, J. R., Lightsey, P. A., García Marín, M., et al. 2023, PASP, 135, 048002

Roberts, I. D., & Parker, L. C. 2020, MNRAS, 495, 554

Roberts, I. D., van Weeren, R. J., McGee, S. L., et al. 2021, A&A, 650, A111

Roberts, I. D., Lang, M., Trotsenko, D., et al. 2022, ApJ, 941, 77

Rodighiero, G., Daddi, E., Baronchelli, I., et al. 2011, ApJL, 739, L40

Rodriguez-Gomez, V., Genel, S., Vogelsberger, M., et al. 2015, MNRAS, 449, 49

Rodriguez-Gomez, V., Snyder, G. F., Lotz, J. M., et al. 2019, MNRAS, 483, 4140

Rodríguez Montero, F., Davé, R., Wild, V., Anglés-Alcázar, D., & Narayanan, D. 2019, MNRAS, 490, 2139

Roediger, E., & Hensler, G. 2005, A&A, 433, 875

Rohr, E., Pillepich, A., Nelson, D., et al. 2023, MNRAS, 524, 3502

Roman Observations Time Allocation Committee, & Core Community Survey Definition Committees. 2025, arXiv:2505.10574

Roman-Oliveira, F., Chies-Santos, A. L., Ferrari, F., Lucatelli, G., & Rodríguez Del Pino, B. 2021, MNRAS, 500, 40

Roper, W., Lovell, C., Vijayan, A., et al. 2026, JOSS, 11, 9436

Rowlands, K., Wild, V., Bourne, N., et al. 2018a, MNRAS, 473, 1168

Rowlands, K., Heckman, T., Wild, V., et al. 2018b, MNRAS, 480, 2544

Ryden, B. 2016, Introduction to Cosmology (Cambridge Univ. Press)

Sackmann, I.-J., Boothroyd, A. I., & Kraemer, K. E. 1993, ApJ, 418, 457

Sagiv, I., Gal-Yam, A., Ofek, E. O., et al. 2014, AJ, 147, 79

Salpeter, E. E. 1955, ApJ, 121, 161

Sánchez, S. F., Kennicutt, R. C., Gil de Paz, A., et al. 2012, A&A, 538, A8

Sánchez, S. F., Rosales-Ortega, F. F., Iglesias-Páramo, J., et al. 2014, A&A, 563, A49

Sánchez, S. F., Avila-Reese, V., Hernandez-Toledo, H., et al. 2018, RMxAA, 54, 217

Sánchez-Blázquez, P., Peletier, R. F., Jiménez-Vicente, J., et al. 2006, MNRAS, 371, 703

Sánchez-Menguiano, L., Sánchez, S. F., Pérez, I., et al. 2016, A&A, 587, A70

Sandage, A. R. 1953, AJ, 58, 61

Sanders, D. B., & Mirabel, I. F. 1996, ARA&A, 34, 749

Sanders, D. B., Soifer, B. T., Elias, J. H., et al. 1988, ApJ, 325, 74

Sarrouh, G. T. E., Asada, Y., Martis, N. S., et al. 2026, ApJS, 282, 3

Sazonova, E., Morgan, C., Balogh, M., et al. 2024, OJAp, 7, 77

Scalo, J. M. 1986, FCPh, 11, 1

Schaefer, A. L., Croom, S. M., Allen, J. T., et al. 2017, MNRAS, 464, 121

Schaefer, A. L., Croom, S. M., Scott, N., et al. 2019, MNRAS, 483, 2851

Schaller, G., Schaerer, D., Meynet, G., & Maeder, A. 1992, A&AS, 96, 269

Schawinski, K., Thomas, D., Sarzi, M., et al. 2007, MNRAS, 382, 1415

Schawinski, K., Urry, C. M., Simmons, B. D., et al. 2014, MNRAS, 440, 889

Schaye, J., Crain, R. A., Bower, R. G., et al. 2015, MNRAS, 446, 521

Schaye, J., Kugel, R., Schaller, M., et al. 2023, MNRAS, 526, 4978

Schaye, J., Chaikin, E., Schaller, M., et al. 2026, MNRAS, 548, stag375

Schechter, P. 1976, ApJ, 203, 297

Schlegel, D. J., Finkbeiner, D. P., & Davis, M. 1998, ApJ, 500, 525

Schmidt, M. 1959, ApJ, 129, 243

Schmidt, M. 1963, Natur, 197, 1040

Schreiber, C., Glazebrook, K., Nanayakkara, T., et al. 2018a, A&A, 618, A85

Schreiber, C., Labbé, I., Glazebrook, K., et al. 2018b, A&A, 611, A22

Schweizer, F., Burns, C. R., Madore, B. F., et al. 2008, AJ, 136, 1482

Scoville, N., Aussel, H., Brusa, M., et al. 2007, ApJS, 172, 1

Seyfert, C. K. 1943, ApJ, 97, 28

Shen, L., Papovich, C., Yang, G., et al. 2023, ApJ, 950, 7

Shen, S., Mo, H. J., White, S. D. M., et al. 2003, MNRAS, 343, 978

Shibuya, T., Ouchi, M., & Harikane, Y. 2015, ApJS, 219, 15

Shields, G. A. 1999, PASP, 111, 661

Shipley, H. V., Lange-Vagle, D., Marchesini, D., et al. 2018, ApJS, 235, 14

Shu, F. H., Adams, F. C., & Lizano, S. 1987, ARA&A, 25, 23

Shull, J. M., Smith, B. D., & Danforth, C. W. 2012, ApJ, 759, 23

Shuntov, M., Akins, H. B., Paquereau, L., et al. 2025, A&A, 704, A339

Silk, J., & Mamon, G. A. 2012, RAA, 12, 917

Sirianni, M., Jee, M. J., Benítez, N., et al. 2005, PASP, 117, 1049

Skelton, R. E., Whitaker, K. E., Momcheva, I. G., et al. 2014, ApJS, 214, 24

Slipher, V. M. 1913, LowOB, 2, 56

Slipher, V. M. 1915, PA, 23, 21

Smethurst, R. J., Lintott, C. J., Simmons, B. D., et al. 2015, MNRAS, 450, 435

Smith, D. J. B., & Hayward, C. C. 2018, MNRAS, 476, 1705

Sobral, D., Smail, I., Best, P. N., et al. 2013, MNRAS, 428, 1128

Speagle, J. S., Steinhardt, C. L., Capak, P. L., & Silverman, J. D. 2014, ApJS, 214, 15

Spergel, D., Gehrels, N., Breckinridge, J., et al. 2013, arXiv:1305.5422

Spergel, D., Gehrels, N., Baltay, C., et al. 2015, arXiv:1503.03757

Spindler, A., Wake, D., Belfiore, F., et al. 2018, MNRAS, 476, 580

Spinoso, D., Bonoli, S., Dotti, M., et al. 2017, MNRAS, 465, 3729

Springel, V. 2010, MNRAS, 401, 791

Springel, V., Di Matteo, T., & Hernquist, L. 2005a, ApJL, 620, L79

Springel, V., Di Matteo, T., & Hernquist, L. 2005b, MNRAS, 361, 776

Springel, V., Frenk, C. S., & White, S. D. M. 2006, Natur, 440, 1137

Springel, V., White, S. D. M., Tormen, G., & Kauffmann, G. 2001, MNRAS, 328, 726

Springel, V., White, S. D. M., Jenkins, A., et al. 2005c, Natur, 435, 629

Springel, V., Pakmor, R., Pillepich, A., et al. 2018, MNRAS, 475, 676

Stark, D. V., et al. 2025, in Advanced Camera for Surveys Instrument Handbook, Version 25.0 (Baltimore: STScI)

Starkenburg, T. K., Tonnesen, S., & Kopenhafer, C. 2019, ApJL, 874, L17

Steinhardt, C. L., Jauzac, M., Acebron, A., et al. 2020, ApJS, 247, 64

Steinhauser, D., Schindler, S., & Springel, V. 2016, A&A, 591, A51

Stern, D., Eisenhardt, P., Gorjian, V., et al. 2005, ApJ, 631, 163

Stevens, A. R. H., Diemer, B., Lagos, C. d. P., et al. 2019, MNRAS, 483, 5334

Stevens, A. R. H., Lagos, C. d. P., Cortese, L., et al. 2021, MNRAS, 502, 3158

Stevens, A. R. H., Brown, T., Diemer, B., et al. 2023, ApJL, 957, L19

Strateva, I., Ivezić, Ž., Knapp, G. R., et al. 2001, AJ, 122, 1861

Struble, M. F., & Rood, H. J. 1991, ApJS, 77, 363

Su, K.-Y., Hopkins, P. F., Hayward, C. C., et al. 2019, MNRAS, 487, 4393

Suess, K. A., Weaver, J. R., Price, S. H., et al. 2024, ApJ, 976, 101

Tacchella, S., Dekel, A., Carollo, C. M., et al. 2016, MNRAS, 458, 242

Tacchella, S., Carollo, C. M., Renzini, A., et al. 2015, Sci, 348, 314

Tacchella, S., Carollo, C. M., Förster Schreiber, N. M., et al. 2018, ApJ, 859, 56

Tacchella, S., Conroy, C., Faber, S. M., et al. 2022, ApJ, 926, 134

Tacconi, L. J., Genzel, R., Smail, I., et al. 2008, ApJ, 680, 246

Takada, M., Ellis, R. S., Chiba, M., et al. 2014, PASJ, 66, R1

Tan, V. Y. Y., Muzzin, A., Marsan, Z. C., et al. 2022, ApJ, 933, 30

Tan, V. Y. Y., Muzzin, A., Sarrouh, G. T. E., et al. 2024, arXiv:2412.07829

Taylor, E. N., Hopkins, A. M., Baldry, I. K., et al. 2015, MNRAS, 446, 2144

Taylor, M. B. 2005, ASPC, 347, 29

Terrazas, B. A., Bell, E. F., Pillepich, A., et al. 2020, MNRAS, 493, 1888

Tinker, J. L., & Wetzel, A. R. 2010, ApJ, 719, 88

Tinsley, B. M. 1980, FCPh, 5, 287

Tolman, R. C. 1930, PNAS, 16, 511

Tolman, R. C. 1934, Relativity, Thermodynamics, and Cosmology (Clarendon Press)

Tomczak, A. R., Quadri, R. F., Tran, K.-V. H., et al. 2014, ApJ, 783, 85

Toomre, A. 1977, in Evolution of Galaxies and Stellar Populations, ed. B. M. Tinsley & R. B. G. Larson, D. Campbell, 401

Toomre, A., & Toomre, J. 1972, ApJ, 178, 623

Torres, G., Andersen, J., & Giménez, A. 2010, A&ARv, 18, 67

Torrey, P., Vogelsberger, M., Genel, S., et al. 2014, MNRAS, 438, 1985

Trayford, J. W., Theuns, T., Bower, R. G., et al. 2016, MNRAS, 460, 3925

Treu, T., Schmidt, K. B., Brammer, G. B., et al. 2015, ApJ, 812, 114

Treu, T., Roberts-Borsani, G., Bradac, M., et al. 2022, ApJ, 935, 110

Trčka, A., Baes, M., Camps, P., et al. 2022, MNRAS, 516, 3728

Tully, R. B., Courtois, H., Hoffman, Y., & Pomarède, D. 2014, Natur, 513, 71

Tumlinson, J., Peeples, M. S., & Werk, J. K. 2017, ARA&A, 55, 389

Umetsu, K., Broadhurst, T., Zitrin, A., Medezinski, E., & Hsu, L.-Y. 2011, ApJ, 729, 127

Umetsu, K., Zitrin, A., Gruen, D., et al. 2016, ApJ, 821, 116

Urry, C. M., & Padovani, P. 1995, PASP, 107, 803

van den Bosch, F. C., Aquino, D., Yang, X., et al. 2008, MNRAS, 387, 79

van der Burg, R. F. J., Rudnick, G., Balogh, M. L., et al. 2020, A&A, 638, A112

van der Wel, A., Franx, M., van Dokkum, P. G., et al. 2014, ApJ, 788, 28

Vazdekis, A., Sánchez-Blázquez, P., Falcón-Barroso, J., et al. 2010, MNRAS, 404, 1639

Veilleux, S., & Osterbrock, D. E. 1987, ApJS, 63, 295

Vink, J. S. 2020, Galax, 8, 43

Vogelsberger, M., Genel, S., Sijacki, D., et al. 2013, MNRAS, 436, 3031

Vogelsberger, M., Marinacci, F., Torrey, P., & Puchwein, E. 2020, NatRP, 2, 42

Vogelsberger, M., Genel, S., Springel, V., et al. 2014a, MNRAS, 444, 1518

Vogelsberger, M., Genel, S., Springel, V., et al. 2014b, Natur, 509, 177

Voit, G. M., Oppenheimer, B. D., Bell, E. F., Terrazas, B., & Donahue, M. 2024, ApJ, 960, 28

Vollmer, B., Cayatte, V., Balkowski, C., & Duschl, W. J. 2001, ApJ, 561, 708

Von Der Linden, A., Best, P. N., Kauffmann, G., & White, S. D. M. 2007, MNRAS, 379, 867

Vulcani, B., Treu, T., Schmidt, K. B., et al. 2015, ApJ, 814, 161

Vulcani, B., Treu, T., Schmidt, K. B., et al. 2016, ApJ, 833, 178

Vulcani, B., Treu, T., Nipoti, C., et al. 2017, ApJ, 837, 126

Vulcani, B., Fritz, J., Poggianti, B. M., et al. 2020, ApJ, 892, 146

Wake, D. A., Bundy, K., Diamond-Stanic, A. M., et al. 2017, AJ, 154, 86

Walcher, J., Groves, B., Budavári, T., & Dale, D. 2011, Ap&SS, 331, 1

Walters, D., Woo, J., & Ellison, S. L. 2022, MNRAS, 511, 6126

Wang, B., Leja, J., Bezanson, R., et al. 2023a, ApJL, 944, L58

Wang, B., Leja, J., Labbé, I., et al. 2024, ApJS, 270, 12

Wang, D., Lagos, C. D. P., Croom, S. M., et al. 2023b, MNRAS, 523, 6020

Wang, D., Croom, S. M., Bryant, J. J., et al. 2022, MNRAS, 516, 3411

Wang, E., Li, C., Xiao, T., et al. 2018, ApJ, 856, 137

Wang, X., Teplitz, H. I., Smith, B. M., et al. 2025, ApJ, 980, 74

Weaver, J. R., Davidzon, I., Toft, S., et al. 2023, A&A, 677, A184

Weaver, J. R., Cutler, S. E., Pan, R., et al. 2024, ApJS, 270, 7

Weigel, A. K., Schawinski, K., & Bruderer, C. 2016, MNRAS, 459, 2150

Weigel, A. K., Schawinski, K., Caplar, N., et al. 2017, ApJ, 845, 145

Weinberger, R., Springel, V., & Pakmor, R. 2020, ApJS, 248, 32

Weinberger, R., Springel, V., Hernquist, L., et al. 2017, MNRAS, 465, 3291

Weinberger, R., Springel, V., Pakmor, R., et al. 2018, MNRAS, 479, 4056

Werner, M. W., Roellig, T. L., Low, F. J., et al. 2004, ApJS, 154, 1

Wetzel, A. R., Tinker, J. L., & Conroy, C. 2012, MNRAS, 424, 232

Wetzel, A. R., Tinker, J. L., Conroy, C., & van den Bosch, F. C. 2013, MNRAS, 432, 336

Weymann, R. J., Morris, S. L., Foltz, C. B., & Hewett, P. C. 1991, ApJ, 373, 23

Whitaker, K. E., van Dokkum, P. G., Brammer, G., & Franx, M. 2012, ApJL, 754, L29

Whitaker, K. E., Franx, M., Leja, J., et al. 2014, ApJ, 795, 104

White, S. D. M., & Rees, M. J. 1978, MNRAS, 183, 341

Whitney, A., Conselice, C. J., Duncan, K., & Spitler, L. R. 2020, ApJ, 903, 14

Whitney, A., Ferreira, L., Conselice, C. J., & Duncan, K. 2021, ApJ, 919, 139

Williams, C. C., Tacchella, S., Maseda, M. V., et al. 2023, ApJS, 268, 64

Williams, R. J., Quadri, R. F., Franx, M., van Dokkum, P., & Labbé, I. 2009, ApJ, 691, 1879

Willott, C. J., Doyon, R., Albert, L., et al. 2022, PASP, 134, 025002

Windhorst, R. A., Cohen, S. H., Jansen, R. A., et al. 2023, AJ, 165, 13

Windhorst, R. A., Summers, J., Carleton, T., et al. 2025, BAAS, 57

Witt, A. N., & Gordon, K. D. 2000, ApJ, 528, 799

Woo, J., & Ellison, S. L. 2019, MNRAS, 487, 1927

Woosley, S. E., & Weaver, T. A. 1986, ARA&A, 24, 205

Wright, E. L. 1998, ApJ, 496, 1

Wright, G. S., Rieke, G. H., Glasse, A., et al. 2023, PASP, 135, 048003

Wright, R. J., Lagos, C. d. P., Davies, L. J. M., et al. 2019, MNRAS, 487, 3740

Wright, R. J., Lagos, C. d. P., Power, C., et al. 2022, MNRAS, 516, 2891

Wright, R. J., Somerville, R. S., Lagos, C. d. P., et al. 2024, MNRAS, 532, 3417

Wu, H., Shao, Z., Mo, H. J., Xia, X., & Deng, Z. 2005, ApJ, 622, 244

Wuyts, S., Förster Schreiber, N. M., van der Wel, A., et al. 2011, ApJ, 742, 96

Wyder, T. K., Martin, D. C., Schiminovich, D., et al. 2007, ApJS, 173, 293

Yan, R., Bundy, K., Law, D. R., et al. 2016, AJ, 152, 197

York, D. G., Adelman, J., Anderson, Jr., J. E., et al. 2000, AJ, 120, 1579

Yoshida, N., Omukai, K., Hernquist, L., & Abel, T. 2006, ApJ, 652, 6

Yun, K., Pillepich, A., Zinger, E., et al. 2019, MNRAS, 483, 1042

Zhang, C., Peng, Y., Ho, L. C., et al. 2019, ApJL, 884, L52

Zhang, C., Peng, Y., Ho, L. C., et al. 2021, ApJ, 911, 57

Zhang, D. 2018, Galax, 6, 114

Zhang, K., Yan, R., Bundy, K., et al. 2017, MNRAS, 466, 3217

Zheng, X. Z., Hammer, F., Flores, H., Assémat, F., & Pelat, D. 2004, A&A, 421, 847

Zhou, X., Yang, H., Li, N., et al. 2025, A&A, 700, A120

Zibetti, S., Charlot, S., & Rix, H.-W. 2009, MNRAS, 400, 1181

Zinger, E., Pillepich, A., Nelson, D., et al. 2020, MNRAS, 499, 768

Zubovas, K., & King, A. 2012, ApJL, 745, L34

APPENDICES

Appendix A

Appendices from Chapter 2

A.1 Example diagnostic figures for an inside-out quenched galaxy

Here, we show example postage stamps and radial profiles for an inside-out quenched galaxy in Figure A.1, similar to Figure 2.4 above. The projections in the top panels highlight the lack of evolution of the size of the star forming disk when considering its outer extent, but do show strong evolution from the inside out for the star forming particles. The size of the stellar disk remains nearly unchanged, only growing by $\sim$4%. The radial sSFR profiles in the bottom panels show modest evolution from the leftmost panel to the middle panel, but show very strong evolution from the middle to the rightmost panel. In this case, the rightmost panel highlights $R_{\rm inner}$, as there is a clear discontinuity in the sSFR profile for this quenched galaxy, where $R_{\rm inner}/R_{\rm e} \approx 0.5$.

In addition, we show the evolution of the morphological metrics for the same inside-out quenched galaxy in Figure A.2, similar to Figure 2.5 above. This galaxy's morphological evolution is consistent with an inside-out signature, seen through the increase of $R_{\rm SF}$ and $R_{\rm inner}$, along with $C_{\rm SF}$ modestly decreasing. This galaxy shows no evolution for $R_{\rm outer}$, a feature commonly noticed for inside-out quenched galaxies in our sample.

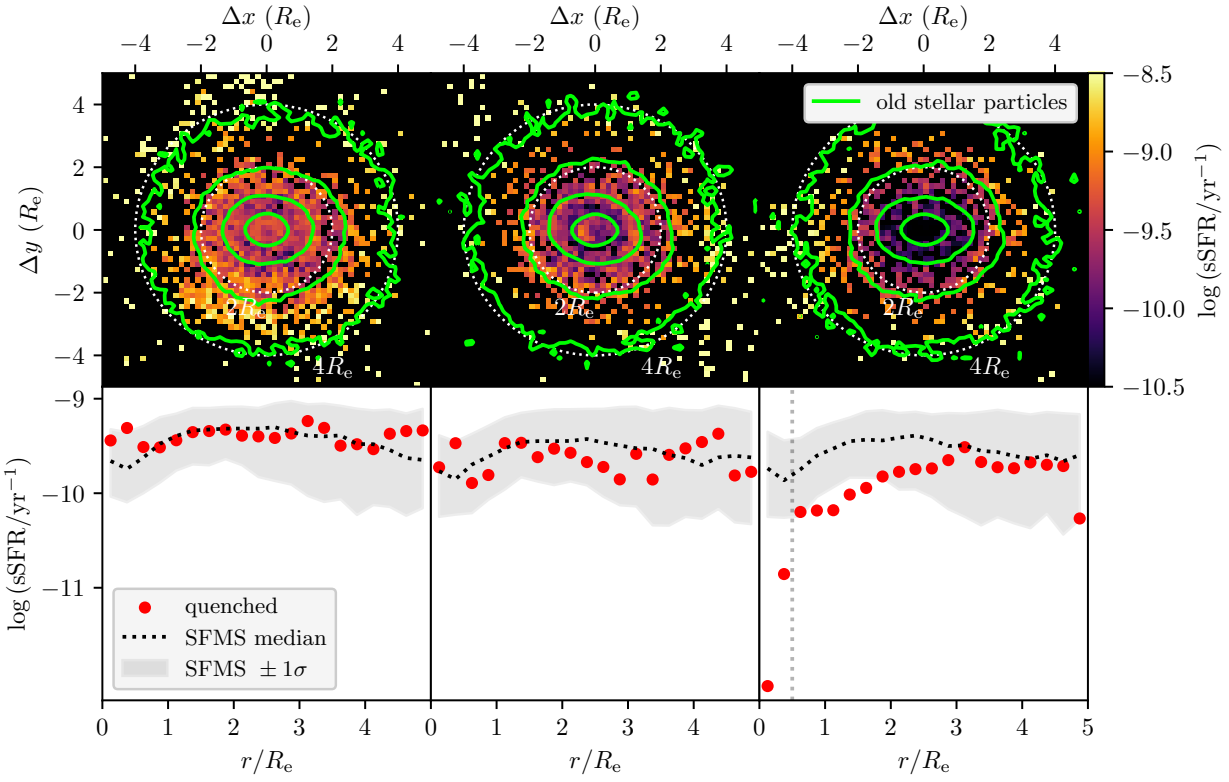


Figure A.1: Similar to Figure 2.4, but now for an example inside-out quenched galaxy. This galaxy has a $z = 0$ stellar mass of $M_* = 10^{10.01}\ M_\odot$, and the time from the leftmost panels to the middle panels is 336 Myr, while the rightmost panels are an additional 306 Myr after the middle panels. The bottom rightmost panel highlights $R_{\rm inner}$ with a vertical dotted line, where $R_{\rm inner}/R_{\rm e} \approx 0.5$. The subhalo ID for this galaxy is 220606 at $z = 0$.

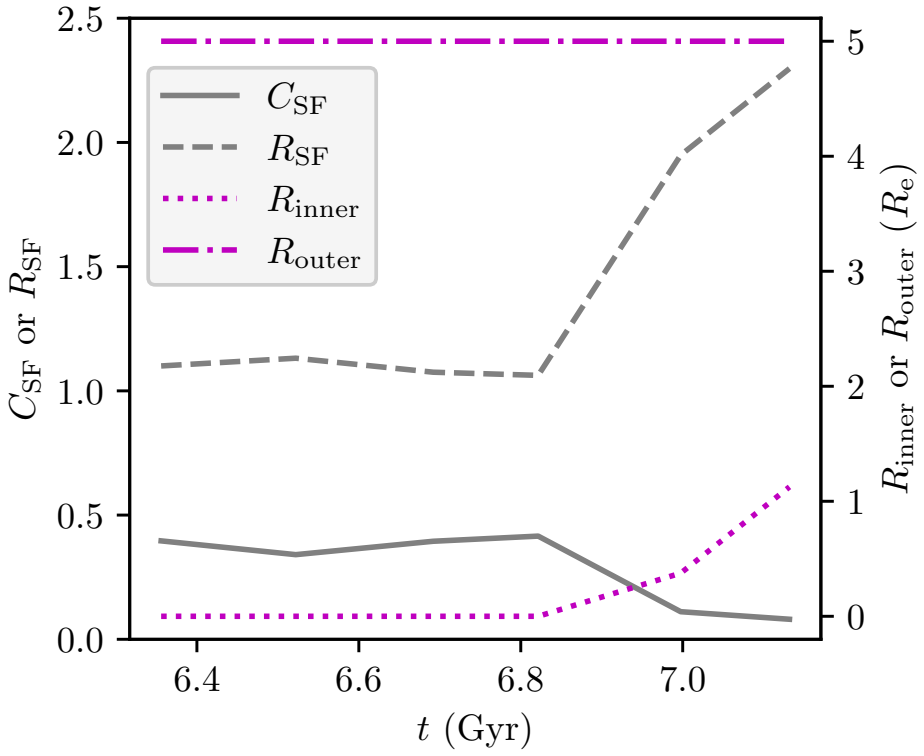


Figure A.2: Similar to Figure 2.5, but now for the same example inside-out quenched galaxy as is shown above in Figure A.1. As above, the left y-axis records the values for $C_{\rm SF}$ and $R_{\rm SF}$, shown in gray solid and dashed lines, respectively. The right y-axis records the values for $R_{\rm inner}/R_{\rm e}$ (dotted magenta line) and $R_{\rm outer}/R_{\rm e}$ (dotted–dashed magenta line). The extent of the x-axis reflects the primary quenching episode for this galaxy, which lasts for <1 Gyr.

A.2 Morphological metrics using 3D positional information

Here, we present comparisons between the morphological metrics in Figure A.3 for the full sample of quenched galaxies and control star forming galaxies. As mentioned above, our full sample comprises 69,493 unique galaxy+snapshot pairs, which we collectively consider unique galaxies, and which we plot in each panel. We compare the default version of the metric (plotted on the x-axis, where 2D positional information was used to compute distances to the stellar particles) to versions using the full 3D positional information to compute distances (y-axis). In all panels, we employ a logarithmic normalization given the large number of data points per plot, and also display a line of equality in gray.

For the concentration of star formation, $C_{\rm SF}$, we find that using the full 3D positional information produces concentration values that are always less than the default 2D versions. This behavior is not unexpected, as the additional information provided in the third dimension is reflected in locations that are more accurate for the stellar particles, and given how the concentration metric is defined, this results in concentration values that are likewise more accurate. We note that the colormap used in this panel creates a false sense of systematic offset, but given the logarithmic normalization that is being used, histogram counts away from the line of equality quickly fall off, with typical values being $\lesssim$100. In general, we find good agreement between the 2D versions of $C_{\rm SF}$ and the 3D versions.

For the disk size ratio, $R_{\rm SF}$, we find excellent agreement between the 2D versions and the 3D versions, with small scatter around the line of equality. Moving away from the line of equality, we quickly find histogram bins that contain very few galaxies or no galaxies at all. For the inner truncation radius, $R_{\rm inner}$, we see that the 3D versions can have modest scatter, especially to slightly higher values, from their 2D counterparts at low $R_{\rm inner}$ values. Beyond $\sim$1.5 $R_{\rm e}$, there is generally very low levels of scatter around the 2D versions, extending to 2 $R_{\rm e}$ and beyond. In general, there exists good agreement between 2D versions and 3D versions of $R_{\rm inner}$, especially at very low $R_{\rm inner}$ values ($\sim$0 $R_{\rm e}$).

Finally, for the outer truncation radius, $R_{\rm outer}$, we find that 3D versions lie along the line of equality or show modest enhancement compared to their 2D counterparts, below $\sim$4 $R_{\rm e}$. Moving above $\sim$4 $R_{\rm e}$, 2D versions can take a slightly broader range of values at a fixed 3D version value, with this trend becoming most noticeable when 3D $R_{\rm outer} \approx 5$ $R_{\rm e}$. Similar to the other metrics previously discussed, in general we find very good agreement between the 2D versions of $R_{\rm outer}$ and the 3D versions, and overall we find agreement for all metrics that ranges from good to excellent. We do not expect that using the 3D versions of our metrics should significantly change the results presented, with only minor effects

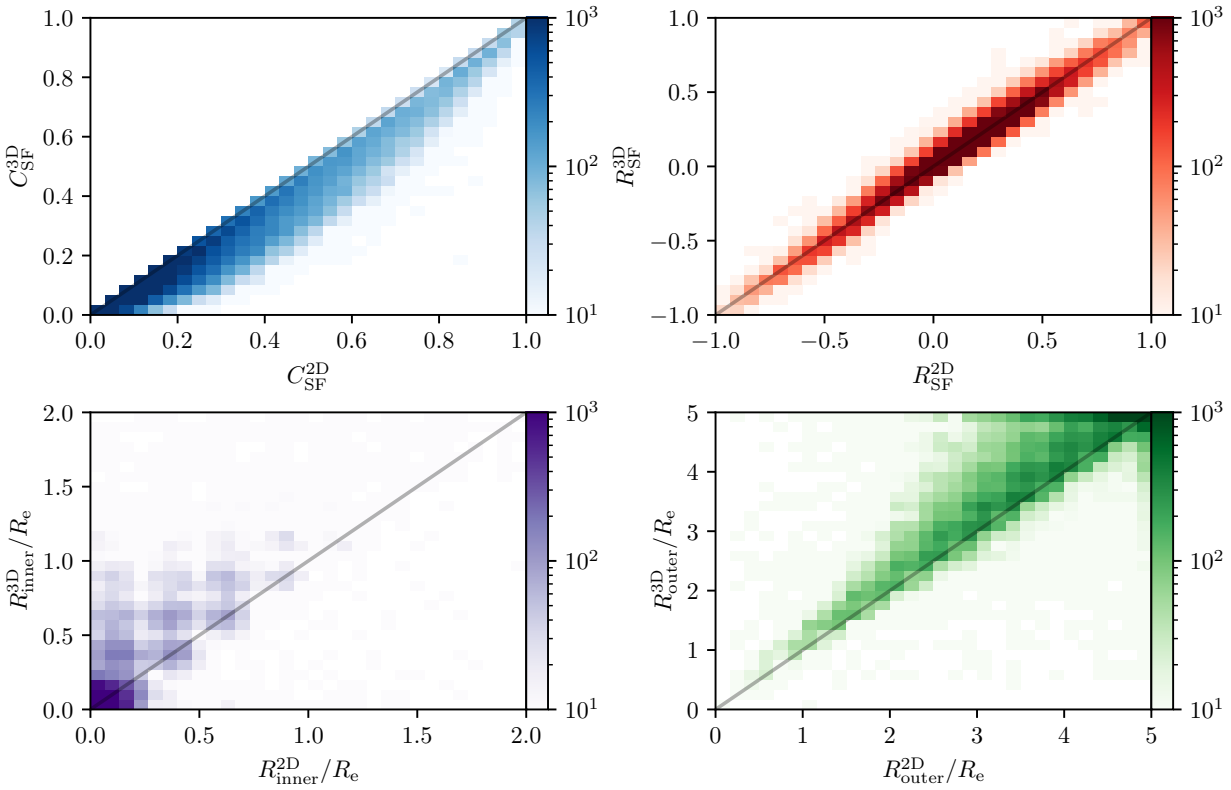


Figure A.3: Comparisons between the morphological metrics using the default versions (x-axis, where 2D positional information is used) and versions using full 3D positional information (y-axis). For all panels, we use 2D histograms to show the density of points, described with the color scale. For the inner truncation radius, we zoom into the region of interest for clarity.

anticipated, especially given the investigation presented in Appendix A.4 (see below).

A.3 Morphological metric evolution plots for the ambiguously quenched class

Here, we present the evolution of the morphological metrics for the ambiguously quenched class in Figure A.4, along with the star forming population for reference. By comparing with Figure 2.8, which shows the evolution of the metrics for normal star forming galaxies, the galaxies that have an inside-out signature, and the galaxies that have an outside-in signature, we can see that, in most cases, the ambiguous class resides in an intermediary space. Specifically, when comparing $C_{\rm SF}$ at early times, the ambiguous class is between the inside-out and outside-in classes, and at later times, it remains between these two classes. For $R_{\rm SF}$, the ambiguous class most closely resembles the star forming class, with little evolution, but with a slight shift to lower values. At late times, the resemblance to the star forming population remains. For $R_{\rm inner}$, the ambiguous class is most similar to the inside-out class at early times, but at late times, it has evolved to sit between the inside-out and star forming classes. Finally, for $R_{\rm outer}$, at early times, the ambiguous class resembles the star forming class, but at late times, it evolves in a similar fashion to the outside-in class, though to a lesser extent. Given the above, it is clear that the ambiguously quenched galaxies do reside in an intermediary parameter space between the inside-out and outside-in quenched populations and are therefore properly classified as such.

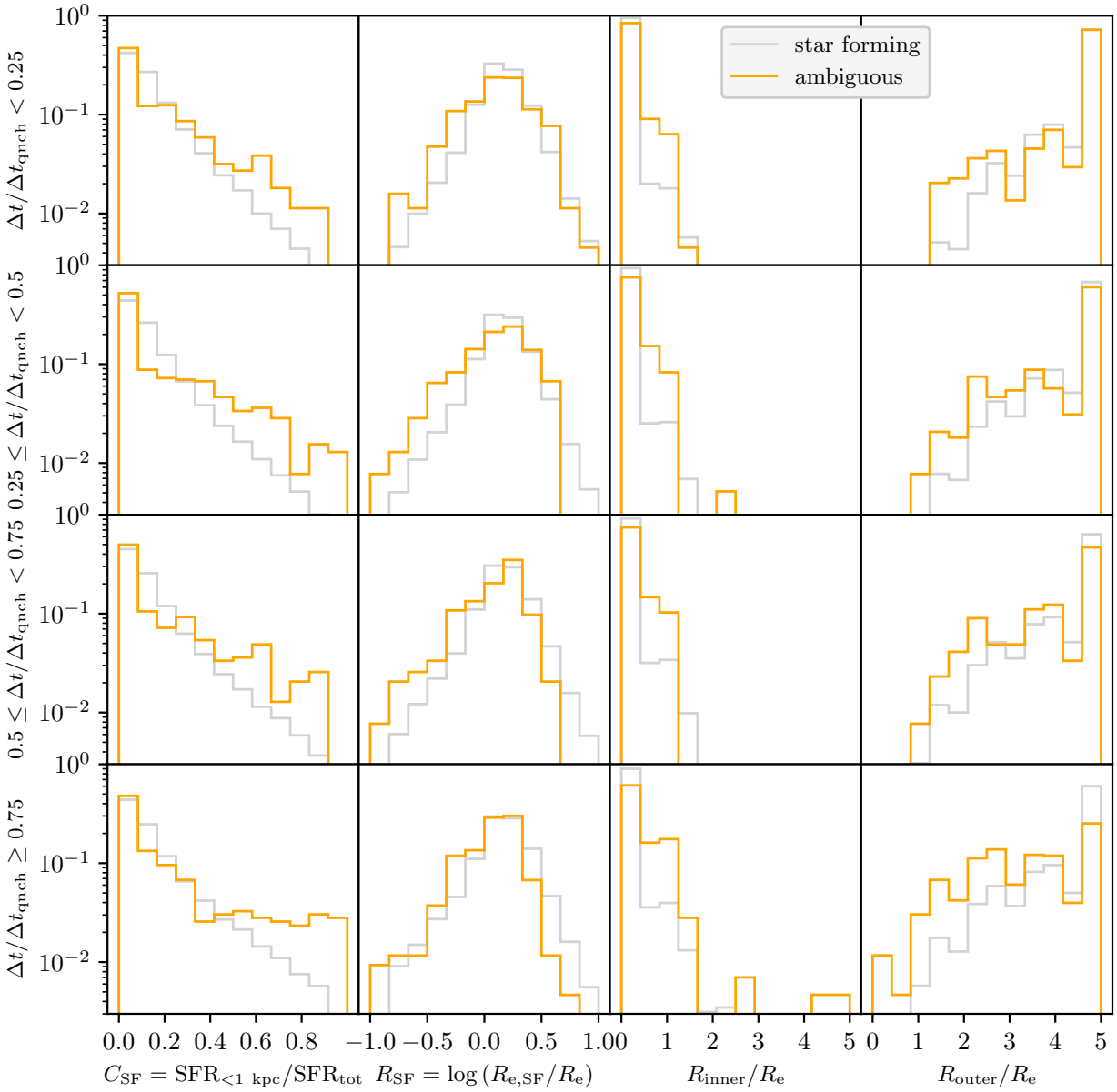


Figure A.4: Morphological metric evolution for the ambiguously quenched class of galaxies, similar to Figure 2.8.

A.4 Relative importance of the morphological metrics

Here, we discuss the relative importance of the morphological metrics when compared to each other for classification and prediction purposes, using a random forest classifier algorithm (Breiman 2001). This algorithm is available in the package `scikit-learn` (Pedregosa et al. 2011) and uses an ensemble of randomized decision trees, where each tree is created from a sample of the training set drawn using bootstrap sampling (sampling with replacement). The algorithm then uses averaging to control for overfitting and to improve the accuracy of predictions (Pedregosa et al. 2011). As in Section 2.3.3, we bin the progress through the quenching episode into deciles, and again randomly select the same number of star forming galaxies as quenched galaxies for each progress bin, using 1000 iterations. We use 100 randomized decision trees per forest.

In Figure A.5, we show the results of this investigation. We find that the ratio between the size of the star forming disk and the stellar disk, $R_{\rm SF}$ (red), is the most important metric for accurately predicting the true population (see Figure 2.10) for all epochs through the quenching episode. We note the relative decrease in importance at late times, but this is compensated with increases in other metrics, as discussed below. The concentration of star formation, $C_{\rm SF}$ (blue), is the second most important metric, especially at early times, but decreases in importance through the quenching episode, notably at very late times. The outer truncation radius, $R_{\rm outer}$ (green), is next most important, with importance values near 0.15 for much of the episode, with a steady increase in importance through the quenching episode clearly visible. This suggests that, at later times, $R_{\rm outer}$ has more distinguishing power (compared to earlier times) for correctly predicting the true population of a given galaxy. Finally, we find that $R_{\rm inner}$ has the lowest importance in general, but that the importance gradually increases with increasing time, similar to $R_{\rm outer}$, with importance $\sim$0.15 at very late times. This indicates that the characteristic radius that traces sharp truncations in the inner part of the star forming disk has more distinguishing power once galaxies have had sufficient time to develop a suppression of star formation in their central regions.

Taken together, these results indicate that no single morphological metric, or even two morphological metrics used simultaneously, would be able to properly classify and predict the true population for a collection of star forming galaxies and inside-out and outside-in quenched galaxies. However, one could argue whether it is necessary to include $R_{\rm inner}$ and $R_{\rm outer}$ in the above analysis, given their low ($<$0.1) importance values at very early times. Regardless, this consideration is beyond the scope of the present work.

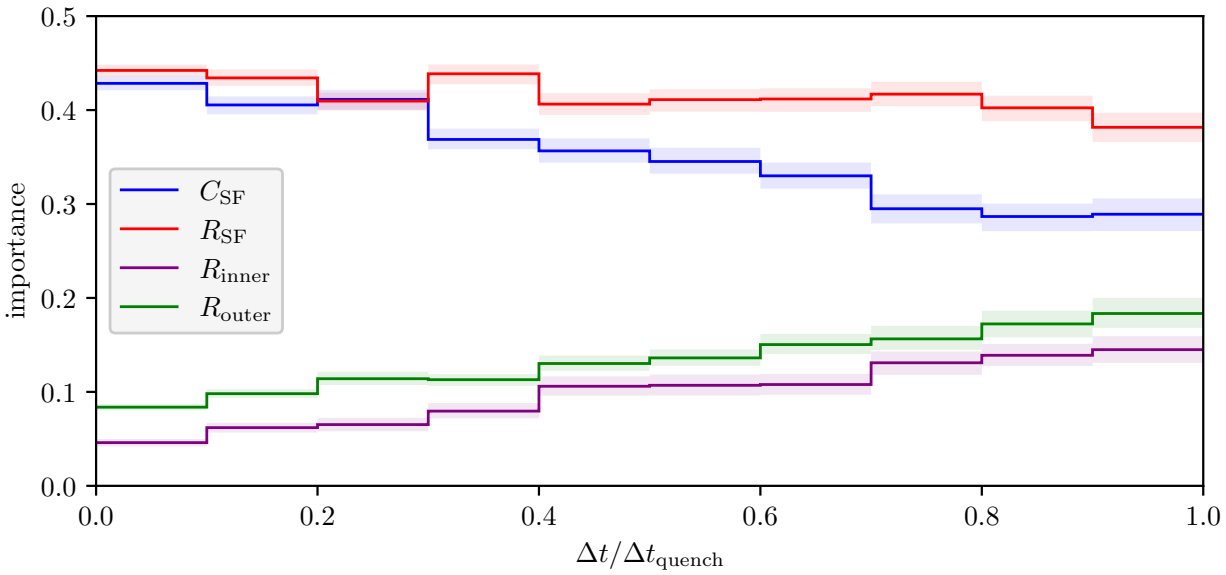


Figure A.5: The importance (mean decrease in impurity, or Gini impurity) of the morphological metrics for accurate classification as a function of progress (time) through the quenching episode. For each metric, $C_{\rm SF}$ (blue), $R_{\rm SF}$ (red), $R_{\rm inner}$ (purple), and $R_{\rm outer}$ (green), we show median values across 1000 iterations as solid lines, with the corresponding shaded contours denoting the $\pm1\sigma$ range. For each iteration, a randomly selected sample of star forming galaxies is chosen to closely mirror the same number of quenched galaxies (inside-out+outside-in).

Appendix B

Appendices from Chapter 3

B.1 Alternative Morphological Metric Adaptations

Here, we present and discuss alternative adaptations to the morphological metrics, as initially described in Section 3.2.6. In the course of identifying appropriate adaptations that must be made for the morphological metrics from Paper I, given that we are applying these metrics to mock observations, we investigated several versions of some of the morphological metrics, namely $C_{\rm SF}$ and $R_{\rm SF}$. In the body of the text we present our preferred observational adaptations that are based on interpolations of cumulative mass profiles for both metrics. These adaptations are preferred as they best recover the morphological metrics as applied in the simulation, as described in Paper I. However, we also examined the recovery using versions based solely on the photometry, without using the fitted SED results.

For $C_{\rm SF}$, we considered the CASTOR *UV* image as a proxy for the star formation rate, and used the luminosity within 1 kpc (projected) and the total integrated luminosity, taking the ratio as $C_{\rm SF}$. We show the results of this investigation in the left panel of Figure B.1. We find a systematic offset to lower values for the photometry-based values, where at a fixed value of $C_{\rm SF}^{\rm TNG}$ the value of $C_{\rm SF}^{\rm phot}$ is almost exclusively lower. However, we do find that $C_{\rm SF}^{\rm phot}$ nearly covers the entire range of $C_{\rm SF}^{\rm TNG}$ values, as we might expect. The median difference and scatter are 0.03 and 0.07, respectively, when considering all values, and 0.03 and 0.06 when considering $C_{\rm SF}^{\rm TNG} \leqslant 0.5$. These results indicate that solely relying on the CASTOR *UV* photometry to form an observational proxy for $C_{\rm SF}$ is an appropriate starting point, but completing SED fitting is crucial to recover the associated star formation rate (and profile) from which $C_{\rm SF}$ is best derived.

For $R_{\rm SF}$, we similarly considered the CASTOR UV image as a proxy for the star formation rate and the NGRST H-band image as a proxy for the stellar mass. For both images, we determined the radius enclosing half of the total flux, taking these radii as proxies for the effective radii, respectively. Finally, we use the logarithm of the ratio of these radii as $R_{\rm SF}$. As above, we show the results of this alternative parametrization in the right panel of Figure B.1. We find that using the photometry alone produces $R_{\rm SF}^{\rm phot}$ values with less range compared to their $R_{\rm SF}^{\rm TNG}$ counterparts, where the values for $R_{\rm SF}^{\rm phot}$ almost exclusively lie between -0.5 and 0.5. Taken alone, this reduced range is not critically detrimental, but in addition, there exists an apparent rotation of the shape of the distribution, where values of $R_{\rm SF}^{\rm phot}$ at low $R_{\rm SF}^{\rm TNG}$ are above the line of equality (gray), while those at high values of $R_{\rm SF}^{\rm TNG}$ are below the line of equality. The median difference and scatter are -0.03 dex and 0.19 dex, respectively, for all values, -0.20 dex and 0.21 dex for $R_{\rm SF}^{\rm TNG} < 0$, and 0.01 dex and 0.12 dex for $R_{\rm SF}^{\rm TNG} \geqslant 0$. As above, these results indicate that completing SED fitting is necessary in order to best find observational proxies for $R_{\rm SF}$ with a similar range and with small non-systematic offsets.

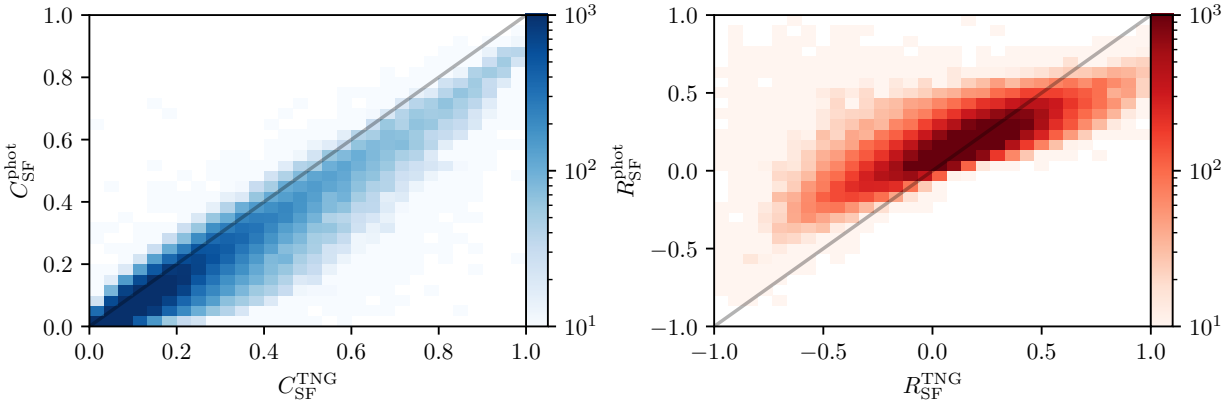


Figure B.1: Similar to the top panels of Figure 3.7, comparisons of the alternative observational proxies of the morphological metrics using only the photometry as a function of the morphological metrics as computed using TNG. In both panels, we show 2D histograms where the color scale describes the density of points, and a line of equality is shown in gray.

Appendix C

Appendices from Chapter 4

C.1 Filters per Cluster/Field

Here, we tabulate the available filters per cluster/field for the Frontier Fields. In Table C.1, for each cluster we show the available HST filters, as well as the passbands available for that cluster's parallel field.

Table C.1: Available HST filters per pointing (clusters and parallel fields).

Cluster	Cluster Filters	Parallel Filters
Abell 2744	*UV'*, *u*, *B*, V^{W}, *I*, *Y*, *J*, *JH*, *H*	*B*, V^{W}, *I*, *Y*, *J*, *JH*, *H*
Abell 370	*UV'*, *u*, *B*, *g*, V^{W}, *r*, *I*, *Y*, Y^{W}, *J*, *JH*, *H*	*B*, V^{W}, *I*, *Y*, *J*, *JH*, *H*
MACS J0416	*UV*, *UV'*, *u*, *C*, *B*, *g*, V^{W}, *r*, *i*, *I*, *z*, *Y*, Y^{W}, *J*, *JH*, *H*	*B*, V^{W}, *i*, *I*, *z*, *Y*, *J*, *JH*, *H*
MACS J0717	*UV*, *UV'*, *u*, *C*, *B*, *g*, *V*, V^{W}, *r*, *i*, *I*, *z*, *Y*, Y^{W}, *J*, *JH*, *H*	*B*, V^{W}, *I*, *Y*, *J*, *JH*, *H*
MACS J1149	*UV*, *UV'*, *u*, *C*, *B*, *g*, *V*, V^{W}, *r*, *i*, *I*, *z*, *Y*, Y^{W}, *J*, *JH*, *H*	*B*, V^{W}, *I*, *Y*, *J*, *JH*, *H*
Abell S1063	*UV*, *UV'*, *u*, *C*, *B*, *g*, V^{W}, *r*, *i*, *I*, *z*, *Y*, Y^{W}, *J*, *JH*, *H*	*B*, V^{W}, *I*, *Y*, *J*, *JH*, *H*

C.2 IllustrisTNG and Phase Space Diagrams

As described in Section 4.2.3, we followed the method of Dou & Yu (2025) to determine infall time (e.g., Oman et al. 2013; Oman & Hudson 2016; Rhee et al. 2017; Pasquali

et al. 2019) for our clusters galaxies based on location in phase space (e.g., Diaferio 1999; Mahajan et al. 2011). Here, we describe the method of Dou & Yu (2025), beginning with a description of the IllustrisTNG simulations, that they use to determine the orbital histories of simulated galaxies.

The IllustrisTNG simulations[1] (e.g., Nelson et al. 2018; Pillepich et al. 2018a; Springel et al. 2018) are the successor to the original Illustris simulation (Genel et al. 2014; Vogelsberger et al. 2014b,a), and are cosmological grave-magneto-hydrodynamical simulations with a revised galaxy formation model (Weinberger et al. 2017; Pillepich et al. 2018b) that builds on that used in Illustris (Vogelsberger et al. 2013; Torrey et al. 2014). Using a cosmology consistent with the Planck Collaboration et al. (2016) results, IllustrisTNG employs the moving-mesh code AREPO (Springel 2010; Pakmor et al. 2011, 2016; Weinberger et al. 2020), and draws stellar populations from the Chabrier (2003) initial mass function (Pillepich et al. 2018b). As detailed in Rodriguez-Gomez et al. (2019), the IllustrisTNG model aims to reproduce several observable phenomena at $z = 0$, including the galaxy mass function, the stellar mass–halo mass relation, the black hole–stellar mass relation, as well as halo gas fractions and galaxy sizes. Further, the model is tuned to match observations of the global star formation density from $z = 8$ to $z = 0$ (Rodriguez-Gomez et al. 2019). All simulation data from IllustrisTNG are publicly available (Nelson et al. 2019a).

As stated above, we use TNG300 (Nelson et al. 2019a) and TNG-Cluster (Nelson et al. 2024) for our analysis. TNG300 contains a cubic volume of $205h^{-1} \approx 302.6$ Mpc on a side, and follows the evolution of 2×2500^3 resolution elements (dark matter and baryons), with an average baryon particle mass of $1.1 \times 10^7\ M_\odot$ (Nelson et al. 2018; Pillepich et al. 2018a; Springel et al. 2018). For our purposes, the critical quantity is the number of galaxy clusters that the TNG300 simulation contains, which numbers 239 clusters with $10^{14.0} \leqslant M_{\rm halo}/M_\odot \leqslant 10^{14.5}$ at $z = 0$ (Pillepich et al. 2018a; Nelson et al. 2024), but that shows a steep drop off in the halo mass function beyond $M_{\rm halo} \sim 10^{14.6}\ M_\odot$ (Pillepich et al. 2018a; Nelson et al. 2024). Indeed, in TNG300, there exist only 41 clusters with $M_{\rm halo} \geqslant 10^{14.5}\ M_\odot$, and of these, only three have $M_{\rm halo} \geqslant 10^{15.0}\ M_\odot$ (Pillepich et al. 2018a; Nelson et al. 2024). In total, there are 280 clusters with $M_{\rm halo} \geqslant 10^{14.0}\ M_\odot$ in TNG300 at $z = 0$ (Pillepich et al. 2018a; Nelson et al. 2024).

To better sample the high mass end of the halo mass function, we additionally use the recently available follow-up TNG-Cluster[2] simulation (Nelson et al. 2024). The objective of the TNG-Cluster simulation is to substantially increase the statistical sampling of massive galaxy clusters with $M_{\rm halo} \gtrsim 10^{15.0}\ M_\odot$ (Nelson et al. 2024). It does this by encompassing

[1] https://www.tng-project.org
[2] https://www.tng-project.org/cluster

a cubic volume of $680h^{-1} \approx 1003.8$ Mpc on a side, following the evolution of 2×8192^3 resolution elements[3] (dark matter and baryons), with an average baryon particle mass of $1.2 \times 10^7\ M_\odot$ (thereby matching the resolution of TNG300; Nelson et al. 2024), while maintaining the IllustrisTNG galaxy model of Weinberger et al. (2017) and Pillepich et al. (2018b). TNG-Cluster also uses a cosmology consistent with the Planck Collaboration et al. (2016) results (Nelson et al. 2024). Critically, TNG-Cluster contains 356 clusters with $M_{\rm halo} \geqslant 10^{14.0}\ M_\odot$ at $z = 0$, where 207 have $10^{14.5} \leqslant M_{\rm halo}/M_\odot \leqslant 10^{15.0}$, and 92 are more massive than $M_{\rm halo} = 10^{15.0}\ M_\odot$ (Nelson et al. 2024). Though TNG-Cluster technically re-simulates 352 clusters drawn from a much larger 1 Gpc^3 volume (Nelson et al. 2024), in practice, the results from the TNG-Cluster simulation can be analyzed analogously to those from TNG300. By combining these two large volume simulations, TNG300 and TNG-Cluster, the halo mass distribution becomes flattened from $M_{\rm halo} = 10^{14.0}\ M_\odot$ to $M_{\rm halo} = 10^{15.1}\ M_\odot$, showing a steep drop off after $M_{\rm halo} \sim 10^{15.2}\ M_\odot$ (Nelson et al. 2024). In total, we have 636 simulated clusters at $z = 0$ with $M_{\rm halo} \geqslant 10^{14.0}\ M_\odot$, and using earlier snapshots within the simulation (i.e. higher redshifts) that match the Frontier Fields cluster redshifts, we can therefore track the orbital history of thousands of simulated galaxies, thereby robustly sampling the available phase space.

We note that though Dou & Yu (2025) refer to "phase space" when considering the full three-dimensional components of their simulated galaxies, and use "projected phase space" for their two-dimensional counterparts, here we simply use phase space to discuss the projected two-dimensional version for simplicity.

Dou & Yu (2025) began by selecting simulated clusters from the $z = 0$ snapshot, limiting their analysis to those with $M_{\rm halo} \geqslant 10^{14}\ M_\odot$. They then implemented a requirement that all cluster galaxies must reside within $3R_{200}$ for a cluster to be considered valid, in order to reduce the impact of cluster mergers on the orbital histories of the galaxies (Dou & Yu 2025). Dou & Yu (2025) then use the central galaxies (i.e. BCGs) embedded within the halo as proxies to track the positions and motions of the clusters, where these central galaxies almost always remain at the center of a given cluster. Dou & Yu (2025) further exclude any clusters where the central galaxy is misclassified in more than three consecutive snapshots, as can sometimes happen at high redshift. These misclassifications may be related to the "subhalo switching problem" (Rodriguez-Gomez et al. 2015) that was encountered in Paper I. For all remaining clusters, Dou & Yu (2025) then select the satellite galaxies associated with each cluster, removing central galaxies as well as those that passed through a cluster and subsequently exited (i.e. temporary infall galaxies). Dou & Yu (2025) use a mass limit of $M_* \geqslant 10^9\ M_\odot$ for their galaxies to ensure that they are

[3]The quoted number of resolution elements represents the effective full-volume equivalent (Nelson et al. 2024).

well resolved, consistent with Pillepich et al. (2018a).

Dou & Yu (2025) then construct the phase space diagram by aligning the line-of-sight direction with each of the simulation coordinate axes, thereby tripling their sample size. The line-of-sight velocity is simply the velocity component along the line of sight, while the projected radius, $R_{\rm 2D}$, is the Euclidean distance from a given galaxy to the central galaxy on the projected plane (Dou & Yu 2025). Individual clusters are stacked together after normalizing the projected radii by R_{200}, and the line-of-sight velocities by the line-of-sight velocity dispersions, $\sigma_{\rm LoS}$ (Dou & Yu 2025). A Hubble flow correction is additionally applied along the line of sight using the components of the cluster-centric velocity and radial vectors (Dou & Yu 2025). Dou & Yu (2025) then leverage the merger trees for each galaxy, tracking back along the main branch of the progenitor tree (e.g., Genel et al. 2018; Nelson et al. 2019b) to determine when a galaxy first fell into a cluster. They define the infall time, $t_{\rm infall}$, as the lookback time when a galaxy first crosses $3R_{200}$ of the cluster (Dou & Yu 2025). By stacking their clusters, Dou & Yu (2025) are then able to determine median infall times based on location in phase space (e.g., see the top right panel of their Figure 2).

We use the TNG300-1 (hereafter TNG300; Nelson et al. 2019a) simulation, along with the TNG-Cluster (Nelson et al. 2024) follow-up simulation for our analysis. In our analysis, we extend the work of Dou & Yu (2025), who completed their investigation at $z = 0$, to snapshots 64–79, that cover the redshifts of our Frontier Fields cluster sample ($0.27 < z < 0.58$). Though Dou & Yu (2025) only used the TNG300 simulation in their investigation, we additionally adopt the TNG-Cluster simulation to improve statistics, especially at high halo masses. We limit our analysis along halo and galaxy histories to $z \leqslant 4$ (snapshot 21) to reduce computation time. We use the same simulated galaxy mass and halo mass limits as Dou & Yu (2025), where we require $M_* \geqslant 10^9\ M_\odot$ for galaxies, and $M_{\rm halo} \geqslant 10^{14}\ M_\odot$ for clusters. By binning the resulting phase space plots we are able to determine median infall times computed on a per-snapshot (redshift) basis, based on location in phase space. In practice we use bilinear interpolation when considering the phase space at a single snapshot. By next employing the full redshift range ($z = 0.58$ to $z = 0.27$, as above) of the resulting phase space diagrams, we can determine the infall time of a given galaxy using

$$t_{\rm infall} = t_{\rm median}(R, V, t_{\rm lb}), \tag{C.1}$$

where $t_{\rm median}$ is the median infall time, and is a function of (normalized) position in phase space, $R = R_{\rm 2D}/R_{200}$ and $V = V_{\rm LoS}/\sigma_{\rm LoS}$, as well as the lookback time, $t_{\rm lb}$, of the redshift (i.e. snapshot) under consideration. We correspondingly use trilinear interpolation to determine $t_{\rm infall}$ after accounting for lookback time. Beyond the infall time for our sample galaxies, we can similarly follow Dou & Yu (2025) to determine the associated root mean

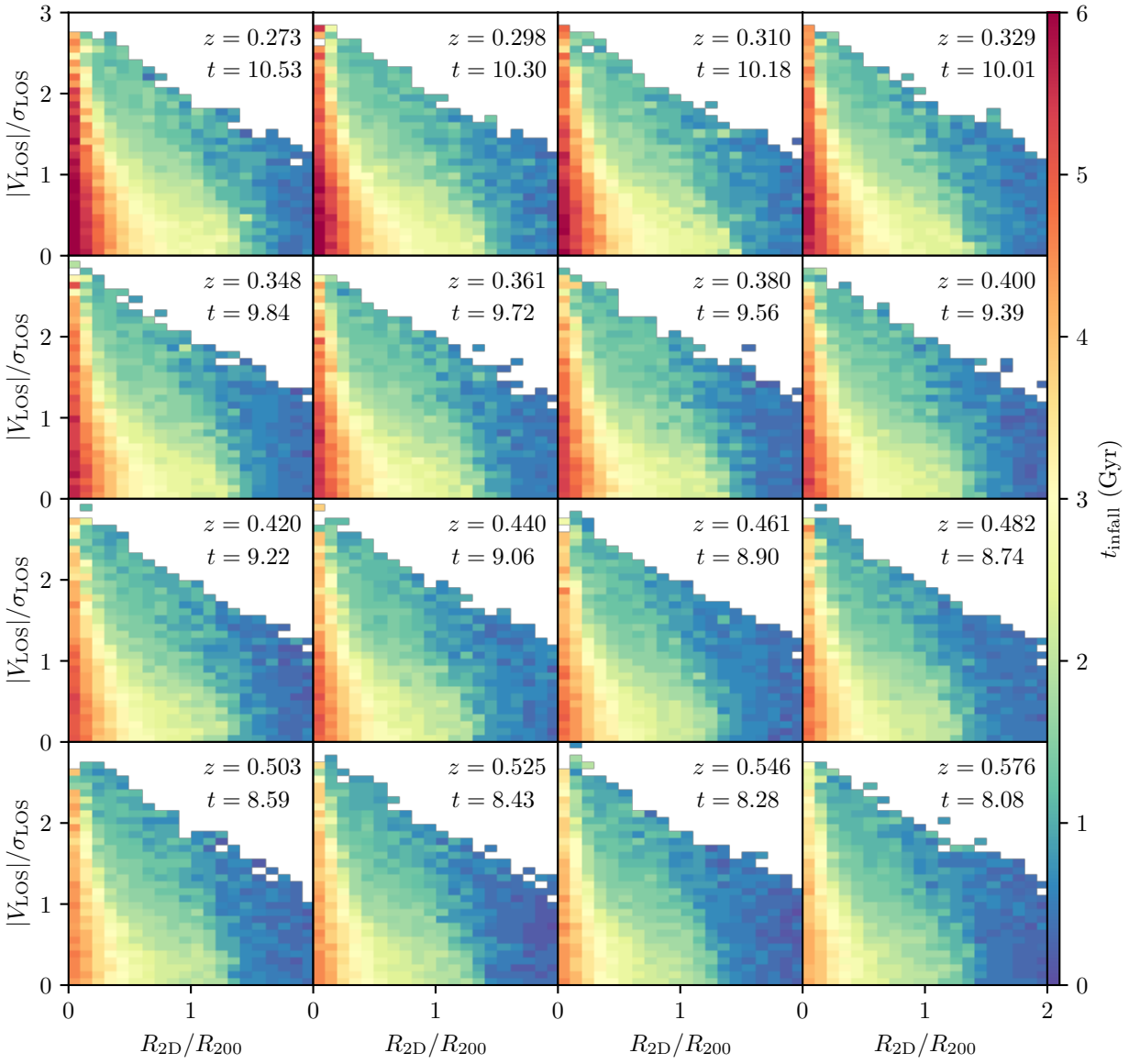


Figure C.1: Phase space diagrams showing the median infall time (in Gyr) per bin for snapshots 64–79. In each panel, the corresponding redshift, z, along with the age of the Universe at that redshift, t (measured in Gyr), are shown in the upper right corners.

square error (RMSE) for the infall times, adopting our extensions to arbitrary redshift as described. Through this process, from snapshot 64–79 we employ >500 simulated clusters per snapshot (median 592), with >90,000 simulated galaxies per snapshot (median 102,000), to determine median infall times. In Figure C.1, we show the resulting phase space diagrams for snapshots 64–79 which show the median infall time in Gyr.

C.3 SED Fitting Procedure for COSMOS-Web

The COSMOS-Web team has produced catalogs of stellar population parameters, including stellar masses and global star formation rates, for galaxies present in the COSMOS survey footprint (Shuntov et al. 2025). We select all secure (`warn_flag = 0`) galaxies (`type = 0`) from the photometric catalog with `LePhare`-derived (Arnouts et al. 1999, 2002; Ilbert et al. 2006) photometric redshifts between $0.25 \leqslant z \leqslant 0.6$, and also require that the photometric redshifts are of high quality: $\sigma_{z,\mathrm{norm}} = (z_{84} - z_{16})/2(1 + z_{50}) \leqslant 0.1$, where z_{50}, z_{84}, and z_{16} are the tabulated median, upper, and lower 1σ confidence values, respectively, computed from the photometric redshift probability distribution functions (Shuntov et al. 2025). The COSMOS-Web galaxy properties we adopt are determined using the `CIGALE` (Boquien et al. 2019) SED modeling code through a Bayesian-like analysis (Arango-Toro et al. 2025; Shuntov et al. 2025), that uses a nonparametric star formation history (Ciesla et al. 2023, 2024), Bruzual & Charlot (2003) stellar population models, the Dale et al. (2014) dust emission library, and a modified Calzetti et al. (2000) attenuation law, as described in Arango-Toro et al. (2025). Arango-Toro et al. (2025); Shuntov et al. (2025) use 27 filters when completing their SED fitting with `CIGALE`, with coverage from the ultraviolet to the mid-infrared, including archival HST/ACS imaging, as well as JWST/Near Infrared Camera (NIRCam; Rieke et al. 2023b; Rigby et al. 2023) and JWST/Mid-Infrared Instrument (MIRI; Wright et al. 2023) data. From the `CIGALE`-derived catalogs we adopt the inferred stellar masses and star formation rates for the galaxies that meet our quality cuts described above.

During our SFMS determination as described above in Section 4.3.3, we additionally investigated the evolution of the SFMS and the resulting fits, by binning the COSMOS-Web galaxies into three redshift bins: $0.25 \leqslant z \leqslant 0.36$, $0.36 \leqslant z \leqslant 0.48$, and $0.48 \leqslant z \leqslant 0.6$. Though we find some evolution across the three considered redshift bins, this evolution is very gentle when we ultimately consider the effect that it has on our sample of Frontier Fields galaxies, where it shifts the number of SFMS and green valley galaxies by a modest amount, on the order of less than tens of galaxies. Given this, we opted to use a single fit for the entire considered redshift range, $0.25 \leqslant z \leqslant 0.6$.

C.4 Morphological Metric Distributions for Star Forming Galaxies

Here, we compare the distributions of the morphological metrics for kNN-classified star forming galaxies in the Frontier Fields with star forming galaxies drawn from the TNG simulation, as described in Paper I. These kNN-classified star forming galaxies number 556 galaxies from the non-quenched primary sample of 1437 galaxies, and predominantly reside in the field ($\sim$76%), though there are a number found in the cluster (131). In Figure C.2, we show the Frontier Fields distributions with solid lines, while the distributions for the simulated galaxies are shown with dashed lines. As in Section **??**, we find very good agreement between the respective distributions for each morphological metric. As above, applying a two-sample KS test, we find that, for each metric, the distribution for the Frontier Fields galaxies is consistent with being drawn from the same distribution as the simulated galaxies. As stated earlier, though we do not focus on this collection of star forming galaxies, the similarity of these distributions, in combination with the results of the KS test, serve as a broad consistency check. These results are encouraging, and suggest that the kNN classification can properly identify star forming galaxies in the Frontier Fields on the basis of their morphological metrics, when trained on unrelated star forming galaxies drawn from the TNG50 simulation.

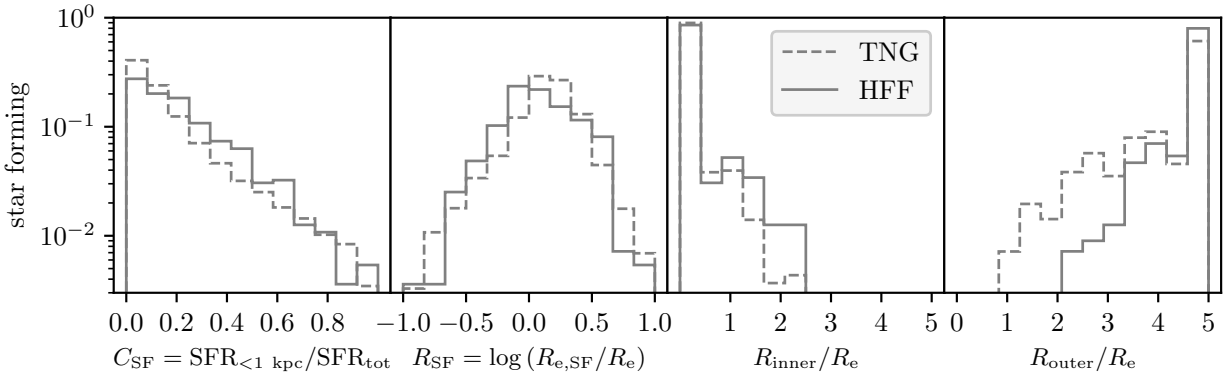


Figure C.2: Similar to Figure 4.5, the morphological metric distributions (columns) for kNN-classified star forming galaxies (solid lines), compared with the corresponding distributions for the simulated galaxies (dashed lines). From left to right, the columns show $C_{\rm SF}$, $R_{\rm SF}$, $R_{\rm inner}$, and $R_{\rm outer}$, respectively, and each distribution has been normalized so that the y-axis can be read as frequency.

C.5 Overlap with CANUCS and UNCOVER

Here, we consider the number and prevalence of galaxies that populate the green valley in the SFR–stellar mass plane (e.g., Figure 4.7), given that we might expect a dominant star forming population based on the additional observations of the flanking/parallel fields. Correspondingly, this would then produce a minority population of green valley galaxies. In particular, we compare with other large programs targeting the Frontier Fields clusters, and consider the results from CANUCS (Willott et al. 2022; Sarrouh et al. 2026) and UNCOVER (Bezanson et al. 2024). Both CANUCS and UNCOVER have produced catalogs of stellar population parameters, including stellar masses and integrated star formation rates, for galaxies present in the Frontier Fields (Wang et al. 2023a, 2024) and flanking fields (Sarrouh et al. 2026). The CANUCS observations include Abell 370, MACS J0416, and MACS J1149 (Willott et al. 2022), while the UNCOVER observations consider Abell 2744 (Bezanson et al. 2024).

Regarding the CANUCS observations, the galaxy properties were determined using the SED fitting code `Bagpipes` (Carnall et al. 2018, 2019) with a Calzetti et al. (2000) dust attenuation law, a Chabrier (2003) initial mass function, Bruzual & Charlot (2003) stellar models, and nebular emission from Ferland et al. (2017), as described in Sarrouh et al. (2026). Sarrouh et al. (2026) use a parametric double power law star formation history, that allows for a rising and falling component, and use the broadband photometric data from CANUCS, the medium and narrowband follow-up "JWST in Technicolor" (GO 3362; PI: A. Muzzin), and archival HST/ACS and HST/WFC3 imaging, spanning from the rest-frame ultraviolet to the near-infrared.

Regarding the UNCOVER observations, the galaxy properties are inferred using the `Prospector` inference code (Leja et al. 2017, 2019a; Johnson et al. 2021) with simple stellar populations drawn from the Flexible Stellar Population Synthesis package (Conroy & Gunn 2010), along with MIST stellar isochrones (Choi et al. 2016; Dotter 2016), using the MILES stellar library (Sánchez-Blázquez et al. 2006), as described in Wang et al. (2023a, 2024). Wang et al. (2023a) employ a nonparametric star formation history, using seven logarithmically-spaced time bins (Leja et al. 2017), and use the complete set of broadband photometric data from UNCOVER (Bezanson et al. 2024; Weaver et al. 2024), the medium-band follow-up MegaScience (Suess et al. 2024), and all available archival HST/ACS and HST/WFC3 imaging, spanning from the rest-frame ultraviolet to the near-infrared. For both the UNCOVER and CANUCS catalogs, we adopt their median stellar mass estimates, along with their median time-averaged ($\Delta t = 100$ Myr) star formation rates.

To the best of our knowledge, no team has yet produced large catalogs of galaxy physical properties for galaxies in Abell S1063 or MACS J0717, though the Vast Exploration for

Nascent Unexplored Sources[4] (VENUS; GO 6882; PIs: S. Fujimoto and D. Coe) program has plans to release such catalogs in late 2026. These catalogs will include stellar population parameters for galaxies in the 60 massive lensing clusters that make up the VENUS program, including Abell S1063 and MACS J0717. Additionally, though the GLIMPSE program (Atek et al. 2025) has released photometric catalogs, catalogs tabulating galaxy physical properties based on SED fitting have yet to be published. Nonetheless, by considering the galaxies available from the UNCOVER and CANUCS programs across the four available Frontier Fields clusters, and by adopting similar redshift limits ($0.14 \leqslant z \leqslant 0.67$) and stellar mass limits ($M_* \geqslant 10^8\ M_\odot$) as above, we arrive at a supplementary sample of some 4700 galaxies from which we can compare with the distribution of our galaxies in the SFR–stellar mass plane. While we do not have comparison galaxies for Abell S1063 and MACS J0717, MACS J0717 is close in redshift to MACS J1149 (see Table 4.1), that is sampled. As well, Abell S1063 sits at a redshift intermediate between Abell 2744 and Abell 370, both of which are sampled.

We find substantial overlap in the SFR–stellar mass plane between the locations of our non-quenched primary sample galaxies and galaxies included in UNCOVER and CANUCS. This suggests that though we do not find a dominant star forming population, even when including the parallel fields, this population is similarly absent in the UNCOVER and CANUCS samples. Given this, we are confident that there are no systematic effects in our SED fitting procedure that lead to suppressed SFRs, and that the inferred stellar masses and SFRs are qualitatively robust against different SED fitting procedures. Furthermore, given that the Frontier Fields target massive lensing clusters, the lack of a dominant star forming population is not completely unexpected (e.g., Lewis et al. 2002; Gómez et al. 2003; Kauffmann et al. 2004).

[4] https://jwst-venus.github.io

Appendix D

Technical Acknowledgments

This research is based on observations made with the NASA/ESA Hubble Space Telescope obtained from the Mikulski Archive for Space Telescopes at the Space Telescope Science Institute, which is operated by the Association of Universities for Research in Astronomy, Inc., under NASA contract NAS 5-26555. These observations are associated with programs 09722, 10420, 10493, 10793, 11103, 11108, 11507, 11582, 11591, 11689, 12068, 12103, 12458, 12459, 13386, 13389, 13459, 13495, 13496, 13498, 13504, 13790, 14037, 14038, 14041, 14209, 14216. This work is additionally based on data and catalog products from HFF-DeepSpace, funded by the National Science Foundation and Space Telescope Science Institute.

The IllustrisTNG simulations were undertaken with compute time awarded by the Gauss Centre for Supercomputing (GCS) under GCS Large-Scale Projects GCS-ILLU and GCS-DWAR on the GCS share of the supercomputer Hazel Hen at the High Performance Computing Center Stuttgart (HLRS), as well as on the machines of the Max Planck Computing and Data Facility (MPCDF) in Garching, Germany. The TNG-Cluster simulation has been executed on several computer clusters: with compute time awarded under the TNG-Cluster project on the HoreKa supercomputer, funded by the Ministry of Science, Research and the Arts Baden-Württemberg and by the Federal Ministry of Education and Research; the bwForCluster Helix supercomputer, supported by the state of Baden-Württemberg through bwHPC and the German Research Foundation (DFG) through grant INST 35/1597-1 FUGG; the Vera cluster of the Max Planck Institute for Astronomy (MPIA), as well as the Cobra and Raven clusters, all three operated by the MPCDF; and the BinAC cluster, supported by the High Performance and Cloud Computing Group at the Zentrum für Datenverarbeitung of the University of Tübingen, the state of Baden-Württemberg through bwHPC and the German Research Foundation (DFG) through grant no INST 37/935-1 FUGG.

The authors acknowledge the use of the Canadian Advanced Network for Astronomy Research (CANFAR) Science Platform operated by the Canadian Astronomy Data Center (CADC) and the Digital Research Alliance of Canada (DRAC), with support from the National Research Council of Canada (NRC), the Canadian Space Agency (CSA), CANARIE, and the Canadian Foundation for Innovation (CFI).

This research has made use of the Astrophysics Data System, funded by NASA under Cooperative Agreement 80NSSC25M7105, as well as `TOPCAT`,[1] an interactive graphical viewer and editor for tabular data (Taylor 2005), in addition to `Astropy`,[2] a community-developed core Python package and an ecosystem of tools and resources for astronomy (Astropy Collaboration et al. 2013, 2018, 2022), and `Photutils`, an Astropy package for detection and photometry of astronomical sources (Bradley et al. 2025).

[1] https://www.star.bris.ac.uk/∼mbt/topcat
[2] https://www.astropy.org